

https://dspace.org/

# Hollow and hemispherical bowl-like hollow carbon spheres and their doped counterparts as supports for platinum for use in fuel cell oxygen reduction reactions

**Mashindi, Victor**

**2021**

https://hdl.handle.net/10539/32296

Downloaded from a DSpace repository. https://dspace.org/

# Hollow and hemispherical bowl-like hollow carbon spheres and their doped counterparts as supports for platinum for use in fuel cell oxygen reduction reactions.

**by**

## Victor Mashindi

## Student number: 1589881

**Supervisors: Prof Neil. J. Coville**

**: Prof Kenneth. I. Ozoemena**

**: Dr Pieter. B. Levecque**

**Johannesburg, November 2020**

Submitted to the Faculty of Science, University of the Witwatersrand, Johannesburg, as part of the requirements for the Degree of Doctor of Philosophy in Chemistry

UNIVERSITY OF THE
WITWATERSRAND,
JOHANNESBURG

# Declaration

I Victor Mashindi, hereby declare that the work that forms the basis of this thesis is my own work, that was performed under the able supervision of Prof Neil. J. Coville (School of Chemistry, University of the Witwatersrand), Prof Kenneth. I. Ozoemena (School of Chemistry, University of the Witwatersrand) and Dr Pieter. B. Levecque (HySA Catalysis University of Cape Town). This work has not been and will not be submitted to any other University. It is hereby submitted to the University of the Witwatersrand, Johannesburg, as part of the requirements for the degree, Doctor of Philosophy in Chemistry. I further declare that work done by other people, which assisted in the study and writing of this thesis, was cited, and referenced accordingly.

Signed (Victor Mashindi) 

On this 3rd of February 2021

# Abstract

Proton exchange membrane fuel cells (PEMFCs) are being used in the automobile industry as one of the replacements for gasoline powered engines. This is because PEMFCs have many advantages over traditional engines including their being light weight and that they are a cleaner energy conversion system. There are, however, challenges with PEMFCs. These include their low durability due to dissolution of the metal catalysts; the electrochemical oxidation of the carbon supports that are used due to the corrosive acid media found in PEMFCs, and the highly oxidising potentials reached during start up or during load cycling. Therefore, there is a quest to find highly active catalysts that are durable, and which are essential for the full-scale commercialization of PEMFCS for a range of applications such as in automobiles and home power generation systems. Even though other corrosion resistant supports like metal oxides and doped metal oxides have been used to replace carbon supports, their low conductivity and high cost still makes carbon- or carbon-based supports more attractive.

Many carbon supports have only shown low durability, but new and novel structured carbon supports have been shown to have a wide range of favourable properties that can make them suitable and durable ORR catalyst supports. Metal-free nitrogen doped structured carbons have also shown catalytic activity and durability towards ORR. In this study new hollow carbon spheres and hemispherical broken bowl-like carbons have been used as carbon supports for potential use in PEMFCS. Hollow, graphitic, mesoporous carbon spheres (HCSs) and their nitrogen doped counterparts (NHCSs) have been made to use as supports for the synthesis of highly active and durable Pt oxygen reduction reaction (ORR) catalysts. HCSs with a large diameter (~ 318 nm) were made by a templating method using Stober spheres as the template. A post synthesis technique using melamine was used to dope the surface of the HCSs with nitrogen to give NHCSs (d ~ 320 nm). Smaller aggregated silica templates were also made and

were used as templates to form hemispherical, broken bowl like hollow carbon spheres (BHCSs) with a diameter of ~ 58 nm. A post synthesis technique (also using melamine) was used to make nitrogen doped broken bowl like hollow carbon spheres (BNHCSs) with a diameter of ~ 60 nm. A metal-organic deposition technique was used to deposit Pt nanoparticles on the different carbon supports and these materials were used to study the Pt catalyst on the different supports for ORR activity and durability. Also, for comparison, a reflux method was used to deposit Pt particles on the HCS and NHCS and the materials were also studied for ORR activity and durability.

The spherical and hemispherical morphology of the supports was confirmed by TEM and SEM analysis. Raman spectra confirmed the incorporation of defects due to nitrogen doping while the thermal stability of the pristine supports was significantly lowed upon nitrogen doping. Nitrogen incorporation on the doped supports, XPS (4.2 - 5.5 atomic %) was found to be due to the presence of pyridinic, graphitic, pyrrolic nitrogen, metal-N-pyridyl groups as well as the oxidised nitrogen groups. Surface oxidation of the supports was significantly decreased upon nitrogen doping. TGA confirmed a loading of about 40 wt.% Pt on the supports and that the thermal stability of the supports decreased upon metal nanoparticle decoration. The supports were decorated with Pt nanoparticles (d = 3.8 – 4.6 nm) with Pt – Pt distances between 5.8 – 6.5 nm on all supports. ADF-BF-STEM and in-situ PXRD studies confirmed pore confinement of the Pt which enhanced the durability of the catalysts. Nitrogen doped supports had smaller Pt particle sizes (d = 4.0 ± 0.6 nm (Pt/HCSs) and d = 4.6 ± 0.9 (Pt/BNHCSs)) and shorter Pt - Pt distances between 5.8 – 6.5 nm.

ORR studies were performed on the Pt/BHCSs, Pt/BNHCSs, Pt/HCSs and the Pt/NHCSs catalysts. The materials exhibited ECSA values between 50 – 69 $m^2.g^{-1}$ consistent with the Pt particle sizes obtained from TEM. The obtained mass activity (MA) was between 90 – 263 $A.g^{-1}$ compared to between 65 - 203 $A.g^{-1}$ for the commercial Pt/Vulcan benchmark catalyst.

The obtained surface area specific activity was between 134 – 391 μA.cm$^{-2}$ compared to 107 – 350 μA.cm$^{-2}$ for the commercial benchmark catalyst. After 6000 durability cycles, the catalysts retained between 57.2 – 65.4 % of the initial ECSA compared to 47.6% for the commercial benchmark catalyst. Enhanced activity in ORR of the catalysts was attributed to the small Pt particle sizes, the thin carbon shells that enabled better electronic conductivity and faster mass transport of reactive gases. The presence of nitrogen in the support also modified the electronic structure of the Pt. For the smaller Pt/BHCSs and Pt/BNHCSs catalysts, the very thin support shell (d = 4.5 – 4.6 nm) promoted higher Pt utilization of the supports. A better electronic conductivity resulted in better activity.

Our studies thus confirmed that the high activity and durability of the catalysts could be attributed to a thin graphitic mesoporous shell, the presence of defects and the presence of nitrogen functionalities. Nitrogen doping altered the electronic state of the Pt. The thinner and broken shells of the Pt/BHCSs and Pt/BNHCSs materials allows for deposition of Pt on either side of the support thereby enhancing the electronic conductivity and gas mass transport of the materials leading to higher activity. We also confirmed that different synthetic procedures for Pt nanoparticles can yield Pt particles with comparable ORR activity.

# Dedication

This work is dedicated to:

The women who raised me, My dear mother Ms Georgina Manyanga and her caring little sister Ms Syangisiwe Manyanga. Thank you for raising me and sending me to school even though it was not easy for you. Thank you for being strong for us.

The memory of my late father Mr Muringwa Eleki Mashindi

# Acknowledgements

I would like to acknowledge my supervisor Prof Neil. J. Coville for his immense support and academic contribution to this work. Your encouragement sir, your patience, and your deep knowledge and understanding of science is humbly appreciated. Finally, I would like to acknowledge you for the opportunity to be part of your research group and the financial assistance to complete the work. With the competition for places and scarcity of funding, it could easily have been someone else benefitting.

Prof Kenneth. I. Ozoemena for your deep contributions in electrocatalysis, for the motivation to work and finish and for the opportunity to use your state-of-the-art electrochemistry laboratory. For allowing me to be part of your research group where I enjoyed deep discussions on the many facets of electrocatalysis.

Dr Pieter B. Levecque for the deep-rooted introduction to electrocatalysis and the oxygen reduction reaction. Your patience in teaching and supervision and your tireless encouragement is immensely appreciated. Thank you for allowing me access to probably the best fuel cells research labs on the African continent at HySA catalysis at UCT.

To Dr Prakash M. Gangatharan I would like to say thank you for helping me in the lab and for urgent BET analyses. Your contribution was immensely appreciated.

To Ms Nobuhle Mpofu at the University of Cape Town, for allocating me the required electro catalysis equipment during my visits there. For assisting with cell connections and trouble shooting. Thank you for your patience and understanding. Even when I was at the Wits labs, thank you for the ‘over the phone’ trouble shooting with electrocatalysis issues and EC lab related problems.

To Dr Colleen Jackson, thank you for assisting with electrocatalysis and cell connection issues.

To Dr Adrian Fortuin, thank you for assisting with the Nochromix formulations and for assistance when using the UNISA Florida electrochemistry laboratory.

Sincere gratitude to Dr Roy Forbes for assisting with catalyst durability in-situ PXRD measurements.

Sincere gratitude towards Mr Ofentse Makgae who at the University of Oxford carried out ADF-BF STEM and atomic resolution measurements needed for this study.

The work would not have run smoothly without the assistance of Ms Rhandzu Rikhotso's assistance with HRTEM measurements at the CSIR.

Many thanks to Dr Zikhona Tetana for assistance with some of the electrochemistry accessories. Your gold counter electrode was very useful for my catalyst durability studies.

Many thanks to Mr Werner Jordaan at NMISA/CSIR for performing XPS measurements required for this work.

To Kabelo Ledwaba at UNISA Florida, thank you for allowing me access to the state-of-the-art electrochemistry equipment in the labs at UNISA, Florida.

To Dr Tumelo Phaahlamohlaka, thank you for teaching me how to use CVD furnaces.

To Dr Boitumelo J. Matsoso, thank you for encouraging me to work hard and to deliver results.

To the CATMAT group: thank you for the support in the laboratories and in social groups. Thank you for the stimulating discussions and thought-provoking questions during group presentations and in between. Thank you for being a caring family. I depended on you for numerous things during my study.

Let me specifically acknowledge my colleagues in labs 120, 330 and lab 113: Mr Thomas Mongwe, Ms Pumza Mente, Ms Thuli Buthelezi, Ms Boitumelo Thlaole, Mr Prince Ndivhuwo

Shumbula, Mr Zakhele Ndala, Ms Tswarela Kolokoto Ms Lerato Mokoloko, Mr Tshepo Molefe, Ms Alice Magubane, Dr Aderemi Haruna, Mr Thapelo Mofokeng, Dr Adewale Ipadeola for friendship and the rewarding scientific discussions we had over the course of my study.

To my family, my sisters Zvipo Mashindi, Lydia Mashindi and Sthabile Mashindi, thank you for financial and moral support. Thank you for your prayers and patience during this tough but rewarding journey. Thank you to my brother-in-law Bothwell Moyo for the support in many forms you provided especially in the year 2016.

I would like to acknowledge my long-time friends Mr Gabriel Chipoyi, Mr Evidence Moyo, Mr Mandlaenkosi Sibanda, Mr Patron Bruce Sibanda, Mr Farai Ncube and Mr Bethany Chenyika. Thank you, brethren, for your prayers and good friendship.

To the love of my life, my wife, thank you Gloria Tariro Mandizvidza for the support and encouragement. Your understanding and support are immensely appreciated. My acknowledgement to my mother in-law Ms Jane Nyagumbo for all the support you provided in prayers and in guidance.

The work would have been extremely difficult to conduct without the assistance of the Microscopy and Microanalysis unit at the University of the Witwatersrand. Special thanks to Dr Zikhona Tetana, Dr Manoko Maubane, Dr Ella Cebisa Linganiso, Dr Dieran Reddy, Mr Jacques Gerber and Prof Alexander Ziegler for your instrumentation training and trouble shooting.

I would like to thank Mrs Miranda Waldron and Mr Mohammed A. Jaffer from the University of Cape Town Aaron Klug Centre for Imaging and Analysis for assistance with electron microscopy imaging during my visits there.

Sincere gratitude to Mr Tapuwa Dzara our glassblower for the timeous glassware supply and for fixing my broken glassware. Without your availability and approachability, my work would have significantly delayed. Thank you, Sir.

Sincere gratitude to Ms Amanda Morgan for the timeous chemicals' orders and travel arrangements. Ms Safiya Ooni for the stipend and fees payment processes.

My deepest appreciation to my old friend Lovemore Mawere and Sihle for keeping me company in Cape Town during my HySA Catalysis, University of Cape Town, visits. The mountain hikes, the drinks, the discussions, and the super rugby matches we attended together made the Cape Town stay awesome.

My deepest appreciation to the Department of Science and Innovation (DSI) through HySA catalysis for funding this research in the form of an MSc and Ph.D. bursary. I would also like to thank the University of the Witwatersrand for a Postgraduate Merit award for providing supplementary funding during my study.

The University of the Witwatersrand, School of Chemistry staff for providing me with facilities and personnel that enabled me to learn and study with minimal hindrance and challenges.

And finally, I would like to thank myself for putting up a good fight working in the labs, writing, and submitting this work.

***"No man can walk out on his own story".***

# Publications, presentations, and awards

## Publications

1) **Victor Mashindi**, Pumza Mente, Nobuhle Mpofu, Tumelo Phaahlamohlaka, Ofentse Makgae, Angus Kirkland, Roy Forbes, Kenneth I. Ozoemena, Pieter B. Levecque and Neil J. Coville, *Platinum supported on pristine and nitrogen doped bowl-like broken hollow carbon spheres as oxygen reduction reaction catalysts*–submitted and under review.
2) Pumza Mente, Tumelo N. Phaahlamohlaka, **Victor Mashindi** and Neil J. Coville, *Polystyrene-b-poly (acrylic acid) nanospheres for the synthesis of size-controlled cobalt nanoparticles encapsulated inside hollow carbon spheres* – published
3) **Victor Mashindi**, Pumza Mente, Tumelo Phaahlamohlaka, Ofentse Makgae, Roy Forbes, Kenneth I. Ozoemena, Pieter B. Levecque and Neil J. Coville, *Pristine and nitrogen doped hollow carbons spheres promotes the activity and durability of platinum oxygen reduction reaction catalysts* -to be submitted – *to be submitted*
4) **Victor Mashindi** and Neil J. Coville, *Synthesis of broken bowl like and nitrogen doped broken bowl like hollow carbon spheres and the decoration with Pt nanoparticles* – to be submitted
5) **Victor Mashindi**, Roy Forbes, Dean Barrett, Kenneth I. Ozoemena, Pieter Levecque and Neil Coville, *Electronic metal support interactions of Pt/BHCSs and Pt/BNHCSs and the relationships with electrocatalytic activity and durability in ORR.* - to be submitted
6) **Victor Mashindi** and Neil J. Coville, *Parameters affecting the synthesis of monodisperse microporous small silica particles (40 < d < 90 nm) and the subsequent use as hard templates* – to be submitted

## Awards

- Postgraduate Merit Award 2017 – 2020, University of the Witwatersrand
- Spirit of CATMAT award 2019, CATMAT group, School of Chemistry, University of the Witwatersrand
- HySA catalysis MSc Scholarship, 2016 – 2017 (2 years)
- HySA catalysis Ph.D. Scholarship, 2018 -2020 (3 years)

## Presentations

- Enhanced activity and durability of Pt/BHCSs and Pt/BNHCs as ORR catalysts, **Oral presentation**, International Society of Electrochemistry (ISE) Conference, Durban 2019
- Enhanced activity and durability of Pt/BHCSs and Pt/BNHCs as ORR catalysts, **Oral presentation**, South Africa Chemical Institute (SACI -ENSTIN) (Energy Storage and Industry), KwaMaritane, July 2020
- Activity of Pt/HCSs and Pt/NHCs in oxygen reduction reaction, **Oral presentation**, Catalysis Society of South Africa Conference (CATSA), Legend golf and safari resort, Mookgophong 2018
- Activity of Pt/HCS and Pt/NHCSs in oxygen reduction reaction, **Poster presentation**, Catalysis society of South Africa Conference (CATSA), KwaMaritane and Bakubung Bush Lodges 2017
- Synthesis and characterization of hollow carbon spheres, **Poster Presentation**, Catalysis society of South Africa Conference (CATSA), Champagne sports resort Drakensberg, Winterton 2016.

- Enhanced activity and durability of Pt/BHCSs and Pt/BNHCs as ORR catalysts, Grad flash **Oral presentation**, Postgraduate cross faculty symposium, University of the Witwatersrand, 2019
- Activity of Pt/HCSs and Pt/NHCs in oxygen reduction reaction, **Poster presentation**, Postgraduate cross faculty symposium, University of the Witwatersrand, 2018
- Synthesis and characterization of hollow carbon spheres, **Poster Presentation**, Postgraduate cross faculty symposium, University of the Witwatersrand, 2017
- Enhanced activity and durability of Pt/BHCSs and Pt/BNHCs as ORR catalysts, **Oral presentation**, Wits – Sasol meeting, Sasol Industrial site, Sasolburg, June 2019

## Research Visits and collaborations

- Attended the HySA Catalysis organized experimental electrochemistry course, University of Cape Town, Under the invitation and supervision by Dr Pieter B. Levecque, July 2016, (2 weeks)
- Visiting PhD researcher at the HySA catalysis laboratories at the University of Cape town, under the guidance and invitation of Dr Pieter. B. Levecque, July 2016 (2 weeks)
- Visiting PhD researcher at the HySA catalysis laboratories at the University of Cape town, under the guidance and invitation of Dr Pieter. B. Levecque, March – June, 2019 (3 months)
- Visiting MSc researcher (for electrochemistry experiments), University of South Africa, Florida campus July - November 2018

# Table of Contents

Declaration ..... i

Abstract ..... ii

Dedication ..... v

Acknowledgements ..... vi

Publications, presentations and awards ..... x

Publications ..... x

Awards ..... xi

Presentations ..... xi

Research Visits and collaborations ..... xii

List of abbreviations ..... xxxii

Chapter 1 ..... 1

1.1: Introduction ..... 1

1.2: Fuel Cells - PEMFCs ..... 5

1.3. Advantages of PEMFCs ..... 9

1.4: Reactions in the PEMFC ..... 11

1.5: Approaches to higher activity and durability in ORR – a review ..... 13

1.5.1: Pt catalysts deposited on various carbon- and carbon-based supports ..... 14

1.5.2: Pt Catalysts deposited on nitrogen doped supports ..... 20

1.5.3: Unsupported Pt, Pt-alloy and binary Pt–M (M = metal) catalysts ..... 25

1.5.4: Pt catalysts supported on metal oxides and other supports ..... 31

1.5.5: Metal free ORR catalysts.....35

1.6: Degradation of fuel cell catalysts.....37

1.6.1: Carbon support corrosion.....37

1.6.2: Ostwald Ripening.....39

1.6.3: Agglomeration.....39

1.6.4: Particle Detachment.....40

1.7: Carbon supports in catalysis.....40

1.8: Hollow Carbon Spheres.....42

1.8.1: Hollow carbon spheres in catalysis.....43

1.9: Templating.....45

1.9.1: Broken HCSs or hemispherical carbon spheres.....51

1.10: Aims of the study.....54

1.11: Objectives of the Study.....57

1.12: Thesis Outline.....58

**Chapter 1**.....58

**Chapter 2**.....58

**Chapter 3**.....58

**Chapter 4**.....59

**Chapter 5**.....59

**Chapter 6**.....59

**Chapter 7**.....59

**Chapter 8**……64

1.13: References.....60

2.1: Summary of chapter content.....77

2.2: Synthesis of large silica templates.....78

2.3: Synthesis of small silica templates.....79

2.4: Synthesis of hollow carbon spheres (HCSs).....79

2.5: Synthesis of nitrogen doped hollow carbon spheres (NHCSs).....81

2.6: Synthesis of Pt/HCSs - metal organic deposition route.....81

2.7: Synthesis of Pt/NHCSs - - metal organic deposition route.....82

2.8: Synthesis of Pt/HCS and Pt/NHCS – the ethanol reflux route.....82

2.9: Synthesis of small broken bowl like hollow carbon spheres (BHCSs).....83

2.10: Electrochemical analysis.....86

2.10.1: Cyclic Voltammetry (CV).....86

2.10.2: Linear sweep voltammetry – rotating disk electrode.....88

2.10.3: Preparation of the catalysts ink.....91

2.10.4: Working electrode preparation.....91

2.10.5: Electrochemical cell cleaning.....92

2.11: Powder X-ray Diffraction (PXRD).....96

2.12: Transmission electron microscopy (TEM).....97

2.13: Scanning electron microscopy (SEM).....98

2.14: BET analysis.....99

2.15: Thermogravimetric analysis (TGA).....100

2.16: Raman spectroscopy .....101

2.17: X-ray photoelectron Spectroscopy (XPS).....101

2.18: Annular dark field bright field scanning transmission electron microscopy ……...110

2.19: References.....104

3.1: Introduction.....109

3.2: Experimental.....111

3.3 Discussion.....112

3.3.1 TEOS Study .....112

3.3.2: Ammonia solution study.....117

3.3.3: Deionized water study .....123

3.3.4: Controlled addition of TEOS.....127

3.3.4: Effect of EtOH. .....130

3.4: Textual properties .....131

3.4.1 Effect of DI .....131

3.5: Controlled synthesis of small silica particles.....133

3.6: Conclusions.....133

3.7: References.....135

Synthesis and characterization of large HCSs, NHCSs and the Pt supported materials (Pt/HCSs and Pt/NHCSs).....140

4.1: Introduction.....140

4.2: Synthesis of the hollow carbon and nitrogen doped hollow carbon spheres. .....142

4.3: Morphology and size of the silica, HCS, and NHCS.....143

4.4: Raman spectroscopy analysis .....145

4.5: Synthesis of Pt/HCSs and Pt/NHCSs.....147

4.6: Pt/HCSs and Pt/NHCSs materials.....147

4.7: Thermal gravimetric analysis (TGA).....151

4.8: Surface area and porosity of the supports and the catalysts .....153

4.9: Powder X-ray diffraction (PXRD) studies.....155

4.10: X-ray photoelectron spectroscopy (XPS) analysis .....158

4.11: Conclusions.....163

4.12: References.....164

Synthesis and characterization of small hemispherical BHCSs, BNHCSs and the Pt supported materials (Pt/BNHCSs and Pt/BNHCSs).....174

5.1: Introduction.....174

5.2: Morphology of the BHCS and BNHCS.....176

5.3: Raman Spectroscopy.....180

5.4: Synthesis of Pt/BHCSs and Pt/BNHCSs .....183

5.5: Morphology of the Pt/BHCSs and Pt/BNHCSs.....184

5.6: Surface area and porosity of the supports and the catalysts .....188

5.7: Thermogravimetric analysis (TGA).....192

5.8: Powder X-ray diffraction (PXRD).....194

5.9: X-ray photoelectron spectroscopy (XPS) .....196

5.10: Conclusions.....203

5.11: References....204

ORR activity and durability studies of the Pt/HCSs, Pt/NHCSs, Pt/BHCSs and Pt/BNHCSs prepared with metal-organic deposition....213

6.1: Introduction....213

6.2: Experimental....215

6.3: Electrochemical Characterization....216

6.4: Cyclic Voltammetry (CV)....218

6.5: Linear Sweep Voltammetry (LSV)....219

6.6: Durability measurements....220

6.7: Results and Discussion....221

6.7.1: Electrochemical Characterization....221

6.7.2: Catalyst durability....227

6.8: Conclusion....246

6.9: References....249

7.1: Introduction....257

7.2: Experimental....261

7.2.1: Chemicals....261

7.2.2: Synthesis of silica templates....261

7.2.3: Synthesis of hollow carbon spheres (HCSs) and nitrogen doped hollow carbon spheres (NHCSs)....262

7.2.4: Synthesis of Pt/HCSs and Pt/NHCSs. ....263

7.2.5: Catalyst characterization....263

7.2.6: Electrochemical characterization.....265

7.3: Results and Discussion.....268

7.3.1: Synthesis and characterization of HCSs and NHCSs.....268

7.4: Electrochemical characterization.....283

7.4.1: Catalyst activity.....283

7.4.2: Catalyst Durability.....286

7.5: Conclusions.....289

7.6: References.....290

8.1:General Conclusions……..…….296

8.2: Outlook ……..……298

# List of tables

Table 1. 1: Some of the fuel cell types. [11,13–17].....5

Table 1. 2: Examples of platinum catalysts supported on various carbon supports for the ORR. .....18

Table 1. 3: ORR activity data for the Fe and Ni-rich Pt supported on nitrogen-doped mesoporous graphitic carbon. .....23

Table 1. 4: Platinum catalysts supported on various nitrogen doped carbon supports. .....24

Table 1. 5: Unsupported, alloyed and binary Pt -M (M- metal) catalysts and the explanation of properties contributing to enhanced activity and durability. .....30

Table 1. 6: Platinum catalysts supported on various metal oxides and other supports.....35

Table 1. 7: Metal free ORR catalysts and the possible explanation for the observed activity.36

Table 3. 1: Data showing variation of SEM particle sizes due to changes in TEOS concentration .....116

Table 3. 2: Changes in particle size due to variation of ammonia concentration .....122

Table 3. 3: Particle size variation of the silica spheres due to changes in deionized water concentration.....126

Table 3. 4: Comparison of textual properties of silica spheres on different deionized water concentrations .....131

Table 4. 1: Raman spectroscopy data for the HCSs, NHCSs and Vulcan carbon. .....146

Table 4. 2: Comparison of the Pt particle size and the Pt – Pt distance of the Pt/HCSs and Pt/NHCSs.....150

Table 4. 3: Comparison of the BET surface area and pore properties of the HCSs, Pt/HCSs, NHCSs and Pt/NHCSs. ..... 155
Table 4. 4: Comparison of the Pt particle sizes of the Pt/HCSs, Pt/NHCSs and Pt/Vulcan as determined using TEM, PXRD Scherrer equation and rietveld refinement. ..... 156
Table 4. 5: Deconvoluted O1s data for Pt/HCSs and Pt/NHCSs ..... 159
Table 4. 6: Deconvoluted C1s data for Pt/HCSs and Pt/NHCSs ..... 161
Table 4. 7: Deconvoluted N1s data for Pt/NHCSs ..... 161
Table 4. 8: Deconvoluted Pt4f data for Pt/HCSs and Pt/NHCSs ..... 162

Table 5. 1: Deconvoluted Raman spectra data for BHCSs and BNHCSs. ..... 183
Table 5. 2: TEM Pt particle size and Pt – Pt distance for Pt/BHCSs and Pt/BNHCSs ..... 188
Table 5. 3: Textual properties of BHCSs, BNHCSs, Pt/BHCS and Pt/BNHCS. ..... 190
Table 5. 4: Pt particle sizes of Pt/BHCSs, Pt/Vulcan and Pt/BNHCSs as measured by TEM and PXRD techniques. ..... 196
Table 5. 5: Data of deconvoluted high resolution C1s spectra for Pt/BHCSs and Pt/BNHCSs. ..... 199
Table 5. 6: Data of deconvoluted high resolution O1s spectra for Pt/BHCSs and Pt/BNHCSs. ..... 199
Table 5. 7: Data of deconvoluted high resolution N1s spectra for Pt/BNHCSs. ..... 200
Table 5. 8: Data of deconvoluted high resolution Pt4f spectra for Pt/BHCSs and Pt/BNHCSs. ..... 201

Table 6. 1: Calculated ECSA and theoretical metal nanoparticles surface area based on average particle size. Platinum utilization was calculated based on the theoretical surface area (MSA) ..... 224

Table 6. 2: Calculated ECSA and ORR activity for the 40 wt% catalysts at 0.90 V vs RHE. .....227

Table 6. 3: Comparison of normalized ECSA between BOL and after 1000 cycles. Also shown is the percentage loss in ECSA due to accelerated cycling. .....232

Table 6. 4: Comparison of the textual properties of the supports and the complete catalysts showing reductions in BET surface area, BJH pore volume and BJH pore widths due to Pt deposition. .....233

Table 6. 5: Comparison of normalized ECSA between $1000^{th}$ and EOL ($6000^{th}$ cycles) The total loss in ECSA due to accelerated cycling is shown. .....234

Table 6. 6: Comparison of normalized ECSA between $5000^{th}$ and EOL ($6000^{th}$ cycles). The loss in ECSA in the final 1000 cycles due to accelerated cycling. .....236

Table 6. 7: Correlation between $I_D/I_G$ ratio, TEM particle sizes and Pt-Pt interparticle distances for the catalysts. .....237

Table 6. 8: Comparison of normalized ECSA between BOL and EOL (6000 cycles), also shown is the total loss in ECSA due to accelerated cycling. .....238

Table 6. 9: Growth of Pt crystallite size (Rietveld refinement) for Pt/BHCSs as a function of reaction temperature .....239

Table 6. 10: Growth of Pt crystallite size (Rietveld refinement) for commercial Pt/HCSs as a function of reaction temperature .....242

Table 6. 11: Growth of Pt crystallite size (Rietveld refinement) for commercial Pt/C as a function of reaction temperature .....244

Table 7. 1: Raman spectra of HCSs (a) Raman spectra of NHCSs (b) TGA profiles of HCSs, NHCSs, Pt/HCSs and Pt/NHCSs (c) TGA derivative profiles of HCSs, NHCSs, Pt/HCSs and Pt/NHCSs .....270

Table 7. 2: Textual properties of HCSs, NHCSs, Pt/HCSs and Pt/NHCSs .....276
Table 7. 3: Pt crystallite sizes of Pt/HCSs, Pt/NHCSs and the commercial benchmark Pt/C as measured by TEM, the Scherrer equation and Rietveld refinement .....279
Table 7. 4: Data for the deconvoluted high resolution N1s spectra for Pt/NHCSs .....280
Table 7. 5: Data for the deconvoluted high resolution Pt 4f spectra for Pt/BHCs and Pt/BNHCSs .....281
Table 7. 6: Calculated ECSA and ORR activity for the Pt/HCSs, Pt/NHCSs and the commercial benchmark Pt/C catalysts. MA, SA, $I_k$ measurements obtained at 0.90 V vs. RHE.....285
Table 7. 7: Comparison of Pt/BNHCSs and Pt/BHCSs to other Pt/C catalysts reported. MA, and SA data are calculated from data at 0.90V vs. RHE. .....286
Table 7. 8: Comparison of the activity of the Pt/HCSs, Pt/NHCSs and commercial Pt/C before and after 6000 durability cycles .....288
Table 7. 9: Loss of ECSA due to durability cycling for the Pt/BHCSs, Pt/BNHCSs and the commercial benchmark Pt/C catalysts .....289

# List of figures

Figure 1. 1: Global energy sources for all purpose use in 2019[1] .....1
Figure 1. 2: Sources of energy for all purpose use in 2019 China[1] .....2
Figure 1. 3: Hydrogenics' 1 Megawatt fuel cell power generation platform.....7
Figure 1. 4: (a) PEMFC run passenger train from Germany, (b) Toyota PEMFC heavy duty truck, (c) Toyota Mirai fuel cell passenger sedan and (d) Hyundai Nexo crossover SUV running a hydrogen fuel cell. [38,45–47].....11
Figure 1. 5: Schematic illustration of a PEMFC[54] .....12

Figure 1. 6: (a) to (d) are DF-STEM images showing pore confined Pt in the hollow carbon supports and (e) variable temperature in-situ PXRD diffractograms for a Pt/C catalyst confirming pore confinement. [73] ..... 23

Figure 1. 7: Schematic illustrations of the proposed mechanisms of degradation of Pt/C catalysts.[101] ..... 38

Figure 1. 8: SEM images of some of the carbon materials that have been used in catalysis either as supports or as catalysts themselves: (a) carbon nanotubes, (b) carbon nanofibers, (c) solid carbon spheres and (d) graphene sheets.[118–121] ..... 41

Figure 1. 9: Schematic illustration of the encapsulation of Cu inside HCSs to form Cu@HCS[125] ..... 43

Figure 1. 10: Schematic of the formation of HCSs from polystyrene[128] ..... 46

Figure 1. 11: Schematic illustration of the formation of NHCSs using silica and ionic liquids.[135] ..... 49

Figure 1. 12: SEM and TEM images of NHCS synthesized using different ratios of silica and ionic liquid [$C_{16}$Mim]Br (a – c) [135] ..... 49

Figure 1. 13: Schematic illustration of the formation of NHCS using hard template silica spheres, dopamine as carbon precursor and PS-b-PEO as pore forming agent.[136] ..... 50

Figure 1. 14: TEM images of NHCSs with identical internal diameter and various shell thickness.[136] ..... 50

Figure 1. 15: Schematic illustration of the synthesis procedure of the HCHs.[137] ..... 51

Figure 1. 16: SEM micrograms of the HCHs with the mass ratios of PSs to glucose were (a) 1:4, (b) 1:3, (c) 1:2 and (d) 1:1.[137] ..... 52

Figure 1. 17 : Schematic of the preparation of hollow carbon hemispheres (HCHS).[138] ..... 53

Figure 1. 18: Sem images of hollow hemispherical carbon[138] ..... 54

Figure 1. 19: Schematic showing Pt (grey octahedra) deposited both sides of a (BHCS/BNHCS) shell (black region) with high support utilization. .....56

figure 2. 1: Steel cylindrical reactor (a), Horizontal tubular furnace used for Pt deposition, carbonization of $SiO_2$@RF and annealing of HCSs and NHCSs (b).....84

figure 2. 2 : Cyclic voltammograms of a Pt/C catalyst of various catalyst film quality.[10] .....87

figure 2. 3: (a) Schematic of electrolyte flow towards a RDE surface and (b) electrolyte flow near its surface. .....89

figure 2. 4: (a) Linear sweep voltammograms at various rpm and (b) Koutecky-Levich plot for three different overpotentials.[17] .....90

figure 2. 5: ORR polarization profiles for a Pt/C catalyst of different catalyst film quality[10].94

Figure 2. 6: Three electrode setup showing RDE box, potentiostat, electrochemical cell and electrodes. .....95

Figure 2. 7: D8 Advanced diffractometer (a), Internal components of an X – ray diffractometer (b).....96

Figure 2. 8: Schematic of a TEM (a), F20 Tecnai transmission electron microscope (b)[22] ..97

Figure 2. 9: Schematic of a SEM (a), Tescan MIRA3 RISE scanning electron microscope (b)[23] .....98

Figure 2. 10: A Micrometrics Tristar 3000 physisorption instrument.....99

Figure 2. 11: A Perkin Elmer STA6000 TGA instrument.....100

Figure 2. 12: A Horiba Jobin-Yvon Raman spectrometer.....101

Figure 2. 13: A Thermo Scientific ESCALAB 250Xi spectrometer .....102

Figure 2. 14: The schematic of the mode of operation of a STEM microscope (a)[34] and A JEOL ARM200F scanning transmission electron microscope (b)……..….111

Figure 3. 1: SEM images of silica particles synthesized with $NH_4OH$ (2 M), DIW (5 M), EtOH (8 M) and increasing concentrations of TEOS (a) 0.1 M, (b) 0.2 M, (c) 0.4 M, (d) 0.8 M, (e) 1.6 M, (f) 3.2 M .....114

Figure 3. 2: Particle size distributions of silica particles synthesized with $NH_4OH$ (2 M), DIW (5 M), EtOH (8 M) and increasing concentrations of TEOS (a) 0.1 M, (b) 0.2 M, (c) 0.4 M, (d) 0.8 M, (e) 1.6 M, (f) 3.2 M .....115

Figure 3. 3: Particle size changes of silica particles synthesized with $NH_4OH$ (2 M), DIW (5 M), EtOH (8 M) and increasing concentrations of TEOS (a) 0.1 M, (b) 0.2 M, (c) 0.4 M, (d) 0.8 M, (e) 1.6 M, (f) 3.2 M .....116

Figure 3. 4: SEM images of not formed silica particles at very low ammonia solution concentrations below 0.1 M, with (a) 0. 01 M, (b) 0.02 M, (c) 0.04, (d) 0.08 M $NH_4OH$ ....118

Figure 3. 5: SEM images of the silica spheres formed at an optimum of the other reagents with TEOS (2 M), DIW (5 M), EtOH (8 M) and various ammonia concentrations of $NH_4OH$ (a) 0.5 M, (b) 1.0 M, (c) 1.5 M, (d) 2.0 M, (e) 2.5 M and 3.0 M.....120

Figure 3. 6: Particle size distribution showing variation due to changes in the concentration of $NH_4OH$ (a) 0.5 M, (b) 1.0 M, (c) 1.5 M, (d) 2.0 M, (e) 2.5 M and 3.0 M and at an optimum of the other reagents with TEOS (2 M), DIW (5 M), EtOH (8 M).....121

Figure 3. 7: Dependence of Silica particle sizes on the concentration of $NH_4OH$ and at an optimum of the other reagents with TEOS (2 M), DIW (5 M), EtOH (8 M) .....122

Figure 3. 8: SEM images as the deionized water concentration is varied from (a) 5 M, (b) 10 M, (c) 15 M, (d) 20 M, (e) 25 M, (f) 30 M and optimum concentration of the other reagents NH4OH (2 M), TEOS ( 2 M) and EtOH (8 M) .....124

Figure 3. 9: Particle size distribution of the silica spheres as the deionized water concentration was varied from (a) 5 M, (b)10 M, (c) 15 M, (d) 20 M, (e) 25 M, (f) 30 M at optimum concentration $NH_4OH$ (2 M), TEOS (2 M), EtOH (8M).....125

Figure 3. 10: Changes in the silica particle size due to the variation of the deionized water concentration was varied from 5 - 30 M at optimum concentration of $NH_4OH$ (2 M), TEOS (2 M), EtOH (8M).....126

Figure 3. 11: SEM images of polydisperse silica spheres formed with slow addition of TEOS (a) 20 $ml.min^{-1}$ (b) 30 $mil.\ min^{-1}$ (c) 40 $mil.min^{-1}$ (d) 50 $mil.min^{-1}$ using a syringe pump.....128

Figure 3. 12: Particle size distributions of polydisperse silica spheres formed with slow addition of TEOS (a) 20 ml.min-1 (b) 30 $mil.\ min^{-1}$ (c) 40 $mil.min^{-1}$ (d) 50 $mil.min^{-1}$ using a syringe pump. .....129

Figure 3. 13: SEM(a), TEM(b) images and particle size distribution (c) of the small silica particle (d < 100 nm) formed at low concentrations of TEOS (2 M), $NH_4OH$ (2 M) and DI (5 M) and EtOH (15 M) .....130

Figure 3. 14: BET properties of the formed silica at varying DI concentrations.....132

Figure 4. 1: SEM micrograph of silica particles (a), TEM micrographs of HCSs (b) and particle size distribution of the HCSs (c).....144

Figure 4. 2: Deconvoluted Raman spectra of (a) HCSs, (b) NHCSs, (c) Vulcan carbon and (d) stacked Raman spectra for all supports showing the different G peak positions.....146

Figure 4. 3: SEM image of Pt/HCSs (a), SEM image of Pt/NHCSs (b), TEM image of Pt/HCSs (c), TEM image of Pt/NHCSs (d), higher magnification TEM image of Pt/HCSs (e) and higher magnification TEM image of Pt/NHCSs (f).....149

Figure 4. 4: Diameter distribution of HCSs (a) and NHCSs (b), shell thickness distribution of HCSs (c) and NHCSs (d).....150

Figure 4. 5: TGA profiles of HCSs, NHCSs and Vulcan (a) and the corresponding derivative profiles (c), TGA profiles of Pt/HCSs, Pt/NHCSs, Pt/Vulcan (b) and the corresponding derivative profiles (d).....152

Figure 4. 6: Type II BET isotherm for HCSs (a) and NHCSs (b), Pore size distribution for HCSs (c) and for NHCSs (d) .....154
Figure 4. 7: PXRD diffractograms for HCSs, NHCSs, Vulcan (a) and for Pt/HCSs, Pt/NHCSs, Pt/Vulcan (b).....157
Figure 4. 8: XPS low resolution survey spectra for Pt/HCSs, Pt/NHCSs (a), High resolution C1s (b), O1s (c), Pt4f (d) spectra for Pt/HCSs.....159
Figure 4. 9: High resolution C1s (a), O1s (b), N1s (c), Pt4f (d) spectra for Pt/NHCSs .....160

Figure 5. 1: SEM micrograph (a), TEM micrograph of $SiO_2$ (b) and particle size distribution of the small silica particles.....177
Figure 5. 2: TEM micrograph for BHCSs (a) and BNHCSs (b), SEM micrograph of BHCSs (c) and BNHCSs (d). .....179
Figure 5. 3: Particle size distribution of BHCSs (a) and BNHCSs (b), Shell thickness of BHCSs (c) and BNHCSs (d).....180
Figure 5. 4: Deconvoluted Raman spectra for BHCSs(a) and BNHCSs(b) showing the shift in the G peak position (blue and red grid lines). .....182
Figure 5. 5: Schematic diagram of the metal-organic deposition equipment[21].....184
Figure 5. 6: SEM micrographs of (a) Pt/BHCSs, (b) Pt/BNHCSs, TEM micrographs of (c) Pt/BHCSs, (d) Pt/BNHCSs, ADF-BF STEM images of (e-f) Pt/BNHCSs .....185
Figure 5. 7: High resolution ADF-BF STEM images of (a-b) Pt/BHCSs and (c-f) Pt/BNHCSs. The insert in (b) is the power spectrum of a <110> projection of the fcc Pt .....186
Figure 5. 8: Pt particle size distribution of Pt/BHCSs (a) and Pt/BNHCSs (b), Pt – Pt interparticle distance of Pt/BHCSs (c) and Pt/BNHCSs (d). .....188
Figure 5. 9: DF-STEM images of Pt/BHCSs and Pt/BNHCS (a – f) showing support shell confinement of Pt. .....**Error! Bookmark not defined.**

Figure 5. 10: BET Isotherms for Pt/BHCSs (a) and Pt/BNHCSs (b), pore size distribution for Pt/BHCSs (c) and Pt/BNHCS (d). .....190
Figure 5. 11: TGA profile for BHCSs and BNHCSs (a), Pt/BHCSs and Pt/BNHCSs (b); DTA profiles for BHCSs and BNHCSs (c), Pt/BHCSs and Pt/BNHCSs (d). .....192
Figure 5. 12: PXRD diffractograms of BHCSs and BNHCSs (a), Pt/BHCSs and Pt/BNHCSs (b). .....195
Figure 5. 13: XPS surveys for Pt/BHCSs and Pt/BNHCSs (a), High resolution C1s (b), O1s (c) and Pt4f spectra for Pt/BHCSs (d). .....197
Figure 5. 14: Deconvoluted high resolution C1s (a), O1s (b), N1s (c) and Pt4f spectra (d) for Pt/BNHCSs. .....198
Figure 5. 15: Stacked deconvoluted Pt4f XPS spectra for Pt/BHCSs (a) and Pt/BNHCSs (b) showing binding energy shifts. .....203

Figure 6. 1: Cyclic voltammograms for ECSA and load cycling (catalyst durability cycle) recorded in 0.1 M $HClO_4$ (room temperature and in argon saturated electrolyte) for Pt/BHCSs .....220
Figure 6. 2: Load cycle durability test protocol for the Pt corrosion test. .....221
Figure 6. 3: Theoretical total Pt surface area (MSA) as calculated using the density of Pt, assuming uniform spherical morphology and a given particle diameter. .....223
Figure 6. 4: Schematic illustration of the Pt nanoparticles supported on top and inside pores of interconnected broken bowl like and broken bowl like nitrogen doped hollow carbon spheres .....225
Figure 6. 5: Electrocatalysis characterization data for the 40 wt% catalysts showing (a) Cyclic voltammograms, (b) ORR polarization I-V curves, (c) Tafel plots and (d) Mass specific (MA), area specific (SA) activities and electrochemical surface area (ECSA) .....226

Figure 6. 6: Durability cyclic voltammograms from beginning of life (BOL) to 6000 cycles showing the change in the structure due to the accelerated degradation for (a) Pt/HCS, (b) Pt/NHCS and (c) Pt/BHCSs, (d) Pt/BNHCSs and (e) the commercial benchmark Pt/Vulcan catalyst. Cycling was done between 0.6 – 1.0 V vs RHE at 20 mV.s-1 and at room temperature (25ºC).....229

Figure 6. 7: Catalyst durability study showing the change in normalized ECSA (a) from BOL to 6000 cycles, (b) From BOL to 1000 cycles, (c) from 2000 to EOL (end of life – 6000 cycles) and (d) from the 5000$^{th}$ to the end of life (EOL) 6000$^{th}$ cycle.....232

Figure 6. 8: Variable temperature PXRD diffractograms for Pt/BHCSs (a) and the corresponding variable temperature dependent Pt crystallite growth (b). See Table 6.7: In-situ PXRD Pt crystallite size change due to the variable temperature for Pt/BHCSs .....240

Figure 6. 9: DF-STEM images (a – d) of platinum particles confined inside the carbon shell of the supports for the Pt/BHCSs sample.....241

Figure 6. 10: Variable temperature PXRD diffractograms for commercial Pt/HCS (a) and the corresponding variable temperature dependent Pt crystallite growth (b). See Table 6.8: In-situ PXRD Pt crystallite size change due to the variable temperature for Pt/BHCSs .....243

Figure 6. 11:DF-STEM images of Pt/HCSs showing the bright edges of the HCSs support due to Pt (a), the Pt map showing location of Pt in the shell region of the support (b) and (c), EDX showing the presence of Pt on the supports, the copper is due to the copper grid used for analysis (d).....244

Figure 6. 12: Variable temperature PXRD diffractograms for commercial Pt/C (a) and the corresponding variable temperature dependent Pt crystallite growth (b). See Table 6.8: In-situ PXRD Pt crystallite size change due to the variable temperature for Pt/BHCSs .....246

Figure 7. 1: Schematic of the formation of Pt/HCSs and Pt/NHCSs. (i) $SiO_2$ to $SiO_2$@RF (ii) $SiO_2$@RF to HCSs or NHCSs, (iii) HCSs or NHCSs to Pt/BHCSs or Pt/BNHCSs .....268

Figure 7. 2: Raman spectra of HCSs (a) Raman spectra of NHCSs (b) TGA profiles of HCSs, NHCSs, Pt/HCSs and Pt/NHCSs (c) TGA derivative profiles of HCSs, NHCSs, Pt/HCSs and Pt/NHCSs.....270

Figure 7. 3: TEM image of (a) Pt/HCSs (b) Pt/NHCSs (c) particle size distribution of Pt on Pt/HCSs (d) particle size distribution of Pt on Pt/NHCSs .....272

Figure 7. 4: TEM image of (a) Pt/HCSs (b) Pt/NHCSs (c) Pt – Pt interparticle distance of Pt/HCSs (d) Pt – Pt interparticle distance of Pt/NHCSs .....273

Figure 7. 5: After durability study TEM image of (a) Pt/HCSs (b) Pt/NHCSs (c) particle size distribution of Pt on Pt/HCSs (d) particle size distribution of Pt on Pt/NHCSs .....274

Figure 7. 6: BET isotherms for (a) BHCSs and Pt/BHCSs, (b) BNHCSs and Pt/BNHCSs. Pore size distribution plots for (c) BHCSs and Pt/BHCSs and (d) BNHCSs and Pt/BNHCSs. ....275

Figure 7.7: PXRD diffractograms of (a) HCSs and NHCSs, (b) Pt/HCSs and Pt/NHCSs….318

Figure 7. 8: Deconvoluted high resolution XPS spectra for Pt/HCSs (a) C1s, (b) low resolution surveys of Pt/HCS and Pt/NHCS (c) O1s and (d) Pt 4f.....281

Figure 7. 9: Deconvoluted high resolution XPS spectra for Pt/NHCSs (a) C1s, (b) N1s (c) O1s and (d) Pt 4f .....282

Figure 7. 10: The (a) Cyclic voltammograms, (b) ORR polarization I-V curves, (c) log ($I_k$)Tafel plots and (d) ORR activity and ECSA data for the Pt/HCSs, Pt/NHCSs and the commercial benchmark Pt/C (e) Tafel plots for the three catalysts.....284

Figure 7. 11: (a) Normalized ECSA% degradation of the catalysts, (b) catalyst LSVs before and after durability studies for the Pt/HCSs, Pt/NHCSs and the commercial benchmark Pt/C catalysts (c) SA data before and after durability studies (d) MA data before and after durability studies .....287

# List of abbreviations

ACO:Antimony doped cerium oxide ..... 154

AFCs: Alkaline fuel cells ..... 12

ATO: Antimony doped tin oxide ..... 154

B-CNTs: Bamboo Knot carbon naotubes ..... 18

BET-BJH:Brunaeur - Emmett - Teller - Barrett - Joyner and Halenda ..... 18

BHCSs: Broken bowl like hollow carbon spheres ..... 60

BNHCSs: Nitrogen doped broken bowl like hollow carbon spheres ..... 61

BOL: Beginning of life ..... 18

CTAB:Cetrimonium bromide ..... 127

CV: Cyclic voltammetry ..... 61

DF-STEM: Dark field Scanning Tunneling electron microscopy ..... 22

DMFCs: Direct methanol fuel cells ..... 12

EOL:End of life of a catalyst ..... 18

FCEVs: Fuel cell - electric vehicles ..... 12

HCSs:Hollow carbon spheres ..... 34

HF:Hydroflouric acid ..... 61

HOR:Hydrogen oxidation reaction ..... 16

HQ/Q: Hydroquinone / quinone ..... 174

HySA: Hydrogen South Africa ..... 14

LSV:Linear sweep voltammetry ..... 67

MCFCs:Molten carbonate fuel cells ..... 12

MSA:Metal nanoparticles total surface area ..... 168

MSI:Metal support interaction ..... 33
NCNFs:Nitrogen doped carbon nanofibers ..... 23
NCNTs:Nitrogen doped carbon nanotubes ..... 24
NHCSs:Nitrogen doped hollow carbon spheres ..... 23
NMGC:Nitrogen doped mesoporous graphitized carbon ..... 23
OLC:Onion like carbon ..... 34
OMCS:Ordered mesoporous carbon ..... 19
ORR: Oxygen reduction reaction ..... 16
PAFCs: Phosphoric acid fuel cells ..... 12
PDDA:Polydiallyldimethylammonium chloride ..... 19
PEMFCs: Proton exchange membrane fuel cells ..... 11
Pt/HCSs: Catalyst of platinum nanoparticles deposited on hollow carbon spheres ..... 59
Pt/MWCNT: Platinum deposited on top of multiwall carbon nanotubes ..... 17
Pt/NHCSs:Catalyst of platinum nanoparticles deposited on nitrogen doped hollow carbon spheres ..... 59
PXRD: Powder X-ray diffraction ..... 18
RDE: Rotating disk electrode ..... 156
RGO:Reduced graphene oxide ..... 20
RHE: Reversible hydrogen electrode ..... 168
SA:Surface area specific activity ..... 22
SOFCs: Solid oxide fuel cells ..... 12
TEM:Transmission electron microscopy ..... 18
TEOS: Tetraethyl orthosilicate ..... 38
TGA:Thermogravimetric analysis ..... 57
WE:Working electrode ..... 63

XPS:X-ray photoelectron spectroscopy.....57

# Chapter 1

# Introduction to the study and literature review

## 1.1: Introduction

The demand for energy, globally, has been increasing dramatically over this past century. This has been due to industrialization of previously less industrialized nations like China, India and Saudi Arabia. Also, the further growth in industrialization in previously industrialized nations like the United Kingdom, the United States of America and Germany, among many others, has contributed to the increase in energy demand globally.

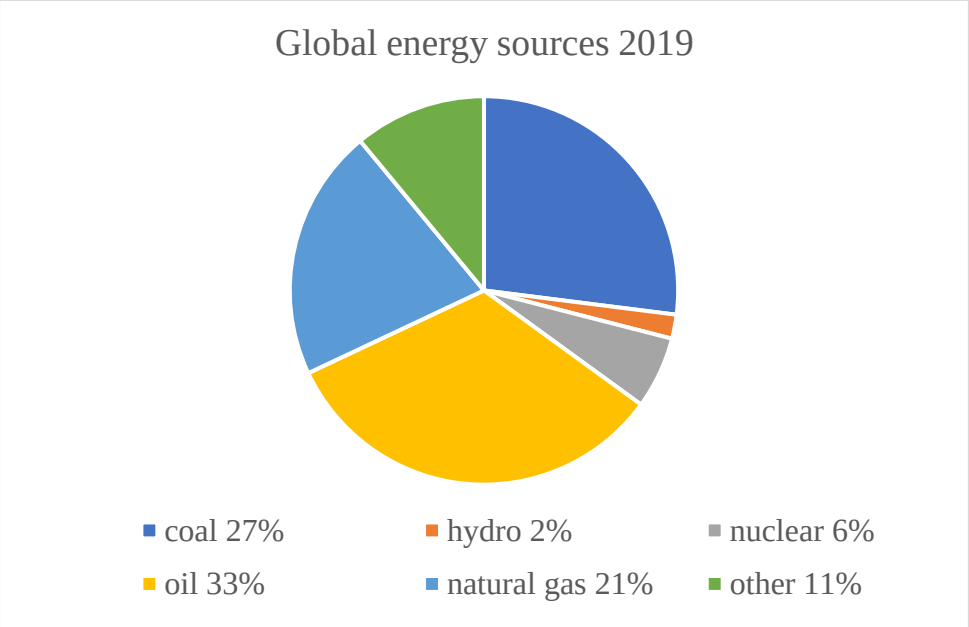



Figure 1. 1: Global energy sources for all purpose use in 2019.[1]

Globally energy sources for all countries stand at 27% coal, 2% hydro, 6 % nuclear, 33% oil, 21% natural gas and 11 % for other sources like wind, solar and biomass (Figure 1.1), clearly showing an over dependence on fossil fuels.

Rapid industrialization in China, the second-largest economy in the world, has resulted in annual growth in demand for energy of about 5.7%.[2] On its own, China is the largest consumer of energy accounting for about 22% of energy demands globally. In 2019 China's main source of energy (Figure 1.2) was coal accounting for about 66% of its demand. Renewable energy sources like wind, hydro and solar accounted for only about 28%.

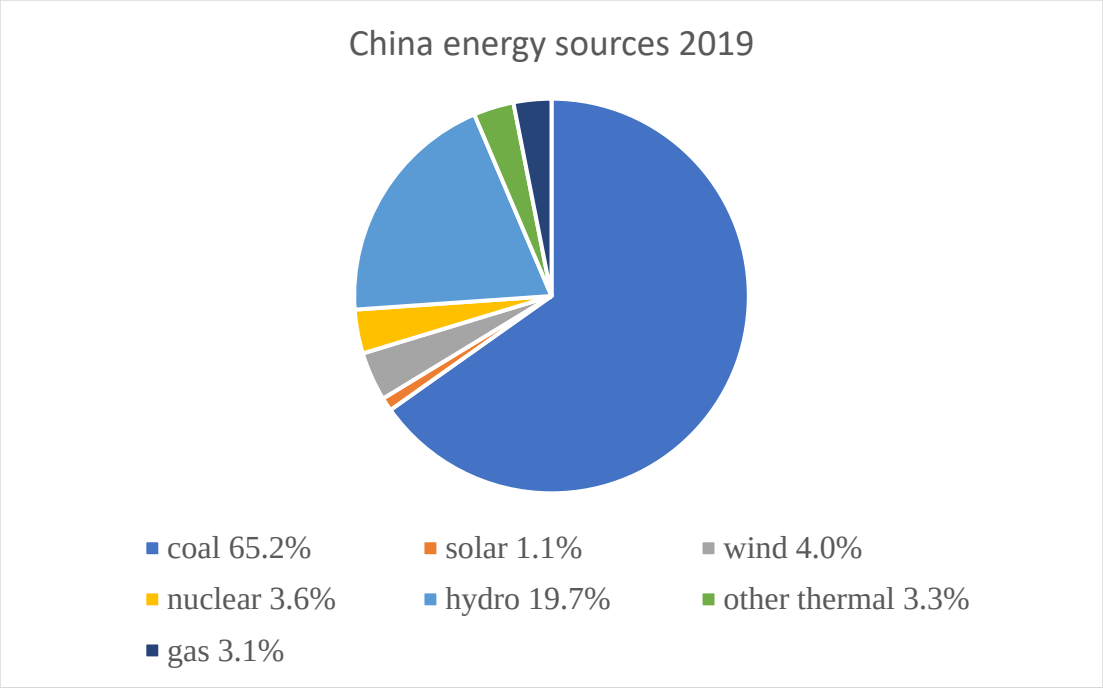



Figure 1.2: Sources of energy for all purpose use in 2019 China.[1]

The same applies to South Africa where coal usage is about 68%, biofuels and waste 11%, natural gas 3%, renewables 0.3%, crude oil 16% and nuclear energy is 2.2% as of December 2015.[3]

In contrast, countries like Germany and the UK have a lower coal usage for energy than China. About 6% of the energy consumed in the UK is from coal and Germany consumes about 36%

of its energy from burning coal. However, in Iceland, 100% of the energy consumed is from renewable sources. Hydropower and geothermal are the main sources of energy in Iceland. Thus, the global values may not reflect national usage. [4,5]

The challenge associated with the high use of fossil fuels like coal and petroleum is the limited supply and the pollution they cause. At the current consumption rate of about 11 billion tonnes of oil per year, the current proven oil reserves and global supply cannot go beyond 53 years for crude oil.

British Petroleum (BP) predicted in 2016, in a review of the world energy consumption, that the global reserves for coal and crude oil will only last 115 years and roughly about 50 years for both crude oil and natural gas. This implies that within 115 years, new sources of energy will be required to meet the daily needs of the global population While predictions like this have been made before and proven incorrect in terms of usage, there is no doubt that there is an eventual limit to coal/oil/gas supplies.[6]

Besides the depletion of these fossil fuels, the other challenge associated with using non-renewable energy sources based on carbon is the polluting gases, in particular $CO_2$, $NO_2$ and NO, that these fuels produce. These polluting gases and other drivers have been shown to accelerate climate change. Climate change has been manifested as global warming, rising of sea levels, erratic weather patterns, massive recurring droughts, and fires. Globally hundreds of billions of dollars have been lost due to extreme weather. [7,8]

At the current rate of emissions, the melting glaciers in the Arctic and Antarctic will result in at least a 30 cm rise in sea levels in some places by the year 2050. Rising sea levels negatively impact low-lying places and cities like Miami, Guangzhou, Mumbai, New Orleans, and Osaka. These cities have a total population of about 55 million inhabitants and a GDP of about 3 trillion American dollars (US$ 3 trillion). Rising sea levels would affect the economies and livelihoods

of these individuals and the global population dependent on these cities in terms of supply chains of goods and services.[9]

Evidence suggests that extreme weather events and rising sea levels are due to the use of highly polluting fossil fuels. [7]Fossil fuels like coal, natural gas, and petroleum produce greenhouse gases which have been linked to an increase in global temperatures. Rising temperatures cause the melting of glaciers causing sea levels to rise. An increase in the levels of these gases also causes an imbalance in the way the earth regulates temperatures affecting rainfall patterns and causing droughts. Higher temperatures are known to spontaneously cause wildfires in areas where there is vegetation that can be burned. Also, the clearing of forests for agriculture and residential purposes particularly in the Amazon and Congo basin is causing an imbalance in the way nature regulates the excess carbon dioxide levels.[10]

There is, therefore, a great need for alternative energy sources and energy conversion systems that have a neutral carbon footprint but that are equally efficient when compared to fossil fuels.

Renewable energy sources that can be harnessed globally are geothermal, wind, solar energy, and hydroelectricity among others. Also, fuel cells can be used as an energy conversion system transforming chemical energy stored in hydrogen or carbon containing sources like methanol into usable electricity.

In this thesis the focus will be on using hydrogen, an abundant, renewable and sustainable energy source and using a process to convert the chemical energy source to products that are electricity and the by-products heat and water. Fuel cells do not have to use only $H_2$ as the energy source. Fuel cells can use carbon-based reactants, but these fuel cells also generate $CO_2$. However, this thesis does not report on carbon fuel-based fuel cells.

## 1.2: Fuel Cells - PEMFCs

Fuel cells are attractive energy conversion systems that can significantly contribute to the use of renewable energy resources. Fuel cells are devices that convert chemical energy into a usable electrical current. The current is used to power machinery and technological devices. Different types of fuel cells exist and among them are solid oxide fuel cells, proton exchange membrane fuel cells, direct alcohol fuel cells, alkaline fuel cells, phosphoric acid fuel cells, molten carbonate fuel cells, and reversible fuel cells. The fuel cells that have been studied are classified according to their properties (Table 1.1) [11]

Fuel cells can be used in mobile applications like cars, airplanes, and ships. They are lightweight and portable and when hydrogen and oxygen, used as fuel and oxidant in proton exchange membrane fuel cells (PEMFCs), is sourced from the solar electrolysis of water, they have a zero-carbon footprint. Heat and water produced can be reused during the operation of these fuel cells making them clean and sustainable. [12]

Table 1. 1: Some of the fuel cell types [11,13–17]

| **Type** | **Electrolyte** | **Temp °C** | **Fuel** | **Advantage** | **Problems** |
|---|---|---|---|---|---|
| Polymeric (PEMFC) | Polymeric membrane | 30 - 100 | $H_2$ | Fast start-up solid electrolyte | Pure $H_2$ needed, expensive catalysts |
| Direct methanol (DMFC) | Polymeric membrane | 30 - 100 | $CH_3OH$ | Liquid fuel no reforming step for fuel | Slow reaction, fuel crossover from anode to cathode |

| | | | | | |
|---|---|---|---|---|---|
| Alkaline (AFC) | KOH liquid | 65 - 220 | KOH | Better current response fast cathode reaction | Reactants must be removed |
| Phosphoric acid (PAFC) | $H_3PO_4$ | 150 - 220 | $H_2$ | High efficiency with heat cogeneration | Low power and current, expensive catalysts |
| Molten Carbonate (MCFC) | Carbonates of (Li, Na, K) | 600 - 1000 | $H_2$ | Better conductivity high current density | Slow start-up, material problems |
| Solid Oxide (SOFC) | Oxides of (Zr, Y) $O_2$ | 600 - 1000 | $H_2$ | Solid electrolyte low-cost material | Material problems, corrosion of metal |

The proton exchange membrane fuel cell (PEMFC) is the most appealing of the fuel cells due to its properties and mode of operation. The PEMFC or hydrogen fuel cell converts chemical energy stored in hydrogen gas into current in the presence of oxygen. The other products are heat and water. PEMFCs are attractive because they possess other good properties such as light weight, fuel efficiency, applicability in mobile use and the use of lightweight hydrogen fuel. This type of fuel cell is portable and is the number one choice for the FCEV (fuel cell electric vehicles) car makers. The PEMFC is also versatile when cells are placed in series and they can be assembled to produce electricity in the mega and gigawatt-scale.[18]

Some examples of the role of industries in developing fuel cell technologies are given below.

Currently, companies like Hydrogenics are global leaders in the use of megawatt-scale fuel cell stations (figure 1.3). They have a flagship 1 MW (Megawatt) PEMFC plant that can generate a system output voltage of between 380 – 480 VACS (alternating current-voltage) at >50% hydrogen fuel efficiency at the beginning of their life before factoring important parameters

like catalyst durability. This standby power unit has a system output frequency of between 50 – 60 Hz and noise levels of less than 75 decibels. To put it into perspective, an average motorcycle produces about 90 decibels of noise. This fuel cell system is also advantageous as it has a lifespan package design life of about 20 years with fuel consumption of about 750 $Nm^3/h$ per 1 MW. [19,20]




Figure 1. 3: Hydrogenics' 1 Megawatt fuel cell power generation platform.

Recently Ballard Power systems (Ballard is a fuel cells developer) and Hydrogen de France (HDF Energy), an independent power producer from France, signed a product development contract for the manufacture and connection of a multi-megawatt PEMFC fuel cell system for addition to the HDF energy network for stationary power applications.[21]

Toyota and Fuel Cell Energy signed an agreement to produce a fuel cell system to be in operation by the end of 2020. The Tri-Gen plant will produce about 2.4 MW of electricity and

1.2 tonnes of hydrogen per day to support the Toyota Mirai passenger cars that are powered by PEMFCs.[22]

These kinds of investments into fuel cell technologies are an indication that many companies see a future that will depend on a hydrogen economy. If this occurs, fuel cells will be a primary energy conversion system used by future generations. These investments come at the back of increases in sales of fuel cell and non-fossil fuel-based cars [23,24]

In mobile applications, Ballard is working with several companies that operate motor vehicles for various purposes. In 2019, Ballard received a purchase order from Anglo American for 900 KW of fuel cell modules for use in an experimental mining dump truck demonstration project. The fuel cell dump trucks would be tested in 2020 in South African mines followed by deployment of these trucks in its global network of operations. Anglo American plans to implement these mining trucks using MW scale fuel cell modules in the future in its global mining operations.[25]

PEMFCs are platinum dependent and platinum or its alloys or core shells have proven to be the best catalysts for the oxygen reduction reaction.[26] Other catalysts that are platinum independent have either been shown to be highly active and less durable or possess low activity such that they cannot be commercially viable.[27–29]

Platinum is abundant in South Africa and Zimbabwe and therefore this puts these countries in a better PEMFCs supply chain position if research on these is prioritized. South Africa has the largest proven platinum group metals reserves globally. For many decades South Africa has been looking at ways to promote value addition of the Pt as well as to find new markets for the Pt group metals. Now, South Africa is seeking to place itself at the top of fuel cell components supply chain. Unfortunately, Pt which is abundant in South Africa, is the most expensive component of a PEMFC.

In the past the Pt market has been largely driven by catalytic converter industry. The catalytic converter market is expected to fall dramatically in the future when international restrictions on fossil fuel cars come into place. Most countries in the European Union have already put in place legislature that prevents the use of fossil fuel powered cars by 2040.[30–33] Fossil fuel cars are to be replaced by battery driven cars and fuel cell electric vehicles (FCEVs) and these cars use fuel cells or a fuel cell-battery combination.

Platinum is one of the major components of a PEMFC, mostly used to power cars. As a result, the Department of Science and Innovation (DSI) in South Africa through its fuel cell research arm, HySA (Hydrogen South Africa) has been involved in several research initiatives to develop the use of Pt in fuel cells. HySA catalysis has been developing PEMFC electrocatalysts and through its business vehicle company, HyPlat, has been selling catalysts and fuel cell components to numerous global customers. [34]

## 1.3. Advantages of PEMFCs

Some of the advantages of PEMFCs are listed below.

- PEMFCs can be used in both stationary and mobile applications. They can be used to power both homes and moving cars. This makes it possible to replace gasoline and natural gas-powered engines with fuel cells.[35]
- Fuel cells have a theoretical energy efficiency of about 40% which is double that of the gasoline-powered engine. [36,37]
- They are lightweight and therefore favourably applicable for use in cars, buses and other engine powered vehicles. Recently Hyundai commercialized an FCEV for the market that is powered by a PEMFC. The Hyundai ix35 FCEV or Tucson FCEV is a hydrogen-powered fuel cell vehicle with an 80-kW electric motor engine and a 152 V battery plus a 153 L hydrogen tank. The car has a range of 300 Km and a top speed of

150 Km.h$^{-1}$. Another fuel cell automobile manufactured by Hyundai is the Hyundai Nexo, a crossover SUV with a range of 600 Km powered by an upgraded 120 Kw electric motor. Other automobiles manufacturing companies have produced these fuel cell electric vehicles (FCEV) including the Toyota (Mirai), Mercedes Benz, Honda, BMW among many others.[38–43]

- For fuel cell cars, PEMFCs offer a driving range comparable to the gasoline engine. [44]
- Hydrogen and oxygen which are highly abundant materials are the fuel and oxidant used in PEMFCs. Hydrogen can be produced by the catalytic electrolysis of water.
- Fuel cell vehicles are carbon neutral, the only by-products are heat which can be reused in the fuel cell engine and portable water which can be consumed.
- Hydrogen is one of the lightest elements and as a result does not provide challenges in terms of tank volume to weight ratio in transportation and mobile applications.
- PEMFCSs produces more power per volume of fuel that is used compared to other fuel cell types.
- PEMFCs are compact and lightweight due to the low-density fuel and as a result, are easily applicable in mobile applications.
- PEMFCs have a low operating temperature, below 100 °C, making rapid start-up easier thereby making this fuel cell type more convenient for use.[23]
- PEMFCs can be modelled to suit various sizes of vehicles (figure 1.4). They can power aeroplanes, ships, cars, heavy duty trucks and passenger vehicles.
- PEMFCs can be used off-grid and in remote places providing clean energy.

To date, fuel cells have been used in stationary applications as well as in transportation. Hydrogen fuel cells have been used to power trains, heavy-duty trucks, passenger sedan

vehicles like the Toyota Mirai as well as passenger SUV crossover vehicles like the Hyundai Nexo (figure 1.4).




Figure 1.4: (a) PEMFC run passenger train from Germany, (b) Toyota PEMFC heavy duty truck, (c) Toyota Mirai fuel cell passenger sedan and (d) Hyundai Nexo crossover SUV running a hydrogen fuel cell. [38,45–47]

## 1.4: Reactions in the PEMFC

The critical reactions for the PEMFC are the hydrogen oxidation reaction (HOR) at the anode and the oxygen reduction reaction (ORR) at the cathode. The hydrogen oxidation reaction has favourable kinetics and occurs at an affordable over-potential. Very low loadings of the highly active Pt are needed for this reaction to occur with ease and to go to completion. In the acid type electrolytes, ORR occurs mainly via two known mechanisms. The direct four-electron pathway from $O_2$ to $H_2O$ or the slower and indirect two-electron pathway via the formation of hydrogen peroxide.[48–50] To prevent the unfavourable $H_2O_2$ pathway, high loadings of Pt are

used. High Pt loadings in cathodes are major cost drivers in the development and adoption of fuel cells. Lower loaded Pt catalysts are being developed with better activity and durability.[51,51–53]

The schematic of a PEMFCS is shown in Figure 1.5.

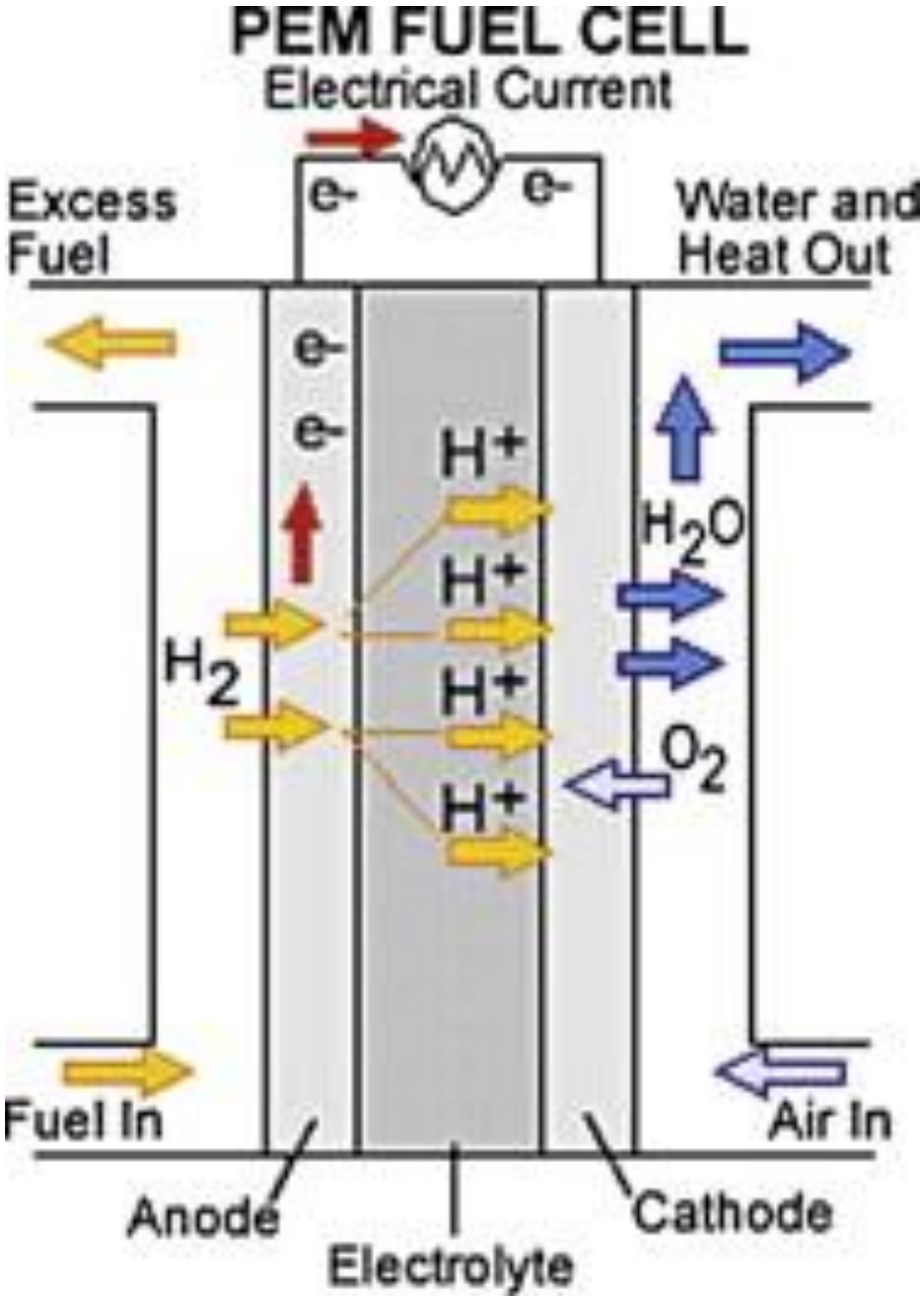



Figure 1.5: Schematic illustration of a PEMFC.[54]

At the PEMFC anode the hydrogen oxidation reaction occurs resulting in the formation of protons and electrons. The produced electrons flow across the circuit to the cathode where they combine with the protons which would have flowed through the proton selective membrane. Here they will encounter oxygen. The hydrogen oxidation reaction (Equation 1.1) is a thermodynamically and kinetically favourable reaction that occurs at a very low overpotential.[55]

$$2H_2 \rightarrow 4H^+ + 4e^- \qquad (1.1)$$

At the cathode, the oxygen reduction reaction occurs (Equation 1.2). Here the oxygen gas that is fed to the cathode reacts with the electrons from the circuit and protons from the hydrogen oxidation forming water and completing the fuel cell reactions.

$$O_2 + 4H^+ + 4e^- \rightarrow 2H_2O \qquad (1.2)$$

The overall PEMFC reaction is shown in Equation (1.3).[26]

$$O_2 + 2H_2 \rightarrow 2\,H_2O \quad E° = 1.229\ V \qquad (1.3)$$

## 1.5: Approaches to higher activity and durability in ORR – a review

Commercialization of fuel cell vehicles is peaking, and the markets are ready for the change. Demand for fuel cell vehicles will increase and this must be met by reliable fuel cell driven engines and active and durable catalysts. In this regard, numerous approaches have been adopted to make the fuel cell catalysts. Among the many initiatives to find highly active and durable catalysts, metal oxide supports, structured carbon-based supports and other supports have been used to stabilize the catalyst which is made of Pt nanoparticles for the ORR. Precious metal-free ORR catalysts have also been studied in-order to bypass the high cost factor when using Pt. [56–58] The quest for highly active and durable ORR catalysts is thus an ongoing one.

## 1.5.1: Pt catalysts deposited on various carbon- and carbon-based supports

In early studies, various pristine carbon supports were used in the quest of finding durable and highly active ORR catalysts. Carbon supports have many advantages, one of which is that they can readily be oxidized (burnt off) in air after their use in fuel cells allowing for the recovery of the precious metal catalyst components.

The supports studied include reduced graphene oxide, boron carbide, single wall carbon nanotubes, multiwall carbon nanotubes, Ketjen and acetylene black, bamboo like carbon nanotubes, ordered mesoporous carbon and Vulcan carbon. The carbons can be doped with heteroatoms like nitrogen to improve the properties of the whole catalyst system thereby improving parameters like selectivity, durability, and reusability. The pore structures of carbon materials can also be tailored such that supports with enhanced properties can be synthesized. The tunability of the carbon supports to yield materials with specific properties makes them attractive as fuel cell cathode supports. Examples of some carbon materials that have been studied as carbon-based supports for Pt in ORR catalysis are described below (Table 1.2).

The studies involving platinum and the various forms of carbon highlight the versatility of carbon in fuel cell supports. It is imperative to say that a well-dispersed Pt catalyst of optimum particle size, deposited on the surface of a nanostructured carbon or doped carbon support can be used as a good ORR catalyst offering high activity and durability beyond the envisaged 5000 h.[59,60]

Hasche and colleagues[61] studied the activity, stability, and degradation of multiwall carbon nanotube supported Pt in fuel cell reactions. Their study aimed at obtaining insight into the mechanisms controlling the degradation of the catalysts, focusing on nanoparticle coarsening and the corrosion of supports. They studied platinum nanoparticles supported on both multiwall

carbon nanotubes (Pt/MWCNTs) and platinum nanoparticles supported on a Vulcan carbon (Pt/Vulcan XC 72R) catalyst with comparable mean Pt particle sizes (diameter between 1 – 4 nm). The catalysts were subjected to two durability tests (at 0.5 – 1.0 V vs. RHE and at 0.5 – 1.5 V vs. RHE) for lifetime and start-stop simulation studies respectively. The group studied the beginning of life (BOL) by ORR activity and physical characterization (TEM, PXRD, BET-BJH) studies followed by end of life (EOL) characterization studies. Their ORR results did not indicate any kinetic benefit of using MWCNTs over Vulcan XC 72 R as a support. In the lifetime durability test, the Pt/MWCNT showed smaller losses in mass specific activity (MA), area specific activity (SA) and electrochemical active surface area (ECSA) compared to the Pt/Vulcan XC 72 R. Similar trends were observed for the start-up but bigger losses were observed in the Pt/Vulcan XC 72 R material relative to the Pt/MWCNT catalyst. Using the obtained data, they suggested that ECSA loss during the durability studies was not associated with particle growth but rather was due to carbon support corrosion, Pt detachment and loss of electrical contact between the nanoparticles of the metal and the support.

To better explain the dissolution mechanism, they used the relation of particle size and dissolution potential given in the combination Nernst and Gibbs–Tomson equation (Equation 1.4)

$$E = E(0) - RT/(nF)\ln K - (2\Upsilon\Omega)/rnF \qquad (1.4)$$

where E - particle dissolution potential, E(0) - dissolution potential of a flat metal surface, n – number of transferred electrons , Ω – molar volume, ϒ – the surface energy and r – the particle radius. Using the above relationship, they postulated that ECSA loss due to durability cycling as a result of dissolution and redeposition, would be significantly larger at higher electrode potentials and smaller Pt particle sizes.

Carbon corrosion is known to be facilitated by unsaturated dangling bonds and as Vulcan XC 72 R is an amorphous carbon it would exhibit more $sp^3$ dangling bonds than ordered $sp^2$ domains in MWCNTs. The graphitization extent (G) was determined from the averaged spacing of the studied carbon supports using the formulae (Equation 1.5)

$$(G) = (3.440 - d_{002})/ (3.440 - 3.354) \quad (1.5)$$

A graphitization extent of near zero was determined for the Vulcan XC 72 R compared to the graphitization extent of 19% for the MWCNT support. Both catalysts had similar crystallite Pt sizes, but the Vulcan support had a higher BET surface area (205 $m^2.g^{-1}$) compared to the MWCNTs (153 $m^2/g$). Under a lifetime durability protocol, the ECSA value for Pt/MWCNT dropped a mere 12% compared to 25% for the Pt/Vulcan XC 72 R. Under the more severe start-up cycling conditions, the ECSA of the Pt/MWCNT dropped by 48% whereas the Pt/Vulcan experienced a 68% decrease. They concluded that high durability was dependent on high extent of graphitization of the support and its lower BET surface area.

Platinum supported on bamboo carbon nanotubes was studied for ORR activity and durability by Shao and colleagues[61]. They discovered that Pt nanoparticles were preferentially deposited on the highly defective bamboo knots of bamboo CNTs (Pt/B-CNTs). They attributed the better durability to the metal-support interactions associated with the special nanostructure of the bamboo CNTs.

Kongkanand and co-workers[62] studied Pt/CNT catalysts for ORR activity and durability with similar Pt loading of 14 $\mu g.cm_{Pt}^{-2}$ for the CNT catalyst and a commercial benchmark catalyst. Despite the similar Pt loading, the ECSA for the commercial catalyst was 33.5 $m^2.g^{-1}$ compared to 17.8 $m^2.g^{-1}$ for the Pt/CNT catalyst. The lower ECSA for the CNT catalyst was attributed to the poor dispersion of the Pt nanoparticles. However, despite the lower ECSA, a 10 mV earlier onset ORR potential was observed for the Pt/CNT catalysts indicating that the CNTs

themselves were involved in the electrochemical process. The high ORR activity was attributed to the porous nature of the supports. Potential cycling for 36 h resulted in a 70% reduction in ECSA for the commercial catalyst and a negative shift of the ORR onset potential. However, a small 15 mV negative decrease in onset potential for ORR was observed for the Pt/CNT catalyst coupled with a 40% loss in ECSA. The minimal losses in onset potential and ECSA were attributed to the better anchoring between the Pt and the support.

Nagasawa and co-workers[63] studied various Pt/Ketjen black and Pt/Acetylene black carbon-based catalysts for ORR activity and durability. Their findings indicated that the differences in MA originated from the differences in the fraction of Pt on the carbon supports which was available for utilization. They attributed the low durability observed in the Pt/Ketjen black catalyst to the surface oxidation of the Pt catalysts which led to the formation of PtO layers. These layers were more easily removed when compared to the Pt/Acetylene black catalysts. PtO layers of the Pt/Ketjen black catalysts were readily reduced to metallic Pt resulting in better durability. They attributed this behaviour to the variation in Pt coordination numbers and Pt-Pt distances due to the surface properties of the various supports examined.

He and colleagues[64] synthesized poly(diallyl dimethyl)ammonium chloride (PDDA; a surfactant and passivation agent) stabilized Pt nanoparticles and Pt-Pd catalysts supported on reduced graphene oxide. They observed high activity and durability and attributed this to better Pt dispersion facilitated by PDDA passivation of the Pt. They proposed that the PDDA coating hindered the dissolution of the Pt. They also proposed that preferential dissolution of the Pd would occur resulting in the formation of Pt rich surfaces. Confinement of Pt-Pd to the RGO sheets was the explanation for the reduced agglomeration that they observed. After 3000 potential cycles, the catalyst without PDDA passivation denoted as no PDDA-Pt/RGO, retained about 50% ECSA compared to about a 78% ECSA retention for the PDDA passivated catalyst denoted as PDDA-Pt/RGO. Also, the oxophilic Pd facilitated the favourable binding

of oxygenated groups on the Pt thereby limiting the binding of the OH groups to the Pt, and as a result facilitating enhanced ORR activity.

Zhang and colleagues[65] studied Pt nanoparticles supported on three-dimensional ordered mesoporous carbon (Pt/OMCS) for ORR activity and durability. They compared the catalysts with a commercial Pt/C catalyst. They attributed the higher activity and durability to the high dispersion of the Pt and availability for ORR of the active sites on the Pt/OMCS. The three-dimensional connected mesopores facilitated facile mass transport of the gases, increasing ORR. The pore confined Pt was restricted from detachment due to its partial or complete exclusion from the surface. Higher activity was attributed to the abundant Pt active sites with hydroxyl intermediates that facilitated CO oxidation leading to enhanced tolerance.

Other corrosion-resistant materials have been used as supports. Jackson and her co-authors used boron carbide with a low BET surface area as a support for a 20wt% Pt catalyst. MA and SA activity was high, eclipsing 0.20 $A.mg^{-1}$ and 0.17 $mA.cm^{-2}$ respectively. They observed more than a 50 % ECSA retention after 6000 potential cycles using an aggressive rectangular wave profile. The strong metal to support interactions were attributed to the high durability of the boron carbide supported Pt catalyst and the enhanced activity was attributed to the modification of the electronic structure of the Pt by the BC support due to charge transfer between metal and support.[66]

Table 1. 2: Examples of platinum catalysts supported on various carbon supports for the ORR

| Catalyst | Comment/ reason for enhanced activity and durability | ref |
|---|---|---|
| | | |

| | | |
|---|---|---|
| Pt/BC | Change in electronic structure of Pt, enhanced metal -support interaction between graphite rich boron carbide (BC) and Pt. | 66 |
| Pt/SWCNT | High porosity of SWCNT allowing diffusion of gases, higher electron transfer rate, | 62 |
| PDDA-Pt/RGO<br>Pt-Pd/RGO | PDDA coating hindered the dissolution of the Pt. Preferential dissolution of the Pd resulted in the formation of Pt rich surfaces. Confinement of Pt-Pd to the RGO sheets caused reduced agglomeration. Oxophilic Pd facilitates favourable binding of oxygenated groups facilitating ORR activity | 64 |
| Pt/Ketjen black<br>Pt/Acetylene black | High durability of Pt/AB attributed to the variation in Pt coordination numbers and Pt-Pt distances induced by support surface properties. | 63 |
| Pt/B-CNT | Bamboo like nanostructure which provide more bamboo knot defects and edge plane like defects. Enhanced Pt – support interaction | 61 |
| Pt/OMSC | Unique hierarchical structure with ordered macropores and mesopores that facilitate the mass transfer and improve the Pt particle dispersion. Meso structure and pore | 65 |

| | | |
|---|---|---|
| | confinement prevents dissolution and agglomeration of Pt. | |
| Pt/Vulcan XC 72 R<br>Pt/MWCNT | Lower BET surface area for Pt/MWCNT and high extent of graphitization promoted better durability. $sp^3$ dangling bonds and defects promoted degradation of Pt/Vulcan XC 72 R | 61 |

## 1.5.2: Pt Catalysts deposited on nitrogen doped supports.

Nitrogen doped carbon has been studied extensively due to the favourable properties associated with the nitrogen dopant. The electron density associated with the extended π conjugation of the nitrogen functional groups has been shown to influence the Pt particle size and subsequent activity and durability of the Pt catalyst.[67] Nitrogen groups rich in electron density actively influence nucleation and growth of Pt nanoparticles thereby controlling the final Pt particle size. Also, the introduction of nitrogen functional groups generates defects in the carbon support. These defects enhance the surface area of the support and provides places where Pt favourably deposits. Highly defective materials have been shown to enhance the formation of smaller particle sizes of Pt and have led to subsequent improved activity.[68,69] Some examples of Pt supported on N-doped carbons are given in Table 1.4

Melke and co-workers[70] studied the metal–support interaction (MSI) between Pt and nitrogen-doped carbon nanofibers for ORR. In their study, they showed that Pt shifted its electrons into the π conjugated system of the support thereby increasing the support electron density. This then enabled the nitrogen centres to operate as nucleation centres where smaller Pt nanoparticles were grown, resulting in better dispersion being observed in the nitrogen-doped supports.

Higgins and co-workers[68] studied nitrogen-doped carbon nanotubes as supports for platinum in oxygen reduction reactions. They made comparisons between three catalysts, a pristine Pt/CNT, Pt/ED-CNT with about 35% pyridinic nitrogen and Pt/PY-CNT with a lower content of pyridinic nitrogen. They found similar Pt particle sizes for the nitrogen-doped supports. The Pt was in the 2 – 4 nm size range whereas for the pristine CNTs, Pt particle sizes were slightly larger and in the 3- 6 nm range. Nitrogen doping enhanced the better Pt dispersion and the resulting Pt particle sizes. The Pt/ED-CNT catalysts had better ORR activity with an earlier onset potential when compared to the Pt/PY-CNT with less pyridinic nitrogen. The order of ORR onset potential was Pt/ED-CNT > Pt/PY-CNT > Pt/CNT. Their findings consolidated the idea that nitrogen doping improved support surface properties and enhanced characteristics like dispersion of metal nanoparticles and the final particle size. They could not explain why a higher pyridinic nitrogen proportion was responsible for better ORR activity. However, it was clear that pyridinic nitrogen was responsible for better ORR than the other forms of nitrogen.

Wang and co-authors[71] studied platinum supported on nitrogen-doped carbon nanofibers for ORR. The nitrogen-doped supports had higher proportions of graphitic nitrogen compared to pyridinic nitrogen. Nevertheless, higher ORR activity was observed for all the catalysts studied. After 3000 cycles of durability studies, the commercial catalyst had a -53 mV change in the half-wave potential compared to the -21 mV for the nitrogen-doped carbon nanofiber support. Pore confinement of the Pt was attributed to the minimal loss in the ORR activity after durability tests. The improved stability of the nitrogen-doped catalysts was also attributed to the Pt-π orbital bonding strength and the presence of functional anchoring groups. Mass and specific activity were more than 100% larger than the commercial JM20 catalysts used for benchmarking. This trend was attributed to the presence of defects (as shown by Raman spectroscopy), pores, roughness, and nitrogen doping.

Galeano and co-workers[72] synthesized mesoporous graphitic and nitrogen-doped hollow carbon spheres and supported Pt nanoparticles on the carbon supports. Using dark field scanning tunnelling electron microscopy (DF-STEM), they discovered that the Pt nanoparticles were mostly confined within the pores of the HCS shell and thereby reduced the tendency of the Pt particles to undergo detachment and agglomeration. Pore confined Pt was found to be less prone to migration and coalescence. In their study, the mass specific activity (MA) and surface area specific activity (SA) of the catalysts was enhanced due to the nitrogen doping. The hollow graphitic carbon spheres had a diameter of about 250 nm and a shell thickness of about 25 nm. In situ XRD data showed restricted growth of the Pt crystallites after the catalysts were annealed in argon up to 850°C (Figure 1.6). The restricted growth was attributed to pore confinement of the Pt. The authors concluded that the observed durability during potential cycling was due to the confinement of the Pt nanoparticles as well as the favorable anchoring of the Pt to the nitrogen groups after doping. DF-STEM data showed the presence of Pt clusters concentrated in the HCS or NHCS shell, an indication that indeed most of the Pt was confined inside the pores of the catalyst supports (figure 1.6 a -d). Using identical location – transmission electron microscopy (IL-TEM), they were able to trace the growth of the Pt nanoparticles during ORR durability studies. Pore confined Pt was shown not to grow at the same rate as free surface embedded nanoparticles. Meier's group observed that incorporating nitrogen into the structure of the support was advantageous. Nitrogen doping restricted the growth of the Pt particle size resulting in enhanced dispersion and better ORR activity for smaller Pt sizes. XPS studies confirmed the presence of pyridinic-N groups.

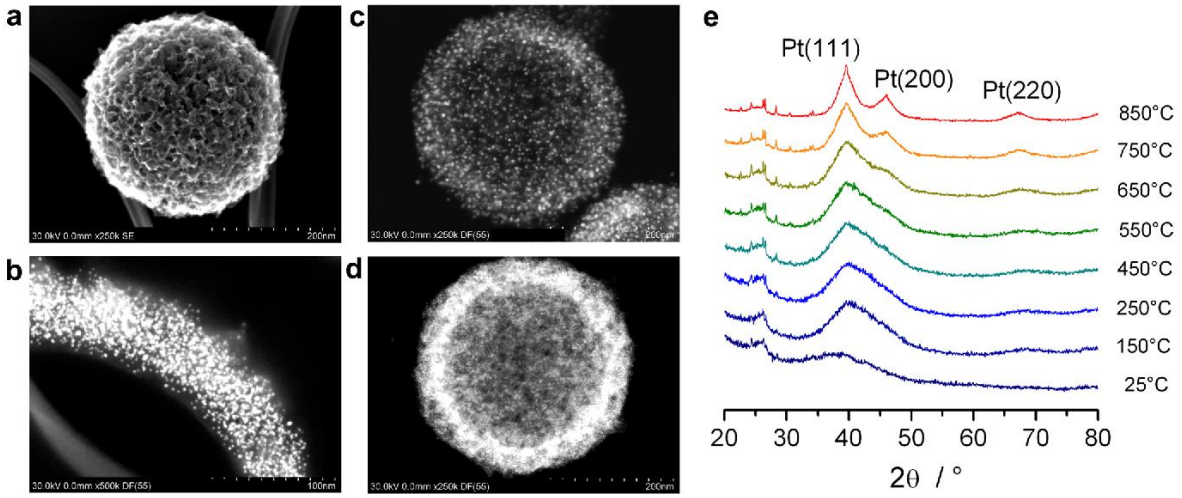



Figure 1.6: (a) to (d) are DF-STEM images showing pore confined Pt in the hollow carbon supports and (e) variable temperature in-situ PXRD diffractograms for a Pt/C catalyst confirming pore confinement. [72]

Jukk and co-authors[73] studied Pt deposited on nitrogen-doped graphene nanosheets for ORR. They observed better dispersion of Pt on the nitrogen-doped surfaces and Pt particle sizes smaller than 6 nm. They attributed the small Pt particle sizes and good dispersion to the favourable electronic interaction between Pt and the electrons in the nitrogen functionalities.

Jung and colleagues[74] observed improved durability of Pt supported on N-doped graphitized carbon in ORR (Pt/NMGC) (Table 1.3). The NMGC was enhanced with traces of Ni and Fe respectively for improved graphitization.

Table 1.3: ORR activity data for the Fe and Ni-rich Pt supported on nitrogen-doped mesoporous graphitic carbon

| Sample | ECSA ($m^2.g^{-1}$) | MA ($A.mg^{-1}$) | SA ($\mu A.cm^{-2}$) |
|---|---|---|---|
| Pt/C | 79.8 | 0.08 | 100 |
| Pt/NMGC-Fe | 61.7 | 0.10 | 150 |
| Pt/NMGC-Ni | 60.5 | 0.07 | 120 |

They speculated that the enhanced ORR activity was due to the interaction between the Pt and the various supports which resulted in a positive synergistic effect. The observed durability for Pt/NMGC-Fe was attributed to the interaction between Pt and the support due to the enhanced π sites on carbon induced by a high degree of graphitization and the structurally improved stability of the Pt that reduced Pt dissolution. This was due to delocalization sites of $sp^2$ hybridized carbon overlapping with the d orbitals of the Pt.

Table 1. 4: Platinum catalysts supported on various nitrogen doped carbon supports

| Catalyst | Comment/ reason for enhanced activity and durability | ref |
|---|---|---|
| Pt/NCNFs | High Pt utilization due to improved dispersion. Improved Pt – support interaction. Pt electron density accepted by nitrogen doped CNF support improving metal -support interaction. | 71 |
| Pt/NHCSs$_{\Delta T}$ | nitrogen doping of the carbon supports lead to high initial mass activities due to improved high platinum dispersion. however, it did not lead to an improvement of the catalyst stability. Heat treatment caused slight growth of Pt prior to ADT leading to better durability. | 72 |
| Pt/NCNTs | Increase in performance is attributed to distinct structure and electronic enhancement from nitrogen doping. | 68 |
| Pt/NGSs | High dispersion of Pt on nitrogen doped graphene nanosheets due to strong interaction between Pt and N functionalities. Nitrogen groups amounting to between 6 – 7 at.%. | 73 |
| Pt/NMGC - Fe | The strong interaction between Pt and NMGC-Fe contributes to high durability. Electron | 74 |

| | | |
|---|---|---|
| | density of nitrogen functionalities caused small Pt size and higher dispersion. The Fe in the NMGCs improved graphitization and electronic conductivity. | |
| Pt/NHCS | Durability due to pore confinement of Pt, Nitrogen enhanced tethering between Pt and support, favourable metal -support interaction. | 72 |
| Pt/Py-CNT<br>Pt/EDA-CNT | Nitrogen doping improved support surface properties enhancing characteristics like dispersion of metal nanoparticles and the final particle size. | 68 |

## 1.5.3: Unsupported Pt, Pt-alloy and binary Pt–M (M = metal) catalysts

Pt and its alloys offer the best-known ORR activity. However, Pt alloyed with transition metals suffer from leaching of base metals in acid electrolyte.[50,75-78] Therefore, with careful tailoring of the catalysts, better activity and durability has been achieved.

Reports have indicated that alloys and core-shell catalysts made of Pt and another component possess better activity and durability than pure Pt catalysts.[79-82] This is as a result of the interaction between the Pt and the other metal where synergistic effects have been reported to enhance the Pt activity. Some of the base metals or precious metals alloyed with Pt have been shown to either have a stabilization effect on Pt or possess sacrificial properties in durability studies whereby the base metal or precious metal catalysts undergo sacrificial dissolution resulting in a cleaner, higher surface area Pt surface. Examples of these types of studies are given in Table 1.5.

Zhang and co-workers[49] studied the stabilization of Pt ORR electrocatalysts using gold clusters. The catalysts were used in simulated durability studies in the 0.6 – 1.1 V vs. RHE in over 30 000 cycles. They observed insignificant changes in the MA, SA, and ECSA of the Au modified Pt in contrast to the significant losses observed with the pure Pt catalyst. They attributed the better stability of the catalyst to the Au conferring stability to the Pt catalyst by raising the Pt oxidation potential. The Au is not an active ORR catalyst, but rather spontaneously produces $H_2O_2$ in the 2-electron process, at the Au (100) and its vicinal surface in alkaline solutions. The ORR results were not consistent with this reaction. The authors, therefore, ascribed the activity of the Au clusters to their interaction with the oxides resulting in charged Au particles. A spill over of the $H_2O_2$ formed from Au clusters to the surrounding Pt atoms where the $H_2O_2$ is reduced to $H_2O$ was thus proposed to explain the data. They alternatively proposed that if the AuOH is formed at certain potentials, it would reduce the $H_2O_2$ to $H_2O$.

In a study by Alia and colleagues, Pt coated Pd nanotubes were applied in ORR activity and durability studies. The materials were synthesized using the galvanic displacement of Pd nanotubes. The Pt coatings were limited to loadings of 9, 14 and 18 wt%, (PtPd9), (PtPd14) and (PtPd18). The synthesized Pt/PdNTs had a wall thickness of 6 nm and a length of 5 – 20 μm. The metal layer was estimated to have a thickness of 1.1, 1.7 and 2.2 Pt atoms assuming a uniform and continuous coating. They observed cost and area normalized ORR activities for the Pt/PdNTs exceeding the US DoE targets. PtPd9, PtPd14, and PtPd18 produced cost activities of 10.4, 9.4 and 8.7 $A\$^{-1}$ respectively. PtPd9 exceeded the DoE dollar activity target (9.7 $A\$^{-1}$) by about 70%. The PtPdNTs catalysts further exceeded the DoE area-specific activity targets by 40 – 43%. [83]

In another study on ORR activity and durability, Su and colleagues studied platinum copper nanotubes (PtCuNT). They discovered that the PtCuNT was 10-fold better than Pt/C in terms of specific activity and 3-fold better than the DoE (US Department of Energy) technical target

of 0.72 $mA.cm^{-2}_{Pt}$ @0.9 V vs. RHE. The PtCuNT experienced enhanced durability as shown by the -9-mV shift in the ORR polarization, compared to -25 mV experienced by commercial Pt/C. The high specific activity could be explained by the numerous active sites available for the reaction. In pure Pt, the Pt d band centre is close to the Fermi level and the adsorption of spectator species is strong and the desorption of oxygenated species is weak. Therefore, a downshifted d band centre dramatically decreases the pre-covering of spectator species, enhancing activity. The preferable orientation of the (111) and (110) facets on the PtCuNTs are less vulnerable to strong OH adsorption than the (100) facet, resulting in an enhanced activity. The authors also postulated that the PtCuNTs alloy resembled extended Pt surfaces that have shown to be advantageous in terms of the specific activity. Also, the one-dimensional structure could facilitate the mass transport of gases compared to zero-dimensional materials. The durability of the catalysts was confirmed by the minimal ECSA loss of - 14% and an ORR polarization negative shift of -9 mV. This was in comparison to the -40% ECSA loss and -25 mV negative shift of the $E_{1/2}$ for Pt/C. The dissolution of Pt occurs at a higher electrode potential (than Cu) as shown in the equation 1.6,

$$Pt^{2+} + 2e^- \rightarrow \quad Pt\ E° = 1.188\ V \qquad (1.6)$$

They proposed that the dissolution of Pt is hindered by the sacrificial dissolution of copper that occurs at a much lower electrode potential, shown in equation 1.7,

$$Cu^{2+} + 2e^- \rightarrow \quad Cu\ E° = 0.340\ V \qquad (1.7)$$

Further, the zero-dimensional structure of the PtCuNTs makes it less susceptible to dissolution compared to multidimensional nanostructures.[84]

Zhang and colleagues studied for ORR activity and durability. They used various Pt:Pd molar ratios of 1:4, 1:1 and 1:2 to form $Pt_1/Pd_2/C$, $Pt_1/Pd_4/C$, and $Pt_1/Pd_1/C$. The ORR activity of $Pt_1/Pd_2/C$ and $Pt_1/Pd_4/C$ were superior to Pt/C. After 40 000 – 80 000 potential cycles in the

0.65 – 1.05 V vs RHE, $Pt_1/Pd_2/C$, and $Pt_1/Pd_1/C$ were found to be more durable than Pt/C. They attributed the higher activity and durability to the sacrificial dissolution of Pd and the corresponding structure transformation from core-shell to Pt-Pd alloy with a Pt enriched surface.[79]

Similar trends were observed when Pt-Ni nanocages that were studied for ORR activity and durability. Peng and colleagues observed that half-wave potential for the PtNi nanocages were +30 mV higher than found for Pt/C. The SA and MA were 2-fold and 4-fold higher than found for Pt/C. After 30 000 potential cycles, the PtNi cages retained a higher than DOE target value 42% of MA compared to 19% for Pt/C. The higher durability was attributed to the reduced dissolution of the 3D framework of the catalyst.[85]

Sasaki and colleagues studied ORR catalysts synthesized by the monolayer deposition of Pt on PdAu. The catalysts demonstrated superior durability over 100 000 cycles for both the 0.6 – 1.0 V window as well as in the 0.6 – 1.4 V vs RHE window. They demonstrated that adding a small amount of gold to Pd and forming highly uniform nanoparticle cores made the Pt monolayer significantly more tolerant to the ORR oxidizing environment.[86]

Zou and co-workers studied the structural transformation of carbon-supported ordered and disordered $Pt_3Cr$ supported on carbon for ORR. They observed an intermetallic nanoparticle size of about 7.2 nm using TEM and PXRD. Using line scanning EDX they observed that the Pt-Cr atomic ratio was approximately 3:1. In terms of activity, the $Pt_3Cr/C$ intermetallic nanoparticles exhibited enhanced MA and SA towards ORR better than the Pt/C but slightly lower than the disordered $Pt_3Cr$ alloy nanoparticles. In 5000 durability cycles, in the 0.5 – 1.0 V vs. RHE, 0.1 M $HClO_4$, nitrogen saturated electrolyte and 50 $mVs^{-1}$, the $Pt_3Cr$ intermetallic nanoparticles displayed negligible decay in MA, however the oxygen reduction reaction mass activity for the disordered $Pt_3Cr$ alloy decreased by about 50%. Much higher durability of the

$Pt_3Cr$ intermetallic nanoparticles was attributed to the higher structural and compositional stabilities of the $Pt_3Cr$/C intermetallic nanoparticles than that of the disordered $Pt_3Cr$/C alloy nanoparticles.[87]

Takahashi and colleagues examined the durability and activity of carbon-supported Pt in liquid electrolytes. They optimized their ink formulation using different ratios of isopropyl alcohol and deionized ultra-pure water. They compared the variations in activity between Pt/C, Pt/C-HT (heat-treated) and a PtCo/C catalyst. Even though the specific activity of the Pt/C was higher due to the smaller Pt nanoparticles, they observed higher mass activity and durability for the heat-treated and the cobalt alloy catalyst. They attributed the higher activity of the PtCo/C to the negative shift in the d-band vacancy centre for the PtCo/C. This negative shift was proposed to lead to lower adsorption of both blocking and spectator intermediates. The observed positive shift in the onset of the oxidation peak of the PtCo/C and Pt/C-HT was attributed to the low amounts of adsorbed spectator intermediates.[88]

Wang and colleagues studied Pt nanoparticle net-like assemblies for ORR activity and durability. They observed changes in the Pt sizes from 5.3 – 5.9 nm for the net-like assemblies and corresponding 3.3 – 4.9 nm for the commercial Pt/C which showed superior durability for the former. The half-wave potential for the PtNNA of 0.912 V vs RHE was higher than the 0.892 V vs RHE and 0.8740 V vs RHE for Pt black and Pt/C respectively. The MA for PtNNA was 1.5 times and the SA was 2.9 times greater than for the Pt/C, respectively. After 20000 potential cycles in the 0.6 – 1.1 V vs RHE in an acid electrolyte, the PtNNA had a minimal loss of ECSA of about -9% compared to -37% for Pt black and -47% for Pt/C. They observed that the netlike feature was preserved after 20 000 cycles and they demonstrated that the control of the assembling mode of Pt nanoparticles can be a promising route to active and durable catalysts.[89]

Kibsgaard and co-workers studied Pt thin films for ORR application. The formed double gyroid Pt (DG-Pt) was observed to exhibit a positive 30 mV shift of the OH adsorption/desorption peak compared to the commercial Pt/C. The positive shift was attributed to the surface sites of the DG-Pt not binding to oxygenate and hydroxylate species as strongly as they do on the Pt/C. They attributed the observed higher durability to the continuous network of the DG-Pt exhibiting a smaller fraction of under-coordinated Pt atoms at the surface having a surface structure that is comparable to large nanoparticles rather than to small nanoparticles. As is known, bigger nanoparticles are less prone to dissolution compared to smaller ones.[90]

Table 1.5: Unsupported, alloyed, and binary Pt -M (M- metal) catalysts and the explanation of properties contributing to enhanced activity and durability

| Catalyst | Comment/ reason for enhanced activity and durability | ref |
|---|---|---|
| $Pt_{ML}/Pd_6Au_1/C$ | Slight contraction of Pt monolayer due to Pd dissolution, rearrangement of Pt surface atoms into smoother and highly coordinated surfaces, sacrificial Pd dissolution leaving Pt rich surface. | 86 |
| DG - $Pt_xNi$ | PtNi thin films with double gyroid morphology, mesostructured nature of DG-Pt inhibits activity losses associated with the high fraction of low coordinated surface atoms present. Sacrificial Ni dissolution leaving Pt rich surfaces. | 90 |
| Pt/CoC | Heat treatment results in less relaxed surface structure forming 'skin like' structures less prone to dissolution. Heat treatment led to alloying of Pt and Co and more resistance to dissolution. | 88 |
| $Pt_1Pd_4/C$<br>$Pt_1Pd_2/C$ | Durability associated with Pd dissolution and corresponding structure transformation from | 83 |

| | | |
|---|---|---|
| $Pt_1Pd_1/C$ | core -shell structure to Pt – Pd alloy with Pt rich surface. | |
| PtNi nanocages | Open cage nanostructure which does not waste Pt like bulk Pt. High intrinsic activity enabled by the alloy shift in the d-band centre as well as the open architecture of cages leading to improved access to active sites. Nanocage structure enhanced durability | 85 |
| PtCu NTs | Sacrificial Cu dissolution leaving Pt rich surface. PtCu alloy bulk and Pt enriched surface with downshifted d band centre position driving activity and durability | 84 |
| Pt NNA | High specific surface area, controlled assembly enhanced activity and durability | 89 |
| $Pt_3Cr/C$ | Higher structural and compositional stabilities of the intermetallic nanoparticles than that of the disordered $Pt_3Cr/C$ alloy nanoparticles. | 87 |

## 1.5.4: Pt catalysts supported on metal oxides and other supports

Metal oxides have also been studied as Pt supports for ORR activity and durability studies. Metal oxides have a low electronic conductivity, show poor Pt dispersion and mostly unfavourable metal-support interactions. However, recently metal oxides have been modified in synthetic procedures to produce favourable properties and to enhance conductivity and surface area for better nanoparticle dispersion. See Table 1.6 for some examples.

Wang and co-workers studied Pt supported on carbon nitride modified with silica for ORR. The $Pt/CNx/SiO_2$ was synthesized by the calcination of polypyrole coated silica ($Ppy/SiO_2$) at 800°C followed by the deposition of Pt nanoparticles onto the support. They observed ECSA of 90 $m^2/g$ for the $Pt/CNx/SiO_2$ and 50 $m^2/g$ for a Pt/Vulcan reference. The supports had

comparable BET surface areas. The MA for Pt/CNx/$SiO_2$ was 2.9 greater than for Pt/C and 2.3 times better than Pt/CNx/C at 0.85V vs RHE. The observed better MA, for Pt/$CN_x$/$SiO_2$ than Pt/C was attributed to the composite nature of the support. The authors proposed that N species gave a synergistic effect between Pt and the support. They proposed that the silica adsorbed harmful oxygenate intermediates resulting in the decreased adsorption of hydroxylate groups on the Pt surface, thereby making Pt more available for ORR which enhanced activity.[91]

Cheng and colleagues synthesized a robust Pt/ZrC nanocomposite catalyst using atomic layer deposition (ALD) to improve the strong metal support interactions (SMSI) at the atomic level. They studied the highly stable ORR electrocatalysts (ALD-Pt/ZrC) and observed atomic-scale enhancement of metal support interactions (MSI) between Pt and the zirconium carbide (ZrC). The catalysts were studied for durability in 4000 potential cycles in the 0.6 – 1.2 V vs. RHE at room temperature. The ALD-Pt/ZrC had a 17% loss in ECSA compared to a -52% loss for CW-Pt/ZrC and a -78% for the Pt/C. The observed durability trends amounted to a 5-fold and a 3-fold better durability than found for Pt/C and CW-Pt/ZrC (conventionally synthesized). The ALD-Pt/ZrC was observed to exhibit higher ORR activity compared to the conventionally synthesized and the Pt/C commercial catalyst. At 0.9V vs. RHE, the ALD-Pt/ZrC activity was 0.09 $Amg^{-1}$, the CW-Pt/ZrC activity was 0.03 $Amg^{-1}$ and the Pt/C activity was 0.01 $Amg^{-1}$. After accelerated degradation tests the Pt particle size changed: ALD-Pt/ZrC from 3-5 nm to 3-7 nm, CW-Pt/ZrC from 3-5 nm to 4-12 nm and the Pt/C from 3-5 nm to the 7-25 nm size range. Using X-ray absorption near-edge spectroscopy (XANES) results, they observed noticeable changes in the electronic structure of the Pt due to the strong metal-support interactions with the ZrC support. They attributed the high activity of the ALD catalyst to the synergistic effects between the Pt and ZrC support. They concluded that better ORR on the ALD catalyst was due to the impeded migration or dissolution of Pt due to the strong MSI

while for the Pt/C catalyst, facile dissolution due to the weaker MSIs was responsible for the lower ORR activity.[92]

In a related study, Cheng and colleagues studied an atomic layer deposited metal oxide/nitrogen-doped graphene hybrid of Pt ($Pt/ZrO_2/NGN_S$) for ORR activity and durability. They compared the composite $Pt/ZrO_2$/NGNs with Pt/NGNs. The synthesized $Pt/ZrO_2$/NGNs had a loading of 14 wt% Pt and a Pt particle size of 3 nm whereas the $Pt/ZrO_2$ had a Pt particle size of 3.2 nm and Pt loading of 21 wt%, as confirmed by ICP-OES (inductively coupled plasma optical emission spectroscopy). The catalysts were applied in the oxygen reduction reaction and for durability studies. Potential cycling was carried out in 0.5 M $H_2SO_4$ saturated with oxygen in the 0.6-1.2 V vs RHE window. They observed that $Pt/ZrO_2$/NGNs were at-least 2.1 and 2.2 times better than Pt/NGNs in terms of methanol oxidation and durability respectively. The peak currents due to methanol oxidation in the forward scan for the Pt - $ZrO_2$/NGNs and the Pt/NGNs were 476 and 231 $mA.mg^{-1}$ respectively. Using HRTEM they observed that the Pt nanoparticles in both supports were located between the grain boundaries of $ZrO_2$ or the NGNs. They proposed that the Pt-metal oxide interaction could promote OH ions removal on the Pt surface by the $ZrO_2$ nanoparticles. They also postulated that the activity towards methanol oxidation was enhanced by the $Pt/ZrO_2$/NGNs hybrid nanostructure. They hypothesized that the Pt-$ZrO_2$/NGNs hybrid nanostructure promoted the Pt catalyst towards methanol oxidation in the following reaction sequence

$$Pt + H_2O \rightarrow Pt - OH + H^+ + e- \quad (1.8)$$

$$ZrO_2 + H_2O \rightarrow ZrO - OH + H^+ + e- \quad (1.9)$$

$$Pt\text{-}CO + Pt - OH \rightarrow 2Pt+ + CO_2 + H^+ + e- \quad (1.10)$$

$$Pt - CO + ZrO_2 - OH \rightarrow Pt + ZrO_2 + CO_2 + H^+ + e- \quad (1.11)$$

The authors suggested that the surface oxygen of a reducible oxide helped in the oxidation of the CO on Pt surfaces. Therefore, the enhancement of the Pt-$ZrO_2$/NGNs towards methanol oxidation is likely to occur at the interface of Pt and $ZrO_2$ in reaction (1.4). Durability cycling over 4000 cycles in the 0.6-1.2 V vs. RHE in oxygen saturated $H_2SO_4$ showed that about 24% of ECSA remained for Pt/NGNs and 51% for Pt-$ZrO_2$/NGNs respectively. They proposed that the better durability observed was due to the triple interaction of the Pt-$ZrO_2$-NGNs hybrid nanostructure.[93]

Xu and colleagues studied a Pt/$CeO_2$/C catalyst for improved ORR activity and durability. They synthesized, using a facile one-pot method, the Pt/$CeO_2$/C composite catalysts. Using $CeO_2$ nanoparticles with high $Ce^{3+}$ concentration ranging from 30.9% to 50.6% they discovered that the defective surface preferentially allowed for the nucleation and growth of Pt nanoparticles. They observed the Pt nanoparticles were preferentially deposited on the $CeO_2$ surface thereby increasing the Pt-$CeO_2$ interface. The high concentration of oxygen vacancies on the $CeO_2$ surface and the large Pt-$CeO_2$ interface led to a favourable Pt-$CeO_2$ interaction and as a result this enhanced the ORR activity and durability. They observed a 50 % increase of the mass activity from 36.44 mA $mg^{-1}$ for Pt/C to 52.09 mA $mg^{-1}$ for Pt/$CeO_2$/C containing 20 wt.% $CeO_2$. Due to its enhanced durability, the Pt/$CeO_2$/C composite catalysts containing 10-30 wt.% $CeO_2$ lost about 80% ECSA after 10,000 cycles compared to Pt/C which lost 79% electrochemical surface area after 2000 cycles. [94]

Mohammed and colleagues studied Pt supported on commercial antimony doped tin oxide (Pt/Sb-$SnO_2$), in ORR reactions. Using a facile deposition technique involving the use of metal-organic deposition of Pt on the supports, they obtained uniform Pt particles in the 2 - 4 nm size. The observed high electrochemical stability during high-potential cycling was attributed to potential-dependent in situ conductivity switching of the antimony-doped tin oxide (ATO) support. They attributed the ORR activity of the Pt/ATO catalysts to a combination of Pt

particle size effects, ATO support in situ conductivity limitations at PEFC operation potentials, and metal-support interactions.[95]

Table 1. 6: Platinum catalysts supported on various metal oxides and other supports

| Catalyst | Comment/ reason for enhanced activity and durability | ref |
|---|---|---|
| $Pt/CN_x/SiO_2$ | N species leads to synergistic effect between Pt and support. $SiO_2$ is oxophilic like Ru, promotes adsorption of harmful oxy species (intermediates) leading to decreased OH adsorption on Pt surface -enhanced ORR activity. | 91 |
| ALD-Pt/ZrC | Strong MSI between Pt and ZrC enabled by atomic layer adsorption (ALD) | 92 |
| $Pt\text{-}ZrO_2$ | Unique triple interaction at the interface of $Pt\text{-}ZrO_2$ -NGNs, synergistic effect, promotion of ORR by $ZrO_2$ on Pt surface | 93 |
| $Pt/CeO_2/C$ | High concentration of oxygen vacancies on $CeO_2$, strong $Pt - CeO_2$ interaction due to large $Pt - CeO_2$ interface | 94 |
| $Pt/Sb\text{-}SnO_2$ | Potential dependent in-situ conductivity switching of the ATO ($Sb - SnO_2$) support, particle size effects, negative MSI enhanced activity and durability | 95 |

## 1.5.5: Metal free ORR catalysts

Metal free ORR electrocatalysts have also been employed in ORR reactions (Table 1.7). These materials do not use expensive precious metals like Pt and therefore can be cheaper alternatives.

However, the challenge associated with metal free catalysts is the low activity that they possess. Numerous studies of ORR activity have been carried out on these materials.

Guo et. al studied the active sites of nitrogen-doped carbon for oxygen reduction reaction applications using model catalysts. In their study, model well-defined model catalysts such as highly ordered pyrolytic graphite (HOPG) with well-defined π conjugation and well-controlled nitrogen doping were studied. Using $CO_2$ adsorption experiments they discovered that the pyridinic nitrogen sites created Lewis base sites on the carbon atoms adjacent to them. They concluded that the ORR active sites are the carbon atoms adjacent to the pyridinic nitrogen and not the nitrogen atoms themselves.[96]

Zhang and colleagues studied highly graphitized nitrogen-doped carbon polyhedral synthesized from ZIF-8 nanocrystals as efficient ORR catalysts. The formed doped carbon showed comparable ORR to Pt/C with the 4-electron process being the dominant mechanism for ORR. The material showed superior methanol tolerance as well as cycling stability in alkaline media. The optimum activity was attributed to the synergistic contribution of the abundant active sites with high graphitic nitrogen contribution.[97]

Table 1. 7: Metal free ORR catalysts and the possible explanation for the observed activity

| Catalyst | Comment/ reason for enhanced activity and durability | ref |
|---|---|---|
| N-doped carbon (HOPG) | Pyridinic nitrogen created Lewis base sites on the carbon atoms adjacent to them. ORR active sites are the carbon atoms adjacent to pyridinic nitrogen and not other types of nitrogen atoms. | 106 |

| | | |
|---|---|---|
| Nitrogen-doped carbon polyhedra | Activity was attributed to the synergistic contribution of the abundant active sites with high graphitic nitrogen contribution | 108 |

The major challenge with metal free catalysts is their inability in some cases, to attain high activity and durability comparable to metal loaded catalysts. This has led to the need to fabricate metal decorated catalysts with good activity, durability, and the accompanied low cost.[98]

## 1.6: Degradation of fuel cell catalysts.

Fuel cells are an attractive energy conversion system and are poised to overtake gasoline engines as the choice automobile powering device in the next three decades. However, low durability of catalysts is proving to be detrimental to the full-scale adoption of these renewable energy systems.[99-101.]

In fuel cell cathodes for ORR, durability decline is normally observed when the electrochemical surface area (ECSA) decreases due to various catalyst degradation processes. Degradation of fuel cell catalysts occurs as a result of the electrochemical oxidation of the carbon supports at potentials above 1.5 V (RHE) as well as dissolution of the Pt catalyst resulting in its redeposition on bigger Pt clusters (agglomeration) and detachment of Pt due to the electrochemical oxidation of carbon. Another process which can occur as a result of catalyst degradation is Ostwald ripening. This process occurs when small Pt clusters migrate and deposit on bigger Pt clusters.

### 1.6.1: Carbon support corrosion

Apart from Pt dissolution, carbon support corrosion significantly contributes to catalyst degradation (Figure 1.7). Carbon is thermodynamically prone to oxidation to carbon dioxide

(standard potential 0.207 V vs. NHE). The reaction does not readily occur, however, at elevated temperatures and a potential above 1.5 V vs. RHE this reaction is significant. During start-stop or load processes in a fuel cell, the cathode potential can reach up to 1.5 V vs. RHE. These are highly oxidizing potentials and can result in the electrochemical oxidation of the various carbon supports used for supporting platinum electrocatalysts.

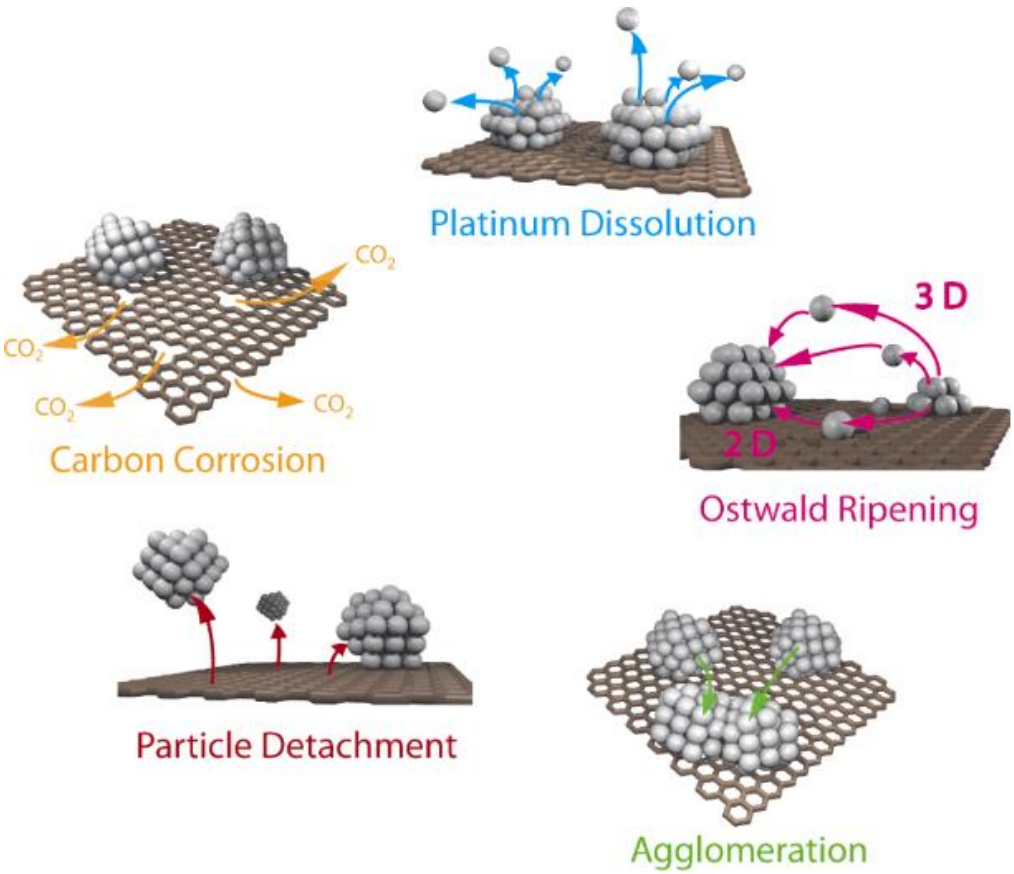



Figure 1.7: Schematic illustrations of the proposed mechanisms of degradation of Pt/C catalysts.[102]

Structured carbon supports have been adopted for use as supports for Pt catalysts. These include mesoporous and graphitized carbon materials such as hollow carbon spheres and carbon nitride. Graphitized carbons are known to be less prone to electrochemical oxidation as reported in the literature. [103-105] However, they tend to have weak interactions with nanoparticles. This weak link between the metal nanoparticles can result in easier degradation through detachment and agglomeration.

## 1.6.2: Ostwald Ripening

Ostwald ripening and agglomeration are the two processes that have been proposed to explain the growth in particle sizes of Pt in fuel cells. Ostwald ripening is a secondary process that follows the primary process of dissolution. Pt dissolves into solution followed by precipitation and deposition onto pre-existing Pt particles causing agglomeration and particle growth. Particle dissolution is more prominent in Pt particles that are less than 2 nm in diameter. High surface energy particles under 2 nm undergo dissolution and agglomeration to minimise the surface energy. Ostwald ripening can occur as a result of the dissolution and redeposition of the Pt (3D ripening). Another form of catalyst Ostwald ripening occurs when the smaller Pt particles diffuse through the carbon supports to form bigger Pt particles. This is known as 2 D ripening.[102,106-107]

## 1.6.3: Agglomeration

Agglomeration is another process suggested to occur during the degradation of fuel cell catalysts. Agglomeration occurs as a result of the migration of Pt particles onto other bound and supported Pt clusters thereby forming bigger agglomerates. Agglomeration is thought to be responsible for the coarsening of pre-existing and supported Pt particles. Another process that is an indicator of existing agglomeration is a phenomenon known as the necking of adjacent Pt particles. Necking can be explained by the existence of a low diameter bridge between two or more Pt particles. Shao-Horn and colleagues also showed that a synthesis procedure alone can also result in necking even in instances where the catalysts were not subjected to degradation processes.[108]

## 1.6.4: Particle Detachment

Detachment occurs when the interaction between the Pt and the support decreases. This process occurs as a result of the weakening of a metal to support interaction (MSI). The precursor to Pt particle detachment is usually corrosion of the carbon support. Detachment and agglomeration occur in parallel as these processes are related. To enhance tethering and better anchoring of the Pt on the supports, heteroatom doping of a carbon support with nitrogen has been studied to enhance durability. [109,110]

The degradation by electrochemical oxidation of Pt loaded carbons can be decreased by using highly graphitized and low BET surface area carbon supports.[105]

# 1.7: Carbon supports in catalysis

Carbon materials have been used extensively as metal catalyst supports in catalysis. This is because of the versatility of the carbon and the properties the carbon exhibits. Carbon exists in many forms and many of these have been applied in catalysis either as supports or the carbon being the catalyst itself. Among the many carbon materials that have been documented in catalysis are carbon nanotubes (CNTs), carbon nanofibers (CNFs), graphene, reduced graphene oxide (RGO), graphite, solid carbon spheres, onion like carbon materials (OLC), hollow carbon spheres (HCSs), activated carbon (AC), diamond and amorphous carbon among many others (Figure 1.8 for some examples). Also, the boron doped, and nitrogen doped counterparts of these carbon materials have also been applied in catalysis with difference in results based on their properties. [111]

The properties of carbon that makes it attractive in catalysis is its high surface area, continuous network of meso and micropores, high thermal stability, the ability to be tailored into various shapes and its stability in acid or alkaline media. The extent of graphitization can also be tailored by annealing the carbon material in inert gases like nitrogen or argon. Carbon materials

can also be post-functionalized using acids for enhanced surface properties. Solutions of nitric and sulfuric acid have been used to post functionalize carbon nanotubes for better applicability.[112]

Nitrogen and boron doping of carbon supports has also been done to enhance properties. For example, through Raman spectroscopy studies, nitrogen doping has been proven to introduce defects in the structure of the carbon.[113-115] Highly defective carbons have been shown to have better carbon to metal interactions which enhances the activity of catalysts or their durability or both. Also, nitrogen doping has been shown to introduce favourable surface properties that affects the nucleation and growth of metal nanoparticles during deposition of the catalysts.[116]

High thermal stability is essential in catalysis where reactor temperatures reach beyond 200℃. Carbon materials have been shown to be thermally stable up to around 700 ℃ in inert environments making them useful in these systems.[117,118]

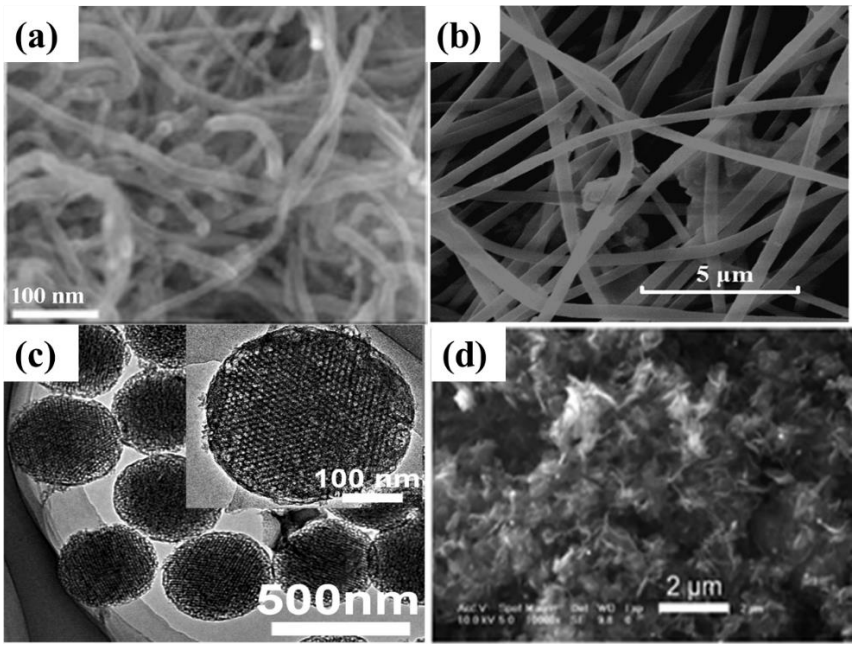



Figure 1.8: SEM images of some of the carbon materials that have been used in catalysis either as supports or as catalysts themselves: (a) carbon nanotubes, (b) carbon nanofibers, (c) solid carbon spheres and (d) graphene sheets.[119-122]

## 1.8: Hollow Carbon Spheres

Of all the carbon morphologies used up to date in catalysis, the spherical carbon materials have shown some novel advantages.[117,123] The spherical morphology is favourable as it has an inherent higher surface area per unit volume compared to other morphologies. Coupled with an intrinsic high BET surface area when associated with the presence of an array of pores and defects, these materials can be applied in a range of suitable applications. Spherical carbons like solid carbon spheres, HCSs and NHCSs have seen widespread application in a wide range of catalytic processes including Fischer-Tropsch synthesis, fuel cell oxygen reduction reaction, lithium ion batteries and in solar cells.[116,117,124,125]

Hollow carbon spheres shells can be fine-tuned to modify their specific porosity and thermal stability. The hollow carbon spheres have also been exploited as nano-reactors due to their spherical nature and the presence of a hollow core.[118] Metal nanoparticles have been encapsulated inside the HCS to minimise loss of surface area due to agglomeration.[124] They have also been used to study spill over effects. In a study by Phaahlamohlaka and colleagues, cobalt nanoparticles were encapsulated inside the HCSs and used to differentiate primary from secondary spill over reactions.[123]

Depending on the target catalyst, metal nanoparticles can be deposited inside the pores of HCSs (pore confinement)[125], on the outside of the shells, or the metal nanoparticles can be deposited inside the HCS shell (encapsulation) to yield a catalyst system that best suits the target reactions. The porous carbon shell can be tuned to a specific thickness, porosity, pore size and its extent of graphitization can be tailored to suit the desired catalytic and stability properties of choice.

## 1.8.1: Hollow carbon spheres in catalysis

Due to the favourable properties and ease of synthesis, the use of HCSs has been widespread in catalysis. Among many other applications, Shi and colleagues studied copper nanoparticles encapsulated inside HCSs (Cu@HCS) for methanol oxidative carbonylation reactions (Fig 1.11). They optimised the catalytic performance by fine tuning of the structure of the support core and the shell thickness. Using a hard silica template, they formed HCSs with an average diameter of 190 nm and an average shell thickness of 15 nm. The size of the Cu nanoparticles was optimized through the control of the parameters for the hydrothermal impregnation and hydrogen reduction processes.

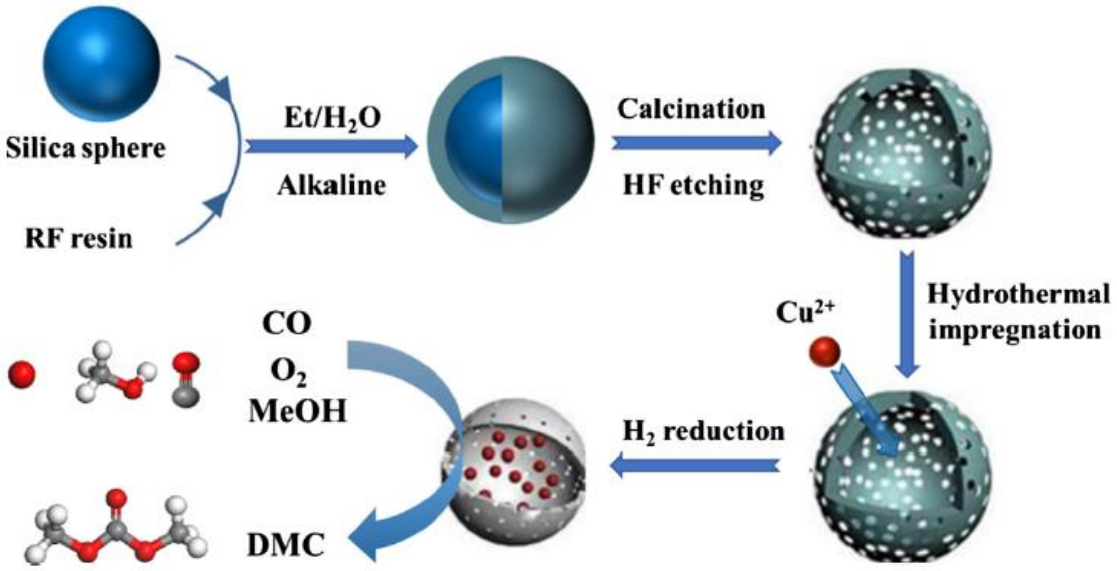



Figure 1.9: Schematic illustration of the encapsulation of Cu inside HCSs to form Cu@HCS.[126]

They discovered that the thin HCS carbon shell was beneficial for the diffusion of reactants and products and that the small copper nanoparticles in the Cu@HCS provided a large active specific surface area and superior activity compared to a commercial CuCl catalyst. The turnover frequency and activation energy reached 23.1 $h^{-1}$ and 20.5 $kJ \cdot mol^{-1}$respectively. They also observed that the Cu@HCS catalyst exhibited higher stability than that of CuCl due to the

carbon shell preventing the aggregation and leaching of copper nanoparticles during the reaction.[126]

Kang and colleagues studied gold nanoparticles supported on mesoporous HCSs for acetylene hydrochlorination. They prepared the mesoporous HCSs using silica spheres followed by the sodium borohydride assisted deposition of gold nanoparticles on the surface of the HCSs. TEM images confirmed that the Au nanoparticles were smaller on the HCSs supports compared to the activated carbon (AC) support. The Au/HCS catalyst displayed superior catalytic activity and stability for acetylene hydrochlorination. The catalytic conversion of acetylene by Au/HCS was maintained above 92% for durations above 500 h. They attributed the superior catalytic activity of Au/HCS to the reduced aggregation of the gold catalyst due to its interaction with the HCS support.[127]

Liu and colleagues studied discrete and highly dispersible hollow carbon spheres (HCSs) prepared by a confined space pyrolysis method. In the method, polystyrene particles were coated with a phenol-formaldehyde polymer inner shell and a silica outer shell. The monodisperse HCSs were obtained after the pyrolysis of the spherical composite followed by the elimination of the outer silica shell. They prepared the PtRu/HCS catalysts using the sodium borohydride assisted impregnation method. Well-dispersed PtRu nanoparticles with a narrow particle size distribution were observed and their size depended on the total metal loadings. They investigated the oxidation of methanol on the supported catalysts using electrochemical impedance spectroscopy, chronoamperometry, and cyclic voltammetry. The results showed that the catalyst with PtRu loading of 15.75 wt% possessed the highest catalytic activity, higher than the other PtRu catalyst studied. They attributed the improved electrocatalytic activity to the high dispersion of the PtRu nanoparticles on the HCSs.[128]

## 1.9: Templating

The use of hard templates is essential for the synthesis of spherical and hollow carbon materials. Templates acts as moulds on which the shell materials are deposited. One of the properties of the hard templates is the ability to be synthesized to a size specific to the properties of the carbon to be synthesized. The templates are typically removed after synthesis using mild conditions with minimal damage to the carbon shell. Among the favourable templates used for the synthesis of hollow carbon spheres are silica and polystyrene. Silica can be etched out using a low concentration of sodium hydroxide or 10% hydrofluoric acid (HF). Polystyrene can be removed by heating in a furnace at temperatures between 300 - 400 ℃. Some examples of the use of polystyrene spheres as templates for the formation of HCSs and NHCSs are given below.

Dai and colleagues prepared hollow carbon spheres from the pyrolysis of a composite of sulfonated polystyrene spheres (d = 200 nm) and polyaniline (Figure 1.10). After pyrolysis at 800ºC for 3 h, they formed HCSs with an average diameter of 205 nm and carbon shell thickness of 35 nm. They also found that the HCSs maintained the spherical shape for the thick carbon shells and for the thinner carbon shells, the HCSs were mostly collapsed. From the XRD diffractograms of the HCSs, they observed two distinct diffraction peaks found at 2θ of 24.5°and 44.8° which were indexed for the graphitic (002) and (101) planes respectively. They attributed the peak broadening of the diffractograms to the low extent of graphitization of the HCSs.

Hassan and colleagues synthesized nitrogen doped HCSs from the pyrolysis at 500ºC for 2 h in nitrogen of a composite of polystyrene spheres (d ~ 450 nm) and polymerized polypyrrole and polyaniline. The formed NHCSs had a carbon shell thickness of about 35 nm and BET surface area above 330 $m^2.g^{-1}$ The materials were applied as supercapacitors and ORR catalysts. The formed NHCSs exhibited specific capacitance of 294.9 F. $g^{-1}$at a 5 $mVs^{-1}$ with good cycling

stability of 95% after 5000 cycles at 0.5 A $g^{-1}$. The materials also showed enhanced ORR activity with an onset potential of 0.83 V vs. RHE at 1600 rpm coupled with a favourable four-electron pathway in an alkaline medium. They attributed the enhanced electrocatalytic performances to the hollow porous morphology and to the presence significant amounts of pyrrolic and pyridinic nitrogen.[130]

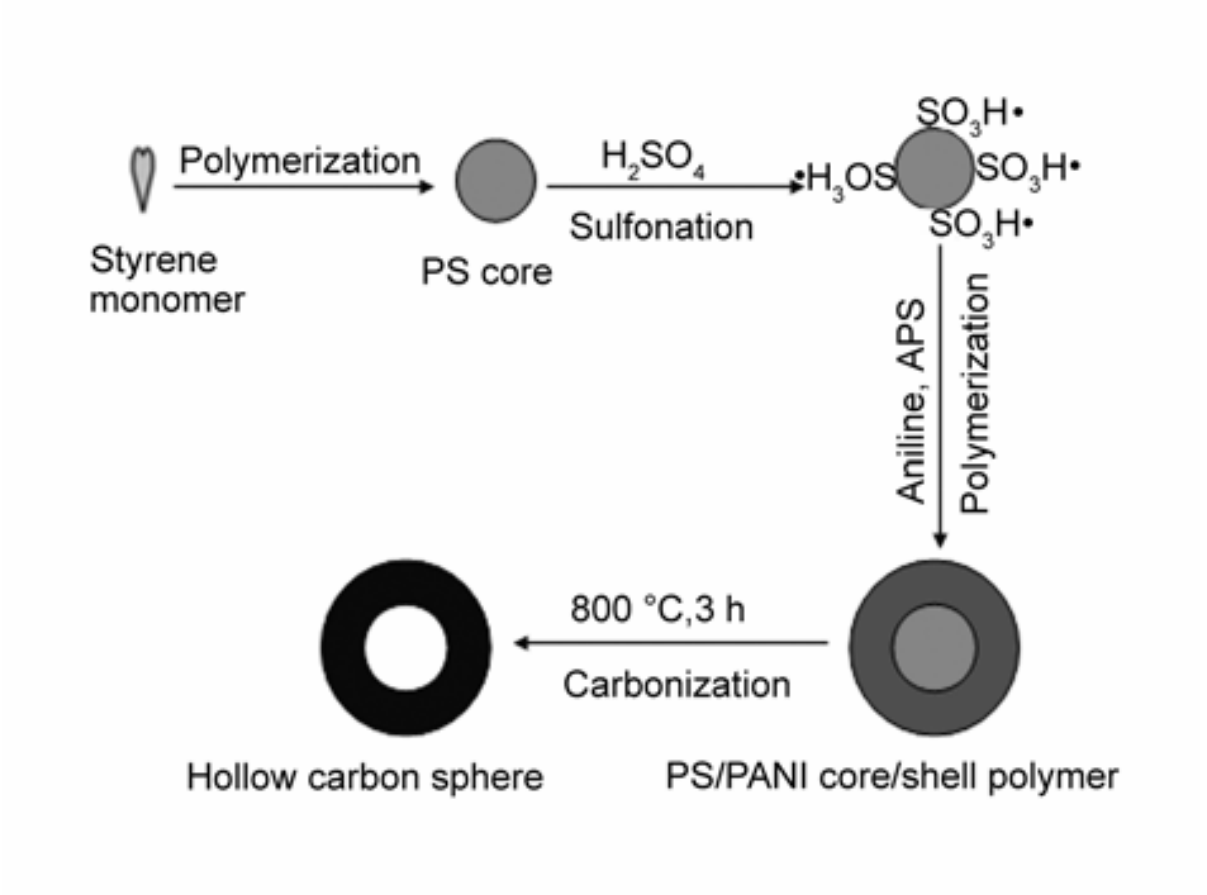



Figure 1.10: Schematic of the formation of HCSs from polystyrene.[129]

Hu and colleagues prepared Pd particles supported on high surface area HCSs (Pd/HCSs) for direct alcohol fuel cell catalysis. The HCSs (d ~ 1.5 µm, carbon shell thickness ~ 150 nm and BET surface area 1249.3 $m^2.g^{-1}$) were prepared by the hydrothermal coating and carbonization of a glucose and polystyrene composite in the presence of poly(ethylene glycol)-block-poly(propylene glycol)-block-poly(ethylene glycol) at 180 °C for 12 h followed by microwave treatment which resulted in the removal of the polystyrene template. They formed the Pd/HCS

and Pd/C electrocatalysts by the microwave aided formic acid reduction of a palladium precursor salt. They attributed the higher catalytic activity to the high electrochemical active surface area due to the hollow carbon structure with open micropores and nanochannels.[131]

Silica spheres have been in widespread use ever since LaMer and subsequently, Stober developed models to explain their growth mechanism.[132,133] Porous silica particles have been applied as adsorbents in waste treatment, as drug delivery agents, and importantly for this thesis, as templates for the synthesis of shaped carbon materials. Silica spheres of various size can be synthesized from the hydrolysis and condensation of tetraethyl orthosilicate in the presence of ethanol, deionized water, and ammonia solution. The formed colloids are then centrifuged, washed in a water-ethanol solution followed by drying. Silica spheres have been used by many researchers as hard templates for the formation of HCSs with varying porosities and BET surface areas. The advantage of using silica templates is that the resulting shape of the formed hollow carbon spheres is predetermined depending on the shape and size of templates used. Silica spheres have been extensively used as templates for the synthesis of shaped carbon materials. Some examples follow.

In one study, Buchel and co-workers synthesized modified sub-micrometre size solid core mesoporous shell silica spheres. To modify the solid core silica sphere, they used $C_{18}$TMS (octadeclytrimethoxysilane) with TEOS (tetraethyl orthosilicate) in a 4.7:1 TEOS/$C_{18}$TMS molar ratio. They formed mesoporous silica spheres with a pore width of 3.8 nm, pore volume of 0.43 $cm^3.g^{-1}$ and a BET surface area of 348 $m^2.g^{-1}$. [134]

Su and co-workers synthesized hollow carbon spheres of a controlled shell thickness using benzene vapor as a carbon source. To synthesize nitrogen-doped hollow carbon spheres, they bubbled the carrier gas, nitrogen, through acetonitrile. They controlled the extent of the graphitization of the formed HCSs by increasing the duration of the chemical vapor deposition

(CVD) process. The shell thickness of the hollow carbon spheres was controlled by the duration in the CVD furnace. In their application of the materials as lithium-ion batteries anodes, they discovered that cyclability as an anode was improved after nitrogen doping.[135]

Chen and colleagues synthesized thin-walled, mesoporous and nitrogen-doped hollow carbon spheres using ionic liquids as precursors (Figure 1.11 and Figure 1.12). They used a simple silica template followed by impregnation with an ionic liquid ([$C_n$Mim]Br, n = 4, 8, 12, and 16; 1-alkyl-3-methylimidazolium bromide) as the precursor for the synthesis of NHCSs. The negatively charged surface of the silica particles induced the assembly of cationic [$C_n$Mim]+. This was subsequently followed by carbonization at 800 ℃ thereby converting the ionic liquid into the nitrogen doped carbon as the shell covering the silica spheres. The NHCS were obtained after etching out the silica using HF solution. The hollow spheres had a uniform wall thickness, which could be altered by controlling the synthesis parameters such as type of ionic liquid and the molar ratio of the ionic liquid to silica spheres. The thin shell NHCSs were mesoporous with BET surface areas ranging from 66 – 210 $m^2/g$.[136]

Using silica templates, NHCSs with tuneable porosity have also been synthesized. Tang and colleagues synthesized mesoporous (pores ~ 20 nm) nitrogen-doped hollow carbon spheres using diblock copolymer micelles as a pore forming agent. They used colloidal silica (hard template) and the block copolymer PS-b-PEO as templates and dopamine as carbon precursor. They carbonized the composite at 800 ℃ under nitrogen and the silica template was removed using HF. They formed NHCSs with an average diameter of 350 nm and shell thickness between 17 – 50 nm depending on the synthesis conditions (Fig 1.13 and Fig 1.14).[137]

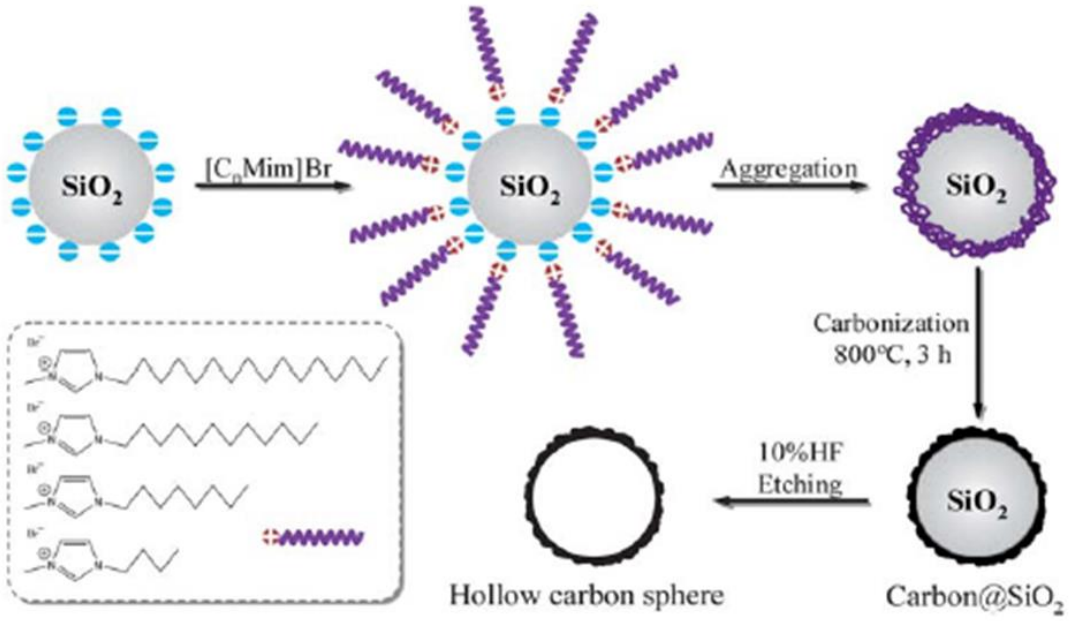



Figure 1.11: Schematic illustration of the formation of NHCSs using silica and ionic liquids.[136]

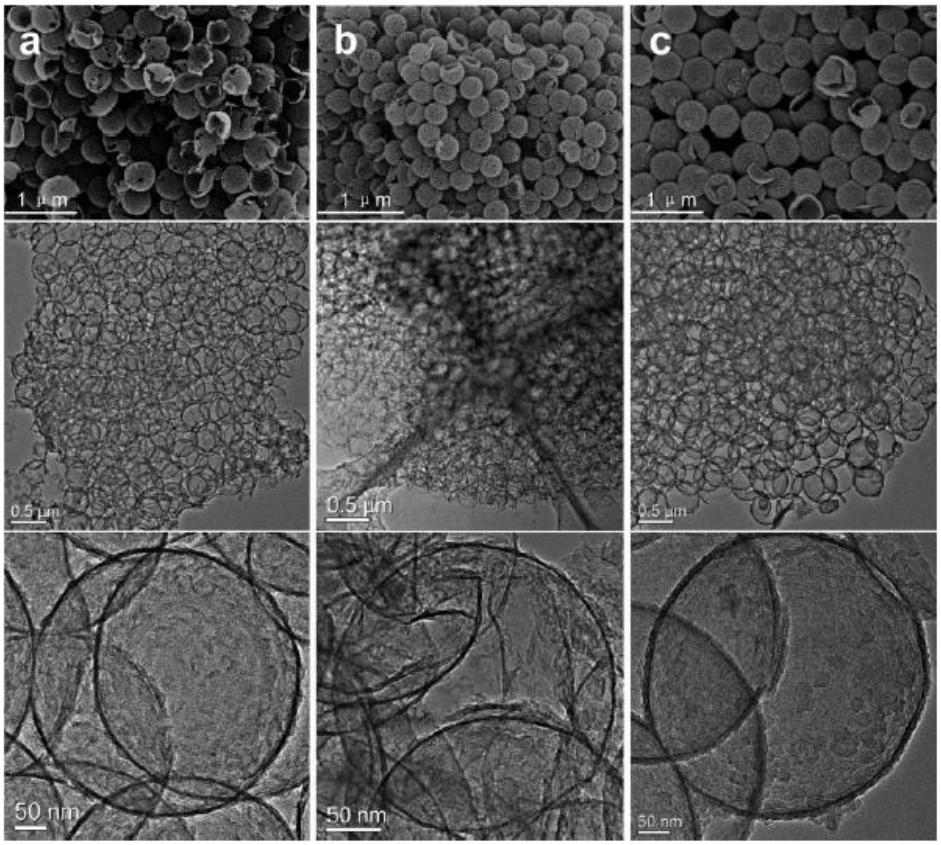



Figure 1.12: SEM and TEM images of NHCS synthesized using different ratios of silica and ionic liquid [$C_{16}$Mim]Br (a – c) [136]

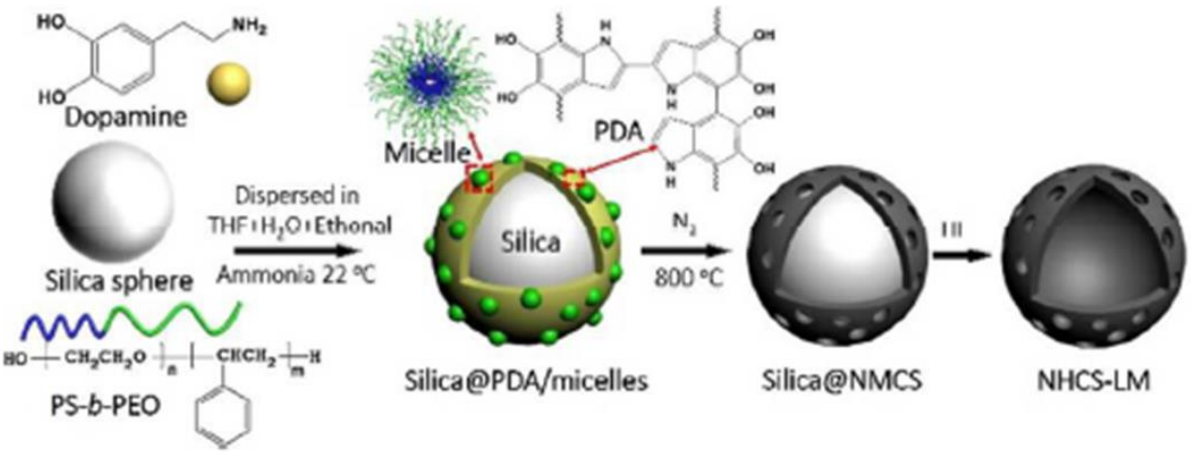



Figure 1.13: Schematic illustration of the formation of NHCS using hard template silica spheres, dopamine as carbon precursor and PS-b-PEO as pore forming agent.[137]

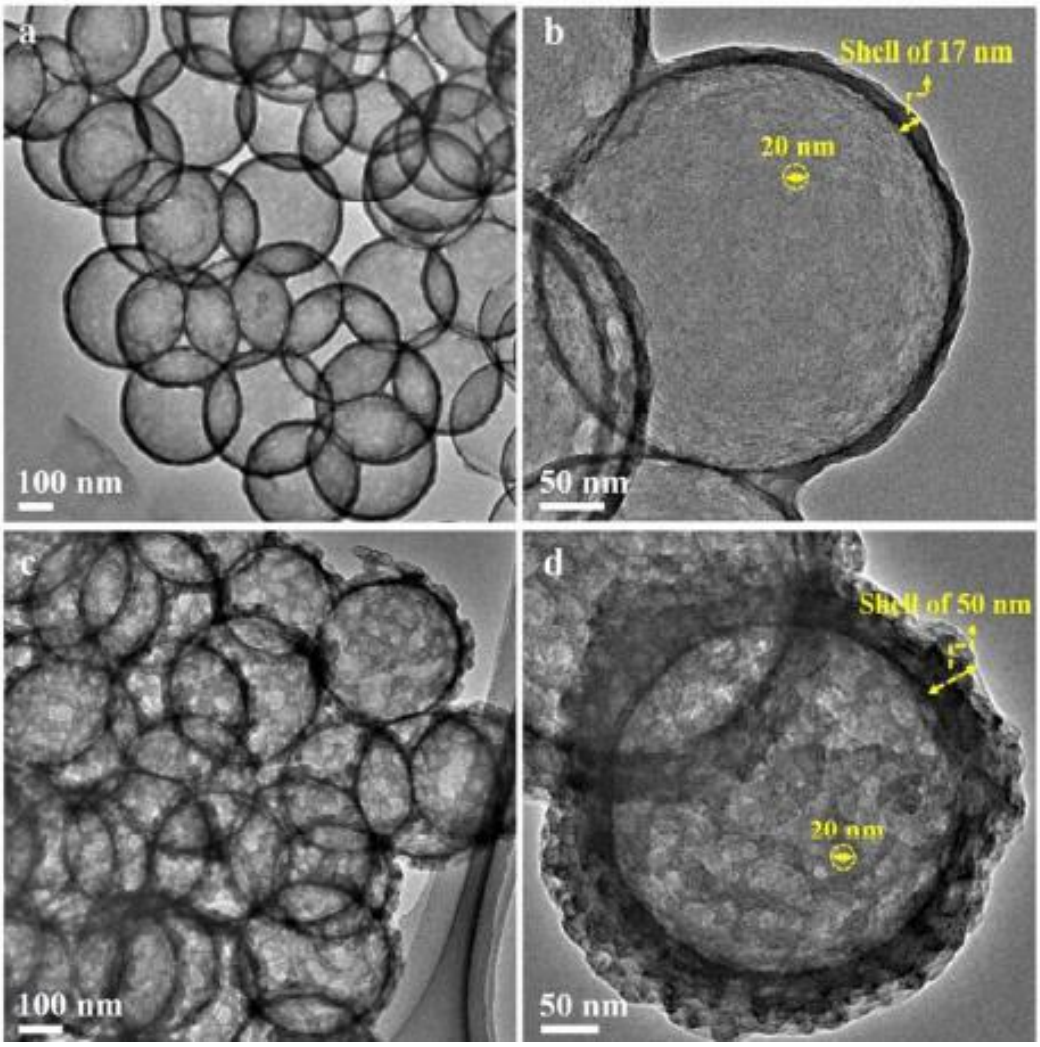



Figure 1.14: TEM images of NHCSs with identical internal diameter and various shell thickness.[137]

Using mesoporous silica spheres as templates, Li and co-workers encapsulated germanium nanoparticles inside mesoporous HCSs for lithium-ion batteries applications. To form the Ge@HCS, they used a mesoporous silica template, CTAB, and resorcinol-formaldehyde to form a coat of carbon precursor around the silica. The formed Ge@HCS had a specific capacitance of 773 mA.h $g^{-1}$ which was higher than the Ge/C benchmark catalyst.[124]

Dlamini and co-workers used silica templates to synthesize Fischer-Tropsch catalysts using porous HCS and NHCS supports. NHCSs synthesized at 600 °C had a higher nitrogen content compared to those synthesized at 900 °C. The 600 °C catalyst had a higher BET surface area of 510 $m^2.g^{-1}$ compared to 440 $m^2.g^{-1}$ for the 900 C catalyst. All the catalysts had CO conversion between 35-50% and were highly selective towards $C_{5+}$ hydrocarbons in the 50 – 60% range.[117]

## 1.9.1: Broken HCSs or hemispherical carbon spheres

Carbon with hemispherical morphology has also been used as catalysts or as catalyst support in several studies. For example, Yan and colleagues prepared hollow carbon hemispheres (HCHs) using glucose as a carbon source and polystyrene spheres as a template and supported palladium nanoparticles for fuel cell alcohol oxidation studies. The glucose precursor and polystyrene template composite was hydrothermal and microwave treatment at 160 °C for 15 h followed by carbonization at 900 ºC for 3 h in nitrogen to yield the HCSs as shown in Figure 1.16.

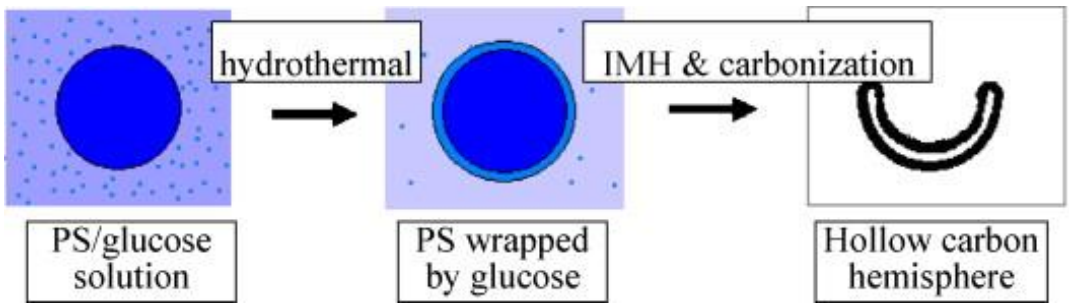



Figure 1.15: Schematic illustration of the synthesis procedure of the HCHs.[138]

The Pd supported catalysts were prepared by the microwave assisted reduction of the composite of a Pd precursor salt and the carbon in the presence of ethylene glycol. The hollow carbon hemispheres (HCHs) prepared with different starting materials are shown in figure 1.16.

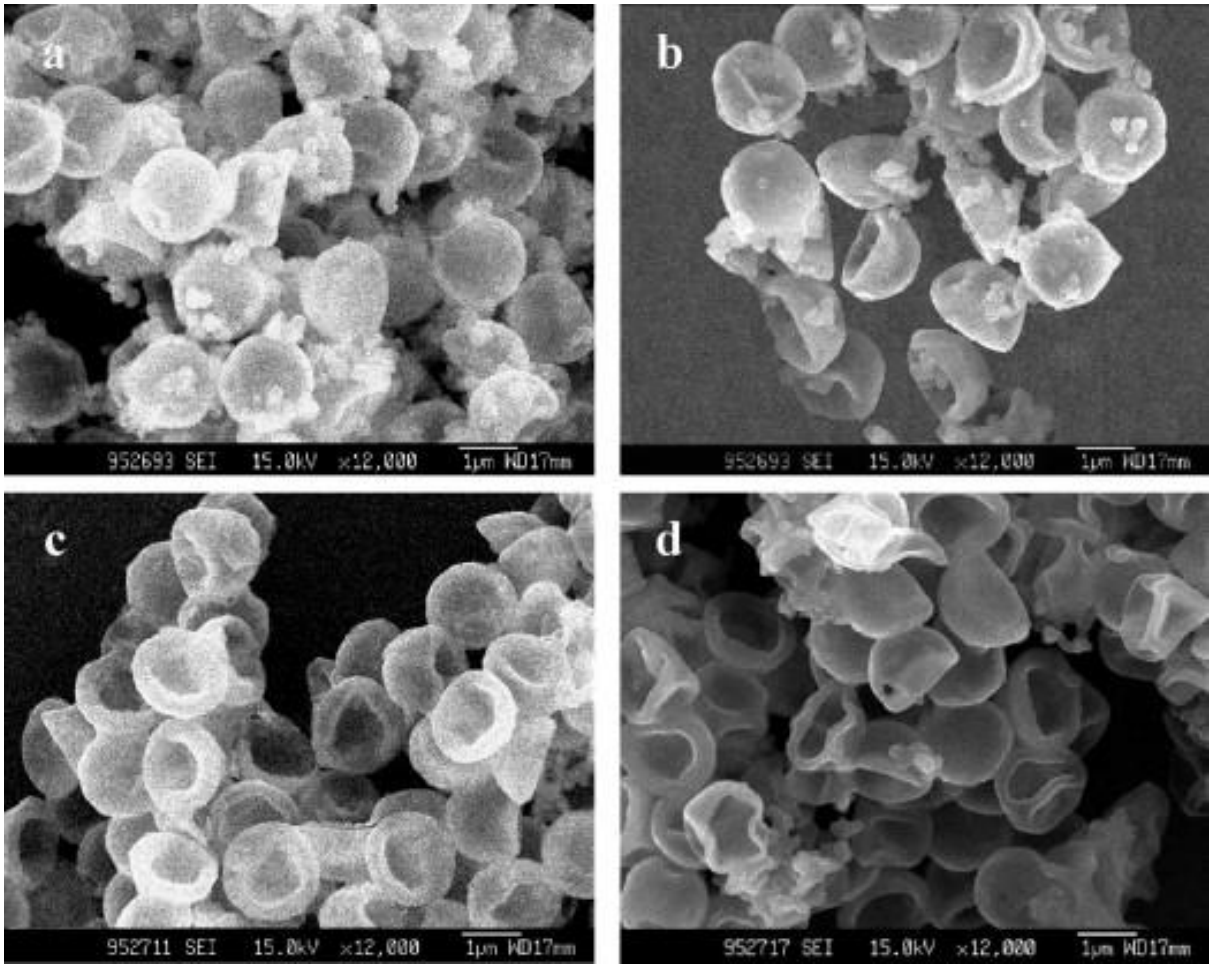



Figure 1.16: SEM micrograms of the HCHs with the mass ratios of PSs to glucose were (a) 1:4, (b) 1:3, (c) 1:2 and (d) 1:1.[138]

They observed a 2.8-times higher electrocatalytic activity in methanol oxidation than the commercial Pd supported on Vulcan XC-72 carbon catalyst with similar Pd loadings. The enhanced activity was attributed to the high surface area of the HCHs which improved the dispersion of the Pd nanoparticles. They further postulated that the hemispherical morphology

with a hollow shell was responsible for improved mass transfer of the concentrated ethanol solution resulting in increased energy density.[138]

Liu and colleagues synthesized hollow carbon hemispheres (Figure 1.18) as support material for platinum nanoparticle catalyst for methanol electro-oxidation studies. For the synthesis of the HCHs, polystyrene spheres were sulfonated in concentrated sulfuric acid followed by the in-situ polymerization of phenol-formaldehyde (PF) covering the polystyrene spheres (Figure 1.18). The PF/PS composite was then carbonized in argon at 900 ºC resulting in the formation of the HCHSs and the removal of the template. Pt nanoparticles were deposited by the reduction of chloroplatinic acid in ethylene glycol at 130ºC.

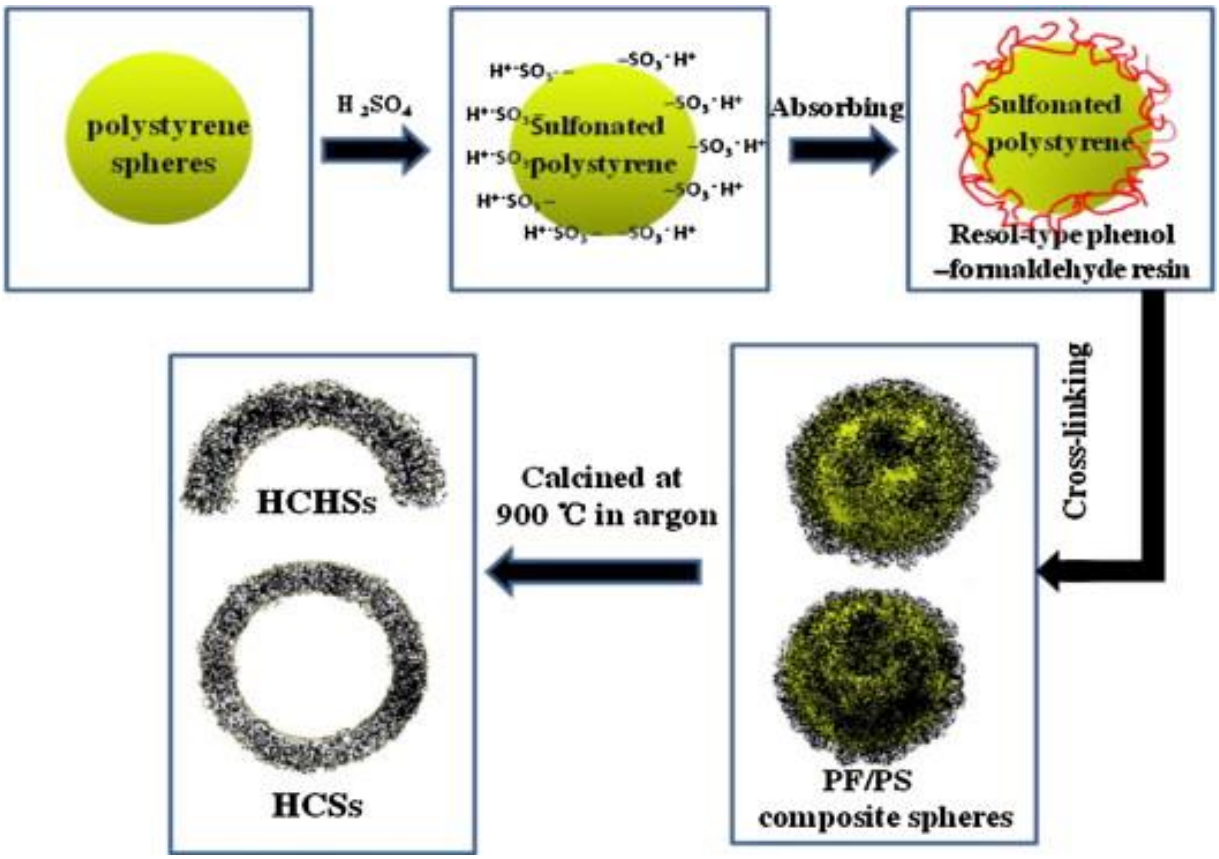



Figure 1.17 : Schematic of the preparation of hollow carbon hemispheres (HCHS).[139]

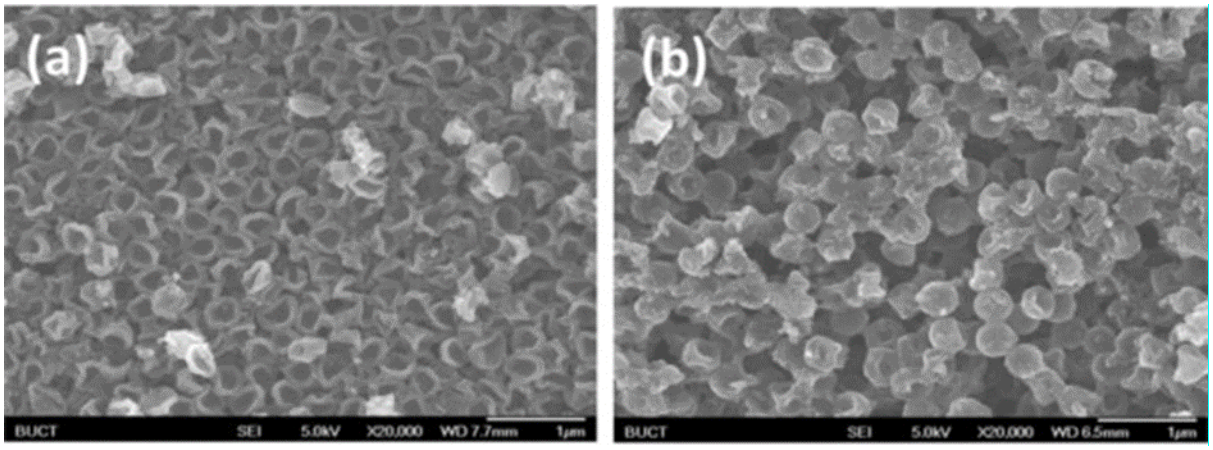



Figure 1.18: SEM images of hollow hemispherical carbon[139]

The Pt/HCHs exhibited enhanced methanol electro-oxidation activity as proved by the early onset potential, current density and stability in alkaline solution compared with carbon black supported Pt catalyst.

From the above review, the synthesis of various carbon supports using either modified Stober silica spheres or polystyrene spheres has been an important area of study over many decades by many researchers. As new synthesis strategies and techniques become available to make and evaluate Pt- structured carbon materials, new studies will generate new information on their use in the ORR and other reactions. This rationale provided the basis for this thesis.

## 1.10: Aims of the study

- To synthesize structured carbon materials in the form of hollow carbon spheres (HCSs) and nitrogen-doped hollow carbon spheres (NHCSs). These materials were to be made in the diameter range of $200 < d < 500$ nm and possessing a mesoporous shell thickness in the range of 5 – 30 nm.
- To synthesize small broken hollow carbon spheres (BHCSs) and nitrogen-doped broken hollow carbon spheres (BNHCSs). These materials were to be in the $40 < d < 100$ nm range with a mesoporous shell thickness range of 2 – 20 nm.

- To synthesize and deposit platinum (Pt) nanoparticles with a small diameter (~ 3 nm) on top and inside the mesopores of the supports thereby forming the following catalyst systems, Pt/HCSs, Pt/NHCSs, Pt/BHCSs, and Pt/NHCSs. The aim was to achieve loadings of 40 wt.% Pt/C.
- To apply the formed catalysts in fuel cell oxygen reduction reactions and to determine mass activity (MA), specific activity (SA) and durability data. The data were to be compared with a commercial benchmark 40 wt.% catalyst from Johnson and Matthey (Hispec) or Tanaka Kikinzoku Kogyo (TKK).
- To modify the observed MA, SA, and durability of the formed catalysts by synthesis procedures and to evaluate these parameters on the MA, SA, and durability of the catalysts.
- To characterize the new Pt/C catalysts by a range of classical techniques.
- To study and understand the correlation between the structure of the catalysts and its durability and activity.
- To derive synthetic strategies to improve the catalyst system for upscaling and testing in a real fuel cell system.

To achieve these aims the synthesis of mesoporous, thin shell, porous, and high surface area HCSs, NHCSs, BHCSs and BNHCSs supports for Pt nanoparticles for fuel cell cathode applications was undertaken. It was expected that a high extent of graphitization of the carbon shell would be needed since previous studies have shown that highly ordered and graphitic carbon supports were highly resistant to electrochemical oxidation during the stop/start or load cycling of a fuel cell. To achieve high graphitization, the use of thin shell HCSs and NHCSs in the 5 – 30 nm size range were to be made. It was expected that nitrogen doping would enhance electrochemical activity through improving metal support interaction as well as promoting high

support utilization by the Pt nanoparticles. A balance between high graphitization and defects was required since defect rich support materials have been shown to possess good metal–support interactions.[93,140]

The Pt nanoparticles were also deposited on the surface outside of the supports instead of being encapsulated inside the HCSs. This was because electro-catalysis is a surface process and reagents need to have enhanced mass transport with unrestricted access to the catalyst surface and swift product removal from the surface of the catalysts for a continuous process.

Initially it was intended to synthesize small HCSs and small NHCSs. However, small broken bowl-like hollow carbon spheres (BHCSs) were instead synthesized, due to aggregation of the small silica templates. There are no literature reports on the study and use of these small materials (BHCSs) or their N doped equivalents (BNHCSs) in Pt based hydrogen fuel cell ORR catalysis, and they were thus studied to evaluate their interaction between the Pt and the shells.

Would these new supports enhance catalytic activity and durability? The small broken bowl-like hollow carbon spheres would enable the deposition of Pt on both the inside and outside of the HCS shell (as shown in figure 1.19 schematic). This would enable a higher Pt density per unit mass of support and enhanced confinement on both sides of the support shell such that the challenge of inferior durability encountered with other carbon supports could be resolved.

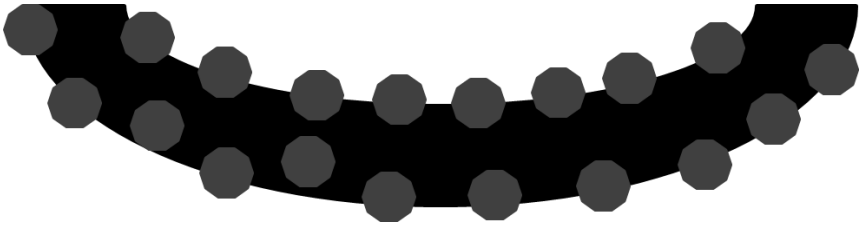


Figure 1.19: Schematic showing Pt (grey octahedra) deposited both sides of a (BHCSs/BNHCSs) shell (black region) with high support utilization.

These supports (BHCSs/BNHCSs) have a higher spherical surface area compared to the larger spheres and as a result, it was expected that a better dispersion of Pt would occur on these

supports. Further, the thinner shells should show enhanced graphitization and better durability when compared to thicker amorphous shells.

## 1.11: Objectives of the Study

The objectives of this study were:

- To synthesize various size silica templates for use in forming the catalyst supports.
- To synthesize a resorcinol-formaldehyde (RF) resin to cover the silica spheres, $SiO_2$@RF.
- To carbonize the $SiO_2$@RF at high temperature forming $SiO_2$@C.
- To etch the silica using hydrofluoric acid solution to form the HCSs.
- To anneal the HCS material at high temperatures to enhance its physico-chemical properties.
- To use ex-situ doping technique to synthesize nitrogen-doped hollow carbon spheres (NHCSs) using the $SiO_2$@RF and a nitrogen rich source.
- To synthesize small $SiO_2$ spheres ($40 < d < 100$ nm) and use them as templates for making small broken hollow carbon spheres (BHCSs).
- To nitrogen dope the BHCSs to form BNHCSs.
- To use a porogen surfactant to enhance the formation of pores in the support (HCSs, NHCSs, BHCSs, and BNHCSs) shell.
- To deposit Pt on the supports using a reliable and reproducible metal-organic deposition technique in use at HySA catalysis at the University of Cape Town.
- To characterize the samples to evaluate structure to function relationships. This involved the use of transmission electron microscopy (TEM), scanning electron microscopy (SEM), scanning tunnelling electron microscopy (STEM), Raman spectroscopy, Brunaeur - Emmett – Teller (BET) and Barrett -Joyner - Halenda (BJH)

surface area and porosity measurements, thermogravimetric analysis (TGA), powder X-ray diffraction (PXRD) and X-ray photoelectron spectroscopy (XPS).

- To carry out electrochemical characterization procedures to evaluate the electrochemical active surface area (ECSA), mass specific activity (MA), surface area specific activity (SA) and durability studies using a three-electrode cell setup that mimics a PEMFC electrode.
- To improve the catalysts based on the observed values obtained for MA, SA, ECSA, and durability studies.
- To upscale the improved catalysts for testing in a real fuel cell system.
- To make available new knowledge for HySA Catalysis for technology uptake.

## 1.12: Thesis Outline

### Chapter 1

This provides background to the study. Introduces fuel cells and various factors affecting activity and durability. Discusses in brief the concept of templating as a route to structured carbon supports in electrocatalysis.

### Chapter 2

Discusses the experimental procedures used in the synthesis and provides background information on the physicochemical characterization techniques used for the materials under study.

### Chapter 3

Discusses the synthesis of various sizes of silica templates. Evaluated parameters that influenced the size and possible growth models.

## Chapter 4

Discusses the use of large silica spheres and the subsequent synthesis of large hollow carbon spheres and nitrogen-doped hollow carbon spheres (HCSs and NHCSs). Additionally, the deposition of platinum nanoparticles to form Pt/HCSs and Pt/NHCSs and the physicochemical characterization of these materials was also discussed in detail.

## Chapter 5

Discusses the use of small silica spheres as templates for the synthesis of broken bowl like hollow carbon spheres (BHCSs) and the nitrogen-doped broken bowl-like hollow carbon spheres (BNHCSs). Furthermore, the subsequent deposition of platinum nanoparticles to form Pt/BHCSs and Pt/BNHCSs and the physicochemical characterization of these materials was also discussed.

## Chapter 6

Discusses the electrochemical characterization of the catalysts (Pt/HCSs, Pt/NHCSs, Pt/BHCSs and Pt/BNHCSs and the commercial benchmark catalyst Pt/Vulcan) in oxygen reduction reactions. Discusses the link between the physicochemical properties of the materials and the observed activity and durability of the catalysts.

## Chapter 7

Discusses the preparation of Pt/HCSs and Pt/NHCSs using the ethanol reflux of a Pt precursor and the subsequent electrochemical characterization through ECSA, MA, SA and durability studies. This chapter provides comparison between Pt prepared via the metal-organic deposition technique and the Pt prepared alternatively.

# Chapter 8

Discusses the general conclusions drawn from the work and the outlook.

## 1.13: References


(1) Annual Energy Outlook 2020 https://www.eia.gov/outlooks/aeo/ (accessed Aug 28, 2020).

(2) Lin, B.; Ouyang, X. Energy Demand in China: Comparison of Characteristics between the US and China in Rapid Urbanization Stage. *Energy Conversion and Management* **2014**, *79*, 128–139.

(3) South Africa Energy Outlook – Analysis https://www.iea.org/articles/south-africa-energy-outlook (accessed Aug 28, 2020).

(4) Iceland - Countries & Regions https://www.iea.org/countries/iceland (accessed Aug 28, 2020).

(5) Government of Iceland | Energy https://www.government.is/topics/business-and-industry/energy

(6) BP Energy Outlook - 2016 edition | News and insights | Home https://www.bp.com/en/global/corporate/news-and-insights/speeches/energy-outlook-2016-edition-launch.html

(7) National Academies of Sciences, E. Attribution of Extreme Weather Events in the Context of Climate Change; 2016.

(8) Littell, J. S.; Mckenzie, D.; Peterson, D. L.; Westerling, A. L. Climate and Wildfire Area Burned in Western U.S. Ecoprovinces, 1916-2003. *Ecological Applications* **2009**, *19* (4), 1003–1021.

(9) Holder, J.; Kommenda, N.; Watts, J.; Holder, J.; Kommenda, N.; Watts, J. The Three-Degree World: Cities That Will Be Drowned by Global Warming. The Guardian.

(10) Knorr, W.; Jiang, L.; Arneth, A. Climate, CO2 and Human Population Impacts on Global Wildfire Emissions. *Biogeosciences* **2016**, *13* (1), 267–282.

(11) Lucia, U. Overview on Fuel Cells. *Renewable and Sustainable Energy Reviews* **2014**, *30*, 164–169.

(12) Wagner, F.T.; Lakshmanan, B.; Mathias, M.F. Electrochemistry and the Future of the Automobile. *J. Phys. Chem. Lett*. **2010**, 14(1), 2204–2219

(13) Peighambardoust, S. J.; Rowshanzamir, S.; Amjadi, M. *Review of the Proton Exchange Membranes for Fuel Cell Applications*; Elsevier Ltd, 2010; Vol. 35, p 9384.

(14) Shao, Z.; Haile, S. M.; Ahn, J.; Ronney, P. D.; Zhan, Z.; Barnett, S. A. A Thermally Self-Sustained Micro Solid-Oxide Fuel-Cell Stack with High Power Density. *Nature* **2005**, *435* (7043), 795–798.

(15) Cao, D.; Sun, Y.; Wang, G. Direct Carbon Fuel Cell: Fundamentals and Recent Developments. *Journal of Power Sources* **2007**, *167* (2), 250–257.

(16) EG&G Technical Services, Inc. Fuel Cell Handbook. *Fuel Cell* **2004**, *7 Edition* (November), 1–352.

(17) Nakićenović, Nebojša.; Grübler, A.; McDonald, A. (Alan). *Global Energy: Perspectives*; Cambridge University Press: Cambridge, NY, **1998**; p 299.

(18) Bagotsky, V. S. Fuel Cells: Problems and Solutions; John Wiley & Sons, 2012.

(19) Fuel Cell Megawatt Power Generation Platform | Hydrogenics.

(20) Stevens, M.; Mendes, C.; Fowler, M.; Fraser, R. Fuel Cell Hybrid Control Strategy Development, SAE Technical Paper 2006-01-0214, 2006, https://doi.org/10.4271/2006-01-0214.

(21) Ballard and HDF Energy Sign Development Agreement For Multi-Megawatt Fuel Cell Systems https://www.ballard.com/about-ballard/newsroom/news-releases/2019/12/10

(22) Toyota and Fuel Cell Energy Plan to Build a Giant Renewable Power and Hydrogen Plant https://www.greentechmedia.com/articles/read/toyota-fuelcell-energy-renewable-power-hydrogen-plant (accessed Aug 28, 2020).

(23) Pollet, B. G.; Kocha, S. S.; Staffell, I. Current Status of Automotive Fuel Cells for Sustainable Transport. *Current Opinion in Electrochemistry* **2019**, *16*, 90–95.

(24) Manoharan, Y.; Hosseini, S. E.; Butler, B.; Alzhahrani, H.; Senior, B. T. F.; Ashuri, T.; Krohn, J. Hydrogen Fuel Cell Vehicles; Current Status and Future Prospect. *Applied Sciences* **2019**, *9* (11), 2296.

(25) Anglo American orders nine 100 kW Ballard fuel cell modules for mining truck demo project https://www.greencarcongress.com/2019/10/20191029-ballard.html

(26) Chen, W.; Huang, J.; Wei, J.; Zhou, D.; Cai, J.; He, Z. D.; Chen, Y. X. Origins of High Onset Overpotential of Oxygen Reduction Reaction at Pt-Based Electrocatalysts: A Mini Review. *Electrochemistry Communications* **2018**, *96*.

(27) Liang, H.W.; Wei, W.; Wu, Z.-S.; Feng, X.; Mü, K. Mesoporous Metal−Nitrogen-Doped Carbon Electrocatalysts for Highly Efficient Oxygen Reduction Reaction. *J. Am. Chem. Soc* **2013**, *17*, 33–33.

(28) Shui, J.; Wang, M.; Du, F.; Dai, L. N-Doped Carbon Nanomaterials Are Durable Catalysts for Oxygen Reduction Reaction in Acidic Fuel Cells. *Science Advances* **2015**, *1* (1), 1–8.

(29) Gong, K.; Du, F.; Xia, Z.; Durstock, M.; Dai, L. Nitrogen-Doped Carbon Nanotube Arrays with High Electrocatalytic Activity for Oxygen Reduction. *Science (New York, N.Y.)* **2009**, *323* (5915), 760–764.

(30) Plötz, P.; Axsen, J.; Funke, S. A.; Gnann, T. Designing Car Bans for Sustainable Transportation. *Nature Sustainability* **2019**, *2* (7), 534–536.

(31) Moriarty, P.; Energy, D. H.-I. J. of H.; 2019, undefined. Prospects for Hydrogen as a Transport Fuel. International Journal of Hydrogen Energy (**2019**), 44, (31) 16029-16037

(32) Rimmer, M. *Investing in the Future: Norway, Climate Change, and Fossil Fuel Divestment*; SSRN Scholarly Paper ID 2770844; Social Science Research Network: Rochester, NY, 2016.

(33) Green, F. The Logic of Fossil Fuel Bans. *Nature Climate Change* **2018**, *8* (6), 449–451.

(34) Home | HySA/Catalysis http://www.hysacatalysis.uct.ac.za

(35) Garland, N. L.; Benjamin, T. G.; Kopasz, J. P. ECS Transactions DOE Fuel Cell Program: Durability Technical Targets and Testing Protocols DOE Fuel Cell Program: Durability Technical Targets and Testing Protocols. *ECS Transactions*, (**2007**), 11, (1)

(36) Hou, Y.; Zhuang, M.; Wan, G. The Analysis for the Efficiency Properties of the Fuel Cell Engine. *Renewable Energy* **2007**, *32* (7), 1175–1186.

(37) Lutz, A. E.; Larson, R. S.; Keller, J. O. Thermodynamic Comparison of Fuel Cells to the Carnot Cycle. *International Journal of Hydrogen Energy* **2002**, *27* (10), 1103–1111.

(38) Hong, B. K.; Kim, S. H. (Invited) Recent Advances in Fuel Cell Electric Vehicle Technologies of Hyundai. *ECS Trans.* **2018**, *86* (13), 3.

(39) Onorato, S.; Kurtz, J. NREL Fuel Cell and Hydrogen Systems Research. 53.

(40) Venturi, M.; Mohrdieck, C.; Friedrich, J. Mercedes-Benz B-Class Fuel Cell: The World Largest Hydrogen Vehicle Fuel Cell Fleet Experience. In *2013 World Electric Vehicle Symposium and Exhibition (EVS27)*; **2013**,1–11.

(41) Mohrdieck, D. C. Next Generation Fuel Cell Technology for Passenger Cars and Buses. *World Electric Vehicle Journal* **2009**, *3* (2), 209–213.

(42) Chan, C. C. The State of the Art of Electric, Hybrid, and Fuel Cell Vehicles. *Proceedings of the IEEE* **2007**, *95* (4), 704–718.

(43) Granovskii, M.; Dincer, I.; Rosen, M. A. Economic and Environmental Comparison of Conventional, Hybrid, Electric and Hydrogen Fuel Cell Vehicles. *Journal of Power Sources* **2006**, *159* (2), 1186–1193.

(44) Kurtz, J. M.; Sprik, S.; Saur, G.; Onorato, S. *Fuel Cell Electric Vehicle Driving and Fueling Behavior*; Golden, CO (United States), 2019.

(45) Coradia iLint – the world's 1st hydrogen powered train https://www.alstom.com/solutions/rolling-stock/coradia-ilint-worlds-1st-hydrogen-powered-train

(46) Yoshida, T.; Kojima, K. Toyota MIRAI Fuel Cell Vehicle and Progress toward a Future Hydrogen Society. *Electrochem. Soc. Interface* **2015**, 24, 45

(47) Toyota Unveils More Advanced Heavy-Duty Fuel Cell Truck Prototype https://www.trucks.com/2018/07/30/toyota-advanced-fuel-cell-truck/

(48) She, Z. W.; Kibsgaard, J.; Dickens, C. F.; Chorkendorff, I.; Nørskov, J. K.; Jaramillo, T. F. Combining Theory and Experiment in Electrocatalysis: Insights into Materials Design. *Science* **2017**, *355* (6321).

(49) Zhang, J.; Kasaki, K.; Sutter, E.; Adzic, R.R. Stabilization of Platinum Oxygen-Reduction Electrocatalysts Using Gold Clusters. *Science* **2007**, 315(5809), 220-222

(50) Holton, O. T.; Stevenson, J. W. The Role of Platinum in Proton Exchange Membrane Fuel Cells. *Platinum Metals Rev.* **2013**, *57* (5), 259–271.

(51) Selvaganesh, S. V.; Sridhar, P.; Pitchumani, S.; Shukla, A. K. A Durable Graphitic-Carbon Support for Pt and Pt3Co Cathode Catalysts in Polymer Electrolyte Fuel Cells. *Journal of the Electrochemical Society* **2013**, *160* (1).

(52) Tan, T. L.; Wang, L. L.; Johnson, D. D.; Bai, K. A Comprehensive Search for Stable Pt-Pd Nanoalloy Configurations and Their Use as Tunable Catalysts. *Nano Letters* **2012**, *12* (9), 4875–4880.

(53) Wu, Y.; Wang, D.; Niu, Z.; Chen, P.; Zhou, G.; Li, Y. A Strategy for Designing a Concave Pt-Ni Alloy through Controllable Chemical Etching. *Angewandte Chemie - International Edition* **2012**, *51* (50), 12524–12528.

(54) Proton-Exchange Membrane Fuel Cells - an overview | ScienceDirect Topics https://www.sciencedirect.com/topics/chemistry/proton-exchange-membrane-fuel-cells (accessed Aug 26, 2020).

(55) Shinagawa, T.; Garcia-Esparza, A. T.; Takanabe, K. Insight on Tafel Slopes from a Microkinetic Analysis of Aqueous Electrocatalysis for Energy Conversion. *Scientific Reports* **2015**, *5*.

(56) Shanmugam, S.; Osaka, T. Efficient Electrocatalytic Oxygen Reduction over Metal Free-Nitrogen Doped Carbon Nanocapsules. *Chem. Commun*. **2011**, 47, 4463-4465

(57) Kundu, S.; Nagaiah, T. C.; Xia, W.; Wang, Y.; Dommele, S. V.; Bitter, J. H.; Santa, M.; Grundmeier, G.; Bron, M.; Schuhmann, W.; Muhler, M. Electrocatalytic Activity and Stability of Nitrogen-Containing Carbon Nanotubes in the Oxygen Reduction Reaction. *The Journal of Physical Chemistry C* **2009**, *113* (32), 14302–14310.

(58) Chung, H. T.; Cullen, D. A.; Higgins, D.; Sneed, B. T.; Holby, E. F.; More, K. L.; Zelenay, P. Direct Atomic-Level Insight into the Active Sites of a High-Performance PGM-Free ORR Catalyst. *Science* **2017**, *357* (6350).

(59) Penner, S.; Appleby, A.; Baker, B.; Bates, J.; Buss, L.B.; Penner, S.S. Commercialization of Fuel Cells. *Energy* **1995** 20 (5), 331-470

(60) Garland, N. L.; Benjamin, T. G.; Kopasz, J. P. ECS Transactions DOE Fuel Cell Program: Durability Technical Targets and Testing Protocols DOE Fuel Cell Program: Durability Technical Targets and Testing Protocols. ECS Transactions,**2007**, 11 (1) 923-931

(61) Shao, Y.; Kou, R.; Wang, J.; Wang, C.; Viswanathan, V.; Liu, J.; Wang, Y.; Lin, Y. The Durability Dependence of Pt/CNT Electrocatalysts on the Nanostructures of Carbon Nanotubes: Hollow-and Bamboo-CNTs. *Journal of Nanoscience and Nanotechnology* **2009**, *9* (10), 5811–5815.

(62) Kongkanand A.; Kuwabata, S.; Girishkumar, G.; Kamat, P. Single-Wall Carbon Nanotubes Supported Platinum Nanoparticles with Improved Electrocatalytic Activity for Oxygen Reduction Reaction. Langmuir **2006**, 22 (5), 2392–2396

(63) Nagasawa, K.; Takao S.; Higashi, K.; Nagamatsu, S.; Samjeske, G.; Imaizumi Y.; Sekizawa O.; Yamamoto, T.; Uruga, T.; Iwasawa, Y. Performance and durability of Pt/C cathode catalysts with different kinds of carbons for polymer electrolyte fuel cells characterized by electrochemical and in situ XAFS techniques. *Phys. Chem. Chem. Phys*. **2014**, 16, 10075-10087.

(64) He, W.; Jiang, H.; Zhou, Y.; Yang, S.; Xue, X.; Zou, Z.; Zhang, X.; Akins, D. L.; Yang, H. An Efficient Reduction Route for the Production of Pd-Pt Nanoparticles Anchored on Graphene Nanosheets for Use as Durable Oxygen Reduction Electrocatalysts. In *Carbon*; 2012.

(65) Zhang, C.; Xu, L.; Shan, N.; Sun, T.; Chen, J.; Yan, Y. Enhanced Electrocatalytic Activity and Durability of Pt Particles Supported on Ordered Mesoporous Carbon Spheres. *ACS Catalysis* **2014**, *4* (6), 1926–1930.

(66) Jackson, C.; Smith, G.; Inwood, D.; Leach, A.S.; Whalley, P.S.; Callisti, M.; Polcar, T.; Russell, A.E.; Levecque, P.; Kramer, D. Electronic metal-support interaction enhanced oxygen reduction activity and stability of boron carbide supported platinum. *Nat Commun* **2017**, 8, 15802

(67) Galeano, C. Meier, J.C. Soorholtz, M. Bongard, H. Baldizzone, C. Mayrhofer, K. J. J. Schüth, F. Nitrogen-Doped Hollow Carbon Spheres as a Support for Platinum-Based Electrocatalysts. *ACS Catal* **2014,** 11**,** 3856–3868.

(68) Higgins, D.C.; Meza, D.; Chen, Z. Nitrogen-Doped Carbon Nanotubes as Platinum Catalyst Supports for Oxygen Reduction Reaction in Proton Exchange Membrane Fuel Cells. *J. Phys. Chem. C* **2010**, 114 (50), 21982–21988.

(69) Zhang, J.; Ma, L.; Gan, M.; Yang, F, Fu, S.; Li, X. Well-Dispersed Platinum Nanoparticles Supported on Hierarchical Nitrogen-Doped Porous Hollow Carbon Spheres with enhanced activity and stability for methanol electrooxidation. *Journal of Power Sources* **2015**, 288(15), 42-52.

(70) Melke J.; Peter, B.; Habereder, A.; Fasel, C.; Nefedov, A, Ziegler, Sezen, H.; Woll, C.; Ehrenberg, H.; Roth, C. Metal–Support Interactions of Platinum Nanoparticles Decorated N-Doped Carbon Nanofibers for the Oxygen Reduction Reaction. *ACS Appl. Mater*. Interfaces **2016**, 8(1), 82–90.

(71) Wang, Y.; Jin, J.; Yang, S.; Li, G.; Jiang, J. Nitrogen-Doped Porous Carbon Nanofiber Based Oxygen Reduction Reaction Electrocatalysts with High Activity and Durability. *International Journal of Hydrogen Energy* **2016**, *41* (26), 11174–11184.

(72) Galeano, C.; Meier, J.C.; Katsounaros, I.; Witte, J.; Bongard, H.J.; Topalov, A.A.; Baldizzone, C.; Mezzavilla, S.; Schüth, F.; Mayrhofer, K.J.J. Toward Highly Stable Electrocatalysts via Nanoparticle Pore Confinement *J. Am. Chem. Soc*. (**2012**), 134(50), 20457–20465

(73) Jukk, K.; Kongi, N.; Rauwel, P.; Matisen, L.; Tammeveski, K. Platinum Nanoparticles Supported on Nitrogen-Doped Graphene Nanosheets as Electrocatalysts for Oxygen Reduction Reaction. *Electrocatalysis* **2016**, 7,428–440

(74) Jung, W.S; Popov, B.N. Improved Durability of Pt Catalyst Supported on N-Doped Mesoporous Graphitized Carbon for Oxygen Reduction Reaction. *Carbon* (2017), 122, 746-755.

(75) Stamatin, S. N.; Speder, J.; Dhiman, R.; Arenz, M.; Skou, E. M. Electrochemical Stability and Postmortem Studies of Pt/SiC Catalysts for Polymer Electrolyte Membrane Fuel Cells. *ACS Applied Materials & Interfaces* **2015**, *7* (11), 6153–6161.

(76) Liu, L.; Samjeské, G.; Takao, S.; Nagasawa, K.; Iwasawa, Y. Fabrication of PtCu and PtNiCu Multi-Nanorods with Enhanced Catalytic Oxygen Reduction Activities. *Journal of Power Sources* **2014**, *253*, 1–8.

(77) Fiçicilar, B.; Bayrakçeken, A.; Eroğlu, I. Effect of Pd Loading in Pd-Pt Bimetallic Catalysts Doped into Hollow Core Mesoporous Shell Carbon on Performance of Proton Exchange Membrane Fuel Cells. *Journal of Power Sources* **2009**, *193* (1), 17–23.

(78) Takao, S.; Sekizawa, O.; Higashi, K.; Samjeské, G.; Kaneko, T.; Sakata, T.; Yamamoto, T.; Uruga, T.; Iwasawa, Y. Visualization Analysis of Pt and Co Species in Degraded Pt3Co/C Electrocatalyst Layers of a Polymer Electrolyte Fuel Cell Using a Same-View Nano-XAFS/STEM-EDS Combination Technique. *ACS applied materials & interfaces* **2020**, *12* (2), 2299–2312.

(79) Zhang, G.; Shao, Z. G.; Lu, W.; Xie, F.; Xiao, H.; Qin, X.; Yi, B. Core-Shell Pt Modified Pd/C as an Active and Durable Electrocatalyst for the Oxygen Reduction Reaction in PEMFCs. *Applied Catalysis B: Environmental* **2013**, *132–133*, 183–194.

(80) Zheng, Z.; Luo, L.; Zhu, F.; Cheng, X.; Yang, F.; Shen, S.; Wei, G.; Zhang, J. Degradation of Core-Shell $Pt_3Co$ Catalysts in Proton Exchange Membrane Fuel Cells (PEMFCs) Studied by Mathematical Modeling. *Electrochimica Acta* **2019**, *323*,134751

(81) Koh, S.; Strasser, P. Electrocatalysis on Bimetallic Surfaces: Modifying Catalytic Reactivity for Oxygen Reduction by Voltammetric Surface Dealloying. *Journal of the American Chemical Society* **2007**, *129* (42), 12624–12625.

(82) Strasser, P.; Koh, S.; Anniyev, T.; Greeley, J.; More, K.; Yu, C.; Liu, Z.; Kaya, S.; Nordlund, D.; Ogasawara, H.; Toney, M.F.; Nilsson, A. Lattice-Strain Control of the Activity in Dealloyed Core-Shell Fuel Cell Catalysts. *Nature Chemistry* **2010**,2, 454–460.

(83) Alia, S.M.; Jensen, K, O.; Pivovar, B, S.; Yan, Y. Platinum-Coated Palladium Nanotubes as Oxygen Reduction Reaction Electrocatalysts. *ACS Catal* **2012**, 2(5), 858–863

(84) Su, L.; Shrestha, S.; Zhang, Z.; Mustain, W.; Lei, Y. Platinum-Copper Nanotube Electrocatalyst with Enhanced Activity and Durability for Oxygen Reduction Reactions. *Journal of Materials Chemistry A* **2013**, *1* (39), 12293–12301.

(85) Peng, X.; Zhao, S.; Omasta, T. J.; Roller, J. M.; Mustain, W. E. Activity and Durability of Pt-Ni Nanocage Electocatalysts in Proton Exchange Membrane Fuel Cells. *Applied Catalysis B: Environmental* **2017**, *203*, 927–935.

(86) Sasaki, K.; Naohara, H.; Choi, Y.; Cai, Y.; Chen, F.W.; Liu, P.; Adzic, R.R. Highly Stable Pt Monolayer on PdAu Nanoparticle Electrocatalysts for the Oxygen Reduction Reaction. *Nat Commun.* **2012**, 3, 1115.

(87) Zou, L.; Liu, Z.; Yuan, T.; Zhou, Y.; Li, X.; Yang, H. Structural Transformation of Carbon-Supported $Pt_3Cr$ Nanoparticles from a Disordered to an Ordered Phase as a Durable. *Nanoscale* **2014**, 6, 10686-10692

(88) Takahashi, I.; Kocha, S.S.; Examination of the Activity and Durability of PEMFC Catalysts in Liquid Electrolytes. *Journal of Power Sources* **2010**, 195 (19), 6312-6322.

(89) Wang, X.; Li, Z.; Qu, Y.; Yuan, T.; Wang, W.; Wu, Y.; Li, Y.; Review of Metal Catalysts for Oxygen Reduction Reaction: From Nanoscale Engineering to Atomic Design. *Chem* **2019**, 14875,1486–1511,

(90) Kibsgaard, J.; Jackson, A.; Jaramillo, T.F.; Mesoporous platinum nickel thin films with double gyroid morphology for the oxygen reduction reaction Nano Energy **2016**, 29, 243-248

(91) Wang, R.; Li, X.; Li, H.; Wang, Q.; Wang, W.; Kang, J.; Chang, J.; Lei, Z. Highly Stable and Effective Pt/Carbon Nitride (CNx) Modified SiO2 Electrocatalyst for Oxygen Reduction Reaction. *International Journal of Hydrogen Energy* **2011**, 36 (10) 5775-5781.

(92) Cheng, N.; Norouzi Banis, M.; Liu, J.; Riese, A.; Mu, S.; Li, R.; Sham, T. K.; Sun, X. Atomic Scale Enhancement of Metal-Support Interactions between Pt and ZrC for Highly Stable Electrocatalysts. *Energy and Environmental Science* **2015**, *8* (5), 1450–1455.

(93) Cheng, N.; Liu, J.; Banis, M. N.; Geng, D.; Li, R.; Ye, S.; Knights, S.; Sun, X. High Stability and Activity of Pt Electrocatalyst on Atomic Layer Deposited Metal Oxide/Nitrogen-Doped Graphene Hybrid Support. *International Journal of Hydrogen Energy* **2014**, *39* (28), 15967–15974.

(94) Xu, F.; Wang, D.; Sa, B.; Yu, Y.; Mu, S. One-Pot Synthesis of Pt/CeO2/C Catalyst for Improving the ORR Activity and Durability of PEMFC. *International Journal of Hydrogen Energy* **2017**, *42* (18), 13011–13019.

(95) Mohamed, R.; Binninger, T.; Kooyman, P.J.; Hoey, A.; Fabbri, E, Patru.; Heinritz, A.; Schmidt, T.J.; Levecque, P. Facile deposition of Pt nanoparticles on Sb-doped $SnO_2$ support with outstanding active surface area for the oxygen reduction reaction. *Catal. Sci. Technol*. **2018**, 8, 2672-2685.

(96) Guo, D.; Shibuya, R.; Akiba, C.; Saji, S.; Kondo, T.; Nakamura, J. Active Sites of Nitrogen-Doped Carbon Materials for Oxygen Reduction Reaction Clarified Using Model Catalysts. *Science* **2016**, 351 (6271) 361-365.

(97) Zhang, L.; Su, Z.; Jiang, F.; Yang, L.; Qian, J.; Zhou, Y.; Li, W.; Hong, M. Highly Graphitized Nitrogen-Doped Porous Carbon Nanopolyhedra Derived from ZIF-8 Nanocrystals as Efficient Electrocatalysts for Oxygen Reduction Reactions. *Nanoscale* **2014**, *6* (12), 6590–6602.

(98) Lin, Z.; Song, M.; Ding, Y.; Liu, Y.; Liu, M.; Wong, C. Facile Preparation of Nitrogen - Doped Graphene as a Metal-Free Catalyst for Oxygen Reduction Reaction. *Physical Chemistry Chemical Physics* **2012**, *14* (10), 3381–3387.

(99) Zhang, S.; Yuan, X.; Wang, H.; Mérida, W.; Zhu, H.; Shen, J.; Wu, S.; Zhang, J. A Review of Accelerated Stress Tests of MEA Durability in PEM Fuel Cells. *International Journal of Hydrogen Energy* **2009**, *34* (1), 388–404.

(100) Zhang, S.; Yuan, X.-Z. Z.; Hin, J. N. C.; Wang, H.; Friedrich, K. A.; Schulze, M. A Review of Platinum-Based Catalyst Layer Degradation in Proton Exchange Membrane Fuel Cells. *Journal of Power Sources* **2009**, *194* (2), 588–600.

(101) Du, L.; Shao, Y.; Sun, J.; Yin, G.; Liu, J.; Wang, Y. Advanced Catalyst Supports for PEM Fuel Cell Cathodes. *Nano Energy* **2016**, *29*, 314–322.

(102) Meier, J. C.; Galeano, C.; Katsounaros, I.; Witte, J.; Bongard, H. J.; Topalov, A. A.; Baldizzone, C.; Mezzavilla, S.; Schüth, F.; Mayrhofer, K. J. J.; De. Design Criteria for Stable Pt/C Fuel Cell Catalysts. *Beilstein J. Nanotechnol.* **2014**, *5*, 44–67.

(103) Wang, J.; Yin, G.; Shao, Y.; Wang, Z.; Gao, Y. Investigation of Further Improvement of Platinum Catalyst Durability with Highly Graphitized Carbon Nanotubes Support. *The Journal of Physical Chemistry C* **2008**, *112* (15), 5784–5789.

(104) Wang, D. D.; Wu, G.; Zhang, C.; Yin, F.; Su, L.; Shrestha, S.; Zhang, Z.; Mustain, W. E.; Lei, Y.; Shao, Y.; Kou, R.; Wang, J. N. J.; Wang, C.; Viswanathan, V.; Liu, J.;. Improved Durability of Pt Catalyst Supported on N-Doped Mesoporous Graphitized Carbon for Oxygen Reduction Reaction in Polymer Electrolyte Membrane Fuel Cells. *Applied Catalysis B: Environmental* **2017**, *42* (52), 265–274.

(105) Takei, C.; Kakinuma, K.; Kawashima, K.; Tashiro, K.; Watanabe, M.; Uchida, M. Load Cycle Durability of a Graphitized Carbon Black-Supported Platinum Catalyst in Polymer Electrolyte Fuel Cell Cathodes. *Journal of Power Sources* **2016**, *324*, 729–737.

(106) Meier, J. C.; Galeano, C.; Katsounaros, I.; Topalov, A. A.; Kostka, A.; Schüth, F.; Mayrhofer, K. J. J. Degradation Mechanisms of Pt/C Fuel Cell Catalysts under Simulated Start–Stop Conditions. *ACS Catal.* **2012**, *2* (5), 832–843.

(107) Dubau, L.; Castanheira, L.; Berthomé, G.; Maillard, F. An Identical-Location Transmission Electron Microscopy Study on the Degradation of Pt/C Nanoparticles under Oxidizing, Reducing and Neutral Atmosphere. *Electrochimica Acta* **2013**, *110*, 273–281.

(108) Shao-Horn, Y.; Ferreira, P. J.; La O, G. J.; Morgan, D.; Gasteiger, H.; Makharia, R. Coarsening of Pt Nanoparticles in Proton Exchange Membrane Fuel Cells upon Potential Cycling. In *ECS Transactions*; 2005; Vol. 1, pp 185–195.

(109) Shui, J.; Wang, M.; Du, F.; Dai, L. N-Doped Carbon Nanomaterials Are Durable Catalysts for Oxygen Reduction Reaction in Acidic Fuel Cells. *Science Advances* **2015**, *1* (1), e1400129.

(110) Bokach, D.; ten Hoopen, S.; Muthuswamy, N.; Buan, M. E. M.; Rønning, M. Nitrogen-Doped Carbon Nanofiber Catalyst for ORR in PEM Fuel Cell Stack: Performance, Durability and Market Application Aspects. *International Journal of Hydrogen Energy* **2016**, *41* (39), 17616–17630.

(111) Yang, L.; Jiang, S.; Zhao, Y.; Zhu, L.; Chen, S.; Wang, X.; Wu, Q.; Ma, J.; Ma, Y.; Hu, Z. Boron-Doped Carbon Nanotubes as Metal-Free Electrocatalysts for the Oxygen Reduction Reaction. *Angewandte Chemie* **2011**, (50), 7132-7135

(112) Ye, J.-S.; Wen, Y.; De Zhang, W.; Cui, H.-F.; Ming Gan, L.; Qin Xu, G.; Sheu, F.-S. Application of Multi-Walled Carbon Nanotubes Functionalized with Hemin for Oxygen Detection in Neutral Solution. *Journal of Electroanalytical Chemistry* **2004**, *562* (2), 241–246.

(113) Liu, J.; Takeshi, D.; Sasaki, K.; Lyth, S. M. Platinum-Decorated Nitrogen-Doped Graphene Foam Electrocatalysts. In *Fuel Cells*; John Wiley and Sons Ltd, 2014; Vol. 14, pp 728–734.

(114) Imran Jafri, R.; Rajalakshmi, N.; Ramaprabhu, S. Nitrogen Doped Graphene Nanoplatelets as Catalyst Support for Oxygen Reduction Reaction in Proton Exchange Membrane Fuel Cell. *Journal of Materials Chemistry* **2010**, *20* (34), 7114–7117.

(115) Chen, Z. Z.; Higgins, D.; Tao, H.; Hsu, R. S.; Chen, Z. Z. Highly Active Nitrogen-Doped Carbon Nanotubes for Oxygen Reduction Reaction in Fuel Cell Applications. *Journal of Physical Chemistry C* **2009**, *113* (49), 21008–21013.

(116) Galeano, C.; Meier, J. C.; Soorholtz, M.; Bongard, H.; Baldizzone, C.; Mayrhofer, K. J. J.; Schüth, F. Nitrogen-Doped Hollow Carbon Spheres as a Support for Platinum-Based Electrocatalysts. *ACS Catal.* **2014**, *4* (11), 3856–3868.

(117) Dlamini, M. W.; Phaahlamohlaka, T. N.; Kumi, D. O.; Forbes, R.; Jewell, L. L.; Coville, N. J. Post Doped Nitrogen-Decorated Hollow Carbon Spheres as a Support for Co Fischer-Tropsch Catalysts. *Catalysis Today* **2020**, *342*, 99–110.

(118) Phaahlamohlaka, T. N.; Kumi, D. O.; Dlamini, M. W.; Forbes, R.; Jewell, L. L.; Billing, D. G.; Coville, N. J. Effects of Co and Ru Intimacy in Fischer−Tropsch Catalysts Using Hollow Carbon Sphere Supports: Assessment of the Hydrogen Spillover Processes. ACS Catal. **2017**, 7(3), 1568–1578

(119) Jiang, S.; Zhu, C.; Dong, S. Cobalt and Nitrogen -Cofunctionalized Graphene as a Durable Non-Precious Metal Catalyst with Enhanced ORR Activity,. *Journal of Materials Chemistry A* **2013**, *1* (11), 3593–3599.

(120) Zhang, C.; Xu, L.; Shan, N.; Sun, T.; Chen, J.; Yan, Y. Enhanced Electrocatalytic Activity and Durability of Pt Particles Supported on Ordered Mesoporous Carbon Spheres. *ACS Catal.* **2014**, *4* (6), 1926–1930.

(121) Liu, K.; Kattel, S.; Mao, V.; Wang, G. Electrochemical and Computational Study of Oxygen Reduction Reaction on Nonprecious Transition Metal/Nitrogen Doped Carbon Nanofibers in Acid Medium. *J. Phys. Chem. C* **2016**, *120* (3), 1586–1596.

(122) Huang, B.; Peng, L.; Yang, F.; Liu, Y.; Xie, Z. Improving ORR Activity of Carbon Nanotubes by Hydrothermal Carbon Deposition Method. *Journal of Energy Chemistry* **2017**, *26* (4), 712–718.

(123) Phaahlamohlaka, T. N.; Kumi, D. O.; Dlamini, M. W.; Forbes, R.; Jewell, L. L.; Billing, D. G.; Coville, N. J. Effects of Co and Ru Intimacy in Fischer–Tropsch Catalysts Using Hollow Carbon Sphere Supports: Assessment of the Hydrogen Spillover Processes. *ACS Catalysis* **2017**, *7* (3), 1568–1578.

(124) Li, D.; Feng, C.; Liu, H. K.; Guo, Z. Hollow Carbon Spheres with Encapsulated Germanium as an Anode Material for Lithium-Ion Batteries. *Journal of Materials Chemistry A* **2015**, *3* (3), 978–981.

(125) Bo, X.; Bai, J.; Ju, J.; Guo, L.; Chen, H. R. H. G.; Shi, J. L.; Li, Y. S.; Yan, J. N.; Toward Highly Stable Electrocatalysts via Nanoparticle Pore Confinement. *Journal of Power Sources* **2012**, *134* (1), 16664–16669.

(126) Shi, R.; Wang, J.; Zhao, J.; Liu, S.; Hao, P.; Li, Z.; Ren, J. Cu Nanoparticles Encapsulated with Hollow Carbon Spheres for Methanol Oxidative Carbonylation: Tuning of the Catalytic Properties by Particle Size Control. *Applied Surface Science* **2018**, *459* (79), 707–715.

(127) Kang, L.; Zhu, M. An Efficient Au Catalyst Supported on Hollow Carbon Spheres for Acetylene Hydrochlorination. *RSC Advances* **2019**, *9* (55), 31812–31818.

(128) Liu, P.; Yang, D.; Chen, H.; Gao, Y.; Li, H. Discrete and Dispersible Hollow Carbon Spheres for PtRu electrocatalyst Support in DMFCs. *Electrochimica Acta* **2013**, *109*, 238–244.

(129) Dai, X. Y.; Zhang, X.; Meng, Y. F.; Shen, P. K. Preparation of Hollow Carbon Spheres by Carbonization of Polystyrene/Polyaniline Core-Shell Polymer Particles. *Xinxing Tan Cailiao/New Carbon Materials* **2011**, *26* (5), 389–395.

(130) Hassan, M.; Qiu, W.; Song, X.; Mao, Q.; Ren, S.; Hao, C. Supercapacitive and ORR Performances of Nitrogen-Doped Hollow Carbon Spheres Pyrolyzed from Polystyrene@polypyrrole-Polyaniline. *Journal of Alloys and Compounds* **2020**, *818*, 152890–152890.

(131) Hu, F. P.; Wang, Z.; Li, Y.; Li, C.; Zhang, X.; Shen, P. K. Improved Performance of Pd Electrocatalyst Supported on Ultrahigh Surface Area Hollow Carbon Spheres for Direct Alcohol Fuel Cells. *Journal of Power Sources* **2008**, *177* (1), 61–66.

(132) Lamer, V. K.; Dinegar, R. H. Theory, Production and Mechanism of Formation of Monodispersed Hydrosols. *Journal of the American Chemical Society* **1950**, *72* (11), 4847–4854.

(133) Stöber, W.; Fink, A.; Bohn, E. Controlled Growth of Monodisperse Silica Spheres in the Micron Size Range. *Journal of Colloid and Interface Science* **1968**, *26* (1), 62–69.

(134) Büchel, G.; Unger, K. K.; Matsumoto, A.; Tsutsumi, K. A Novel Pathway for Synthesis of Submicrometer-Size Solid Core/Mesoporous Shell Silica Spheres. *Advanced Materials* **1998**, *10* (13), 1036–1038.

(135) Su, F.; Zhao, X. S.; Wang, Y.; Wang, L.; Lee, J. Y. Hollow Carbon Spheres with a Controllable Shell Structure. *J. Mater. Chem.* **2006**, *16* (45), 4413.

(136) Chen, A.; Yu, Y.; Lv, H.; Wang, Y.; Shen, S.; Hu, Y.; Li, B.; Zhang, Y.; Zhang, J. Thin-Walled, Mesoporous and Nitrogen-Doped Hollow Carbon Spheres Using Ionic Liquids as Precursors. *Journal of Materials Chemistry A* **2013**, *1* (4), 1045–1047.

(137) Tang, J.; Liu, J.; Salunkhe, R. R.; Wang, T.; Yamauchi, Y. Nitrogen-Doped Hollow Carbon Spheres with Large Mesoporous Shells Engineered from Diblock Copolymer Micelles. *Chemical Communications* **2016**, *52* (3), 505–508.

(138) Yan, Z.; Hu, Z.; Chen, C.; Meng, H.; Shen, P. K.; Ji, H.; Meng, Y. Hollow Carbon Hemispheres Supported Palladium Electrocatalyst at Improved Performance for Alcohol Oxidation. *Journal of Power Sources* **2010**, *195* (21), 7146–7151.

(139) Liu, H.; Zhou, X.; Wang, F.; Ji, J.; Liu, J.; Li, Z.; Jia, Y. Hollow Carbon Hemisphere with Controlled Morphology as Support Material for Platinum Nanoparticle Catalyst towards the Methanol Electro-Oxidation. *Materials Research Bulletin* **2014**, *57*, 280–286.

(140) Jukk, K.; Kongi, N.; Rauwel, P.; Matisen, L.; Tammeveski, K. Well-Dispersed Platinum Nanoparticles Supported on Hierarchical Nitrogen-Doped Porous Hollow Carbon Spheres with Enhanced Activity and Stability for Methanol Electrooxidation. *Journal of Power Sources* **2016**, *8* (5), 220–222.

# Chapter 2

# Experimental procedures for the synthesis and characterization of the carbon supports and the Pt/carbon catalysts

## 2.1: Summary of Chapter Content

Various synthesis techniques were used to produce large and small spherical silica particles. The method developed by Stober and colleagues was modified in order to produce monodisperse silica particles with low surface area by extensive cross linking of the silica reactants used to make the spheres. To obtain small silica particles, dilute reagents were used. However, the concentration of reagents had to be optimum to ensure formation of spherical particles.

HCSs and NHCSs were synthesized using the hard-templating method whereby the large silica was used as sacrificial templates. Among the many carbon coating methods, the resorcinol – formaldehyde coating process was preferred for use in this study due to its simplicity and the high quality of HCSs produced. NHCSs were synthesized using a simple post synthesis doping method using a nitrogen rich precursor, melamine.

Similar methodology was used for the formation of the hemispherical broken bowl-like hollow carbon spheres (BHCSs) and broken nitrogen doped bowl-like hollow carbon spheres

(BNHCSs). The spherical carbon and hemispherical carbon support synthesized were used as supports for Pt using a simple deposition method called metal-organic deposition.

The physico-chemical properties of the catalysts were evaluated using transmission electron microscopy (TEM), scanning electron microscopy (SEM), dark field scanning tunneling electron microscopy (DF-STEM), thermogravimetric analysis (TGA), nitrogen gas physisorption (BET), powder X-ray diffraction (PXRD), X-ray photo-electron spectroscopy (XPS) and Raman spectroscopy. The electrochemical activity and durability of the Pt-carbon materials were evaluated using cyclic voltammetry and linear sweep voltammetry using a glass cell and a three electrodes setup.

## 2.2: Synthesis of large silica templates

All the silica spheres were synthesized according to a method reported by Stober and colleagues.[1] Silica powders were formed by the hydrolysis and condensation of alkyl-alkoxides. The reagents for the hydrolysis and condensation reactions were ethanol (EtOH, Sigma Aldrich, 99.99%), deionized water (DIW) and tetraethyl-orthosilicate (Sigma Aldrich, 98%). Ammonia ($NH_4OH$, Fluka, 25%) was required for the control of spherical morphology and to facilitate hydrolysis and condensation.[2,3]

To synthesize less porous and large $SiO_2$ spherical particles, the solvent EtOH (390 mL) was mixed with DIW (50 mL) in a round bottom flask (1 L) mounted on a magnetic stirrer. The TEOS (50 mL) was added 'all at once' followed by stirring for 30 minutes for thorough mixing. To the above mixture was added 25% $NH_4OH$ (30 mL) followed by sealing of the round bottom flask with three layers of parafilm to prevent any evaporation of the $NH_4OH$ solution.

The solution was stirred vigorously for 6 h whereby the solution changed from an off-white color to a deep white color of suspended silica colloids. After 6 h the silica was centrifuged at 18 000 rpm for a total of 30 minutes. The silica was washed with 200 mL of a solution of

ethanol and water, 50:50 vol.% followed by a DIW wash and centrifugation. The silica powder was dried in an oven at 100°C overnight followed by calcination at 500°C in an oven. The white silica powders were weighed amounting to 22.6 g, equivalent to a 68% yield. The silica powders were characterized using SEM for morphology determination and particle size distribution. Also, the silica was characterized by BET analysis for the determination of textual properties.

## 2.3: Synthesis of small silica templates

In a typical synthesis, EtOH (1.2 L) was mixed with TEOS (50 mL) and DIW (50 mL) and allowed to stir on a magnetic stirrer for 30 minutes. After thorough mixing, to this solution was added 25% ammonia solution catalyst (30 mL) followed by stirring for 6 h. The reaction vessel was sealed with parafilm to prevent the room temperature evaporation of ammonia solution. The solution changed from an off-white to a deep white color as the yield of the formed silica product increased. The silica particles were separated from solution by centrifugation at 18 000 rpm. The silica was further washed with 200 mL of a 50:50 vol% EtOH/DIW solution and centrifugation at the same rpm. The silica was further washed with 100 mL of DIW and allowed to dry in an oven at 100°C overnight. The silica was placed in a ceramic crucible and calcined at 500°C in air in an oven for 5 h. The white silica powder yield was 8.5 g amounting to 60 % product yield. The silica particles were characterized using SEM for the calculation of particle size distribution and BET for textual properties.

## 2.4: Synthesis of hollow carbon spheres (HCSs)

HCSs were synthesized using the resin polymerization method using resorcinol-formaldehyde. The method was adopted due to its ease of application as well as the ability to fine tune the product properties.[4]

In a typical synthesis 3 g of finely ground silica particles were placed in a 1 L round bottom flask mounted in a sonicator followed by the addition of a solution of absolute EtOH (210 mL) and DIW (45 mL). The silica was thoroughly dispersed in solution by sonication for 10 min followed by the addition a solution of resorcinol (1 g) (Sigma Aldrich) plus 1 mL of formaldehyde (Sigma Aldrich, 37%) and subsequent sonication for 10 minutes. Cetyl trimethylammonium bromide (CTAB; 2 g) (Sigma Aldrich), a surfactant and porogen was added to the mixture plus 25% ammonia solution (10 mL). The reaction vessel was sealed using 3 layers of parafilm followed by sonication for another 30 minutes whereupon the temperature of the sonication bath was increased from room temperature to ca. 50°C. During this time the reactor contents changed from white to pale brown due to the formation of the resorcinol-formaldehyde (RF) resin that covered each silica particle. The reactor was placed on a magnetic stirrer for 24 h at room temperature whereby the color intensity of the reactor contents intensified from light brown to deep brown as the concentration of the $SiO_2$@RF product increased.

After 24 h the $SiO_2$@RF was filtered under vacuum with frequent washing with DIW (200 ml) followed by drying at 100°C in an oven for 4 h. The brown $SiO_2$@RF powders were placed in a quartz boat in a tubular furnace set at 900°C and a nitrogen flow rate of 50 $ml.min^{-1}$. The tubular furnace was ramped at a heating rate of 10°$C.min^{-1}$ for 90 minutes followed by holding it at 900°C for another 2 h. The furnace cooled naturally overnight. The carbon soot was etched with 200 mL of a 10% hydrofluoric acid (HF) (Sigma Aldrich, 48%) solution placed in a designated fume-hood for 24 h without stirring to avoid breakage of the HCS shells. The formed HCSs were filtered and washed 5 times with 2 L of DIW to remove the excess HF and other impurities. The HCSs were dried in an oven at 100°C overnight followed by annealing in a tubular furnace (Figure 2.1) at 900°C for 2 h. For annealing, the furnace was ramped at a heating rate of 10°$C.min^{-1}$ for 90 minutes until it had reached 900 °C. The furnace was held at

900°C for a further 120 minutes and cooled to room temperature naturally overnight. A yield of 230 mg HCSs was obtained amounting to a yield of 78% based on the amount of resorcinol used.

## 2.5: Synthesis of nitrogen doped hollow carbon spheres (NHCSs)

$SiO_2$@RF (2 g) was mixed with melamine (2 g) (Sigma Aldrich) followed by dry sonication for 30 minutes. The dry powder mixture of melamine and $SiO_2$@RF was annealed at 900°C for 120 minutes. The furnace was ramped at a heating rate of 2.5°C/min for 6 h followed by a 120 minutes hold at the same temperature. The furnace was cooled naturally overnight followed by removal of the silica by etching of the formed nitrogen doped carbon shell. The material was etched in a 10% HF solution for 24 h. The NHCSs were filtered under vacuum and washed with 2 L of DI to remove contaminants and reagents. The NHCSs were dried in an oven set at 80 ℃ for 2 h and weighed. The yield of the formed NHCs was 280 mg amounting to 73% yield based on the amount of resorcinol used. The NHCSs were annealed in a similar manner as performed for the HCSs.[5]

## 2.6: Synthesis of Pt/HCSs - metal organic deposition route

The supports were loaded with Pt nanoparticles of a nominal 40 wt.% Pt/HCSs and 40 wt.% Pt/NHCSs. Pt was loaded onto the supports according to a metal-organic deposition technique. [6] In a typical synthesis, 100 mg of HCSs or NHCSs were mixed with 200 mg of platinum acetylacetonate ($Pt(acac)_2$, Sigma Aldrich, 97%) and dry sonicated for 30 minutes to allow for homogeneous mixing. During the sonication period, some of the $Pt(acac)_2$ penetrated the pore system of the supports and becomes lodged therein.

The Pt precursor-support mixture was loaded into a steel cylindrical reactor (Figure 2.1) followed by sealing both ends and connection to an argon line. The cylindrical reactor loaded

with the mixture was placed in a tubular furnace (Figure 2.1) and the reaction was allowed to proceed. The furnace was ramped at a heating rate of 2.5 °C.min$^{-1}$ until it reached 100°C followed by a 30 min hold at the same temperature to drive off moisture. The furnace was further ramped up at 2.5 °C/min until it reached 350°C followed by a 120 min hold at the same temperature.

Argon gas was flowed through the cylindrical reactor at a flow rate of 50 ml.min$^{-1}$ for the duration of the reaction. The furnace was cooled naturally overnight. The formed Pt/HCSs was weighed (155.8 mg) catalyst amounting to 93% yield. The 7% loss was attributed to losses due to sample transfer and weighing.

## 2.7: Synthesis of Pt/NHCSs - metal organic deposition route

The synthesis of the Pt/NHCSs used the same synthesis process as that used to make Pt/HCSs.[7] In a typical synthesis, 150 mg of $Pt(acac)_2$ was mixed in a borosilicate vial and dry sonicated with 100 mg of NHCS. The mixture was sonicated for 30 minutes followed by loading into a cylindrical steel reactor. The reactor was attached to an argon gas line and loaded into a tubular furnace. The furnace was ramped at 2.5 °C.min$^{-1}$ until it reached 100 °C followed by a 30 min hold at the same temperature to drive off moisture. The furnace was further ramped up at 2.5°C. min$^{-1}$ until it reached 350 °C followed by a 120 min hold at the same temperature. The furnace and reactor were allowed to cool to room temperature overnight. The Pt/NHCSs sample was weighed (150.3 mg) amounting to 90 % yield.

## 2.8: Synthesis of Pt/HCS and Pt/NHCS – the ethanol reflux route

Typically, 100 mg of HCSs or NHCSs are dispersed in 200 mL of ethanol in a round bottom flask. To this solution was added 135 mg of $Pt(acac)_2$ and the mixture was sonicated for 30 min to allow for thorough mixing. Meanwhile, under reflux, the round bottom flask was mounted

in an oil bath heater and the reaction was ramped to 100 ℃ and kept isothermal for 30 min to allow for the removal of moisture from the reaction. The oil bath temperature was increased to 250 ℃ at a heating rate of 5℃/min and kept isothermal for 1 h. The reaction was allowed to cool to room temperature, the products filtered under vacuum and washed with 500 mL of deionized water. The products were dried at 80 ℃ followed by characterization. The weighed Pt/HCSs and Pt/NHCSs amounting to 148.5 mg and 149.2 mg amounted to 91 % and 90 % yield respectively.

## 2.9: Synthesis of small broken bowl like hollow carbon spheres (BHCSs)

Small broken bowl like hollow carbon spheres were synthesized from small silica particles with a size between 40 – 100 nm. The synthesis procedure followed the same path used for the synthesis of HCSs.

In a typical synthesis a solution of EtOH (280 mL) and DI (60 mL) was mixed with $SiO_2$ (4 g). To the mixture was added CTAB (2 g) and a solution of 37% formaldehyde (1.5 ml) and resorcinol (1.5 g) under sonication. A 25% $NH_4OH$ solution (10 mL) was added and the system stirred magnetically.

The solution turned from an off-white color to brown with stirring. After 24 h the $SiO_2$@RF was filtered and washed with copious amounts of DIW followed subsequently by drying in an oven overnight at 100°C and carbonization in a tubular furnace under argon flow at 900°C.

The carbonization, etching and annealing process was similar to that used for the synthesis of HCSs and NHCSs discussed above. Typically, the $SiO_2$@RF (200 mg) in a quartz boat was placed in a tubular horizontal furnace connected to an argon gas line flowing at 50 $ml.min^{-1}$.

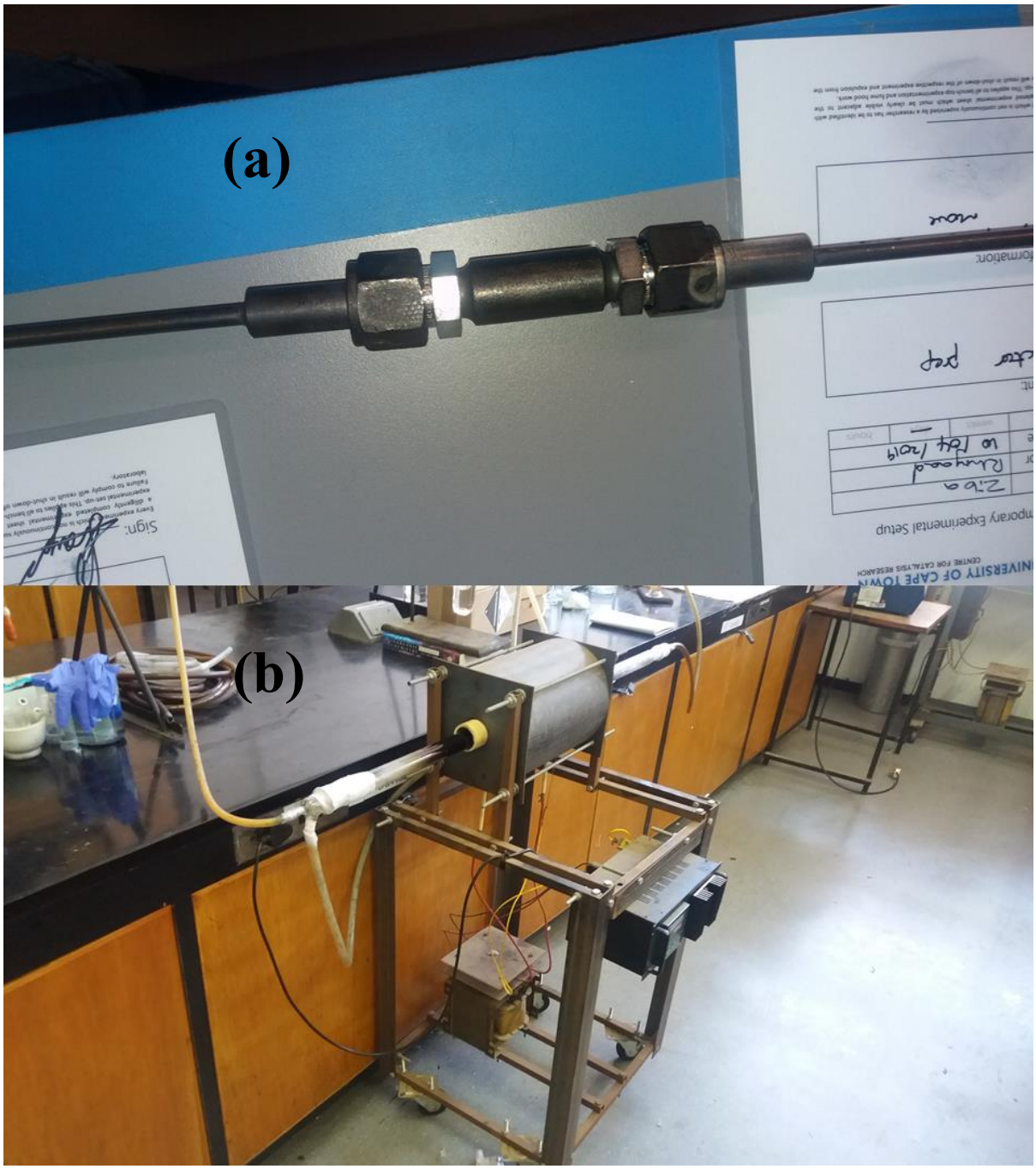



Figure 2.1: Steel cylindrical reactor (a), Horizontal tubular furnace used for Pt deposition, carbonization of $SiO_2$@RF and annealing of HCSs and NHCSs (b).

The furnace was ramped up to 900 ℃ at a heating rate of 10℃.min$^{-1}$ and held at the same temperature for 2 h followed by a natural cooling process overnight. The formed black soot $SiO_2$@C was etched to remove the silica using a 10% HF solution (200 ml) for 24 h. The

solution was vacuum filtered, washed with 500 ml of DI and dried in an oven at 80 ℃. The formed BHCSs were annealed in a tubular horizontal furnace at 900 ℃ for 2 h at a heating rate of 10℃.min$^{-1}$ and an argon flow rate of 50 ml.min$^{-1}$. The yield of the BHCS was 223.5 mg amounting to a 88% yield based on the amount of resorcinol used.

The synthesis process to make nitrogen doped broken bowl like hollow carbon spheres was similar to that used for the synthesis of NHCSs discussed above. Typically, 3 g of $SiO_2$@RF was mixed with 3 g of melamine in a borosilicate vial filled with methanol (20 ml). The composite was sonicated for 30 minutes followed by drying in an oven set at 80 ℃. The composite of melamine and $SiO_2$@RF was carbonized at 900 ℃ for 2 h using a heating rate of 10℃.min$^{-1}$ followed by etching to remove the silica with a 10% HF solution (200 mL) for 24 h. The materials were filtered and washed with DI (500 mL) followed by drying at 80℃ in an oven. The BNHCSs were annealed at 900 ℃ for 2 h at a heating rate of 10 ℃. min$^{-1}$ and an argon flow rate of 50 ml.min$^{-1}$. The yield of the BHCSs was 238.3 mg amounting to a 78 % yield based on the amount of resorcinol used.

Deposition of Pt nanoparticles on top of the BHCSs and BNHCSs was similar to that used for the Pt deposition on HCSs and NHCSs. Typically, BHCSs or BNHCSs (100 mg) was mixed with $Pt(acac)_2$ (200 mg) and sonicated for 10 min to allow for thorough mixing. The composite was then transferred into a cylindrical steel reactor which was placed in a tubular horizontal furnace. The furnace was ramped to 100 ℃ and kept for 30 min to drive moisture off the sample. The furnace was further ramped up to 350 ℃ at a heating rate of 2.5 ℃. min$^{-1}$ followed by a 2 h hold at the same temperature while the reaction continued. The reactor was allowed to cool naturally, and the products weighed. The Pt/BHCSs and Pt/BNHCSs produced a yield of 160.9 mg and 155.7 mg amounting to yields of 95.8% and 93.2% respectively.

## 2.10: Electrochemical analysis

The formed catalysts were tested in electrochemical reactions for oxygen reduction reaction activity and durability.

## 2.10.1: Cyclic Voltammetry (CV)

Cyclic voltammetry was used to measure the ECSA of the Pt-catalysts synthesized in this work. CV is a potentiodynamic technique whereby the potential of the working electrode (WE) is swept between two points while at the same time the current response is measured. The current response measured is a result of electrochemical processes that are being pushed or activated by the applied potential. [8] The WE was made up of a catalyst paste deposited on a glassy carbon electrode (GCE) mounted to a rotator shaft connected to the potentiostat. CV provides information about the electrochemical processes occurring on the catalyst active sites. Lower activation energy reactions occur at lower potentials with the underpotential deposition of protons on a Pt surface being a good example. The evolution of oxygen is a high activation energy process, hence the high activation potential required to activate it.[9]

The CV profile of a typical Pt/C catalyst in acidic media is shown in Figure 2.2.[10] Reversible hydrogen adsorption and desorption occurs at potentials between 0 – 0.5 V vs. RHE and is attributed to the underpotential deposition of a monolayer of protons on the surface of the Pt in the cathodic potential sweep.[11] The desorption of the monolayer of protons occurs in the same potential window during the anodic sweep. The numerous facets of a Pt crystal are responsible for the multiple peaks in the proton adsorption-desorption regions.[12] These Pt facets bind with the protons at differing surface sites that have different energy requirements which results in these peaks occurring at differing potentials.

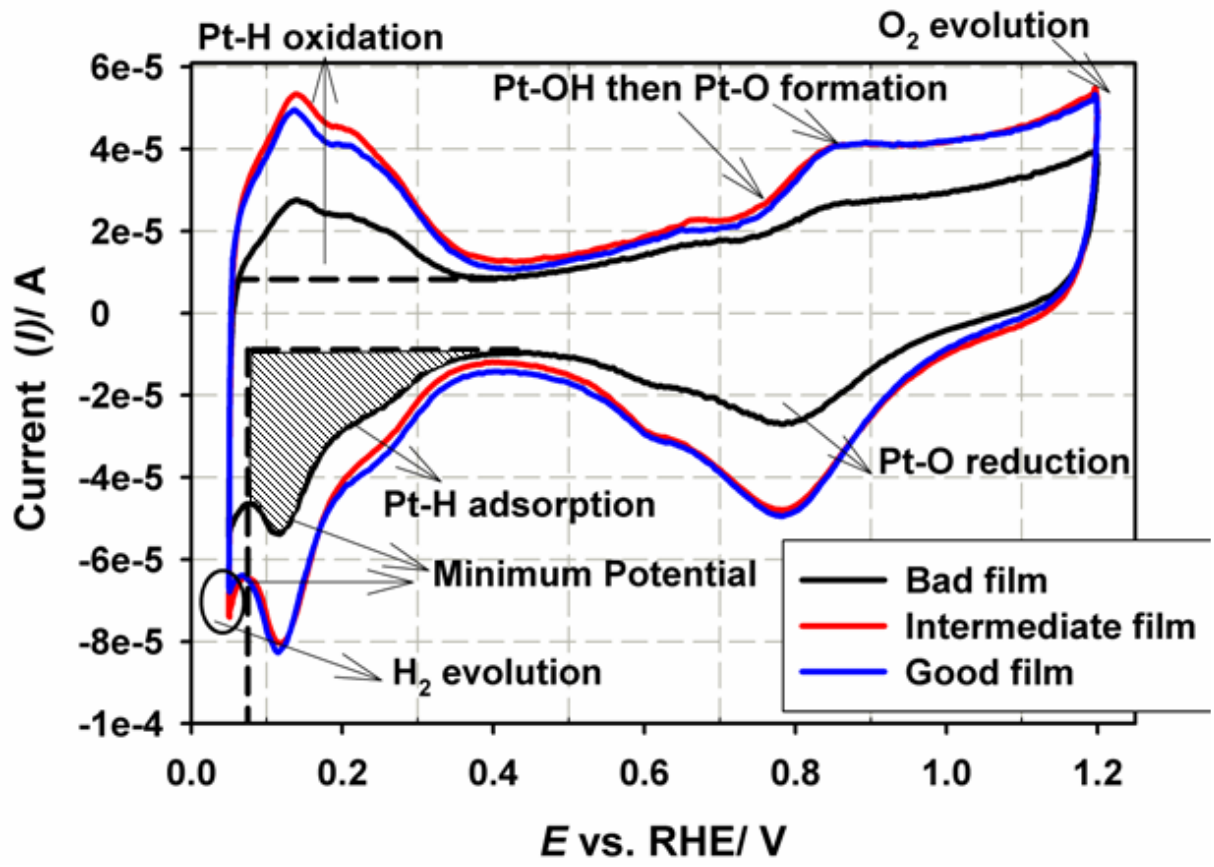



Figure 2.2: Cyclic voltammograms of a Pt/C catalyst of various catalyst film quality.[10]

The region between 0.4 – 0.7 V vs. RHE is featureless because there are no electrochemical processes occurring. In this region the applied potential is not driving a chemical reaction, rather the potential is stored as charge and at this moment the material acts as a double layer capacitor.[13,14] The region between 0.8 – 1.2 V vs. RHE corresponds to the Pt-oxide formation and Pt-oxide reduction.

The Pt catalyst electrochemical active surface area (ECSA) is calculated from the integrated charge associated with the adsorption or desorption of the hydrogen in the 0 – 0.4 V vs RHE region.

The ECSA is calculated according to the Equation (2.1)[10]

$$ECSA\ (m^2.g^{-1}) = (Q_{des}) / (Q_{Pt} \times L_{Pt}) \qquad (2.1)$$

where $Q_{des}$ is the integrated charge due to the desorption of protons from a clean Pt surface. $Q_{Pt}$ is a Pt constant associated with monolayer hydrogen adsorption (210 μC.cm$^{-2}$), and $L_{Pt}$ refers to the loading of Pt per surface area of the glassy carbon electrode.[15]

## 2.10.2: Linear sweep voltammetry – rotating disk electrode.

The catalysts activity towards the oxygen reduction reaction was tested using the hydrodynamic linear sweep voltammetry coupled to a rotating disk. This is a type of electrode which consists of a polytetrafluoroethylene shroud encasing a conductive glassy carbon (GC) cylinder. The top end of the GC cylinder is the working electrode where a catalyst paste of known Pt loading has been pasted. The cylinder is connected to a rotating shaft connected to a potentiostat and rotator for speed control (Figure 2.3). The rotating shaft stirs the electrolyte and in the process pumps fresh, saturated electrolyte to the WE where the catalyst interacts with oxygen from the electrolyte. A diffusion layer is formed at the interface of the WE and the electrolyte. In the diffusion layer there is no convection of the oxygen, rather, the diffusion is the only process responsible for the mass transfer of the oxygen to the WE surface. The thickness of the diffusion layer can be controlled by the rate of the WE rotation. At faster rotation the diffusion layer is thinner whereas at slower rotations, the diffusion layer is thicker.

The mass transfer rate in the diffusion layer is described by a linear form of the Fick's law (Equation 2)[16]

$$J = D(C_0 - C_s)/\delta \qquad (2.2)$$

where J is the mass transfer rate, D is the diffusion coefficient of the transferred ion, $C_0$ is the concentration of the ion in the bulk of the solution, $C_s$ is the concentration of the ion on the surface of the disk and $\delta$ is the thickness of the diffusion layer.

For the RDE the diffusion layer thickness is described by Equation (2.3).[17]

$$\delta = 1.6\ I\ D^{1/3}\ V^{1/6}\ \omega^{-1/2} \qquad (2.3)$$

where, V is the kinematic viscosity of the electrolyte and ω is the rotation rate of the RDE. At the interface between the WE and the electrolyte, the diffusion of the oxygen across the diffusion layer is known as the mass transport and the charge transfer across the interface due to the chemical reactions occurring is a parameter of the kinetics of the chemical reaction.

In mass transfer-controlled reactions, the concentration of the intermediates at the surface of the electrode is zero, i.e. $Cs = 0$. In this kind of reaction, the reaction rate is fast such that any intermediate present is immediately consumed at the WE surface. The current flowing due to

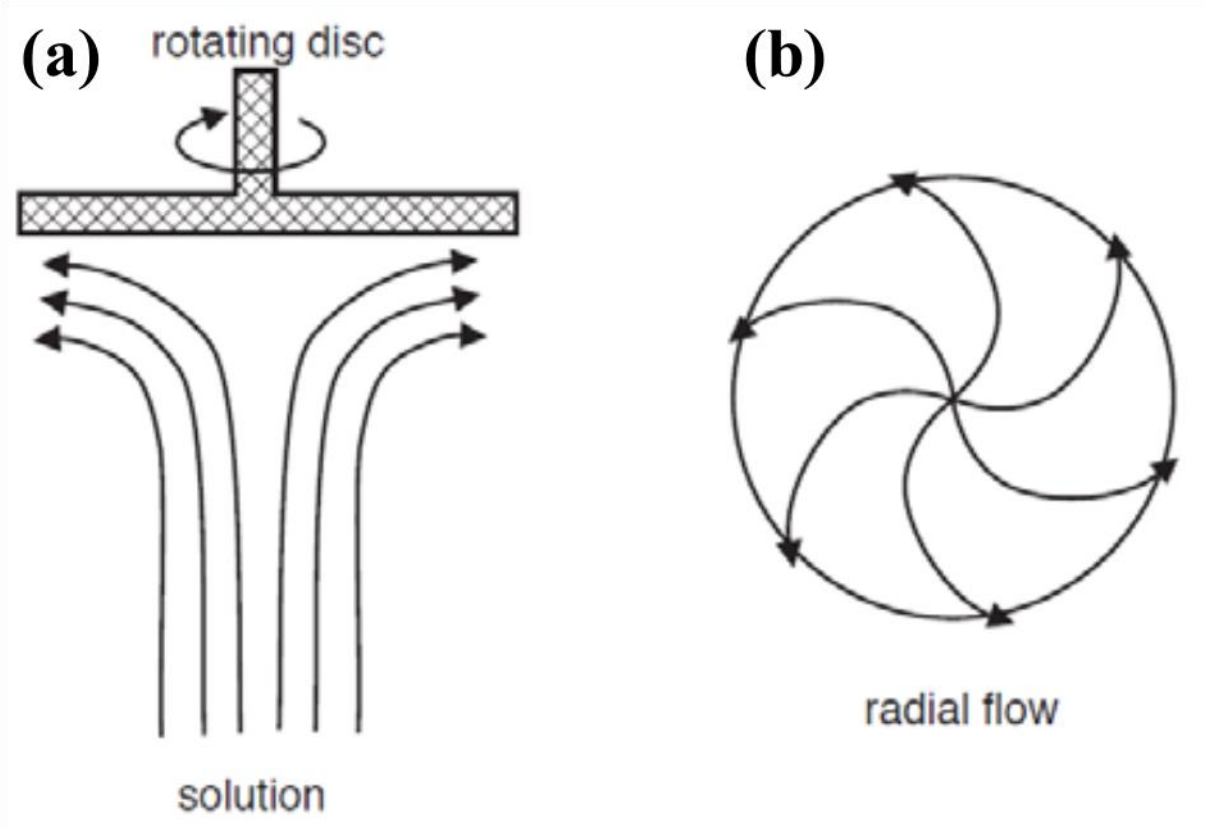



Figure 2.3: (a) Schematic of electrolyte flow towards a RDE surface and (b) electrolyte flow near its surface.

a diffusion process is known as a diffusion limiting current $I_L$ (Figure 2.5). For a combined diffusion-convection driven process, Levich [17] gave an explanatory equation (2.4) of the form -

$$I_L = 0.62zFAD^{2/3}V^{-1/6}\omega^{1/2}C_0 \qquad (2.4)$$

where, F is the Faraday constant (F = 96485 $C.mol^{-1}$) and A is the geometric surface area of the working electrode (GC). In our studies, we used a glassy carbon disk embedded inside a PTFE shroud with a geometric surface are of 0.196 $cm^2$.

Koutecky and Levich formulated the Koutecky-Levich equation[14,18] which describes reactions controlled by both mass transfer and kinetics (Equation 2.5).

$$\frac{1}{I} = (1/I_K) + (1/(0.62\ nFAD^{2/3}V^{-1/6}C\omega^{-1/2}) \qquad (2.5)$$

A plot of 1/I against ($\omega^{-1/2}$) (Figure 2.4) is a straight line with $1/I_k$ is the intercept. The kinetic current is obtained from the intercept.

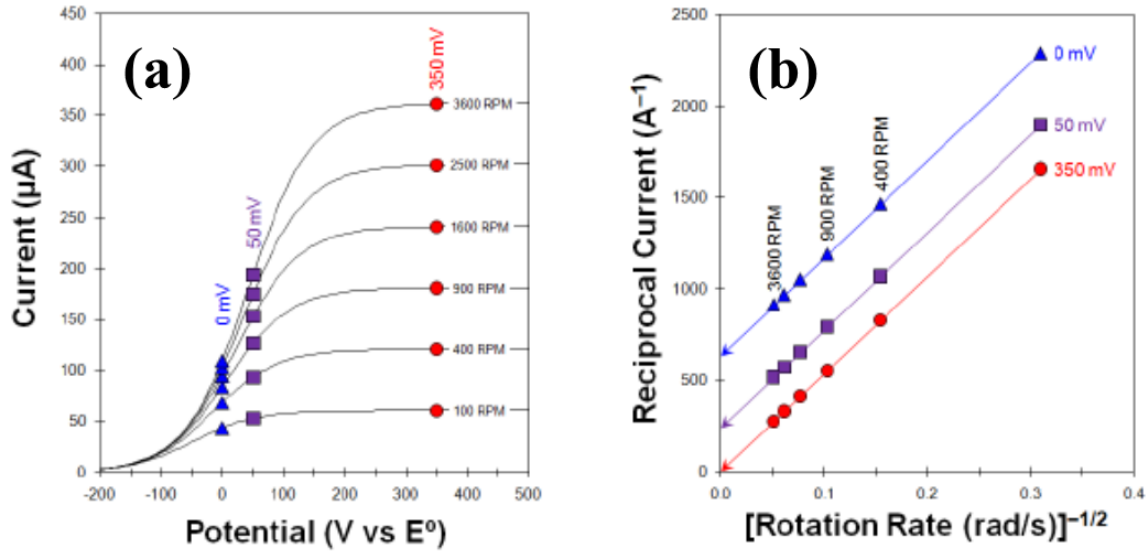



Figure 2.4: (a) Linear sweep voltammograms at various rpm and (b) Koutecky-Levich plot for three different overpotentials.[17]

The kinetic current is the reaction current that would be observed in the absence of mass transport limitations. The standard rate constant for the reactions can be calculated using the kinetic currents at different potentials of the LSV.

## 2.10.3: Preparation of the catalyst ink

The quality of the catalyst paste that is deposited on the WE must be optimized for reproducible, representative data of the catalysts. As shown in the illustration in Figure 2.5, bad films of catalyst paste produce ECSA and ORR data lower in size, when compared to carefully prepared and deposited catalyst pastes.

In a typical preparation, 5 mg of Pt/HCSs was added to a solution of isopropanol (Merck Millipore, HPLC grade; 3.5 mL) and ultrapure water (Merck Millipore, 18.2 $m\Omega.cm^{-2}$; 1.5 mL). Then 20 µL of Nafion perfluorinated resin (Sigma Aldrich, 5 wt% in aliphatic alcohols,) was added to the ink to act as a binder for the catalyst layer. The ink was sonicated for 30 min while maintaining room temperature. Finally, 20 µL of the ink was pipetted onto the GC and allowed to dry under rotation at 400 rpm under a nitrogen stream. The dry WE was immersed into a nitrogen (Afrox, 99.999% purity) saturated 0.1 M $HClO_4$ (perchloric acid) electrolyte. (Merck Suprapur, 70%).[19]

## 2.10.4: Working electrode preparation

The GC electrode was polished using 0.1 µm alumina (Buehler) in a figure eight motion on a polishing cloth (Buehler) for 10 minutes. The polishing cloth was wetted using ultra-pure water.

The polished electrode was rinsed with ultrapure water and sonicated in ultra-pure water for 30 minutes. This was followed by another alumina (0.05 µm) polish and sonication. The electrode was dried under an inverted 50 mL beaker followed by pasting the catalyst layer.[10]

## 2.10.5: Electrochemical cell cleaning

The electrochemical cell, purge tubes, stoppers, bridging tubes, volumetric flasks, beakers and O-rings were placed in a 5 L beaker and immersed into a bucket of prepared Nochromix bath (Gordax Laboratories). The Nochromix was prepared by the mixing of 10 L of concentrated sulfuric acid (Sigma Aldrich, 98%) with a sachet of Nochromix crystals. The glassware remained in the bath for 24 h followed by multiple rinses in ultrapure water. The smaller glassware including the electrochemical cell were loaded into the rinsed 5 L beaker and boiled for 5 h at 100°C. The water was discarded, and all the glassware was rinsed 3 more times with fresh ultrapure water. After all the rinses, all the glassware was stored in an ultrapure water filled 5 L beaker sealed with parafilm until use.

Using the molar weight of perchloric acid and the concentration of the stock solution of 70%, the stock solution is calculated to be 11.595 M with a density of 1.664 $g.mol^{-1}$.

To make a 0.1 M $HClO_4$ solution, 4313 µL of the stock solution was pipetted into a volumetric flask containing 122 mL ultrapure water (18.2 $m\Omega.cm^{-2}$). The solution was swirled for a minute and ultrapure water was used to make up the solution to 500 mL.

The $Hg/HgSO_4$ reference electrode was calibrated by measuring the potential difference between the RHE (reversible hydrogen electrode) and the reference electrode. Firstly 150 mL of 0.1 M $HClO_4$ was poured into the clean electrochemical cell. A clean Pt coil was placed into the cell followed by the saturation of the solution with pure hydrogen gas (Afrox,99.99% purity). The Pt counter electrode was kept under $H_2$ saturation while the voltage difference was recorded using an electrical multimeter. The voltage value was used to convert $Hg/HgSO_4$ values to RHE.

Calculation of the catalyst loading:

For a 39 wt% Pt/C catalyst, 5 mg was used to prepare the working electrode.

$$0.39 \times 5 = 1.95 \text{ mg of Pt}$$

If 5 mg of catalyst was dispersed in a 5 ml (5000 µL) solution of deionized water and isopropanol followed by the extraction of 10 µL ink therefore,

$(10 / 5020) \times 1.95$ mg = mg of Pt deposited on a 0.196 $cm^2$ GC, WE

0.003884462 µg of Pt on a 0.196 $cm^2$ WE GC disk

Therefore = $(1 / 0.196) \times 0.003884462$ $\mu g.cm^{-2}$ and $L_{pt} = 19.82$ $\mu g.cm^{-2}$

As explained above, some reactions are controlled by both mass transport and kinetics. The kinetic region occurs between 0.9 – 1.0 V (Figure 2.5). The region between 0.75 – 1.00 V is the mixed kinetics and diffusion region whereas the diffusion limited current region occurs between 0.20 – 0.70 V. Oxygen evolution occurs at overpotentials above 1.23 V whereas hydrogen evolution occurs at potentials close to 0.0 V. The electrochemical measurements were carried out at 1600 rpm rotation of the WE. The perchloric acid electrolyte was 0.1 M saturated with pure nitrogen for CV measurements and saturated with oxygen for the oxygen reduction reaction. CV measurements were carried out both for ECSA measurements and for accelerated degradation studies.[10,19]

The three-electrode cell system was used for the electrochemical characterization of the catalysts. The three-electrode system consisted of a 200 mL glass electrochemical cell filled with 0.1 M perchloric acid electrolyte. For CV measurements, the electrolyte is saturated with nitrogen or argon. The cell consisted of a $Hg/HgSO_4$ reference electrode, a high surface area counter electrode made of Pt coil plus the GC shrouded in PTFE and connected to a rotator shaft. The catalyst modified electrode was cycled between 0.0 – 1.3 V vs. RHE at a scan rate of 50 $mV.s^{-1}$ and the CVs were recorded. After 50 cleaning cycles, the WE was cycled between 0.05 – 1.2 V vs. RHE at a slow scan rate of 20 $mV.s^{-1}$ three times. The third CV was used for the calculation of the ECSA according to Equation (2.1). After the CVs were recorded the

solution was saturated with pure oxygen (Afrox, 99.99%). While rotating at 1600 rpm, the WE was cycled between 0.05 – 1.2 V vs. RHE. The LSV polarization profile was used in the calculation of the kinetic current (Equation 2.6)[7]

$$I_K = (I_L \times I) / (I_L - I) \qquad (6)$$

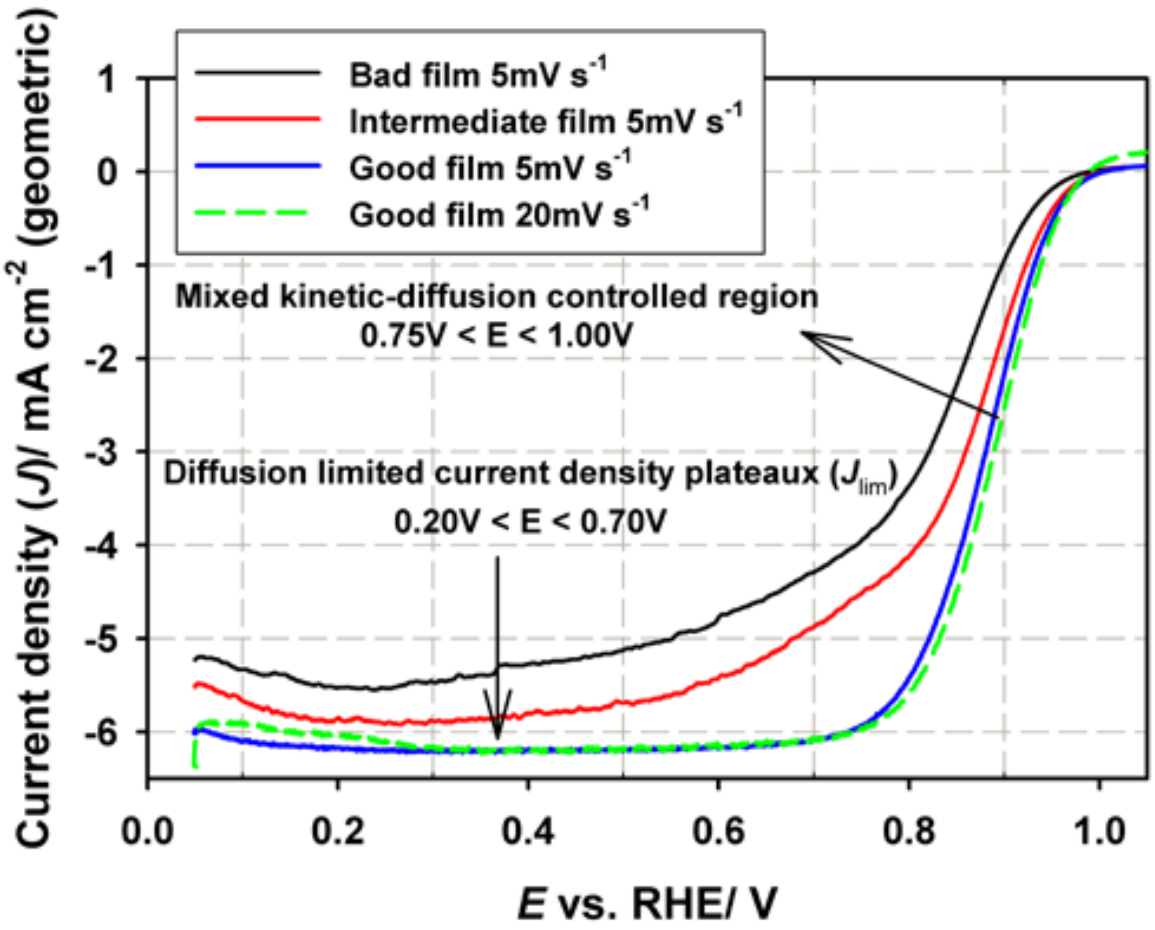



Figure 2.5: ORR polarization profiles for a Pt/C catalyst of different catalyst film quality.[10]

where $I_K$ is the kinetic current, $I_L$ is the diffusion limited current (at E° =0.4 V) and I is the current at 0.9 V vs. RHE (mixed diffusion and kinetic current region).

The Pt mass specific activity (MA) and surface area specific activity (SA) were calculated using the kinetic current. Current readings were carried out at E° = 0.9 V because in this mostly kinetic region, contributions due to mass transport cannot be ignored.

The Pt mass specific activity is the normalization of the kinetic current ($I_K$) with the Pt loading on the GC electrode Lpt (Equation 2.7)[20]

$$MA = \frac{IK(\mu\frac{A}{cm2})}{Lpt(\mu\frac{g}{cm2})} \quad (2.7)$$

The surface area specific activity of the catalyst is obtained by the normalization of the kinetic current with the ECSA (Equation 2.8).[10]

$$SA = \frac{IK(\mu\frac{A}{cm2})}{ECSA(\frac{m2}{g})} \quad (2.8)$$

The mass-transport free kinetic current was used for the calculation of specific and area activity. Electrochemical measurements were executed using a three electrode and cell setup consisting of an electrochemical cell, reference electrode, Pt wire counter electrode and a $Hg/HgSO_4$ reference electrode. The system was coupled with a biologic SP300 potentiostat coupled to a Gamry rotator unit capable rotation of 10 000 rpm (Figure 2.6).



Figure 2.6: Three electrode setup showing RDE box, potentiostat, electrochemical cell and electrodes.

## 2.11: Powder X-ray diffraction (PXRD)

In the technique, X-rays are passed through a sample to determine the crystal structure of materials. Sir W.H. Bragg and his Son Sir W.L. Bragg developed a relationship (Equation 2.9)[21] between the parameters of a crystal and the X- ray diffractogram observed when a measurement is taken. The relationship is as follows:

$$n\lambda = 2d\text{Sin}\Theta \qquad (2.9)$$

where $\Theta$ is the X-ray beam incidence angle, d is the distance between the layers of atoms in a crystal (or lattice spacing), n is an integer and $\lambda$ is the wavelength of the incidence X- ray beam.

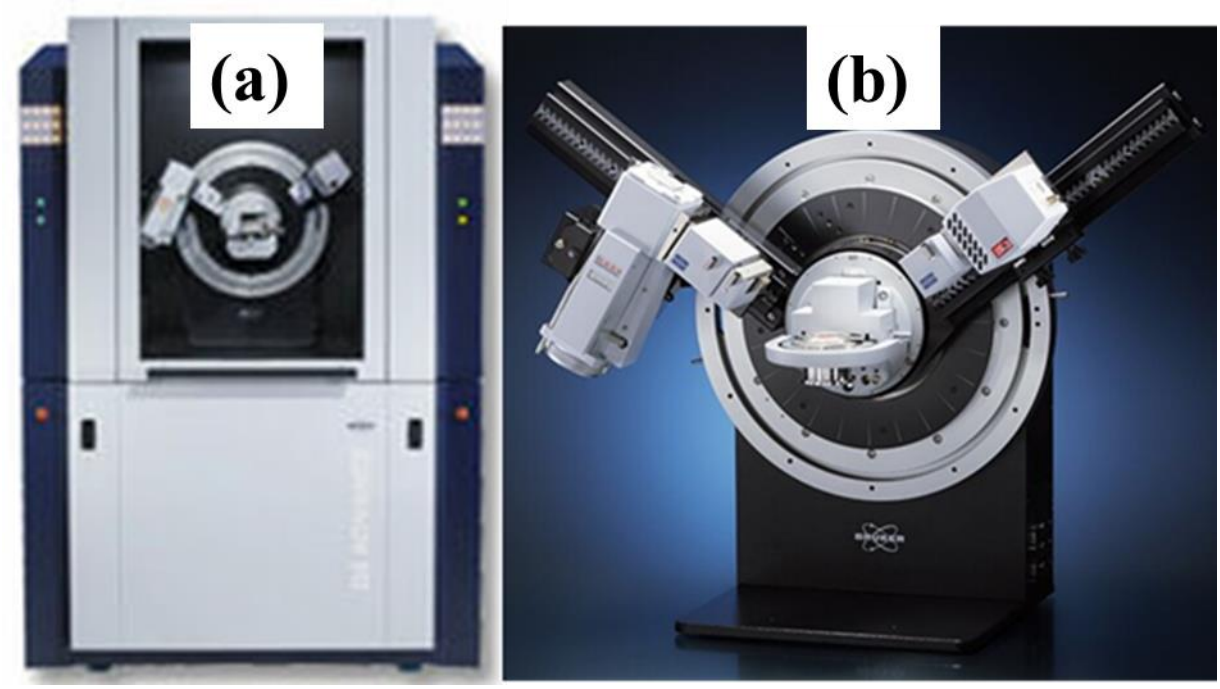



Figure 2.7: D8 Advanced diffractometer (a), Internal components of an X-ray diffractometer (b)

An X-ray diffractometer consists of three main components which are the X-ray tube (source of X-rays), sample holder and X-ray detector. PXRD measurements were carried out on a

Bruker D8 Advance diffractometer (Figure 2.7) with a Cu Kα radiation source operating at 40 kV. Rietveld refinement on the XRD patterns was completed using Bruker AXS TOPAS V 2.8.

## 2.12: Transmission electron microscopy (TEM)

TEM is used for viewing samples in the nanometer size range. In a TEM instrument, a beam of electrons emitted from a source (TEM gun) passes through the sample and interacts with it. The beam that interacts with the sample is focused into an image. Sample preparation involved the dispersion by sonication of 1 mg of the material in 2 ml of ethanol. One droplet of the formed ink was deposited on a copper grid with a lacey carbon film and allowed to dry.

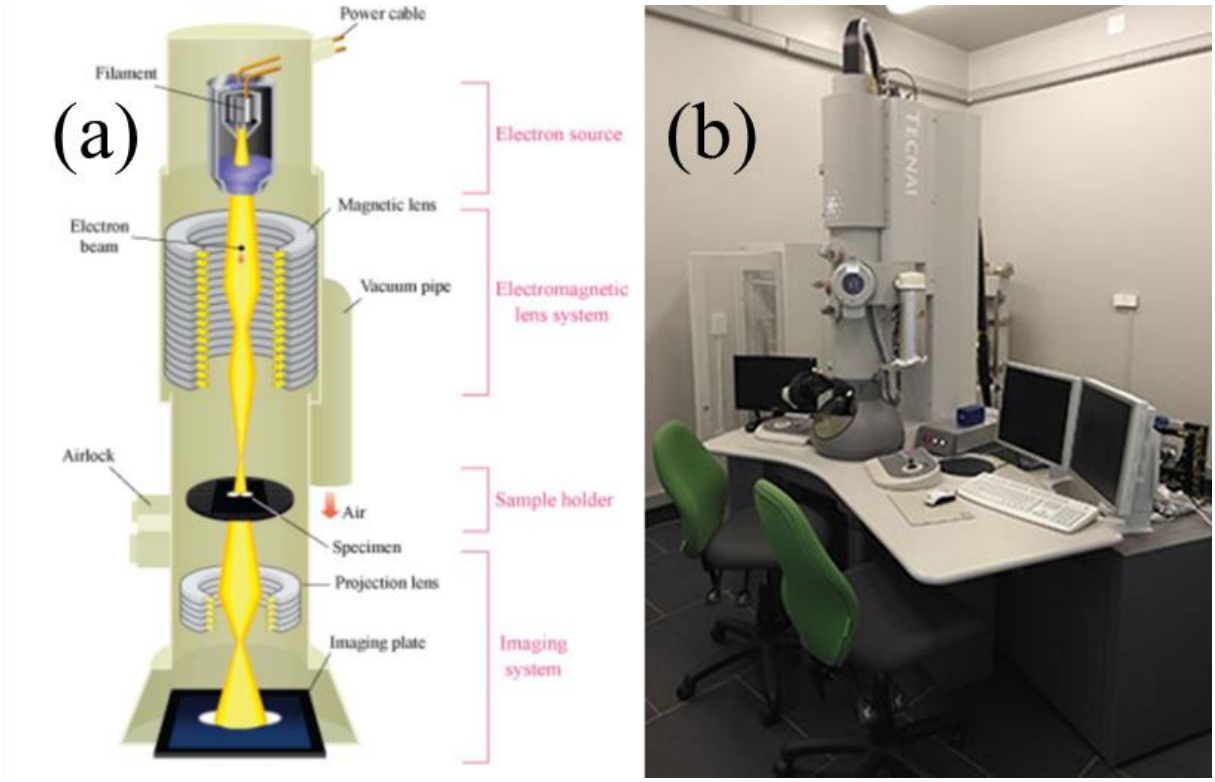



Figure 2.8: (a) Schematic of a TEM and (b) F20 Tecnai transmission electron microscope.[22]

The sample coated copper grid was then loaded into the TEM for viewing. TEM was performed on a Tecnai F20 with a FEG at 200 kV (Figure 2.8) and a Tecnai T12 operating at 120 KV electron microscope operating at 200 kV to determine particle sizes and the morphology of the

catalysts. ImageJ software was used to analyze the particle sizes of the catalysts. About 100 particles per sample were measured to produce particle size histograms.

## 2.13: Scanning electron microscopy (SEM)

In this study, SEM was used to view the morphology of the catalysts. With this technique the surface of the materials could be viewed at high resolution in the experiment. An electron beam of relatively low energy is passed through the specimen just like in TEM. High energy back scattered electrons and low energy secondary electrons from the surface of the sample were then detected and focused to produce an image.

A spatula tip of sample was placed on a double-sided carbon film pasted on an aluminum stub. The sample was sputter-coated with a single layer of graphite and two layers of gold/palladium to reduce the charging effects and enhance the conductivity of the sample. The sample was loaded into the SEM for measurement. SEM data were recorded on a FEI Nova Nanolab 600 microscope operated at a maximum 30 kV and on a Tescan MIRA3 RISE SEM(Figure 2.9) operated also at 30 kV.

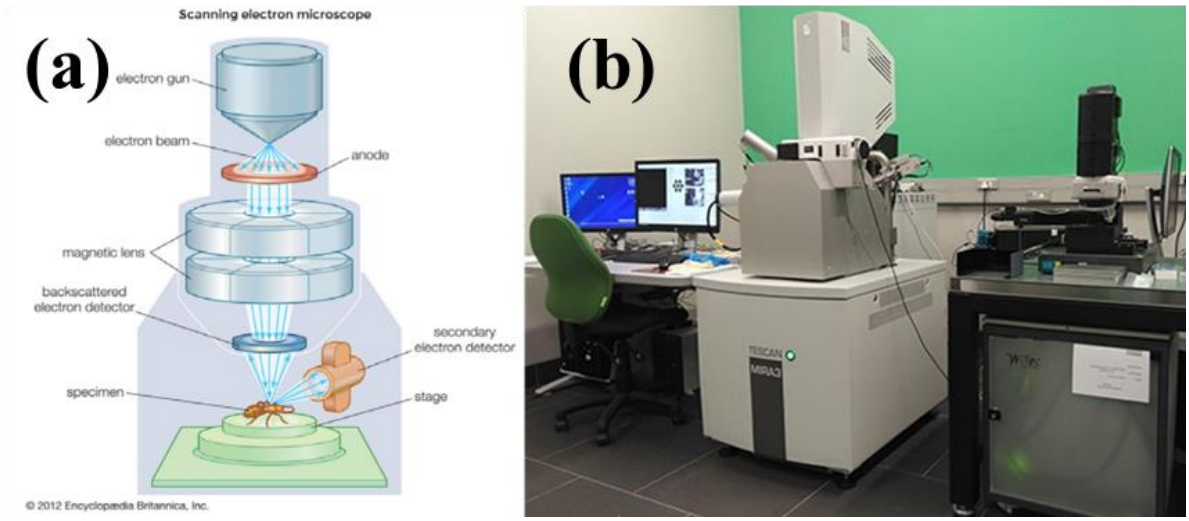



Figure 2.9: (a) Schematic of a SEM and (b)Tescan MIRA3 RISE scanning electron microscope.[23]

## 2.14: BET analysis

Nitrogen physisorption was used to determine the geometric surface area of the materials. In a method devised by Brunaeur, Emmet and Teller (BET), the nitrogen is adsorbed by the material at a certain temperature and relative pressure from a high vacuum to ambient conditions. The method is based on an oversimplified extension of the Langmuir mechanism of multi-layer gas adsorption.[24,25] Nitrogen is passed through the sample at a given temperature and relative pressure and the amount of adsorbed gas is measured. The adsorption process can occur via the chemisorption or by weak van der Waals forces known as physisorption or physical adsorption. BET equations and isotherms were used in the determination of surface area and porosity.

All $N_2$ physisorption measurements were performed under isothermal conditions at -196 °C maintained by using liquid $N_2$. Surface area data were determined in the relative pressure range $P/P_0$ = 0.05-0.30. Pore volumes were determined at a relative pressure of $P/P_0$ = 0.995.




Figure 2. 10: A Tristar 3000 physisorption instrument.

Physisorption experiments were performed on a Tristar 3000 (Figure 2.10) instrument operating at -196 °C, due to the circulation of liquid nitrogen. Prior to measurements, the samples were degassed at 150°C overnight.

## 2.15: Thermogravimetric analysis (TGA)

TGA was used to study the thermal stability of the materials and to confirm the loading of Pt on the catalysts. In a TGA experiment a sample on a microbalance was heated in a chosen temperature range in the presence of a reactive or non-reactive gas at a given flowrate. The technique monitors the change in mass of the sample as a result of the heat/gas treatment and plots a profile. Another profile simultaneously plotted is the derivative weight change with respect to time or temperature. The profiles give data on where significant losses in mass are observed due to either oxidation or decomposition. The residual mass for Pt loaded carbon, analyzed in oxygen for up to 900 °C gives the loading of Pt in wt.% on that catalyst.

To confirm the loading of a nominal 40wt% Pt/HCS catalyst, 10 mg of that sample was loaded to the TGA crucible.



Figure 2.11: A Perkin Elmer STA6000 TGA instrument.

The crucible was placed inside the TGA Perkin Elmer 6000 instrument (Figure 2.11) with oxygen flowing at 10 ml.min$^{-1}$. The TGA reactor cell was heated from room temperature to 900°C at a heating rate of 10°C.min$^{-1}$ The reactor was cooled off under a $N_2$ flow overnight.

## 2.16: Raman spectroscopy

Raman spectroscopy is dependent on a material's ability to scatter monochromatic light inelastically. The scattering ability of the material is dependent on vibrational energy and polarizability of its bonds. Raman spectroscopy can detect and quantify the vibrational modes due to the $sp^2$ and $sp^3$ bonds in carbon. The ratio of the intensity of the $sp^2/sp^3$ bonds describes properties like defect density and graphitization extent.[26–28]

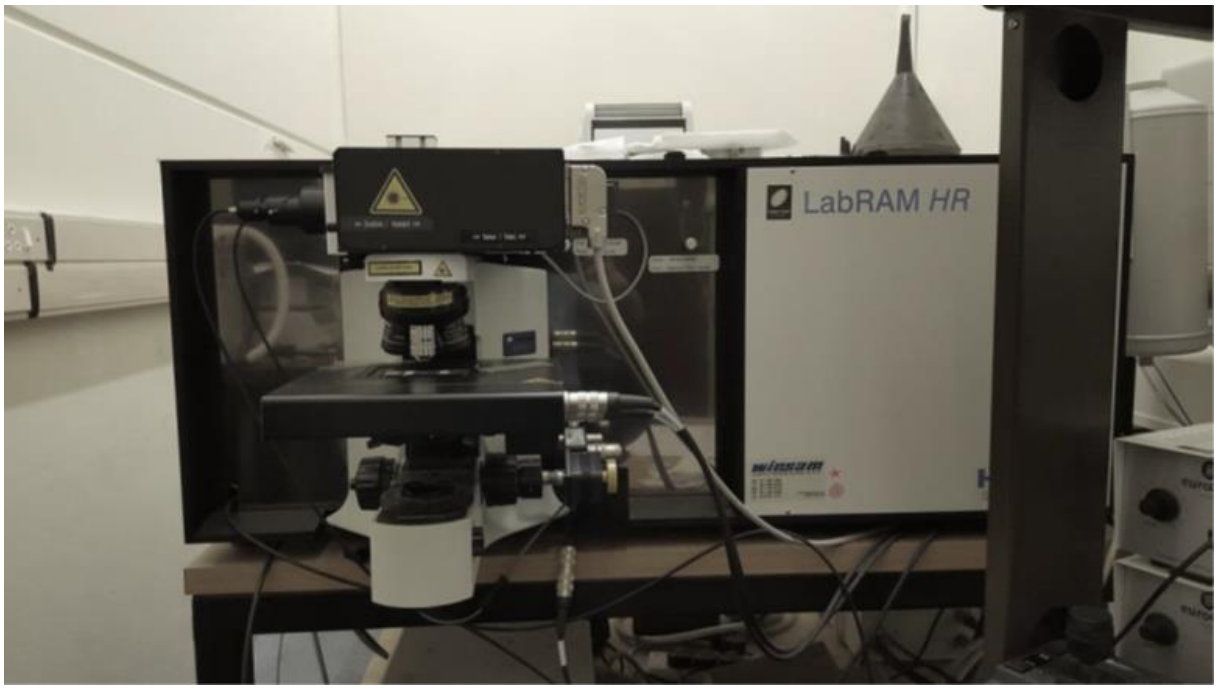



Figure 2.12: A Horiba Jobin-Yvon Raman spectrometer.

Raman spectroscopy measurements were performed on a Horiba Jobin-Yvon Raman spectrometer of $\lambda$ = 514 nm (Figure 2.12).

## 2.17: X-ray photoelectron spectroscopy (XPS)

XPS was used to determine the electronic and chemical state of the Pt, the carbon and the nitrogen doped carbon in the catalysts and the supports. X-ray photoelectrons are produced when a source is irradiated with X-rays.[29–32]

Knowing the energy of the X-ray photons and measuring the kinetic energy of the extracted electrons, one can determine the binding energy of the extracted electrons. Binding energies for electrons are unique and can be used to identify the elements from which the electrons were extracted. To compensate for the charging effects that can manifest as shifted binding energy, the C-C $sp^2$ bond energy is used for calibrating other binding energies.[33]




Figure 2.13: A Thermo Scientific ESCALAB 250Xi spectrometer.

Except for hydrogen and helium, the technique can detect all the elements. However, XPS is not useful in detecting compounds because the binding energy of an element differs from compound to compound. Photoelectrons can only penetrate a sample depth of between 2 – 10 nm, therefore it can only be used mainly as a surface technique unlike PXRD which measures the whole bulk of the sample.

The detection limit of XPS is approximately 0,1 at.%. Information from subsequent layers beneath the outer surface can be obtained by sputtering the surface with energetic argon ions, while monitoring the binding energy regions of specific elements.

The XPS measurements were carried out at the National Institute of Meteorology South Africa situated at the Council for Scientific and Industrial Research (CSIR) in Pretoria, using a Thermo Scientific ESCALAB 250Xi spectrometer (Figure 2.13) with a monochromatic Al kα (1486.7eV) operating with an X-ray power of 300 W, X-ray spot size of 900 µm, low resolution pass energy of 100eV, high resolution pass energy of 20eV and a pressure of $10^{-8}$ mbar.

## 2.18: Annular Bright-Field - dark Field Scanning Transmission Electron Microscopy (ABF-DF STEM)

The catalysts were also studied using scanning transmission electron microscopy (STEM) in a probe corrected JEOL ARM200F at the David Cockayne Centre for Electron Microscopy, University of Oxford, operated at 200 kV. A probe current of 13 pA, convergence semi-angle of 14 mrad, annular dark field (ADF) inner and outer detector angles of 77.43–241.21 mrad, and a bright-field (BF) outer detector angle of 13.2 mrad were used for simultaneous acquisition of both ADF and BF signals. Typically, sample preparation involved the dispersion by sonication of 1 mg of the material in 2 ml of ethanol. One droplet of the formed ink was deposited on a copper grid with a lacey carbon film and allowed to dry. The sample coated copper grid was then loaded into the STEM for analysis.

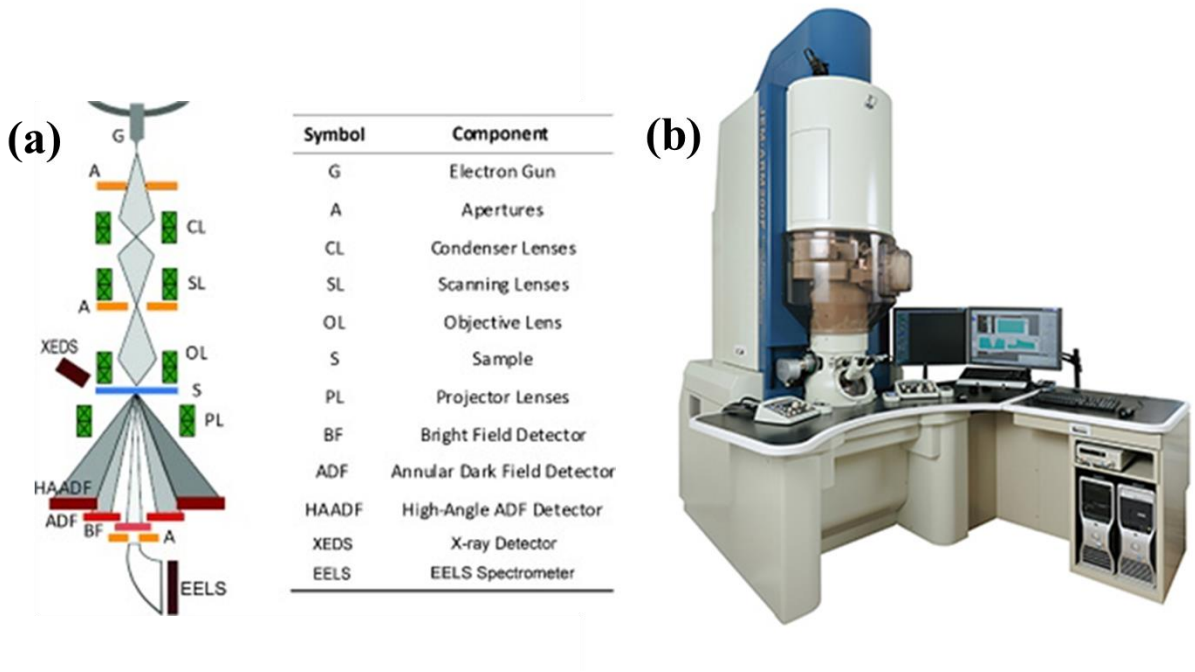



Figure 2.14: The schematic of the mode of operation of a STEM microscope (a)[34] and A JEOL ARM200F scanning transmission electron microscope (b).

## 2.19: References

(1) Stöber, W.; Fink, A.; Bohn, E. Controlled Growth of Monodisperse Silica Spheres in the Micron Size Range. *Journal of Colloid and Interface Science* **1968**, *26* (1), 62–69.

(2) Zerda, T. W.; Hoang, G. Effect of Solvents on the Hydrolysis Reaction of Tetramethyl Orthosilicate. *Chemistry of Materials* **1990**, *2* (4), 372–376.

(3) Look, J. L.; Bogush, G. H.; Zukoski, C. F. Colloidal Interactions during the Precipitation of Uniform Submicrometre Particles. *Faraday Discussions of the Chemical Society* **1990**, *90*, 345–357.

(4) Phaahlamohlaka, T. N.; Kumi, D. O.; Dlamini, M. W.; Forbes, R.; Jewell, L. L.; Billing, D. G.; Coville, N. J. Effects of Co and Ru Intimacy in Fischer–Tropsch Catalysts Using Hollow Carbon Sphere Supports: Assessment of the Hydrogen Spillover Processes. *ACS Catalysis* **2017**, *7* (3), 1568–1578.

(5) Dlamini, M. W.; Phaahlamohlaka, T. N.; Kumi, D. O.; Forbes, R.; Jewell, L. L.; Coville, N. J. Post Doped Nitrogen-Decorated Hollow Carbon Spheres as a Support for Co Fischer-Tropsch Catalysts. *Catalysis Today* **2020**, *342*, 99–110.

(6) Mohamed, R.; Binninger, T.; Kooyman, P. J.; Hoell, A.; Fabbri, E.; Patru, A.; Heinritz, A.; Schmidt, T. J.; Levecque, P. Facile Deposition of Pt Nanoparticles on Sb-Doped $SnO_2$ Support with Outstanding Active Surface Area for the Oxygen Reduction Reaction. *Catalysis Science & Technology* **2018**, *8* (10), 2672–2685.

(7) Mohamed, R.; Binninger, T.; J. Kooyman, P.; Hoell, A.; Fabbri, E.; Patru, A.; Heinritz, A.; J. Schmidt, T.; Levecque, P. Facile Deposition of Pt Nanoparticles on Sb-Doped $SnO_2$ Support with Outstanding Active Surface Area for the Oxygen Reduction Reaction. *Catalysis Science & Technology* **2018**, *8* (10), 2672–2685.

(8) Mabbott, G. A. An Introduction to Cyclic Voltammetry. *Journal of Chemical Education* **1983**, *60* (9), 697–702.

(9) Peng, Q.; Chen, J.; Ji, H.; Morita, A.; Ye, S. Origin of the Overpotential for the Oxygen Evolution Reaction on a Well-Defined Graphene Electrode Probed by in Situ Sum Frequency Generation Vibrational Spectroscopy. *J. Am. Chem. Soc.* **2018**, *140* (46), 15568–15571.

(10) Garsany, Y.; Baturina, O. A.; Swider-Lyons, K. E.; Kocha, S. S. Experimental Methods for Quantifying the Activity of Platinum Electrocatalysts for the Oxygen Reduction Reaction. *Analytical Chemistry* **2010**, *82* (15), 6321–6328.

(11) Lukaszewski, M.; Soszko, M.; Czerwiński, A. Electrochemical Methods of Real Surface Area Determination of Noble Metal Electrodes - an Overview. *International Journal of Electrochemical Science* **2016**, *11* (6), 4442 – 4469

(12) Jr, P. N. R. Structure Sensitivity in the Electrocatalytic Properties of Pt: I. Hydrogen Adsorption on Low Index Single Crystals and the Role of Steps. *J. Electrochem. Soc.* **1979**, *126* (1), 67.

(13) Inagaki, M.; Konno, H.; Tanaike, O. Carbon Materials for Electrochemical Capacitors. *Journal of Power Sources* **2010**, *195* (24), 7880–7903.

(14) Schonvogel, D.; Hülstede, J.; Wagner, P.; Kruusenberg, I.; Tammeveski, K.; Dyck, A.; Agert, C.; Wark, M. Stability of Pt Nanoparticles on Alternative Carbon Supports for Oxygen Reduction Reaction. *Journal of The Electrochemical Society* **2017**, *164* (9), F995–F1004.

(15) Seo, M. H.; Choi, S. M.; Kim, H. J.; Kim, W. B. The Graphene-Supported Pd and Pt Catalysts for Highly Active Oxygen Reduction Reaction in an Alkaline Condition. *Electrochemistry Communications* **2011**, *13* (2), 182–185.

(16) Schmickler, W.; Santos, E, Interfacial Electrochemistry, Chapter 19, Convection Technique, p210-213.

(17) Modulated Speed Rotator (MSR) User Manual, Pine research Instrumentation Store, DRU10002-REV004-Pine-MSR-Rotator-User-Guide. p130 -137

(18) Chaiburi, C.; Hacker, V. Catalytic Activity of Various Platinum Loading in Acid Electrolyte at 303 K. *Energy Procedia* **2017**, *138*, 229–234.

(19) Shinozaki, K.; Zack, J. W.; Pylypenko, S.; Pivovar, B. S.; Kocha, S. S. Oxygen Reduction Reaction Measurements on Platinum Electrocatalysts Utilizing Rotating Disk Electrode Technique: II. Influence of Ink Formulation, Catalyst Layer Uniformity and Thickness. *Journal of the Electrochemical Society* **2015**, *162* (12), F1384–F1396.

(20) Li, M.; Zhao, Z.; Cheng, T.; Fortunelli, A.; Chen, C. Y.; Yu, R.; Zhang, Q.; Gu, L.; Merinov, B. V.; Lin, Z.; Zhu, E.; Yu, T.; Jia, Q.; Guo, J.; Zhang, L.; Goddard, W. A.;

Huang, Y.; Duan, X. Ultrafine Jagged Platinum Nanowires Enable Ultrahigh Mass Activity for the Oxygen Reduction Reaction. *Science* **2016**, *354* (6318), 1414–1419.

(21) Zolotoyabko, E. Basic Concepts of X-Ray Diffraction Chapter 2, Wave Propagation in Periodic Media, p15

(22) Transmission Electron Microscope | Instrument | Britannica.

(23) Scanning Electron Microscope | Definition, Images, Uses, Advantages, & Facts | Britannica.

(24) Brunauer, S.; Emmett, P. H.; Teller, E. Adsorption of Gases in Multimolecular Layers. *Journal of the American Chemical Society* **1938**, *60* (2), 309–319.

(25) Fagerlund, G. Determination of Specific Surface by the BET Method. *Mat. Constr* **1973** 6**,** 239–245

(26) Okuda, H.; Young, R. J.; Wolverson, D.; Tanaka, F.; Yamamoto, G.; Okabe, T. Investigating Nanostructures in Carbon Fibres Using Raman Spectroscopy. *Carbon* **2018**, *130*, 178–184.

(27) Zana, A.; Speder, J.; Reeler, N. E. A.; Vosch, T.; Arenz, M. Investigating the Corrosion of High Surface Area Carbons during Start stop Fuel Cell Conditions A Raman Study *Electrochimica Acta* **2013**, 114, 455-461

(28) Parent, P.; Laffon, C.; Marhaba, I.; Ferry, D.; Reggier, T.Z.; Ortega, I.K.; Chazallon, B.; Carpentier, Y.; Focsa, C. Nanoscale Characterization of Aircraft Soot A High-Resolution Transmission Electron Microscopy, Raman Spectroscopy. *Carbon* **2016**, 101, 86-101

(29) Castle, J. E.; Chapman-Kpodo, H.; Proctor, A.; Salvi, A. M. Curve-Fitting in XPS Using Extrinsic and Intrinsic Background Structure. *Journal of Electron Spectroscopy and Related Phenomena* **2000**, *106* (1), 65–80.

(30) Bluhm, H.; Hävecker, M.; Knop-Gericke, A.; Kiskinova, M.; Schlögl, R.; Salmeron, M. In Situ X-Ray Photoelectron Spectroscopy Studies of Gas-Solid Interfaces at near-Ambient Conditions. *MRS Bulletin* **2007**, *32* (12), 1022–1030.

(31) Wei, J.; Hing, P.; Mo, Z. Q. TEM, XPS and FTIR Characterization of Sputtered Carbon Nitride Films. *Surface and Interface Analysis* **1999**, *28* (1), 208–211.

(32) Alderucci, V.; Pino, L.; Antonucci, P.; Roh, W.; Cho, J.; Kim, H.; Cocke, D.L.; Antonucci, V. XPS Study of Surface Oxidation of Carbon-Supported Pt Catalysts. *Elsevier*. *Materials Chemistry and Physics* **1995**, 41(1), 9-14

(33) Lee, H. S.; Baek, G. Y.; Hwang, I. T.; Jung, C. H.; Choi, J. H. Preparation of Porous Carbon Films from Polyacrylonitrile by Proton Irradiation and Carbonization. *Radiation Physics and Chemistry,* **2017** (141), 369-374

(34) Stropped, D.G.; Zagonel, L.F.; Montoro, L.A.; Leite, E.R.; Ramirez, A. J.; High-Resolution Scanning Transmission Electron Microscopy (HRSTEM) Techniques: High-Resolution Imaging and Spectroscopy Side by Side. *ChemPhysChem* **2012,** (13), 437 - 443

# Chapter 3

# Study of the formation of silica templates under various conditions

## 3.1: Introduction

Silica particles are formed from the hydrolysis and condensation of silicon alkoxides. A classic example of these silicon alkoxides is tetraethyl orthosilicate (TEOS). The hydrolysis and condensation processes are known to occur in the presence of low molecular weight alcohols like ethanol (EtOH) and sufficient amounts of deionized water (DIW). To obtain spherical silica particles, the condensation hydrolysis and precipitation reactions must occur in the presence of ammonia. Without at least small amounts ammonia ($NH_4OH$), the precipitating silica material flocculates into sheets and clumps as shown in Figure 3.4, confirming that the ammonia catalyst is essential. Silica spheres have been used for a variety of applications including as adsorbents of chemicals, in electronics, drug delivery and as templates for the synthesis of shaped nanomaterials.[1–4]

It is known that mixing TEOS, DIW, EtOH and $NH_4OH$ solutions together produces silica particles of different sizes depending on the initial concentrations of reactants and reaction conditions. However, a challenge has been with understanding the growth mechanism of these silica spheres and to understand the reaction parameters and conditions which produce a specific particle size and other desirable properties.[5]

Equation (3.1) shows the TEOS hydrolysis into silicon hydroxide. Equation (3.2) shows the condensation of the silicates into the silica particles.[6,7] Both processes require the presence of ammonia. Formation of a cross linked silica framework occurs naturally in these processes. This can be enhanced by calcination or the use of excess water which yields extra cross linking of the terminal silanol groups resulting in a denser structure as revealed by a low BET surface area as the pores are closed off.[8–10]

$$Si(OR)_4 + 4H_2O \longrightarrow Si(OH)_4 + 4\,ROH \quad \text{.....(3.1)}$$

$$nSi(OH)_4 \longrightarrow nSiO_2 + 2nH_2O \quad \text{.....(3.2)}$$

For the hydrolysed TEOS monomers to develop into spherical silica particles, nucleation or seed growth must occur first. Nucleation can be described as a process whereby hydrolysed TEOS monomers coalesce into a silica or pre-silica core which matures into a silica particle when critical conditions are met.[11] These nuclei then grow until they become stable and precipitates out of the solution. [12] Several parameters affect the final particle size of the formed silica. These include the concentration of reactants, the molar ratio of reactants, presence or absence of stirring, the synthesis reaction temperature and whether the reaction is performed in an open or closed system among many other not yet understood factors.

Several nucleation and growth models have been proposed for the formation and growth of silica particles and these include the Le Mar model, the aggregative growth model and the monomer addition growth model.[10,13,14]

In this work our intention was not to fully investigate and understand the complicated nucleation and growth process of the silica particles. Our intention was to find the combination of parameters that would produce monodisperse and small silica particles and to use these silica

templates to synthesize hollow and nitrogen doped hollow carbon spheres with a small external diameter (d < 100 nm) for application as supports for Pt in ORR catalysis.

## 3.2: Experimental

Silica particles were synthesized according to the method of Stober and co-workers.[15] In a typical synthesis a clean round bottom flask was filled with 390 mL of absolute ethanol (EtOH) solvent. To this solvent was added a solution of 50 mL deionized water (DIW) and 20 mL of 25% ammonia solution ($NH_4OH$) with stirring. Since ammonia evaporates at room temperature, the reaction vessel was sealed to minimise the evaporation of the ammonia catalyst. The solution was stirred for 10 minutes to allow for thorough mixing followed by an 'all at once' addition of 30 mL of tetraethyl orthosilicate (TEOS). The resulting solution was stirred at room temperature at low speed for a period of 6 h. During the stirring period the solution changed colour from colourless, to off-white and then white as silica colloids were formed. The formed silica particles were collected by high speed centrifugation followed by 5 washes in a mix of 50% v/v DIW/EtOH with centrifugation at 18 000 rpm. The silica was dried in an oven overnight at 80ºC followed by calcination in air in oven at 500ºC for 5 h. The formed silica was evaluated with SEM for morphology and to confirm crosslinking, some of the silica was evaluated using BET for textual properties.

Concentrations of these reagents were varied in different experiments in order to determine which parameters gave particles of a specific size (d < 100 nm).

To synthesize silica particles of about 80 nm in diameter, a larger volume of EtOH was used as more dilute reagents were necessary. In this synthesis 1.2 L of EtOH was mixed with 50 ml of DIW and 50 ml of ammonia. The solutions were stirred as above followed by the addition all at once of TEOS (30 mL). The reaction proceeded for 6 h and the silica particles were harvested by centrifugation followed by calcination and characterization.

To investigate the role of ammonia on the silica morphology, TEOS, DI and EtOH were mixed and stirred followed by the syringe pump addition of an ammonia solution for a period of up to 1 h at a flow rate of 1 $ml.min^{-1}$. The formed silica particles were then centrifuged and washed followed by calcination and characterization.

Characterization techniques used (SEM, TEM, BET) were described in Chapter 2. At least 100 particles were counted in SEM images to determine the particle size distributions.

## 3.3 Discussion

A range of variables were investigated to evaluate their effect on the size of the silica spheres produced in the Stober reaction. The focus in the study was to determine the parameters needed to produce small (d <100 nm) silica spheres. These parameters included: the concentration of TEOS, ammonia solution, DIW and the concentration of absolute ethanol.

### 3.3.1 TEOS Study

In this study we investigated the effects of varying the concentrations of TEOS on the silica particle size. The concentration of TEOS in the final reaction mixture were varied from 0.1 M to 3.2 M with a doubling effect after each concentration. The concentrations of DIW (5 M), $NH_4OH$ (2 M) and EtOH (8 M), were kept throughout.

The particle sizes were observed to increase as the TEOS concentration was doubled. SEM images of the synthesized silica spheres are shown in Figure 3.1. The silica was of a spherical morphology with particle sizes ranging from about 57 nm to about 342 nm in diameter as determined by scanning electron microscopy (SEM).[16] The particle size distributions for the silica spheres formed are shown in Figure 3.2. The formed silica spheres were more aggregated in the smaller size range compared to the bigger size range. The bigger silica spheres were cleaner and more isolated when compared to the smaller ones.[17] All the silica spheres had a

narrow size distribution and were mostly monodispersed. Figure 3.1 shows that at low concentrations of TEOS, there are many silica particles per image grid compared to higher concentrations where bigger and fewer silica particles are present. This suggests a growth model in which at low concentrations of TEOS (using the concentrations of other reagents listed), a high rate of nucleation resulted in many silica nuclei whereas at higher concentrations of TEOS, the nucleation process proceeds to a larger extent yielding bigger particles. At higher concentrations of TEOS, the small initial nuclei may have aggregated to form bigger particles.[2,5] Monomer addition of the hydrolysed TEOS could also be occurring to give formation of the bigger particles. Thus, at higher concentrations of TEOS, there is a constant supply of hydrolysed TEOS monomers which resulted in constant addition of these monomers on the initial nuclei seeds resulting in bigger silica spheres.[18]

As shown in Figure 3.3, the particle sizes of the silica formed increase with an increase in TEOS concentration in a near linear manner. This means, from the study, doubling the TEOS concentration will result in a linear increase in silica size.

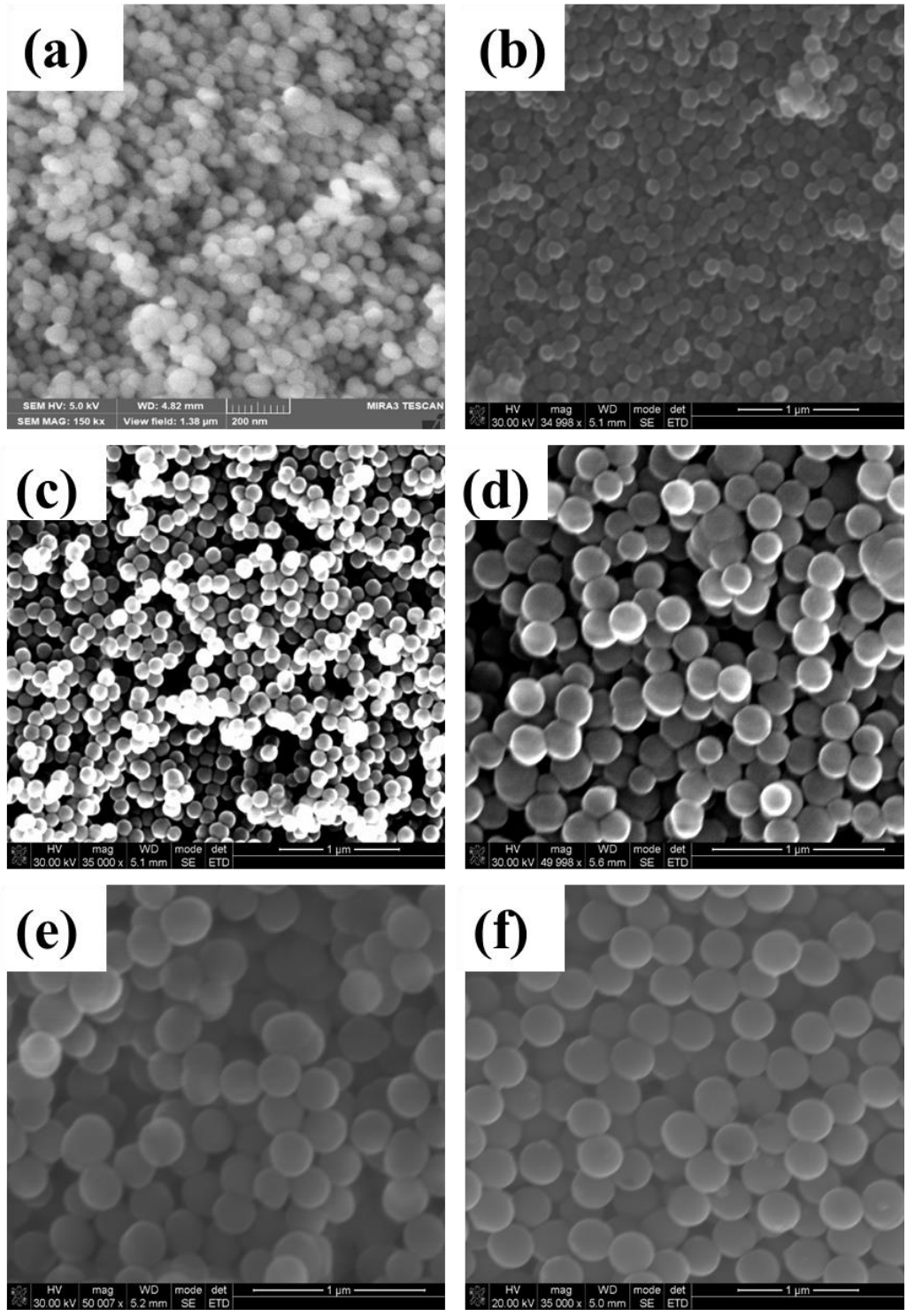



Figure 3.1: SEM images of silica particles synthesized with $NH_4OH$ (2 M), DIW (5 M), EtOH (8 M) and increasing concentrations of TEOS (a) 0.1 M, (b) 0.2 M, (c) 0.4 M, (d) 0.8 M, (e) 1.6 M, (f) 3.2 M

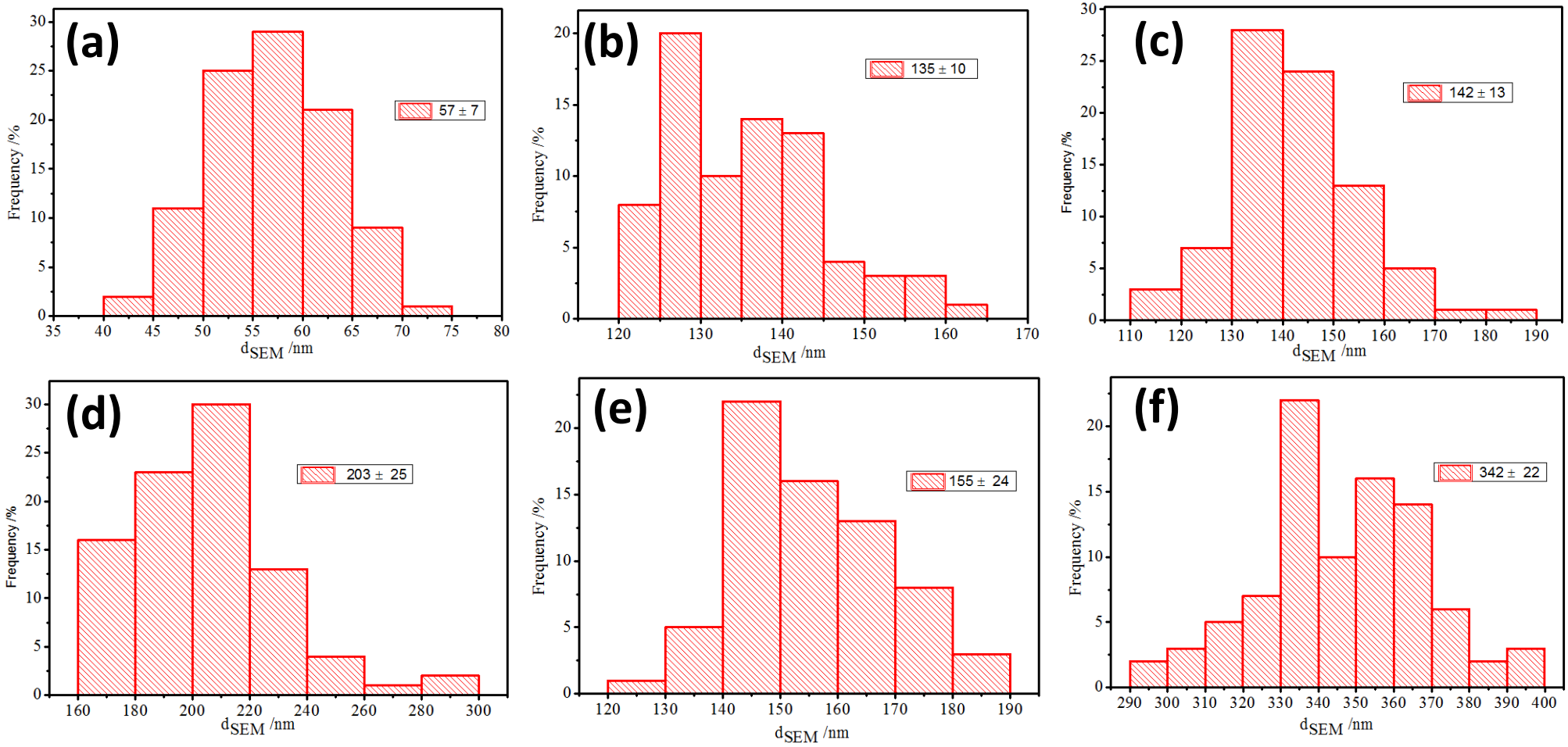



Figure 3. 2: Particle size distributions of silica particles synthesized with $NH_4OH$ (2 M), DIW (5 M), EtOH (8 M) and increasing concentrations of TEOS (a) 0.1 M, (b) 0.2 M, (c) 0.4 M, (d) 0.8 M, (e) 1.6 M, (f) 3.2 M.

Table 3.1: Data showing variation of SEM particle sizes due to changes in TEOS concentration.

| [TEOS] /M | 0.1 | 0.2 | 0.4 | 0.8 | 1.6 | 3.2 |
|---|---|---|---|---|---|---|
| $d_{SEM}$ | 56 ± 6 | 134 ± 10 | 141 ± 13 | 155 ± 24 | 203 ± 17 | 342 ± 22 |

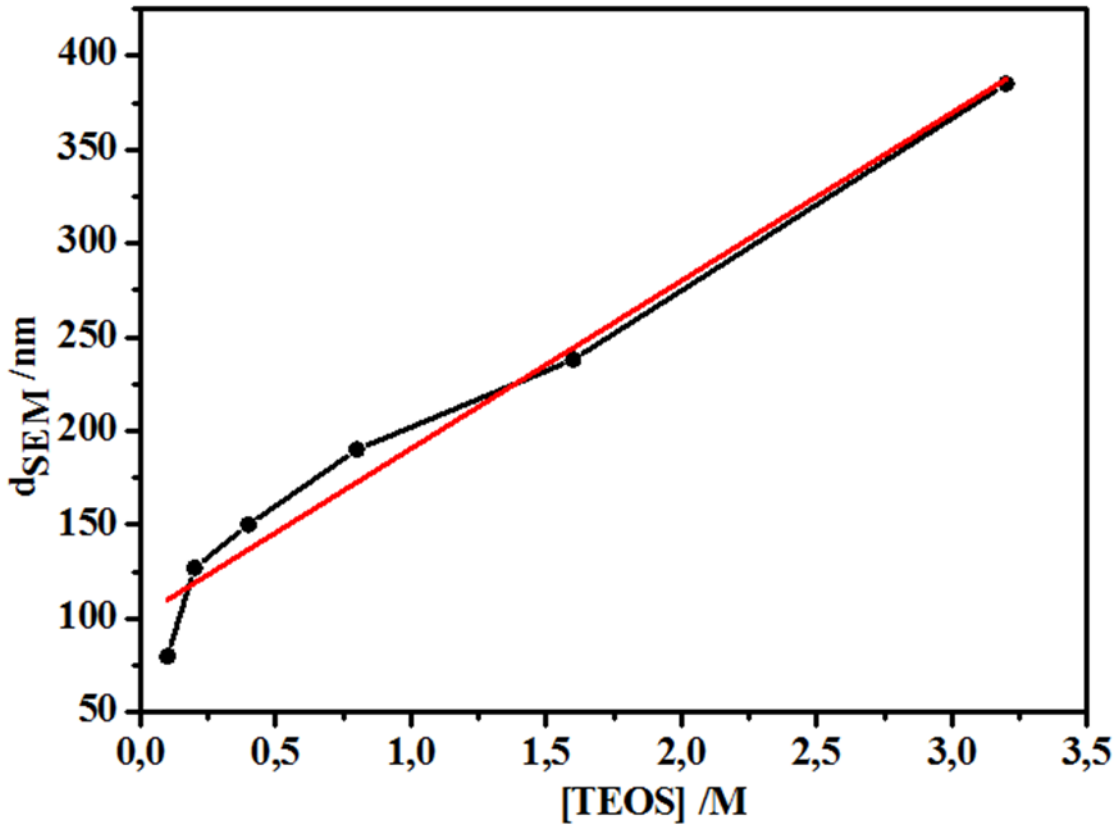



Figure 3.3: Particle size changes of silica particles synthesized with $NH_4OH$ (2 M), DIW (5 M), EtOH (8 M) and increasing concentrations of TEOS (a) 0.1 M, (b) 0.2 M, (c) 0.4 M, (d) 0.8 M, (e) 1.6 M, (f) 3.2 M.

The data are consistent with a growth model in which an initial low concentration of TEOS is required to initiate a short burst of hydrolysis and condensation. This results in a high number of stable nuclei in solution. These small nuclei are stabilized by the negative charge on the

silica surface and the resulting repulsive forces at high pH due to the presence of ammonia.[19]Growth is prescribed to the slow addition of hydrolysed monomers against the repulsive forces of the negatively charged surface of the silica thereby minimizing the extent of growth. This mechanism yields smaller silica particles at the saturation point.[10]

At higher concentrations of TEOS, the hydrolysis process could have taken place at a similar rate as the low TEOS concentration however, the constant supply of the hydrolysed TEOS monomer results in a continuous nucleation process forming new nuclei. Silica particle growth then proceeds via multiple monomer addition steps or the aggregation of the smaller unstable nuclei to form bigger particles.[7,18] Few and bigger spheres occur as a result of the coalescence of the many smaller silica spheres into bigger spheres.[20]

## 3.3.2: Ammonia solution study

Very low concentrations of ammonia solution were used to investigate if indeed ammonia is a morphology catalyst.[21,22] Figure 3.4 below show that as ammonia concentrations were increased, the spherical morphology of the formed silica became more defined. As ammonia is a hydrolysis, condensation and morphology catalyst, low concentrations of this reagent retard these processes resulting in silica material with no defined morphology. Low concentrations of ammonia solution resulted in the formation of the deformed silica indeed confirming the requirement of the reagent in the formation of silica particles.[23]

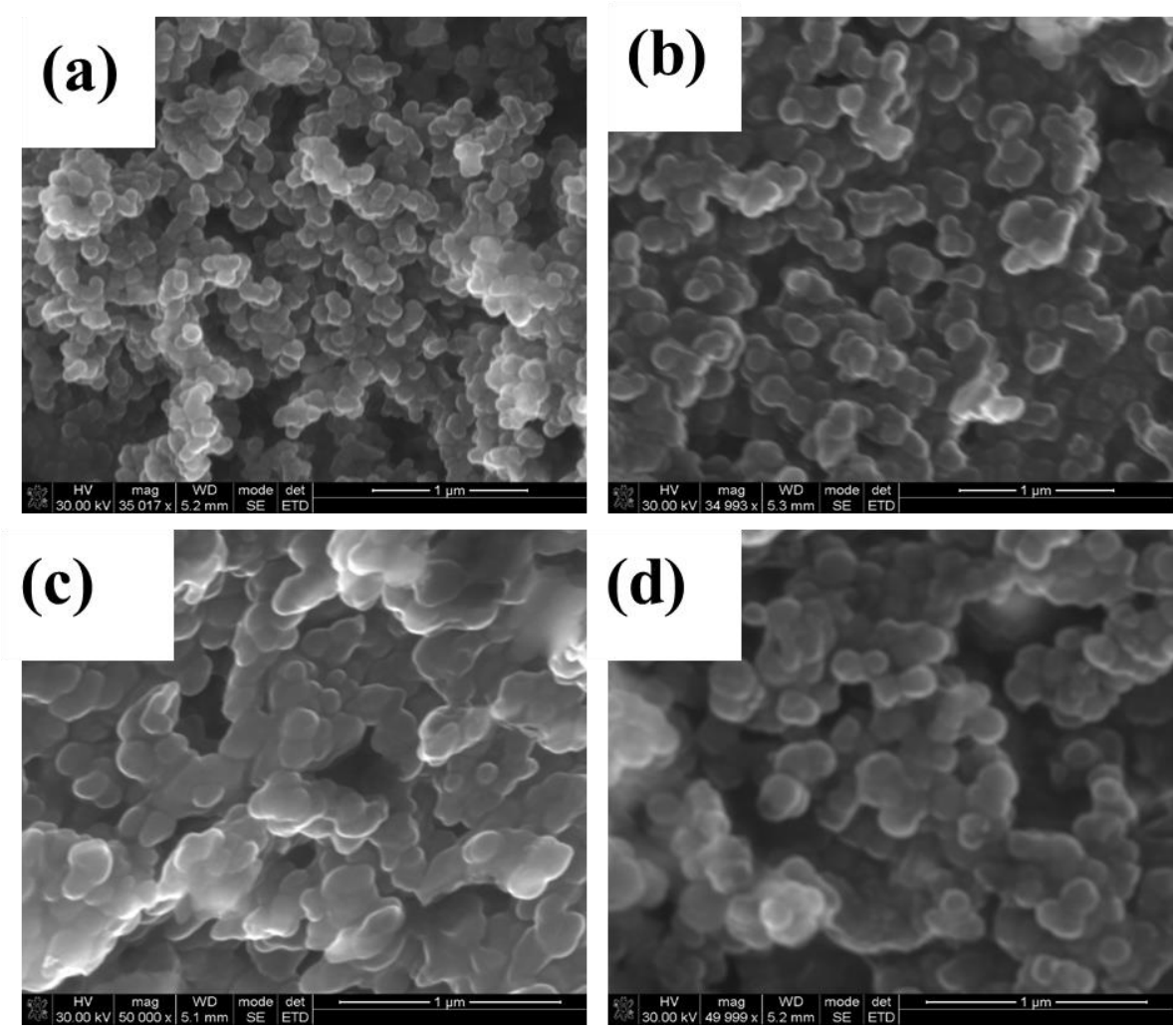



Figure 3.4: SEM images of not formed silica particles at very low ammonia solution concentrations below 0.1 M, with (a) 0. 01 M, (b) 0.02 M, (c) 0.04, (d) 0.08 M $NH_4OH$

Ammonia concentrations were varied from 0.5 – 3.0 M to study the effect on the silica particle size and their growth. The concentrations of the other critical reagents TEOS (2 M), EtOH (8 M) and DIW (5 M) were kept at an optimum constant throughout the study.

The SEM images confirmed the spherical morphology of the silica particles. Few and bigger silica spheres were observed for high ammonia concentrations whereas small and numerous silica spheres are observed for low concentrations of ammonia solution (Figure 3.5). There are many silica spheres in the lower ammonia concentrations of 0.5 M compared to when the concentration is increased to about 2.5 M.

Ammonia solution has three effects in terms of acting as a catalyst in the synthesis of silica spheres from silicon alkoxides. Ammonia is essential for the hydrolysis, condensation as well as for causing the spherical morphology of the silica formed.[24,25] It is important to balance the ammonia concentration in order to maximise the control of these processes.

When the concentration of ammonia is low, it takes longer for the nucleation process to be complete.[21] This results in the number density of formed nuclei gradually increasing over time.[26] This increase in the number of these nuclei will continue until such a time as when saturation occurs and if the amount of ammonia is not increased, the process ceases. At high ammonia concentrations, hydrolysis of the TEOS is faster and subsequent nucleation occurs at a faster rate resulting in the formation of numerous small nuclei.[14] However, as there is a constant supply of the ammonia, further hydrolysis occurs resulting in the monomer addition and growth of the silica.[7] When saturation is reached, solid silica colloids are precipitated, and these can be separated easily from solution by filtration or high-speed centrifugation, depending on their size.[13,27]

For the bigger particles, monomer addition to the bigger, fewer nuclei continues to occur until either the reaction is stopped or until the hydrolysed TEOS precursor is depleted.[13] A spherical morphology is maintained by the presence of the ammonia solution.[2] Growth of the bigger and fewer silica particles at high ammonia concentrations can also be compounded by the [28]mechanism whereby smaller unstable silica nuclei aggregate with similar size nuclei or aggregates to form bigger nuclei.

Neglecting monomer addition as the primary silica growth model, which can be assumed that the nuclei are colloidally unstable. In this model it is proposed that both fresh nuclei and older aggregates forms more stable particles. When the rate of aggregation of large pairs is slower

than for small to small or small to large pairs, the aggregation model can then explain the narrow final size distribution observed in Figure 3.6 and Figure 3.7.[29]

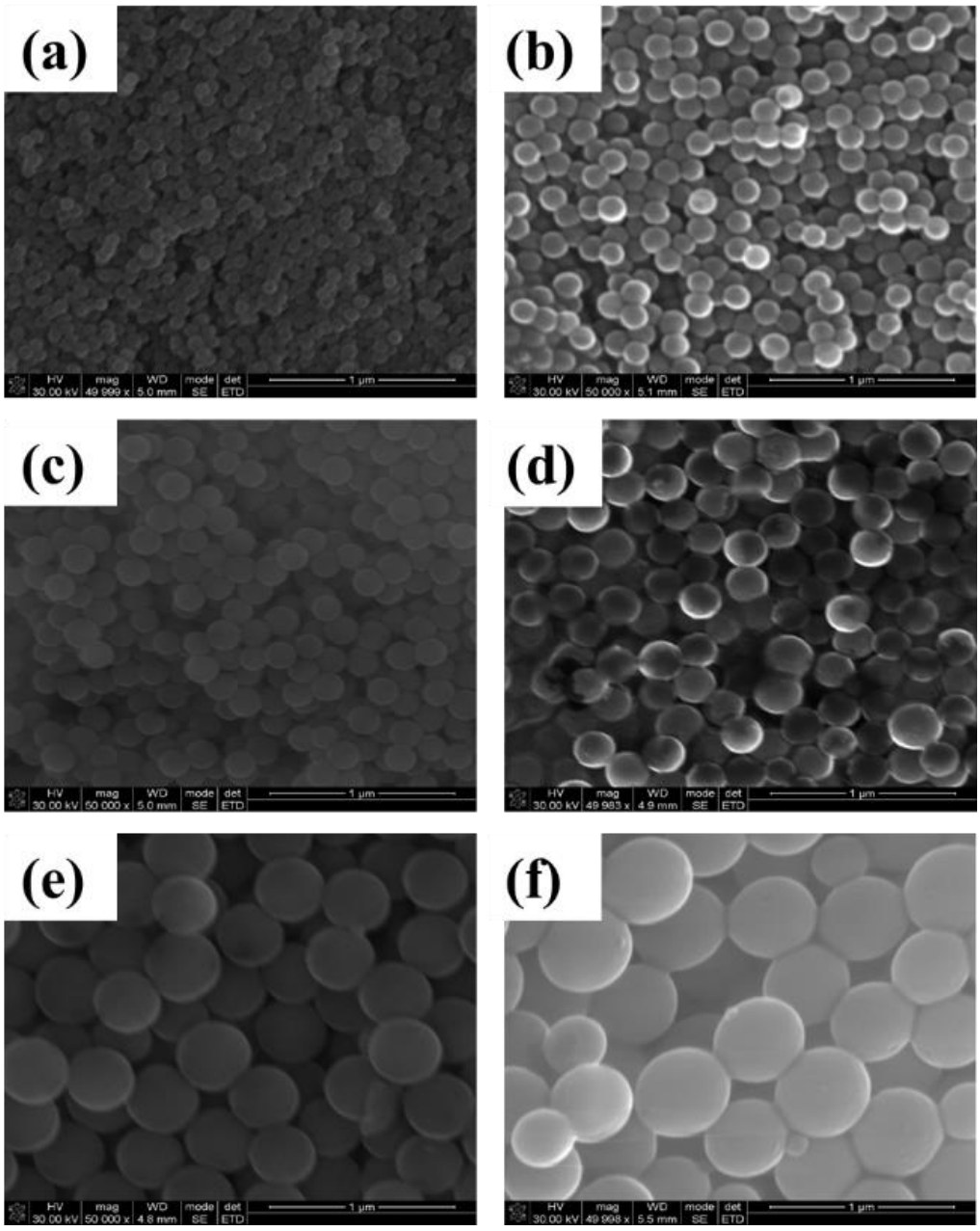



Figure 3.5: SEM images of the silica spheres formed at an optimum of the other reagents with TEOS (2 M), DIW (5 M), EtOH (8 M) and various ammonia concentrations of $NH_4OH$ (a) 0.5 M, (b) 1.0 M, (c) 1.5 M, (d) 2.0 M, (e) 2.5 M and 3.0 M.

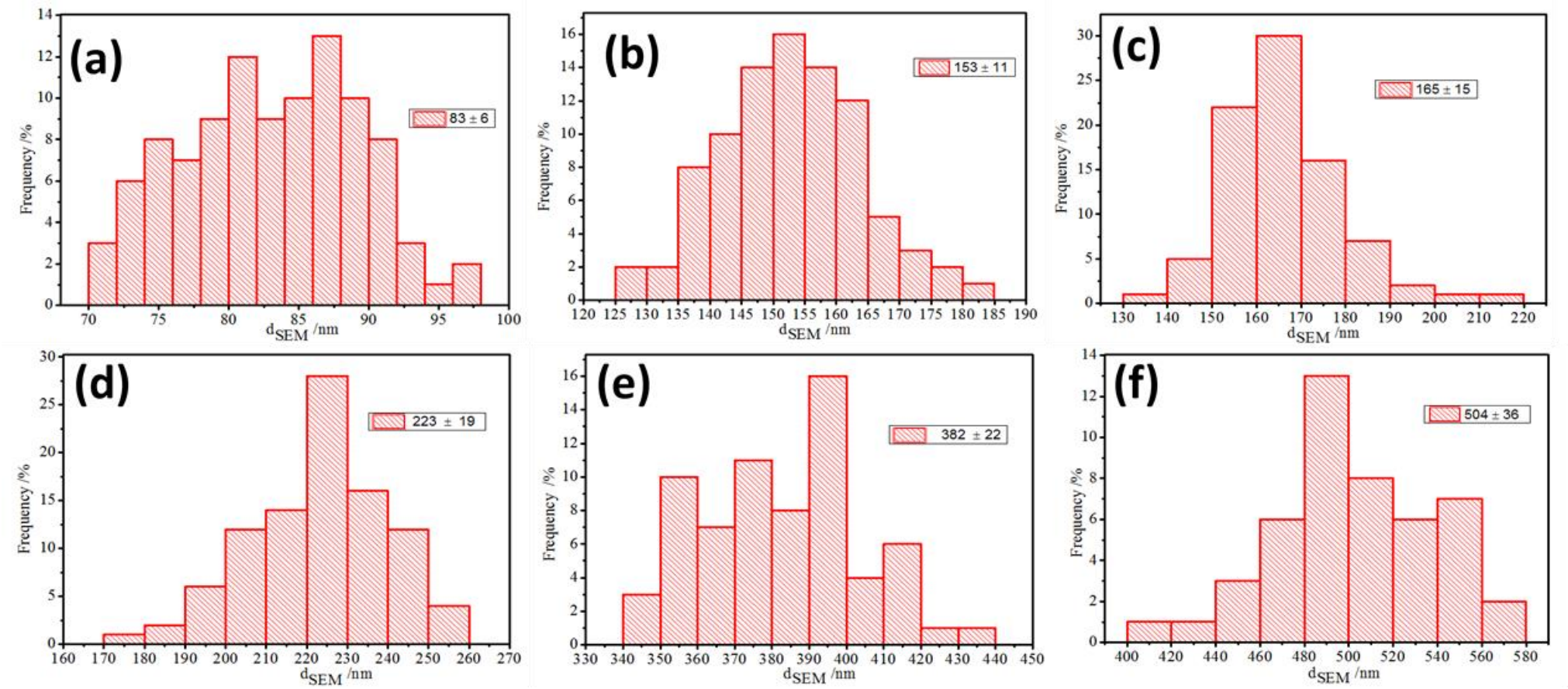



Figure 3.6: Particle size distribution showing variation due to changes in the concentration of $NH_4OH$ (a) 0.5 M, (b) 1.0 M, (c) 1.5 M, (d) 2.0 M, (e) 2.5 M and 3.0 M and at an optimum of the other reagents with TEOS (2 M), DIW (5 M), EtOH (8 M).

Table 3. 2: Changes in particle size due to variation of ammonia concentration.

| [$NH_4OH$]/M | 0.5 | 1.0 | 1.5 | 2.0 | 2.5 | 3.0 |
|---|---|---|---|---|---|---|
| $d_{SEM}$ | 82 ± 6 | 153 ± 11 | 165 ± 15 | 223 ± 19 | 381 ± 22 | 504 ± 36 |

Particle size distributions in Figure 3.5 shows a narrow size range and a high degree of mono dispersity.

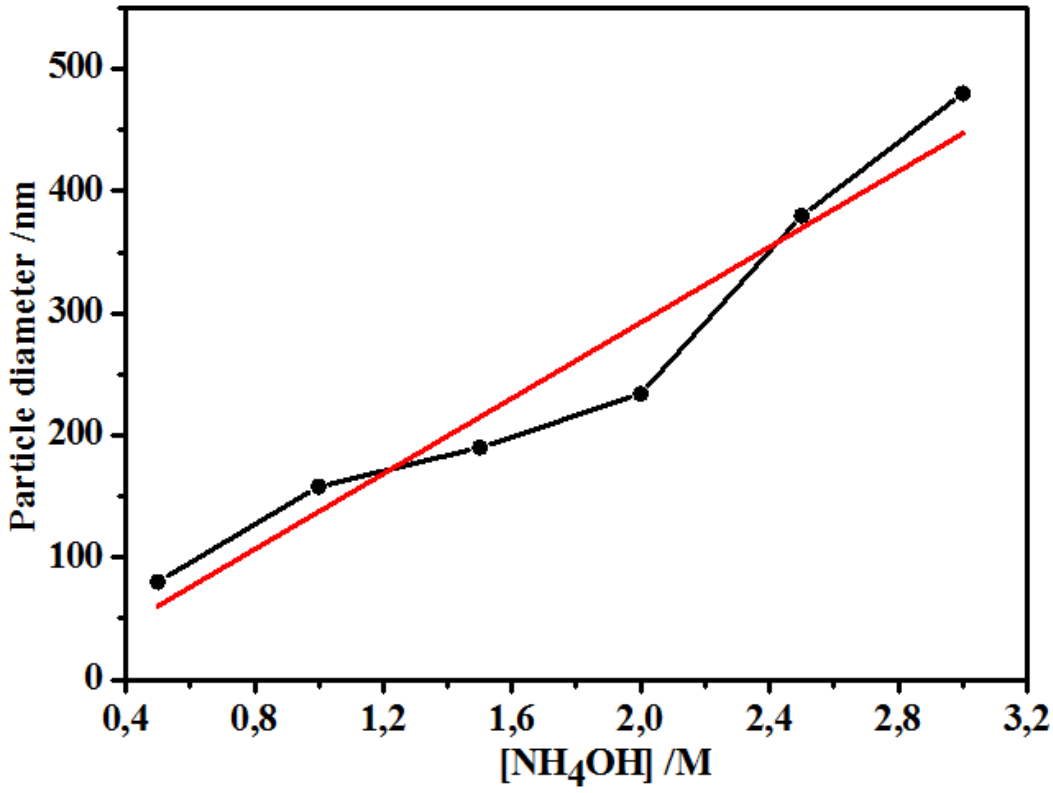



Figure 3.7: Dependence of Silica particle sizes on the concentration of $NH_4OH$ and at an optimum of the other reagents with TEOS (2 M), DIW (5 M) and EtOH (8 M).

## 3.3.3: Deionized water study

Hydrolysis and condensation of TEOS occurred in the presence of water and therefore water plays a key role in the process.[30] As the DIW concentration was increased from 5M – 30 M, silica particles were observed to grow in diameter from about 82 nm to about 390 nm (Table 3.3, Figure 3.8 – 3.9).

As in previous studies with ammonia and TEOS, SEM images show that for low concentrations of DIW, there are more silica spheres formed compared to at 30 M DIW. At low DIW concentrations TEOS hydrolysis and condensation occurs more slowly than at high DI concentrations; resulting in faster nucleation and growth as more TEOS monomers are hydrolysed and added to already formed particles according to a monomer growth model.[31]

At low DI concentrations (and with sufficient TEOS and ammonia), nucleation occurs but is restricted by the low availability of the essential DIW such that the small numerous nuclei that are formed do not continue to grow as the monomer TEOS is not continuously added due to minimal hydrolysis.

Smaller nuclei that form will either dissolve or deposit on bigger silica spheres because of Ostwald ripening.[32] Another growth mechanism could also be due to the hydrolysed TEOS monomers adding onto the smaller silica until they are fully grown.

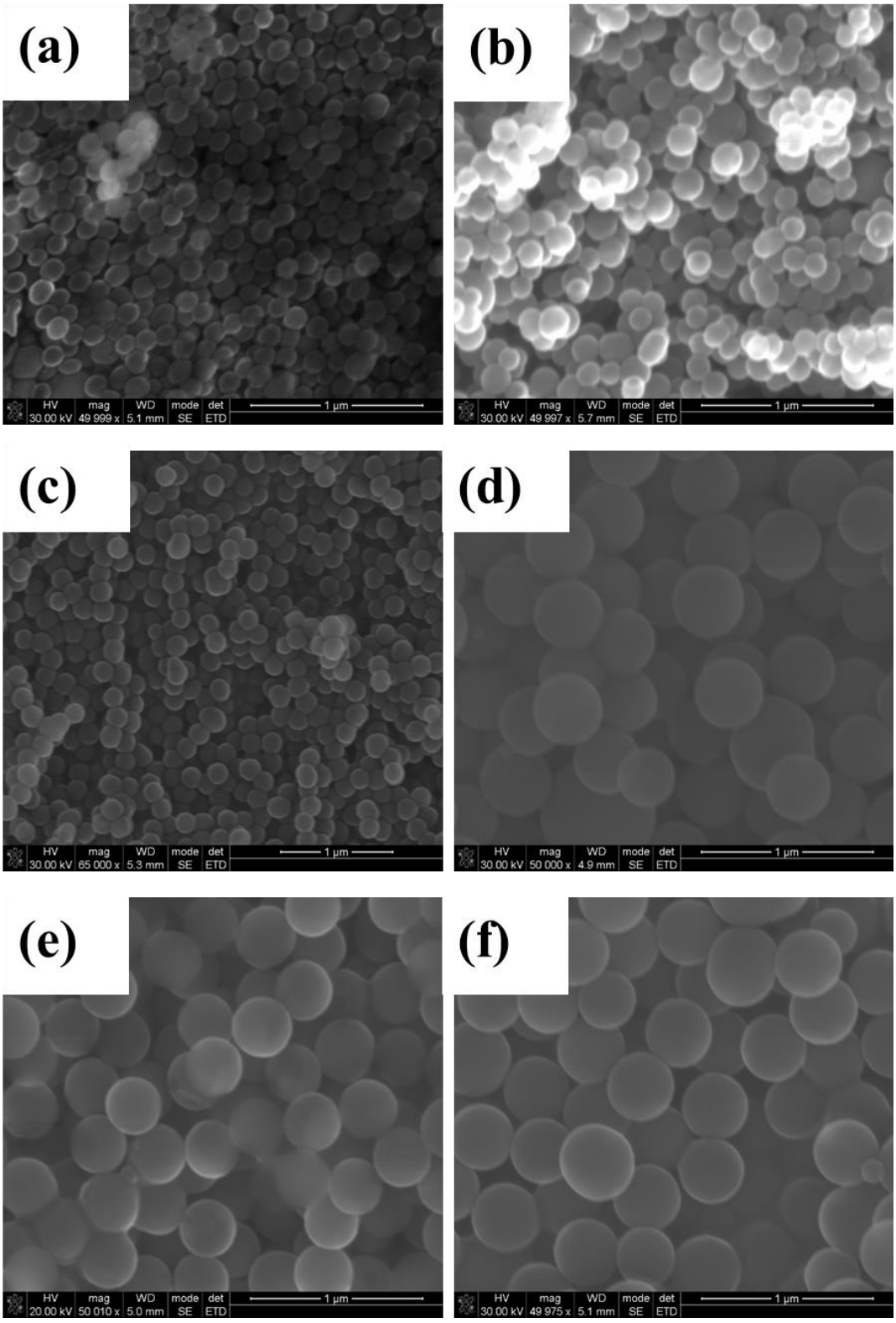



Figure 3.8: SEM images as the deionized water concentration is varied from (a) 5 M, (b) 10 M, (c) 15 M, (d) 20 M, (e) 25 M, (f) 30 M and optimum concentration of the other reagents $NH_4OH$ (2 M), TEOS (2 M) and EtOH (8 M).

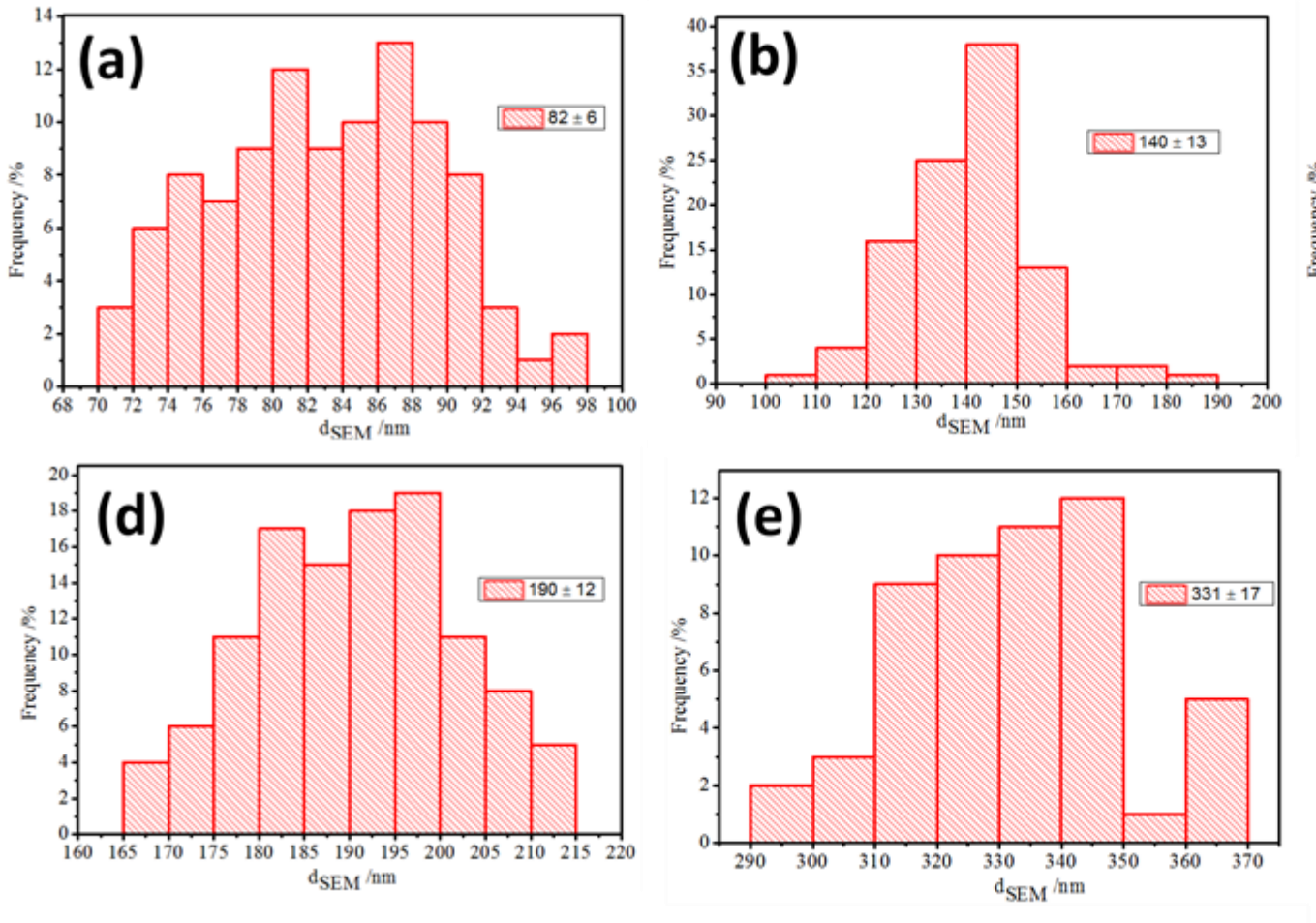



Figure 3.9: Particle size distribution of the silica spheres as the deionized water concentration was varied from (a) 5 M, (b)10 M, (c) 15 M, (d) 20 M, (e) 25 M, (f) 30 M at optimum concentration $NH_4OH$ (2 M), TEOS (2 M), EtOH

Table 3. 3: Particle size variation of the silica spheres due to changes in deionized water concentration

| [DI] /M | 5 | 10 | 15 | 20 | 25 | 30 |
|---|---|---|---|---|---|---|
| $d_{SEM}$ | 82 ± 6 | 140 ± 13 | 151 ± 20 | 190 ± 12 | 332 ± 17 | 386 ± 21 |

As shown in Figure 3.9, the effect of DI concentration on the silica particle size follows a linear relationship.

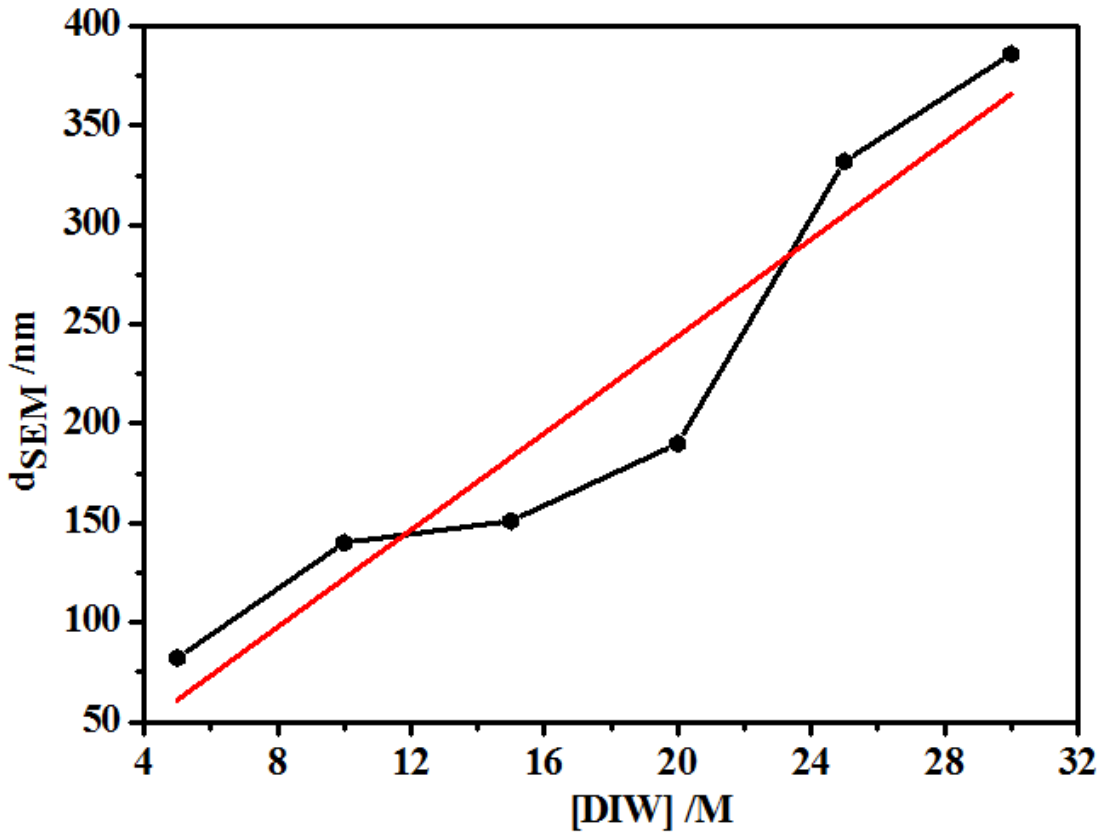



Figure 3.10: Changes in the silica particle size due to the variation of the deionized water concentration was varied from 5 - 30 M at optimum concentration of $NH_4OH$ (2 M), TEOS (2 M), EtOH (8M).

.

## 3.3.4: Controlled addition of TEOS

To better understand the growth mechanism of the silica spheres, controlled addition of the TEOS was done to the optimum concentrations of all the other reagents. It was hoped that the controlled addition would result in controlled hydrolysis and condensation such that small particles would be formed.[33] In the synthesis, DIW (5 M), $NH_4OH$ (2 M) and a dilute solution of EtOH (8 M) were premixed followed by the controlled addition of the TEOS using a syringe pump supplying TEOS at a slow flow rate of 1 $ml.min^{-1}$ to control the addition. The TEOS was continuously supplied to the reaction for a period of 20 min (a), 30 min (b) 40 min (c) and 50 min (d), followed subsequently by stirring up to 6 h. The SEM images of silica particles formed by the different addition durations (Figure 3.11), show that poly disperse particles were formed with a wide standard deviation.[34,35] (As shown in Figure 3.10 both small and bigger particles were simultaneously formed during the 6 h synthesis duration.) 3.3.3

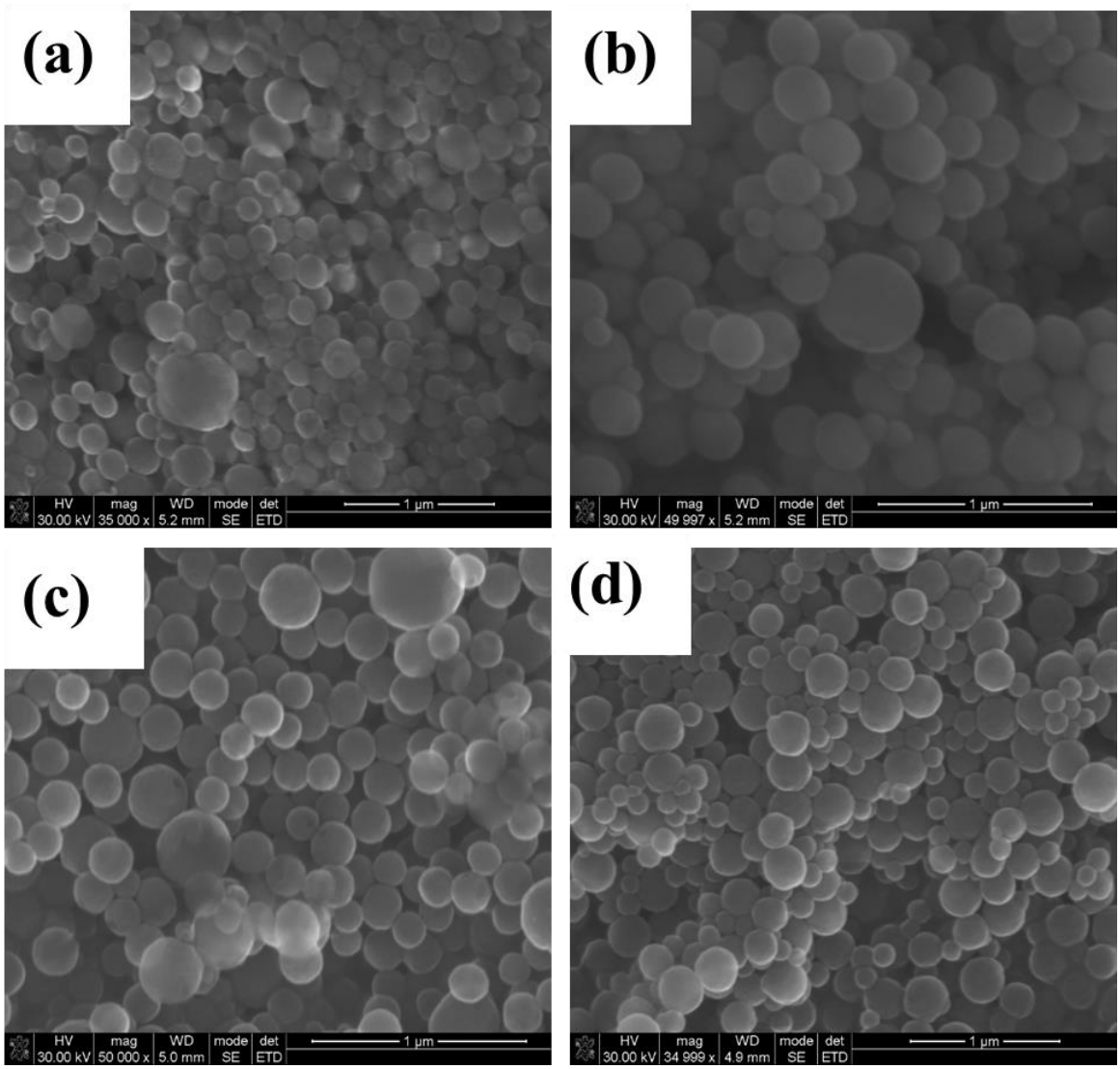



Figure 3. 11: SEM images of polydisperse silica spheres formed with slow addition of TEOS (a) 20 ml.min$^{-1}$ (b) 30 mil. min$^{-1}$ (c) 40 mil.min$^{-1}$ (d) 50 mil.min$^{-1}$ using a syringe pump.

Figure 3.12 (b and d) show that the silica particles are bimodal with particles showing two average diameters of 185 nm and 206 nm respectively. The Figure 3.12b also show a smaller average particle size of 130 nm and a larger average of 250 nm. A similar trend is also shown in Figure 3.11 d where the smaller particles have an average diameter of 150 nm and the larger particles have a diameter of 310 nm.

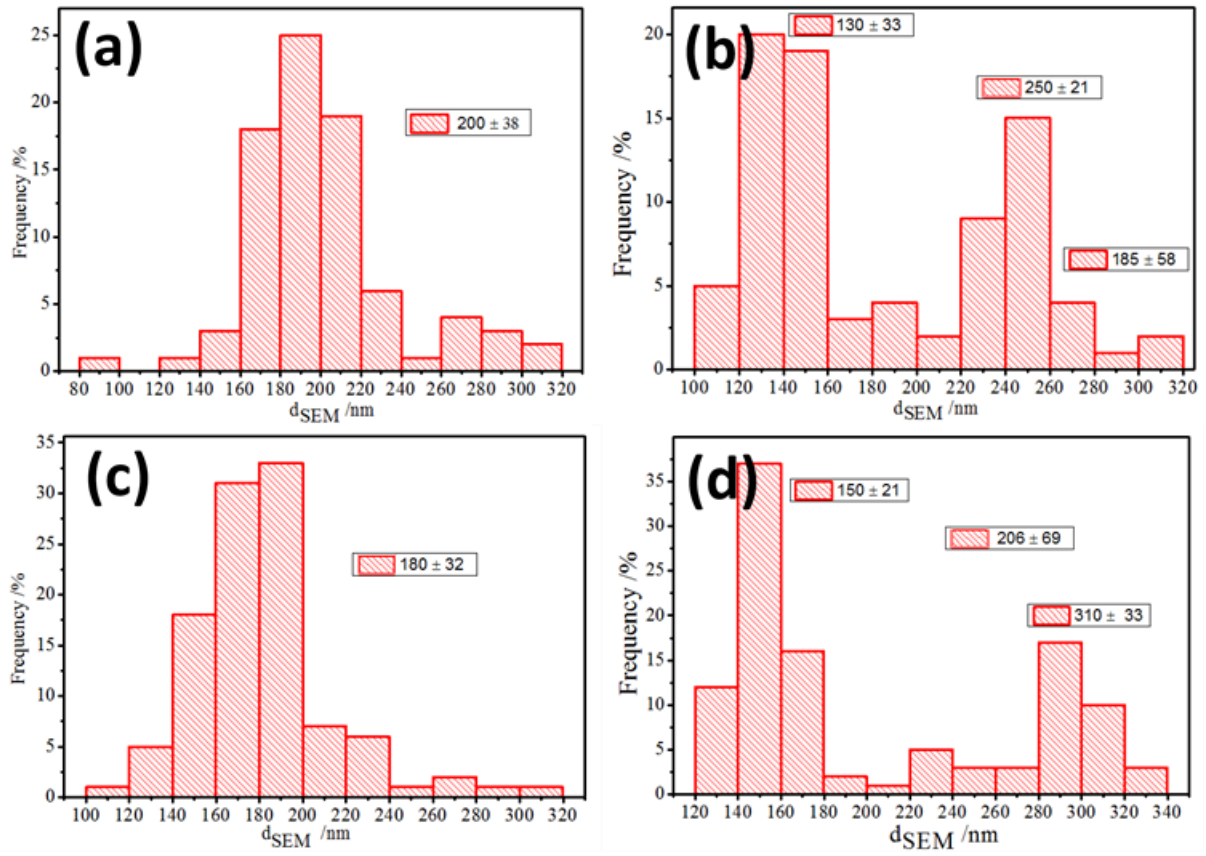



Figure 3.12: Particle size distributions of polydisperse silica spheres formed with slow addition of TEOS (a) 20 ml.min-1 (b) 30 mil. $min^{-1}$ (c) 40 $mil.min^{-1}$ (d) 50 $mil.min^{-1}$ using a syringe pump.

A growth model in which the added TEOS at low concentrations is hydrolysed fully into small silica nuclei can explain the data. Further addition of hydrolysed TEOS monomers results in the formation of more nuclei until the solution is saturated with silica nuclei. Upon further addition of the TEOS precursor, the hydrolysed silica monomers add to the nuclei formed resulting in bigger particles. However not all silica nuclei grow to bigger silica as there is not enough supply of TEOS. This growth models is aligned with the monomer addition growth model suggested by LaMer and co-workers.[25]

## 3.3.4: Effect of EtOH.

The effect of EtOH dilution on the reaction was investigated. In previous studies of the effect of $NH_4OH$, DIW, and TEOS, lower concentrations of EtOH (8 M) were used. In this investigation, a higher concentration of EtOH (15 M) was used to investigate the effect of using very dilute reagents. Small silica particles were formed when dilute solution of reagents was used. The formed silica particles were of a spherical morphology with a smaller average diameter of 82 nm indicating that the use of dilute reagents does indeed result in the formation of smaller particles of silica. However, a degree of aggregation of these small silica particles was noted (Figure 3.13 a and b).

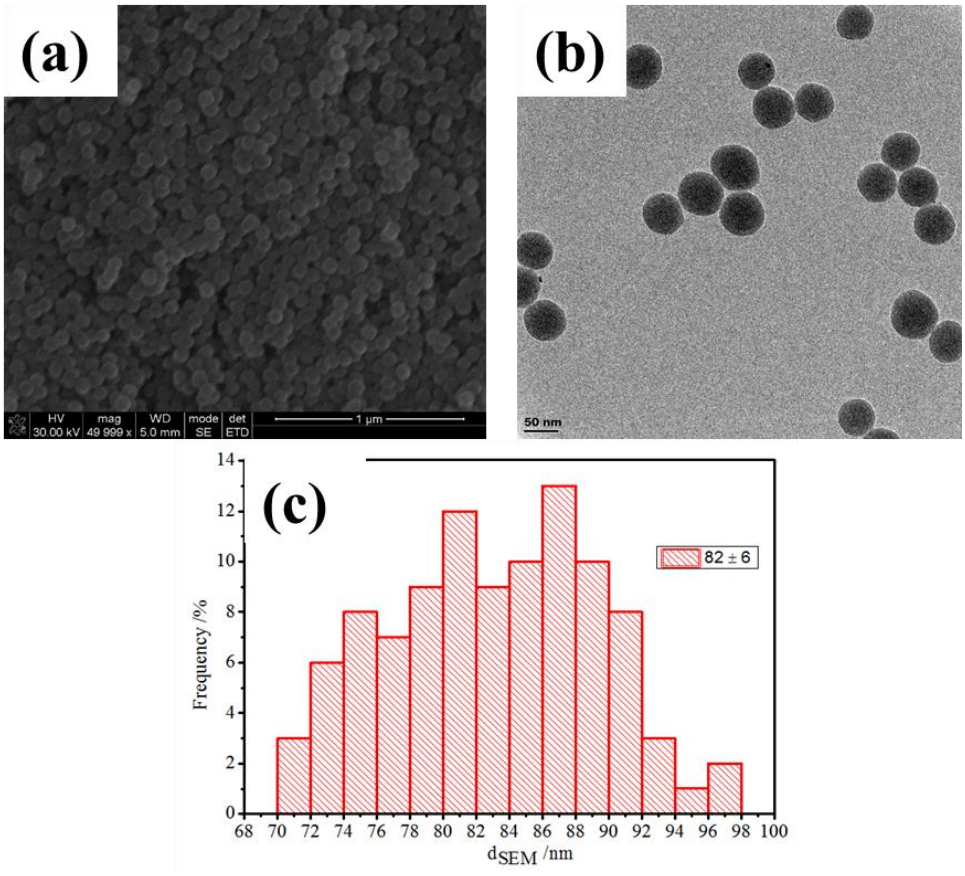



Figure 3.13: SEM(a), TEM(b) images and particle size distribution (c) of the small silica particle (d < 100 nm) formed at low concentrations of TEOS (2 M), $NH_4OH$ (2 M) and DI (5 M) and EtOH (15 M).

## 3.4: Textual properties

## 3.4.1 Effect of DI

To confirm the cross linking due to different levels of water concentration used during the synthesis, the textual properties of the silica formed in these conditions were investigated using BET.[22,36] As shown in the study, DIW was shown to be an important reagent in the formation of silica spheres (section 3.3.3). DIW is needed for the hydrolysis of TEOS to form the silicate species prior to precipitation.[21]

Table 3.4 shows a decrease in BET surface area as the DI concentration was increased. The silica formed with 5 M of DIW had a BET surface area 10 times more than the silica formed using a DIW concentration of 30 M. A similar trend is observed for the pore volume which is 0.41 $cm^3g^{-1}$ for the 5 M DIW reaction compared to the 30 M reaction which is at 0.047 $cm^3g^{-1}$. The BET isotherm data are shown in figure 3.14. The hysteresis loop is attributed to capillary condensation of the adsorbed gas which occurs as a result of the pore structure of the material.[37,38] The absence of the hysteresis loop is further supported by the low pore volumes of the high DIW concentration silica. Silica spheres formed in the presence of high concentrations of DIW tend to be less porous with very low BET surface area below 100 $m^2g^{-1}$. The low BET surface area and low incidence of pores is attributed to the extra cross linking that occurs at the terminal silanol groups resulting in a tight knit silica framework with minimal pores (Table 3.4).

Table 3.4: Comparison of textual properties of silica spheres on different deionized water concentrations

| [DI] /M | 5 | 10 | 15 | 20 | 25 | 30 |
|---|---|---|---|---|---|---|
| BET SA /$m^2$. $g^{-1}$ | 89.87 | 24.21 | 23.93 | 22.10 | 16.83 | 8.62 |
| *Pore Volume /$cm^3$.$g^{-1}$* | 0.41 | 0.025 | 0.023 | 0.021 | 0.025 | 0.047 |
| Pore width /nm | 26.68 | 5.3 | 5.2 | 4.8 | 4.1 | 4.0 |

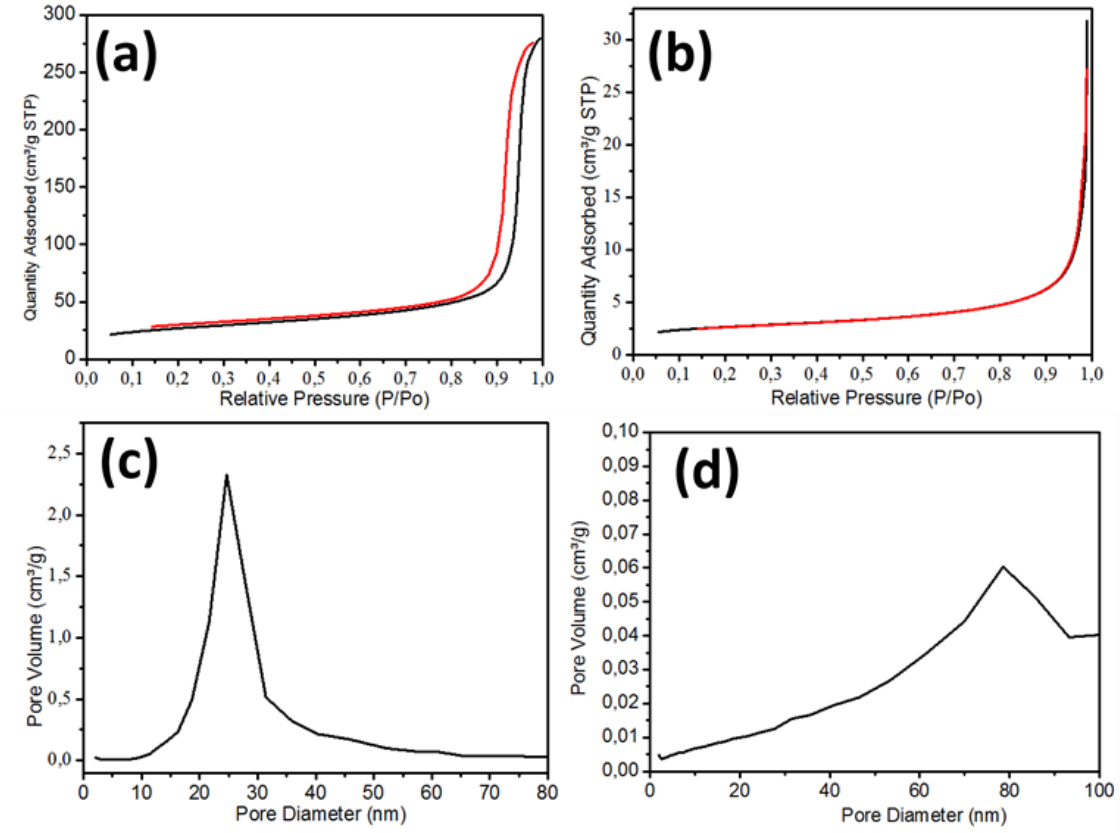



Figure 3. 14: BET properties of the formed silica at varying DI concentrations.

## 3.5: Controlled synthesis of small silica particles

The synthesis of small silica particles is a difficult exercise. A balance must be reached by the use of less concentrated ammonia to initiate hydrolysis and condensation and a sufficient ammonia concentration to build the spherical morphology and at the same time to limit accelerated nucleation and particle growth. At the optimum point, too much ammonia solution would result in the formation of large particles as aggregative growth or monomer addition would occur. A lower ammonia solution would result in the formation of silica flocculates of undefined morphology due to the scarcity of the morphology catalyst (figure 1.09). Further, this study reveals that dilute concentrations are critical to the formation of small silica particles. However, TEOS also limits nucleation. Monomer addition or aggregative growth occurs until the TEOS is used up leading to small particles of different sizes. Due to the variations in surface energy of these small particles of different size, aggregative growth can occur resulting in small and uniformly distributed particles. The dilute solution enabled reasonable separation between these small particles such that aggregative growth was limited.

## 3.6: Conclusions

Silica particles were formed by the hydrolysis, condensation and precipitation of TEOS in the presence of the ammonia catalyst. Low concentrations of ammonia result in the formation of silica particles with undefined morphology and confirm that ammonia is a morphology catalyst. Optimum and low concentrations of ammonia solution are seen to facilitate controlled hydrolysis resulting in a nucleation process that yields smaller silica templates. An increase in the ammonia concentration resulted in the formation of bigger silica particles as the rate of condensation was increased resulting in the primary addition of hydrolysed TEOS monomers.

It was noted that a nonlinear increase in silica particle size occurred if the ammonia solution was exponentially increased at a constant TEOS concentration. We believe that when the TEOS

concentration is not increased at higher ammonia doses, growth of silica particles will level off as there would be no more TEOS monomers to add to the silica cores. Even if the pre-existing smaller silica nuclei are reverse hydrolysed and deposited on the bigger cores, still a final particle size would be reached. Controlled hydrolysis of TEOS also resulted in smaller silica particles. Lower concentrations of TEOS resulted in smaller silica spheres compared to higher concentrations. It was proposed that at lower TEOS concentrations and enough DI, EtOH and ammonia solution, hydrolysis of TEOS occurs faster resulting in the formation of numerous silica nuclei in a process known as nucleation. As the TEOS concentration is low, the further growth of these nuclei is diminished resulting in the formation of small, monodispersed silica at the critical precipitation point. This only occurs with TEOS as it is the primary building block in the building of silica particles.

In the presence of sufficiently large amounts of TEOS, the hydrolysis process proceeds at a fast rate forming nuclei which grows bigger as hydrolysed TEOS monomers are added. The primary addition of TEOS monomers becomes the primary driver of particle growth.

DI has been shown to be an important particle size growth driver. Low concentrations of DI promote subdued hydrolysis and condensation resulting in the nucleation of small silica particles. As the DI concentration is increased, enough hydrolysis of the TEOS occurs resulting in the primary addition of these monomers forming bigger particles. The increase in size can only occur as long there is enough amounts of TEOS as growth would tail off once TEOS is diminished.

Ethanol has been used as a dilution material apart from its role in the hydrolysis and condensation. To form the very small silica particles, large amounts of EtOH were used to dilute the concentrations of the reagents. At optimum amounts of reagents, the data shows that nucleation occurred at a reasonably faster rate. However, as these nuclei diffuse in the large

EtOH solution, they are reasonably separated from one another such that even when small amounts of hydrolysed TEOS are deposited, growth is kept to the minimum. Due to the dilution effect of EtOH, aggregative growth is also minimised as these particles are enough distance apart from one another.

We were successful in synthesizing the very small silica particles as shown in figure 3.13. The silica particles were used as templates in the synthesis of novel broken bowl like hollow carbon spheres and the nitrogen doped counterparts. The materials were subsequently applied as oxygen reduction reaction catalysts with promising area and mass specific activity.

## 3.7: References


(1) Slowing, I. I.; Trewyn, B. G.; Giri, S.; Lin, V. S.-Y. Mesoporous Silica Nanoparticles for Drug Delivery and Biosensing Applications. *Advanced Functional Materials* **2007**, *17* (8), 1225–1236.

(2) Singh, P.; Srivastava, S.; Singh, S. K. Nanosilica: Recent Progress in Synthesis, Functionalization, Biocompatibility, and Biomedical Applications. *ACS Biomaterials Science and Engineering* **2019**, *5* (10), 4882–4898.

(3) Ho, K. Y.; McKay, G.; Yeung, K. L. Selective Adsorbents from Ordered Mesoporous Silica. *Langmuir* **2003**, *19* (7), 3019–3024.

(4) Su, F.; Zhao, X. S.; Wang, Y.; Wang, L.; Lee, J. Y. Hollow Carbon Spheres with a Controllable Shell Structure. *J. Mater. Chem.* **2006**, *16* (45), 4413–4419.

(5) Bailey, J. K.; Mecartney, M. L. Formation of Colloidal Silica Particles from Alkoxides. *Colloids and Surfaces* **1992**, *63*(1–2), 151–161. https://doi.org/10.1016/0166-6622(92)80081-C.

(6) Harris, M. T.; Brunson, R. R.; Byers, C. H. The Base-Catalysed Hydrolysis and Condensation Reactions of Dilute and Concentrated TEOS Solutions. *Journal of Non-Crystalline Solids* **1990**, *121* (1–3), 397–403.

(7) Matsoukas, T.; Gulari, E. Dynamics of Growth of Silica Particles from Ammonia-Catalyzed Hydrolysis of Tetra-Ethyl-Orthosilicate. *Journal of Colloid And Interface Science* **1988**, *124* (1), 252–261.

(8) Plumeré, N.; Speiser, B.; Dietrich, B.; Albert, K.; Pesek, J. J.; Matyska, M. T. Thermally Induced Radical Hydrosilylation for Synthesis of C18 HPLC Phases from Highly Condensed Sih Terminated Silica Surfaces. *Langmuir* **2009**, *25* (23), 13481–13487.

(9) Badley, R. D.; Ford, W. T.; McEnroe, F. J.; Assink, R. A. Surface Modification of Colloidal Silica. *Langmuir* **1990**, *6* (4), 792–801.

(10) Look, J. L.; Bogush, G. H.; Zukoski, C. F. Colloidal Interactions during the Precipitation of Uniform Submicrometre Particles. *Faraday Discussions of the Chemical Society* **1990**, *90*, 345–357.

(11) Green, D. L.; Lin, J. S.; Lam, Y. F.; Hu, M. Z. C.; Schaefer, D. W.; Harris, M. T. Size, Volume Fraction, and Nucleation of Stober Silica Nanoparticles. *Journal of Colloid and Interface Science* **2003**, *266* (2), 346–358.

(12) Bogush, G. H.; Zukoski IV, C. F. Studies of the Kinetics of the Precipitation of Uniform Silica Particles through the Hydrolysis and Condensation of Silicon Alkoxides. *Journal of Colloid And Interface Science* **1991**, *142* (1), 1–18.

(13) Matsoukas, T.; Gulari, E. Monomer-Addition Growth with a Slow Initiation Step: A Growth Model for Silica Particles from Alkoxides. *Journal of Colloid And Interface Science* **1989**, *132* (1), 13–21.

(14) Lee, K.; Sathyagal, A. N.; McCormick, A. V. A Closer Look at an Aggregation Model of the Stober Process. *Colloids and Surfaces A: Physicochemical and Engineering Aspects* **1998**, *144* (1–3), 115–125.

(15) Stöber, W.; Fink, A.; Bohn, E. Controlled Growth of Monodisperse Silica Spheres in the Micron Size Range. *Journal of Colloid and Interface Science* **1968**, *26* (1), 62–69.

(16) Chan, H.B.S.; Budd, P.M.; Naylor, T. Control of Mesostructured Silica Particle Morphology. *Journal of Materials Chemistry* **2001**, *11* (3), 951–957.

(17) Kobayashi, M.; Juillerat, F.; Galletto, P.; Bowen, P.; Borkovec, M. Aggregation and Charging of Colloidal Silica Particles: Effect of Particle Size. *Langmuir* **2005**, *21* (13), 5761–5769.

(18) van Blaaderen, A.; Kentgens, A. P. M. Particle Morphology and Chemical Microstructure of Colloidal Silica Spheres Made from Alkoxysilanes. *Journal of Non-Crystalline Solids* **1992**, *149* (3), 161–178.

(19) Dove, P. M.; Craven, C. M. Surface Charge Density on Silica in Alkali and Alkaline Earth Chloride Electrolyte Solutions. *Geochimica et Cosmochimica Acta* **2005**, *69* (21), 4963–4970.

(20) Destribats, M.; Faure, B.; Birot, M.; Babot, O.; Schmitt, V.; Backov, R. Tailored Silica Macrocellular Foams: Combining Limited Coalescence-Based Pickering Emulsion and Sol–Gel Process. *Advanced Functional Materials* **2012**, *22* (12), 2642–2654.

(21) Yokoi, T.; Wakabayashi, J.; Otsuka, Y.; Fan, W.; Iwama, M.; Watanabe, R.; Aramaki, K.; Shimojima, A.; Tatsumi, T.; Okubo, T. Mechanism of Formation of Uniform-Sized Silica Nanospheres Catalyzed by Basic Amino Acids. *Chemistry of Materials* **2009**, *21* (15), 3719–3729.

(22) Issa, A. A.; El-Azazy, M.; Luyt, A. S. Polymerization of Organoalkoxysilanes: Kinetics of the Polycondensation Progress and the Effect of Solvent Properties and Salts Addition. *Chemical Physics* **2020**, *530*.

(23) Yao, L.; Xu, G.; Dou, W.; Bai, Y. The Control of Size and Morphology of Nanosized Silica in Triton X-100 Based Reverse Micelle. *Colloids and Surfaces A: Physicochemical and Engineering Aspects* **2008**, *316* (1), 8–14.

(24) Liau, L. C. K.; Chen, Y. T. Process Optimization of Preparing Silica Particles with Uniform Distribution in Sub-Micron Sizes Using Artificial Neural Networks. *Colloids and Surfaces A: Physicochemical and Engineering Aspects* **2006**, *286* (1–3), 138–143.

(25) Lamer, V. K.; Dinegar, R. H. Theory, Production and Mechanism of Formation of Monodispersed Hydrosols. *Journal of the American Chemical Society* **1950**, *72* (11), 4847–4854.

(26) Chen, S.-L.; Dong, P.; Yang, G.-H.; Yang, J.-J. Characteristic Aspects of Formation of New Particles during the Growth of Monosize Silica Seeds. *Journal of Colloid and Interface Science* **1996**, *180* (1), 237–241.

(27) Krauskopf, K. B. Dissolution and Precipitation of Silica at Low Temperatures. *Geochimica et Cosmochimica Acta* **1956**, *10* (1), 1–26.

(28) Rahman, I. A.; Vejayakumaran, P.; Sipaut, C. S.; Ismail, J.; Bakar, M. A.; Adnan, R.; Chee, C. K. An Optimized Sol-Gel Synthesis of Stable Primary Equivalent Silica Particles. *Colloids and Surfaces A: Physicochemical and Engineering Aspects* **2007**, *294* (1–3), 102–110.

(29) Bogush, G. H.; Zukoski, C. F. Uniform Silica Particle Precipitation: An Aggregative Growth Model. *Journal of Colloid and Interface Science* **1991**, *142* (1), 19–34.

(30) Zulfiqar, U.; Subhani, T.; Husain, S. W. Synthesis and Characterization of Silica Nanoparticles from Clay. *Journal of Asian Ceramic Societies* **2016**.

(31) Han, Y.; Lu, Z.; Teng, Z.; Liang, J.; Guo, Z.; Wang, D.; Han, M.-Y.; Yang, W. Unraveling the Growth Mechanism of Silica Particles in the Stöber Method: In Situ Seeded Growth Model. *Langmuir* **2017**, *33* (23), 5879–5890.

(32) Crerar, D. A.; Axtmann, E. V.; Axtmann, R. C. Growth and Ripening of Silica Polymers in Aqueous Solutions. *Geochimica et Cosmochimica Acta* **1981**, *45* (8), 1259–1266.

(33) Qiao, Z.A.; Zhang, L.; Guo, M.; Liu, Y.; Huo, Q. Synthesis of Mesoporous Silica Nanoparticles via Controlled Hydrolysis and Condensation of Silicon Alkoxide. *Chem. Mater.* **2009**, *21* (16), 3823–3829.

(34) Boukari, H.; Long, G. G.; Harris, M. T. Polydispersity during the Formation and Growth of the Stöber Silica Particles from Small-Angle X-Ray Scattering Measurements. *Journal of Colloid and Interface Science* **2000**, *229* (1), 129–139.

(35) Plumeré, N.; Ruff, A.; Speiser, B.; Feldmann, V.; Mayer, H. A. Stöber Silica Particles as Basis for Redox Modifications: Particle Shape, Size, Polydispersity, and Porosity. *Journal of Colloid and Interface Science* **2012**, *368* (1), 208–219.

(36) Plumeré, N.; Speiser, B. Redox-Active Silica Nanoparticles. Part 2. Photochemical Hydrosilylation on a Hydride Modified Silica Particle Surface for the Covalent Immobilization of Ferrocene. *Electrochimica Acta* **2007**, *53* (3 SPEC. ISS.), 1244–1251.

(37) Kierlik, E.; Monson, P. A.; Rosinberg, M. L.; Sarkisov, L.; Tarjus, G. Capillary Condensation in Disordered Porous Materials: Hysteresis versus Equilibrium Behavior. *Phys. Rev. Lett.* **2001**, *87* (5), 055701.

(38) Neimark, A. V.; Ravikovitch, P. I. Capillary Condensation in MMS and Pore Structure Characterization. *Microporous and Mesoporous Materials* **2001**, *44–45*, 697–707.

# Chapter 4

# Synthesis and characterization of large HCSs, NHCSs and the Pt supported materials (Pt/HCSs and Pt/NHCSs)

## 4.1: Introduction

Proton exchange membrane fuel cells (PEMFCs) are currently a subject of widespread research as they are a promising energy conversion system applicable in automobiles. [1–3] They have potential to replace the polluting internal combustion engine due to the neutral carbon footprint they possess. For outstanding performance and reliable power output, the PEMFCSs reactions are dependent on electrocatalysts which play the important role of facilitating the fuel cell reactions. The general fuel cell catalysts are platinum particles deposited on top of carbon supports. [4–9] Alloys of Pt with transition metals have also used as fuel cell catalysts.[10–14] However, all these catalyst materials are expensive due to the high cost of platinum and the catalysts also suffer from low durability which has minimised the uptake of fuel cells for commercialization. The low durability of the catalysts due to the support corrosion or agglomeration of the Pt nanoparticles, or the dissolution of the Pt and detachment of the Pt from the support are the major causes of loss of activity of the catalysts and a major contributor to the shortening of the life span of a fuel cell.[15–17]

To mitigate for the loss of durability, various supports have been studied as it is understood that the properties of the support are essential for improving the final properties of activity and durability of a catalysts system. Supports that have been studied with promise in improved activity and durability are doped metal oxides, multiwall carbon nanotube, single wall carbon nanotube, reduced graphene oxide, Vulcan carbon and some nitrogen doped carbons.[18–23]

From these studies, it has become clear that tailoring the structure of the support can improve the resulting catalyst system. Hollow carbon spheres have been attracting huge attention due to their various favourable properties. [24–26] These include their light weight, thermal stability, chemical stability and high surface area among many others. Thus, they are desirable for applications as catalyst electrode supports, composite materials and as gas storage media.[27] Among many methods of synthesising HCSs, the templating method has found widespread application. Other methods include high temperature pyrolysis and hydrothermal methods.[24,25,28,29] Nitrogen doped hollow carbon spheres (NHCSs) also possess favourable properties that are found for the hollow carbon spheres. Nitrogen doping is known to introduce defects in the carbon shell which can enhance the interaction between the support and the metal nanoparticles deposited. Also, the electron density in the extended π–conjugated system of the nitrogen functionalities assists in the electrocatalytic process.[30–32]

HCSs can be made with a range of diameters. If the shell is thin, then the diameter will potentially affect the carbon-carbon bonds that make up the carbon layer. HCSs with a large diameter should not show a large effect as the curvature of the shell will be small. The HCS surface will thus be like that found in a typical graphene layer. Similarly, N doping of large HCSs should have similar properties to those found in N-doped graphene's. However, since the HCSs can be loaded with metals (e.g. Pt) on the outside and inside of the HCSs as well as in the pores of the HCS they will have different properties to those found in graphene supports.

In this study, large, high surface area, graphitic HCSs and NHCSs with thin shells and with a network of pores were synthesized. Small Pt nanoparticles in the 3 -5 nm size were deposited, using the metal-organic deposition technique, on top of these supports. The materials were then tested in the PEMFC oxygen reduction reaction and their activity and durability studied.

## 4.2: Synthesis of the hollow carbon and nitrogen doped hollow carbon spheres.

Silica particles with a diameter of 310 ± 18 nm (Figure 4.1 ) were synthesized according to a modified Stober method.[33] The silica particles were synthesized from the hydrolysis of tetraethyl orthosilicate (TEOS) in the presence of ethanol (EtOH), deionized water (DIW) and ammonia solution ($NH_4OH$). Ammonia solution (25% in water) which was used as both a hydrolysis and condensation catalyst, was also used for the promotion of spherical morphology.[34] The detailed description of the synthesis of spherical silica particles was provided in chapter 2 and chapter 3 of this thesis.

The formed silica particles were used as hard templates [35] for the synthesis of hollow carbon spheres (HCSs) and nitrogen doped hollow carbon spheres (NHCSs). A resorcinol-formaldehyde resin (RF) was used to cover the silica. In the process formaldehyde (1.5 ml) and resorcinol (1.5 g) were added to a suspension of silica particles (3 g) in absolute ethanol (EtOH) (45 ml), ammonia solution ($NH_4OH$) (10 ml) and deionized water (DIW) (210 ml). Cetylammonium bromide (CTAB) (2 g) was added to the mixture to enable the formation of pores in the structure of the RF carbon layer. The mixture was then sonicated in a water bath for 30 minutes whereby the temperature of the water bath and subsequently of the reaction changed from room temperature to about 50 °C. At that point the reaction contents had changed from an off-white colour suspension to light brown due to the formation of the RF resin covering the silica. The reaction was stirred for 24 h and the formed $SiO_2$@RF suspension was filtered, and vacuum washed several times with DI followed by drying

in an oven at 100 °C for 2 h. The dry $SiO_2$@RF was carbonized in a tubular horizontal furnace under a steady argon flow (100 mil.$min^{-1}$) at 900 °C for 2 h and formed a black soot like material $SiO_2$@C which was etched with a 10% solution of HF (48%) to remove the silica and give the HCSs with a yield of 90 % based on the resorcinol used.

After etching, the formed HCSs with an average diameter of about 318 ± 14 nm (figure 4.4) were washed with copious amounts of water (DI) to remove the dissolved silica. The HCSs were annealed in argon at 900 °C for 2 h in a tubular horizontal furnace at a heating rate of 10 °C. $min^{-1}$.

Nitrogen doped hollow carbon spheres (NHCSs) with an average diameter of 320 ± 20 nm (figure 4.4) were synthesized using the similar method as were used to make the HCSs. The variation was that the $SiO_2$@RF (2 g) was mixed with melamine (2 g) and acetone (20 mL) followed by sonication for 30 minutes to obtain a thoroughly mixed composite $SiO_2$@RF@melamine. The composite was carbonized using a similar method as discussed for the HCS synthesis (900 °C for 2 h) albeit at a slower heating rate of 2.5°C.$min^{-1}$. The formed carbon material was etched with HF in a similar manner as used to make the HCSs with a yield of 95% based on the resorcinol used.

## 4.3: Morphology and size of the silica, HCS, and NHCS

The spherical morphology of the formed silica particles was confirmed by SEM images (Figure 4.1). The average diameter of the silica particles was 310 ± 18 nm. The particle size distribution of the silica particles showed a narrow size range.

The spherical morphology, (figure 4.3) particle size and shell thickness (figure 4.4) of the formed HCSs and NHCSs were also confirmed by SEM and TEM analysis. The HCSs and NHCSs had particle sizes of 318 ± 8 nm and 320 ± 11 nm respectively. The thickness of the NHCSs shell (12 ± 6 nm) did not significantly change after nitrogen doping of the HCSs (10 ± 4 nm). The small increase

in the thickness of the shell of the NHCSs material was consistent with the formation of only a few extra layers in the shell due to the melamine added during the post synthesis nitrogen doping process.

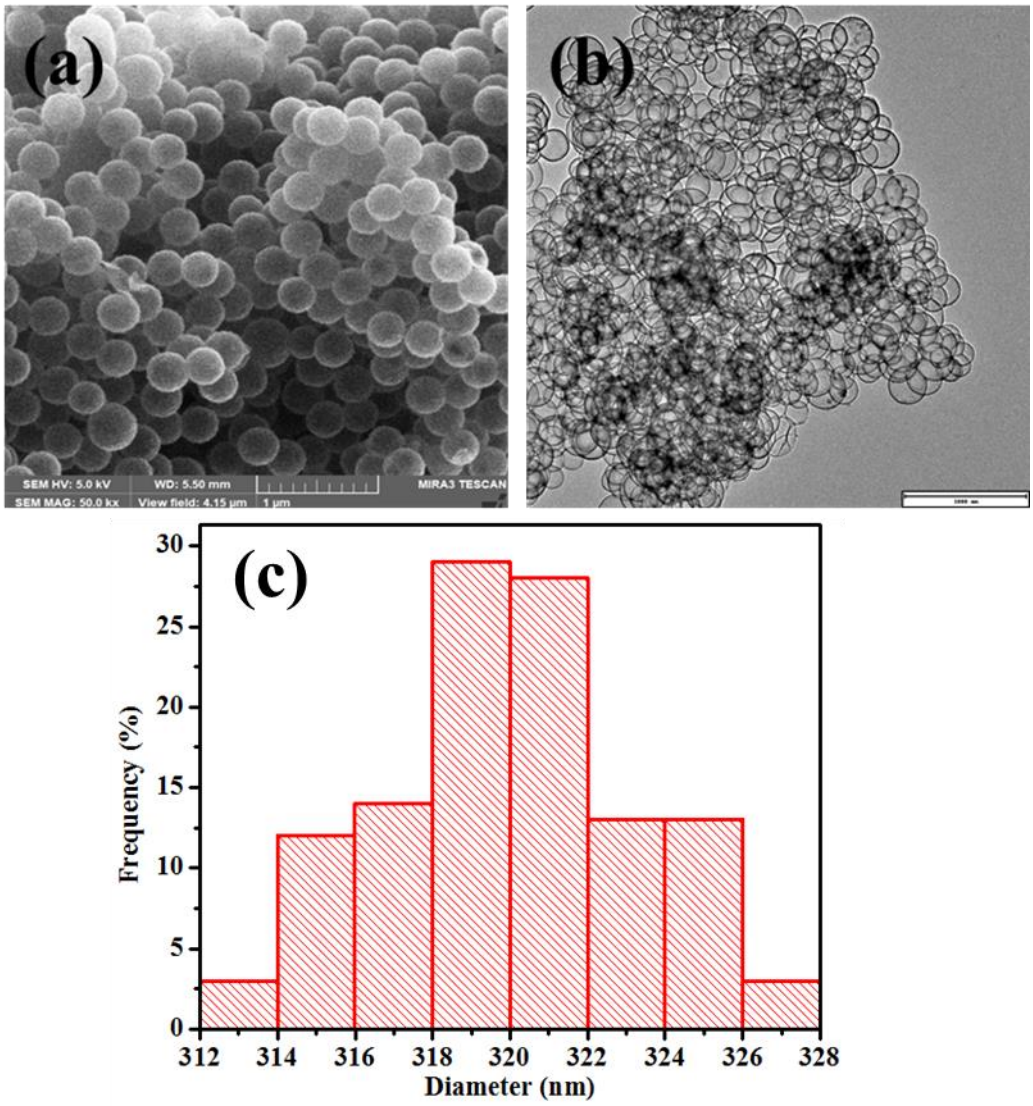



Figure 4.1: SEM micrograph of silica particles (a), TEM micrographs of HCSs (b) and particle size distribution of the HCSs (c).

The particle size distributions of the HCSs and NHCSs (figure 4.4) indicated a uniform distribution of the diameters. The data also indicated that the RF coating was uniform over the spheres. A similar trend in the shell thickness of these materials also confirmed a good coverage during the coating process.

## 4.4: Raman spectroscopy analysis

The extent of graphitization of the materials was investigated using Raman spectroscopy with focus on the D (disorder) and G (graphitic) bands located at about 1350 and 1600 $cm^{-1}$ respectively. (figure 4.2). [36,37] The D band occurred as a result of the vibrational modes of the defects in the $sp^3$ hybridized carbon whereas the G band occurs as a result of the vibrational modes of the $sp^2$ graphite-like hybridized carbons.[38] The D bands could be further deconvoluted into a peak labelled D2 which was attributed to the Raman vibrations for disordered, amorphous and defective carbon present in the sample and a D3 peak that could be attributed to the presence of ionic impurities or polyenes.[8,39]

Raman spectroscopy was also used to study a commercial Pt supported on a Vulcan carbon support material used as a benchmark catalyst. In the highly graphitic Vulcan carbon, the G' or 2G peak is attributed to the disorder occurring in the graphite-like $sp^2$ hybridized carbon and its presence has previously been attributed to the presence of highly graphitized carbon lattices.[40] The $I_D/I_G$ ratio is known to provide information on the graphitic nature of a carbon material[38] The obtained HCSs had an $I_D/I_G$ ratio of 0.97 whereas the nitrogen-doped HCSs had an $I_D/I_G$ ratio of 1.04 (table 4.1). The increase in the $I_D/I_G$ ratio for the doped material indicates an increase in the defect density for the material as nitrogen groups incorporated affects the lattice of the carbon and hence causing defects [41]. The HCSs had narrower D and G bands as evidenced by the smaller full width at half maxima (FWHM) of the peaks compared to the NHCSs, due to the higher degree of $sp^2$ order in the carbon lattice of the pristine HCSs. The FWHM of the pristine HCS was also broader compared to that of the doped NHCSs, another indication of increased crystallinity in the structure of the HCSs compared to the NHCSs. The G band of the HCSs appeared at 1588 $cm^{-1}$ compared to the G band of the NHCSs which occurred at 1590 $cm^{-1}$. This upward shift for the doped material is another indication of the increased defects in the doped material compared to the undoped material. This is also confirmed by the size of the D2 peak for the NHCSs which is bigger than that of HCSs.

The G peak of the Vulcan carbon occured at a lower Raman frequency compared to the HCSs and NHCSs supports and also a distinct G' peak was observed for this material, an indication of higher graphitization and fewer defect sites compared to the HCS/NHCS materials.[42]

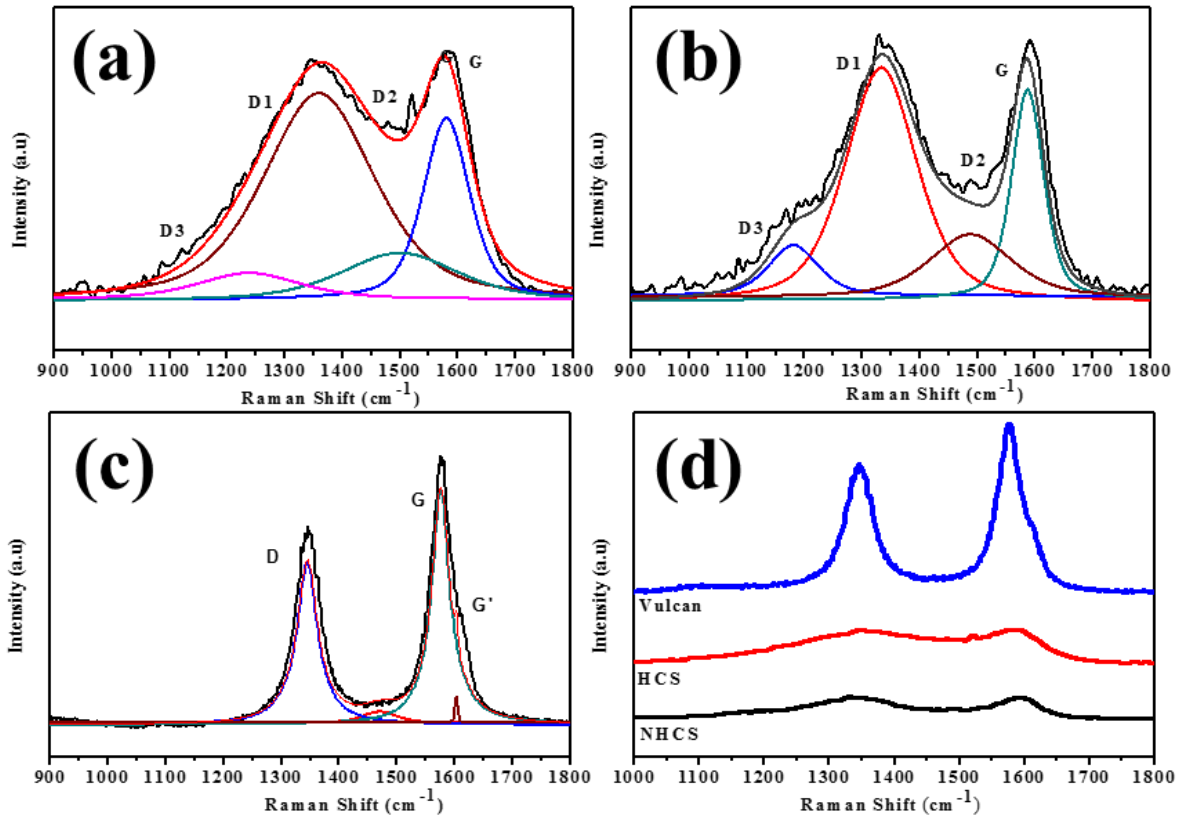



Figure 4.2: Deconvoluted Raman spectra of (a) HCSs, (b) NHCSs, (c) Vulcan carbon and (d) stacked Raman spectra for all supports showing the different G peak positions.

Table 4. 1: Raman spectroscopy data for the HCSs, NHCSs and Vulcan carbon

| | D band | | | G band | | | |
|---|---|---|---|---|---|---|---|
| | FWHM | Intensity | Position | FWHM | Intensity | Position | $I_D/I_G$ |
| Vulcan | 44 | 449 | 1345 | 38 | 649 | 1576 | 0.69 |
| NHCSs | 148 | 86 | 1354 | 80 | 77 | 1590 | 1.12 |

| | | | | | | | |
|---|---|---|---|---|---|---|---|
| HCSs | 144 | 110 | 1334 | 66 | 104 | 1588 | 1.06 |

## 4.5: Synthesis of Pt/HCSs and Pt/NHCSs

The formed HCSs and NHCSs materials were used as supports for Pt nanoparticles. These materials were latter applied as oxygen reduction reaction catalysts for fuel cells. The platinum nanoparticles were deposited on top of these supports using a well-established method known as metal–organic deposition.[43] In a typical deposition synthesis procedure, to attain a nominal 40 wt.% catalyst, HCSs or NHCSs (150 mg) were mixed with a platinum precursor salt, platinum acetylacetonate ($Pt(acac)_2$ (202 mg), in a borosilicate glass vial. The vial was sealed and sonicated for 30 min to allow for the homogeneous mixing of the materials. The mixed materials were loaded into a cylindrical steel reactor and placed inside a tubular horizontal furnace. The furnace was ramped to 250 °C at a slow heating rate (5 °C. $min^{-1}$) followed by a 2 h hold at the same temperature. Meanwhile, argon gas at a slow flow rate (20 $ml.min^{-1}$) was constantly flowed through the reactor to maintain an inert atmosphere, to prevent the combustion of the carbon at the elevated temperatures. The reactor was cooled to room temperature after completion of the reaction. The formed Pt/HCSs and Pt/NHCSs were collected and characterized using TEM, SEM, TGA, XPS, PXRD, DF-STEM. Finally, the materials were characterized using cyclic voltammetry and linear sweep voltammetry to quantify their suitability for application as fuel cell catalysts.

## 4.6: Pt/HCSs and Pt/NHCSs materials

Uniform and small quasi-spherical platinum nanoparticles were successfully deposited on the HCS and NHCS supports. (Figure 4.3) The Pt nanoparticles deposited on the NHCSs ($4.0 \pm 0.6$) were slightly smaller than those deposited on the HCSs supports ($4.2 \pm 0.5$) respectively (table 4.2). The TEM images (figure 4.3) confirmed the uniform distribution of the Pt on these supports. The relatively smaller average particle size of the Pt on the Pt/NHCS were attributed to the nitrogen

doping. The electron density of the nitrogen groups affects the nucleation and growth kinetics of metal nanoparticles resulting in smaller nanoparticles being formed. Nitrogen doping introduced defects on the supports, creating numerous sites where Pt could be deposited. These defects and the enhanced surface area of the support provided numerous sites on the supports where nucleation and growth of the Pt nanoparticles could be initiated and occur.

The numerous sites were evidenced by a smaller Pt-Pt distance (5.8 ± 0.3 nm) on the NHCSs compared to the HCSs (6.3 ± 0.8 nm), (Table 4.2). Shorter inter Pt particle distance are known to enhance the catalytic performance due to a better electronic interaction between neighbouring Pt nanoparticles. The electron density on the nitrogen groups was responsible for the restricted growth of the Pt nanoparticles.[44,45]

SEM micrographs of the Pt/HCSs and Pt/NHCSs (Figure 4.3) did not show the Pt nanoparticles deposited on the surface of these materials due to the small size of the Pt. SEM images did confirm the spherical morphology of the HCSs and that the post doping with nitrogen via the melamine pyrolysis route rendered some surface roughness to the NHCSs (Figure 4.3 (b) due to the additional melamine layer and the defects formed.[46]

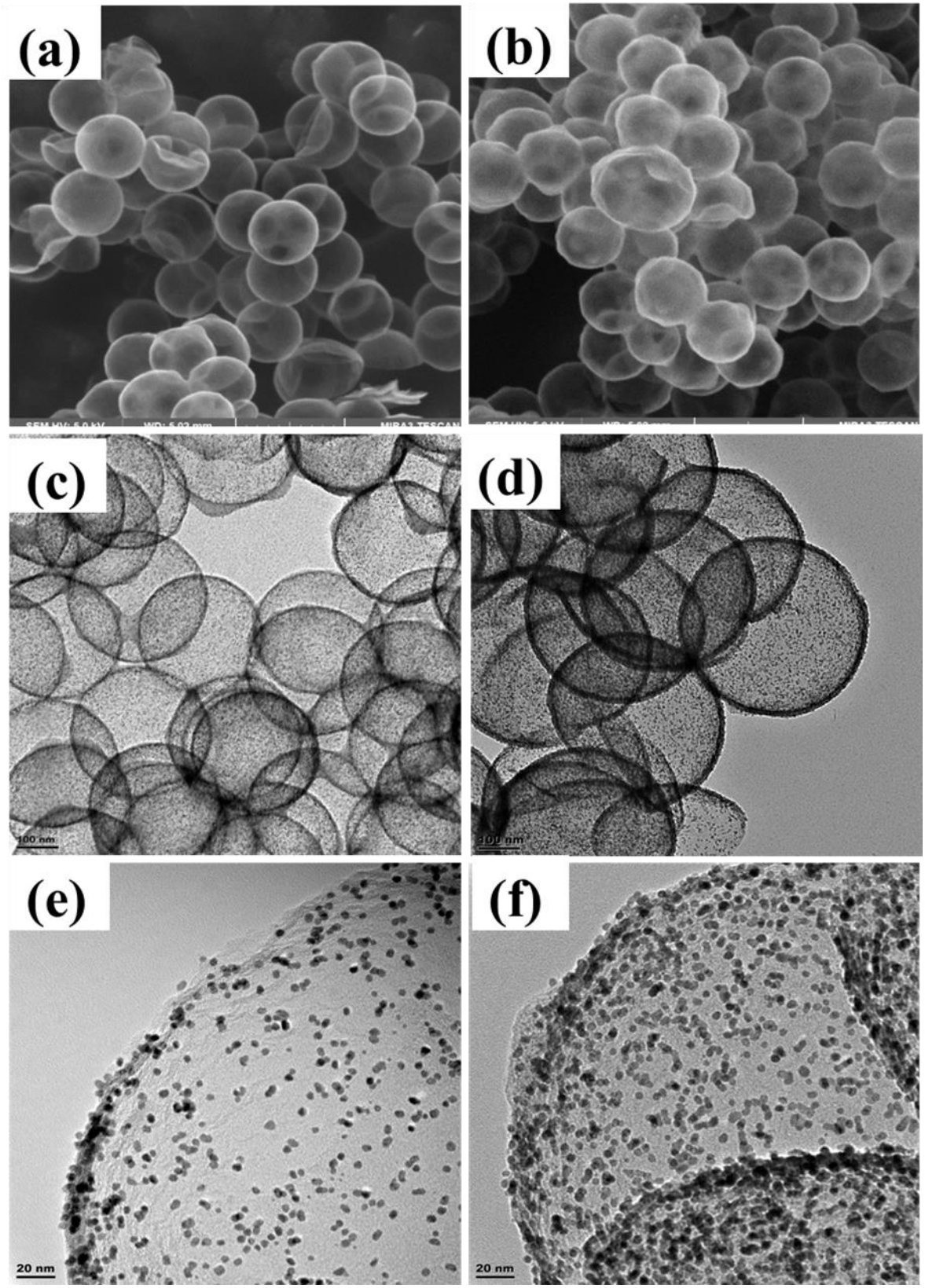



Figure 4.3: SEM image of Pt/HCSs (a), SEM image of Pt/NHCSs (b), TEM image of Pt/HCSs (c), TEM image of Pt/NHCSs (d), higher magnification TEM image of Pt/HCSs (e) and higher magnification TEM image of Pt/NHCSs (f).

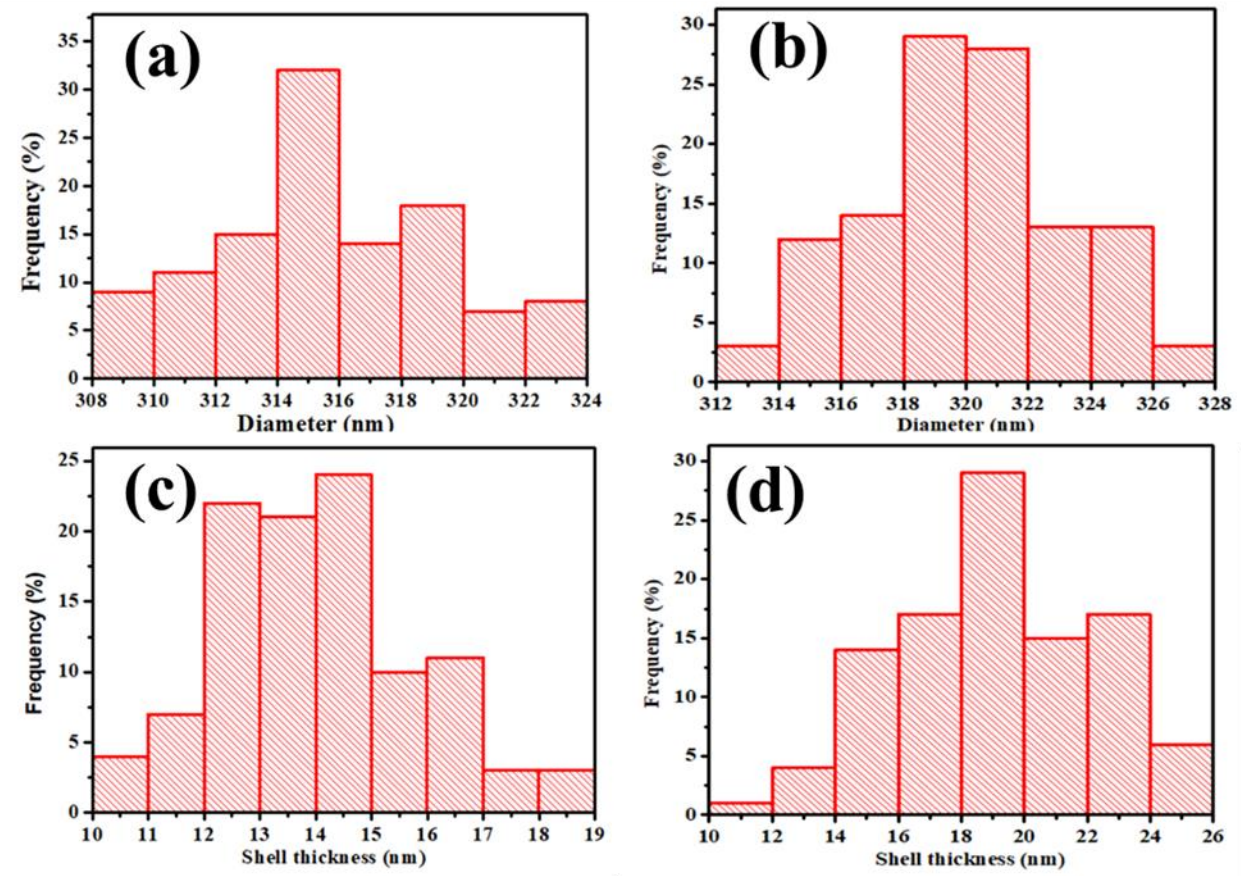



Figure 4.4: Diameter distribution of HCSs (a) and NHCSs (b), shell thickness distribution of HCSs (c) and NHCSs (d)

Table 4.2: Comparison of the Pt particle size and the Pt – Pt distance of the Pt/HCSs and Pt/NHCSs

| | TEM particles | |
|---|---|---|
| Sample | Pt size /nm | Pt – Pt distance /nm |
| Pt/HCSs | 4.2 ± 0.5 | 6.3 ± 0.8 |
| Pt/NHCSs | 4.0 ± 0.6 | 5.8 ± 0.3 |

## 4.7: Thermal gravimetric analysis (TGA)

Both the HCSs and NHCSs gave a residual weight% of < 3 % after the thermogravimetric analysis (TGA) process (figure 4.5). The TGA process was conducted from 25 - 900°C with a heating rate of 10°C.min$^{-1}$ and an oxygen flow rate of 10 ml.min$^{-1}$. The low residual weight below 3% was an indication that the silica etching process was complete. The NHCSs had an early onset decomposition temperature (396 ºC) compared to the onset of the HCSs (450 ºC) material and Vulcan carbon (526 ºC). The final decomposition temperature for the HCSs (652 °C) indicated a higher thermal stability compared to the NHCSs (647 °C). The Vulcan had a higher decomposition final temperature (712 ºC). The lower decomposition temperature for the NHCS material was attributed to the defects that are present as a result of the doping with nitrogen.[46] Vulcan has a higher decomposition temperature due to its higher extent of graphitization and fewer defects, as supported by the Raman spectroscopy data (Table 4.1). The higher decomposition temperature of both the HCSs and the NHCSs indicated good crystallinity in the material and lower levels of amorphous carbon.

The Pt decorated catalysts Pt/Vulcan, Pt/HCSs and Pt/NHCSs were also studied using TGA. The TGA profiles showed that for all the three catalysts, the thermal stability of the materials dramatically decreased compared to the pristine supports. The supports decomposed completely between 390 – 720 ºC for all the material whereas when loaded with Pt, the decomposition occurred between 339 - 450 ºC (Figure 4.5). Platinum is a known oxidation and combustion catalyst[47,48] and its presence on the surface of these supports and inside the pore structure made the material prone to combustion. The higher defect density coupled with the presence of Pt in Pt/NHCSs caused instability and hence an early onset decomposition temperature. (339 ºC) (Figure 4.5).

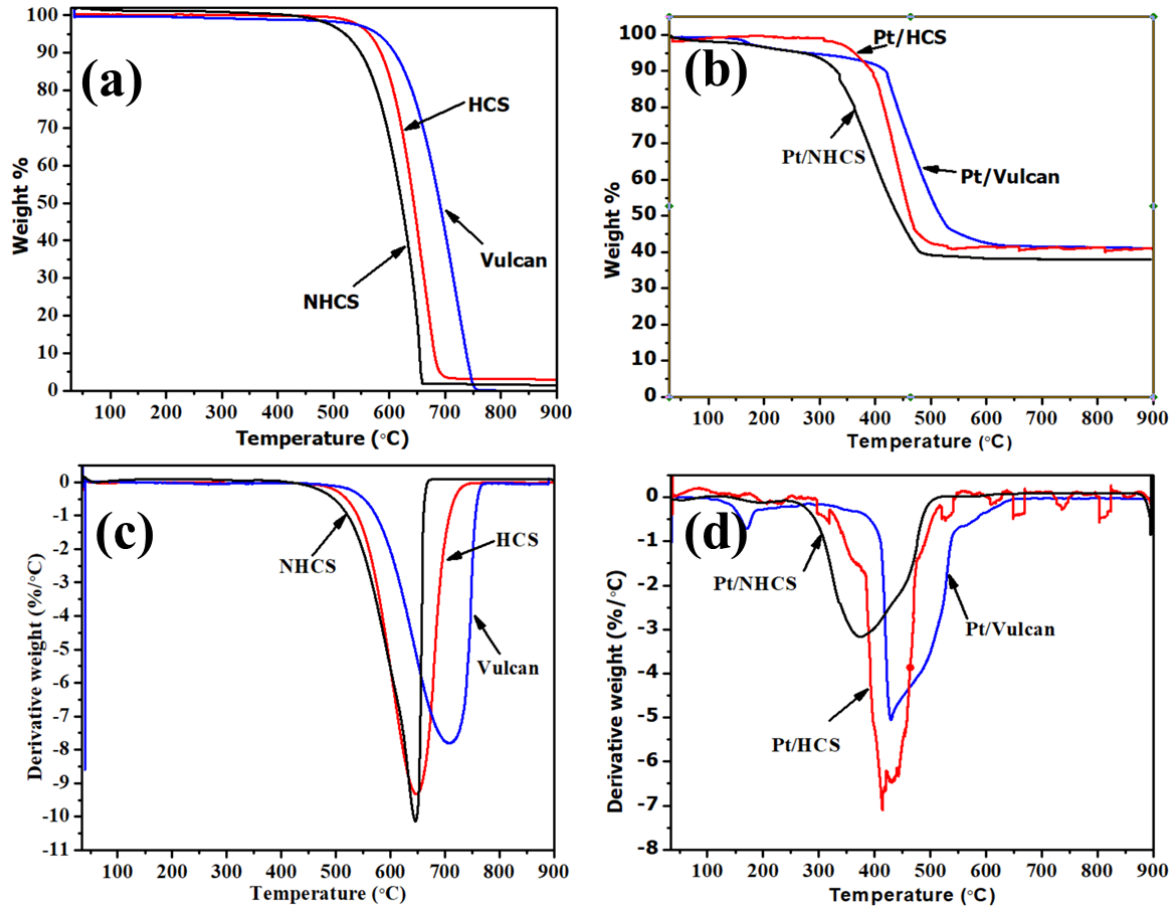



Figure 4.5: (a) TGA profiles of HCSs, NHCSs and Vulcan and (b) the corresponding derivative profiles. (c) TGA profiles of Pt/HCSs, Pt/NHCSs, Pt/Vulcan (d) and the corresponding derivative profiles.

The TGA profile also showed more than two distinct decomposition steps which are an indication of different types of carbon present in the material. The amorphous carbon which is rich in defects tend to have early combustion and decomposition temperatures compared to highly ordered and graphitic carbon like graphite or graphene[49,50] Therefore the less ordered defective carbon exhibits an early onset at 200 ºC and the highly ordered graphite-like carbon initiates combustion at 350 ºC. The Pt/HCSs has a later decomposition onset (362 ºC) due to its highly ordered carbon and smaller defect density. (Figure 4.5).

For the Pt/Vulcan commercial catalyst, the onset degradation temperature was higher (429 ºC). The higher decomposition onset for the Pt/Vulcan catalysts can be attributed to a lower number of defect

sites. Raman data (Table 4.1) showed sharper peaks for the D and the G bands, an indication of crystallinity and higher long-range order in the carbon lattices.

The residue after thermal treatment was attributed to solid metal platinum with traces of platinum oxide (confirmed by XPS, section 4.10) nanoparticles and was used to confirm the actual loading of the catalysts. The Pt loading were determined to be 38.5 wt. % for Pt/Vulcan, 39.4 wt. % Pt/HCSs and 38.2 wt. % for the Pt/NHCSs materials. All three materials had comparable amounts of the active catalyst and the effects of the support structure could be compared between these materials.

## 4.8: Surface area and porosity of the supports and the catalysts

The surface area and porosity of all the materials (HCSs, NHCSs, Pt/HCSs and Pt/NHCSs) were studied using nitrogen physisorption–desorption. The BET equations were used to calculate the surface area and pore properties. The materials were observed to have a mesoporous structure and type IV BET isotherms (Figure 4.6) [51,52] which are characterized by monolayer gas adsorption at low relative pressure and multi-layer adsorption of gas molecules at higher relative pressure. The BET surface area for the HCSs was 577 $m^2.g^{-1}$ whereas for the NHCSs it was 519 $m^2.g^{-1}$. The slightly higher surface area for the NHCSs was probably because of the thin additional layer of melamine added to the surface of the HCSs during nitrogen doping. Nitrogen doping also introduced defects in the carbon structure. The additional melamine layer and the defects were responsible for the creation of new defects surface area.[53] HCSs and NHCSs had comparable pore volume of 0.31 $cm^3.g^{-1}$ and 0.32 $cm^3.g^{-1}$ respectively. The pore diameters for these carbon materials were between 4.5 and 5.0 nm which would enable the confinement of platinum nanoparticles with an average diameter of 4.0 nm.

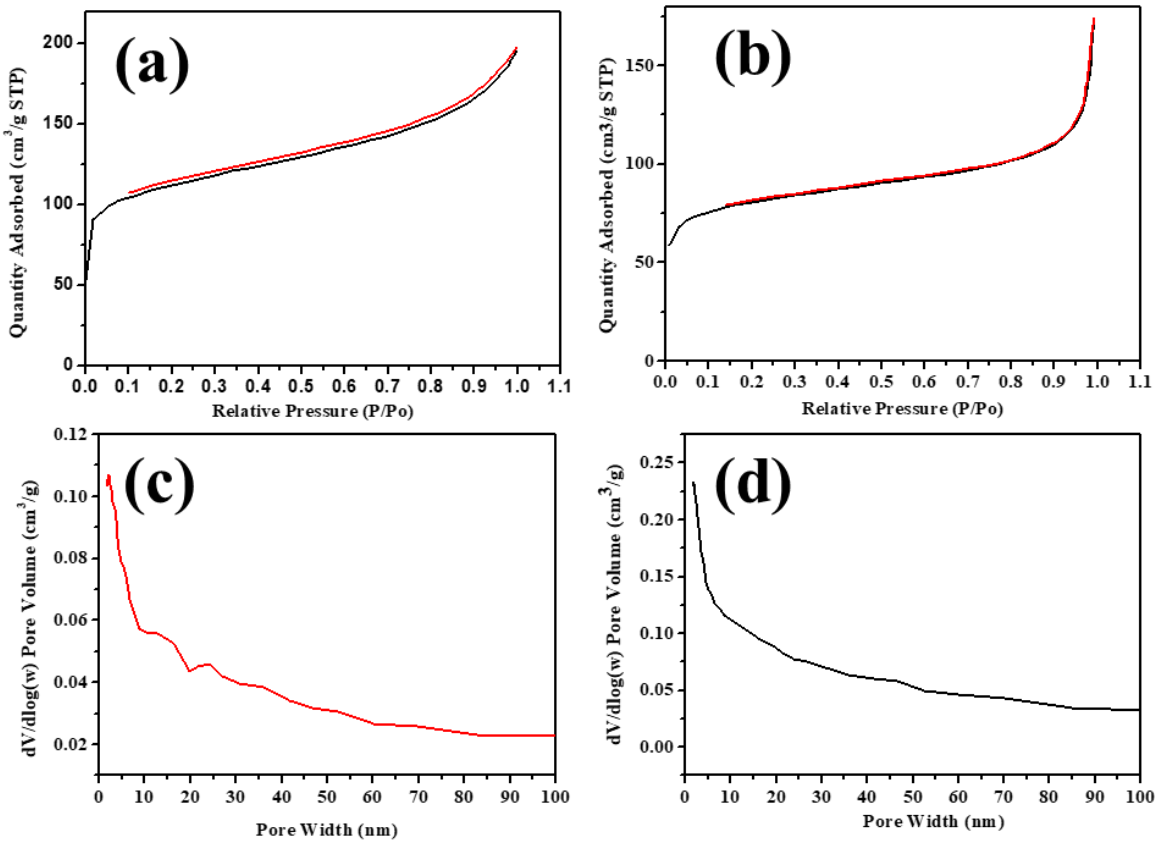



Figure 4. 6: Type II BET isotherm for HCSs (a) and NHCSs (b), Pore size distribution for HCSs (c) and for NHCSs (d)

After deposition of Pt nanoparticles on the HCSs, the BET surface area was reduced to 312 $m^2.g^{-1}$, a 46 % reduction in the Pt/HCSs catalyst surface area. For the NHCSs support, the BET surface was reduced to 363 $m^2.g^{-1}$ for the Pt/NHCSs catalyst, a reduction of 30 % in the surface area. This was accompanied by a corresponding 38 % reduction in pore volume to 0.19 $cm^3.g^{-1}$ and a 51% reduction in pore width to 2.2 nm respectively for the HCSs when compared to the supported Pt/HCSs. Similar pore volume reductions for the Pt/NHCSs relative to the NHCSs were observed with a 38% reduction in pore volume to 0.20 $cm^3.g^{-1}$. This was accompanied by a 50% reduction in pore width to 2.5 nm (Table 4.3). However, the BET isotherms remained type IV isotherms after Pt deposition, suggesting that multilayer gas adsorption remained. These dramatic changes in the textual properties for both materials are an indication that the deposition of Pt nanoparticles resulted in either the partial

blockage of some of the pores or the confinement of Pt nanoparticles inside the pore structure of these materials.

Table 4.3: Comparison of the BET surface area and pore properties of the HCSs, Pt/HCSs, NHCSs and Pt/NHCSs

| Sample | BET Surface Area $m^2/g$ | Pore Volume $cm^3/g$ | Pore Width /nm |
|---|---|---|---|
| HCS | 577 | 0.31 | 4.5 |
| Pt/HCS | 312 | 0.19 | 2.2 |
| NHCS | 519 | 0.32 | 5.0 |
| Pt/NHCS | 363 | 0.20 | 2.5 |

## 4.9: Powder X-ray diffraction (PXRD) studies

PXRD measurements were carried out on all the materials (Vulcan, HCSs, NHCSs, Pt/Vulcan, Pt/HCSs and Pt/NHCSs). The data for the HCSs and NHCSs were obtained in the 2Θ range of 5 to 90 º whereas for the catalysts Pt//HCSs and Pt/NHCSs the range was extended from 20 to 120 ° (Figure 4.7) to accommodate Pt reflections occurring at higher 2Θ values. The obtained diffractograms for the carbon materials showed the 002 and 001 peaks at 28 and 45 degrees, respectively. The peaks at these positions were typically broad, indicating that the carbon was turbostratic and disordered.[37,54] The NHCSs peaks were broader compared to the HCSs due to the higher defect density in the doped material.

The diffractograms for the Pt catalysts had similar peak heights due to the similar loadings of Pt on the different carbon supports. All the diffractograms show the peaks characteristic of the face-centred cubic (fcc) crystal structure of the Pt nanoparticles. This indicates that Pt was successfully deposited on these supports. The peaks are at 2Θ positions of 46.5º, 54.2 º, 80.2 º, 98.2 º and 104.3 º correspond to the Pt(111), Pt(200), Pt(220), Pt(311) and Pt(222) faces of the fcc structure

respectively.[55,56] Rietveld refinement and Scherrer equation calculations for all the catalysts indicated that the Pt average crystallite size was between 4.0 and 5.1 nm (table 4.4) whereas the crystallite sizes determined using TEM images were slightly smaller (3.9 to 4.2 nm). PXRD crystallite sizes are normally slightly larger compared to the TEM determined because the PXRD has a lower detection limit and cannot adequately detect particles smaller than 2 nm.[57] Additionally, the average particle sizes determined by PXRD are volume-weighted which results in the bigger particles having a larger contribution than the smaller particles. As a result, the bigger particles contribute more to the final particle size than the smaller ones.[32] The carbon PXRD peaks are not readily observed in the Pt/C materials due to the higher loading of Pt and the higher mass concentration and effect of the Pt phases.

Table 4.4: Comparison of the Pt particle sizes of the Pt/HCSs, Pt/NHCSs and Pt/Vulcan as determined using TEM, PXRD Scherrer equation and rietveld refinement

| Size/nm | Pt/HCSs | Pt/NHCSs | Pt/Vulcan |
|---|---|---|---|
| TEM | 4.2 ± 0.5 | 4.0 ± 0.6 | 3.9 ± 0.9 |
| Scherrer | 4.3 ± 0.8 | 4.1 ± 0.7 | 4.0 ± 1.2 |
| Rietveld | 5.1 ± 1.2 | 4.5 ± 0.9 | 4.8 ± 0.6 |

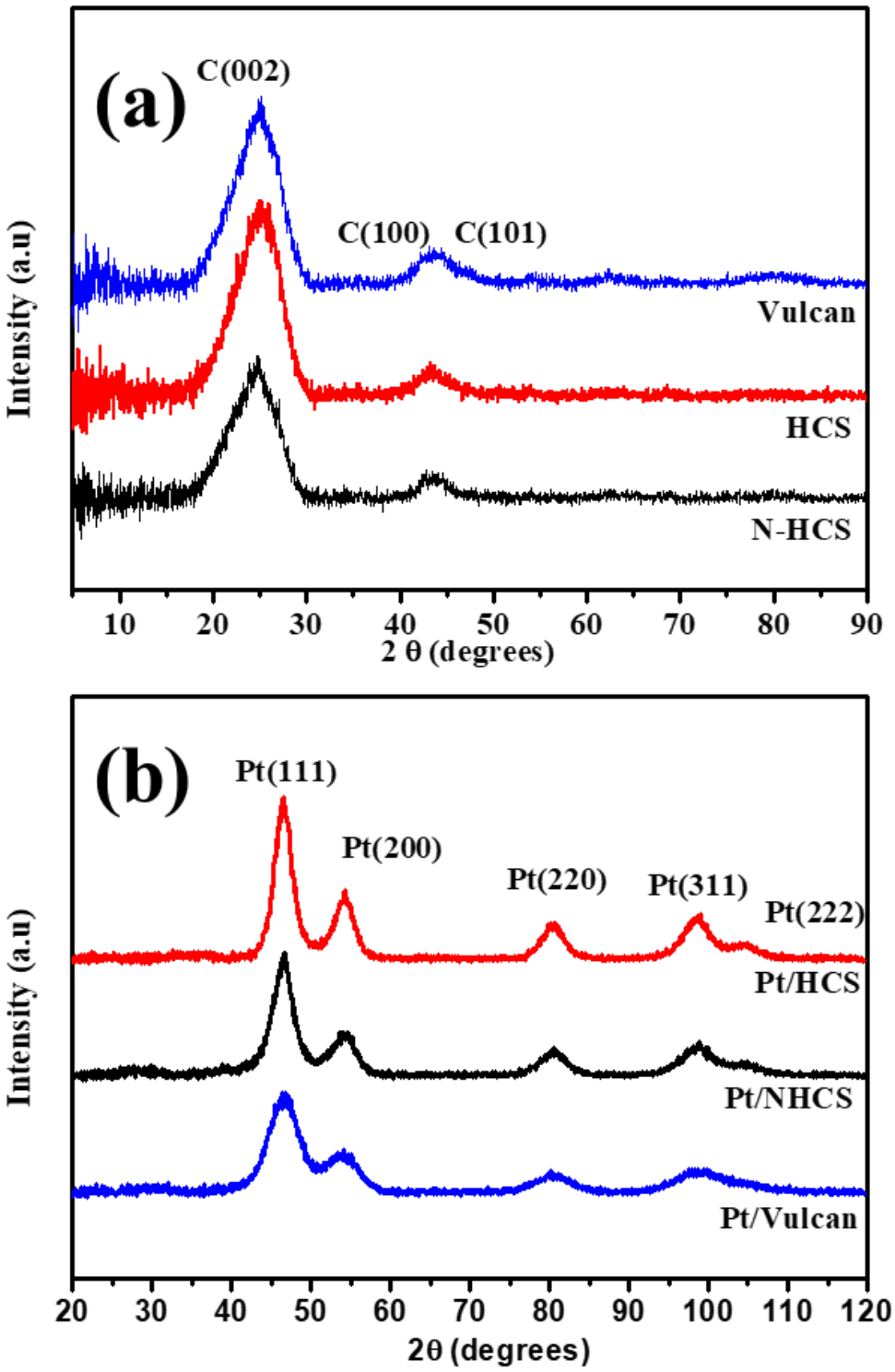



Figure 4.7: (a) PXRD diffractograms for HCSs, NHCSs, Vulcan and (b) for Pt/HCSs, Pt/NHCSs, Pt/Vulcan.

## 4.10: X-ray photoelectron spectroscopy (XPS) analysis

X-ray photoelectron spectroscopy (XPS) was used to investigate the electronic states and bonding of the elements in the Pt/HCSs and Pt/NHCSs materials and the full spectra are shown in Figure 4.8a. To compensate for charging effects of the materials, the instrument calibration was done using the binding energy for $sp^2$ carbon of 284.7 eV.[58,59]

High-resolution O1s data for the Pt/HCSs were deconvoluted into the respective contributions at specific binding energy (figure 4.8). These were C-O bonds (532.4 eV), the C=O bonds (531.6 eV), the O–H bonds (533.8 eV) and the quinones (530.5 eV) respectively (table 4.5).[60] The presence of these double-bonded oxygen groups which are rich in electron density offers numerous nucleation sites for Pt nanoparticles during deposition[61] The binding energy for O1s in the HCSs occurs in the same positions as for the NHCSs and the percentage contributions of the O1s species of the NHCSs was comparable to the HCS material. There was no significant change in the binding energy positions for the O1s of the Pt/NHCS sample even though nitrogen was incorporated into its structure.

The atomic percent contribution of the surface oxygen groups in Pt/HCSs was 7.9 at. % (table 4.5) which was constituted by C=O (2.7%), C–O (4.1%), O–H (0.8 %) and quinones (0.8 %). The contribution of the oxygen groups in the Pt/NHCSs was 5.3%. The lower oxygen content was attributed to the incorporation of nitrogen into the structure of the supports, hence reducing the surface oxygen species. The atomic percent contribution of the oxygen groups in the Pt/NHCS were C=O (1.8%), C–O (2.8%), O-H (0.6%) and the quinones contributed 0.6%.

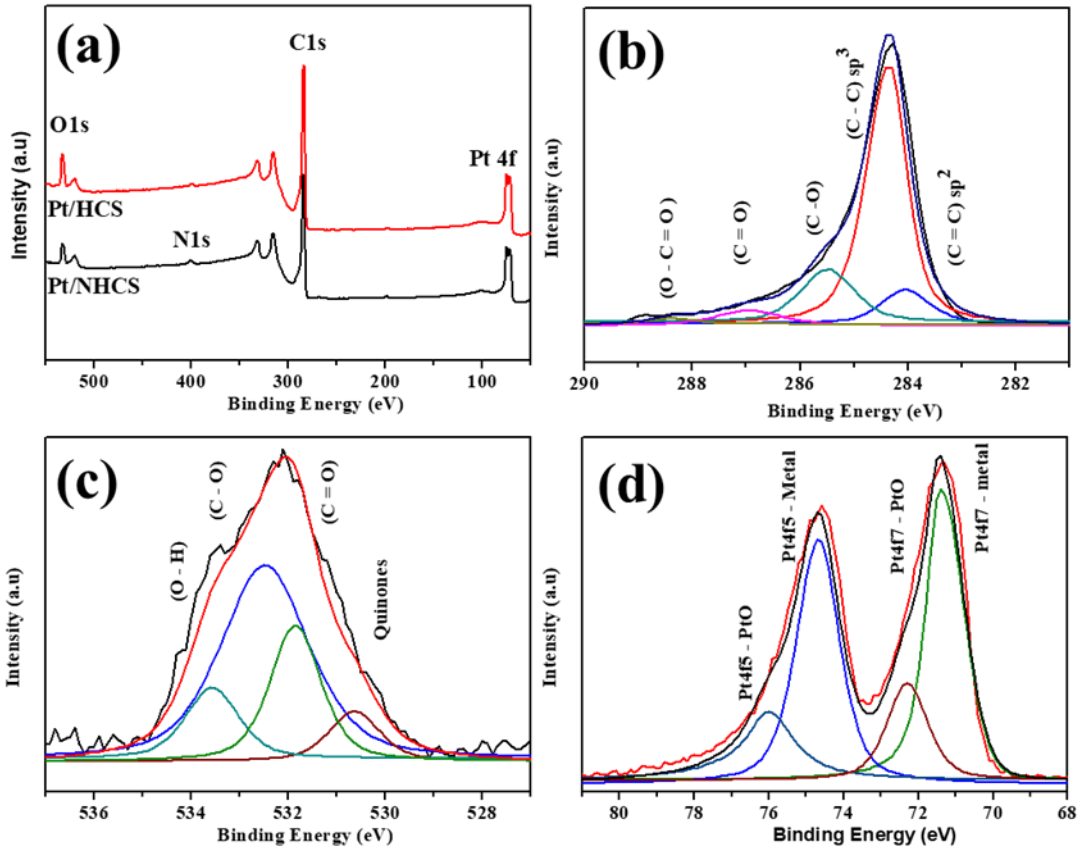



Figure 4.8: (a) XPS low resolution survey spectra for Pt/HCSs, Pt/NHCSs and high resolution (b) C1s, (c) O1s, and (d) Pt4f spectra for Pt/HCSs.

Table 4.5: Deconvoluted O1s data for Pt/HCSs and Pt/NHCSs

| | O1s | | | |
|---|---|---|---|---|
| Sample | C=O | C-O | O-H | Quinones |
| (BE/eV)Pt/HCSs | 531.6 | 532.4 | 533.8 | 530.5 |
| (BE/eV)Pt/NHCSs | 531.6 | 532.4 | 533.9 | 530.5 |
| Δ eV | 0 | 0 | 0.1 | 0 |
| (Atomic%)Pt/HCSs | 2.7 | 4.1 | 0.8 | 0.8 |
| (Atomic%)Pt/NHCSs | 1.8 | 2.8 | 0.6 | 0.6 |
| Δ Atomic % | 0.9 | 1.3 | 0.2 | 0.2 |

High-resolution C1s data for the Pt/HCSs were collected between the binding energy of 282 – 292 eV (Figure 4.8) The peaks were deconvoluted to give C=C ($sp^2$) bonds (284.1 eV), C–C bonds (284.5 eV), C–O bonds (285.8 eV), C=O bonds (287.1 eV) and the least pronounced O-C=O bonds (288.5 eV) (Table 4.6).[62] The $sp^2$ hybridized (C–C) bonded carbon was the most abundant, contributing about 35.9 at.% of all the carbon present and the contribution of the $sp^3$ hybridized carbon was 28.9 at. %.

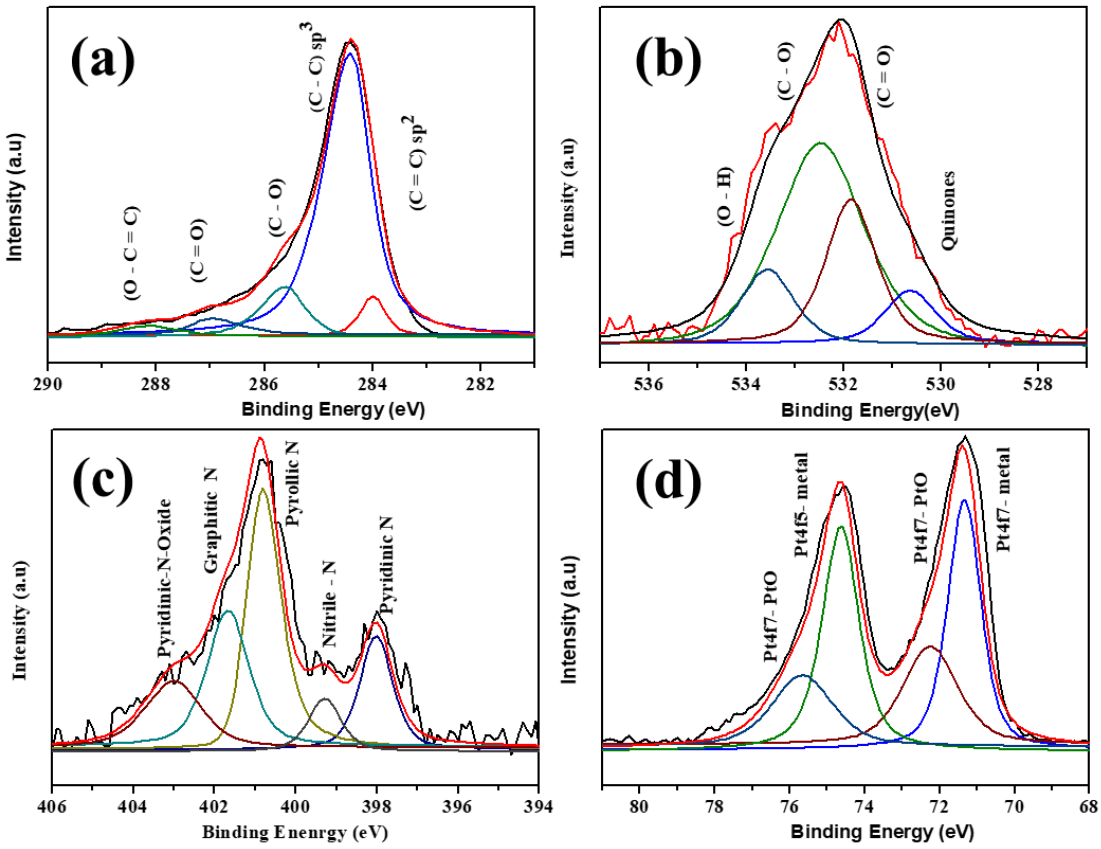



Figure 4.9: High resolution (a) C1, (b) O1s, (c) N1s and (d) Pt4f spectra for Pt/NHCSs.

Even though there were no significant changes in the binding energy of the C1s species, the contribution of the $sp^2$ hybridized carbon decreased in the Pt/NHCSs to about 31.5% (Table 4.6). The contribution of $sp^3$ carbon increased to about 35.4 at.%. Upon doping with nitrogen, the graphitized HCSs were converted into more defective NHCSs as shown by the relative amounts of the $sp^3/sp^2$ carbon. The contributions of the other C1s species did not significantly change due to

nitrogen doping. There were decreases of a 0.1 at. % (C–O), 0.6 at% (C=O) and 0.8 at.% (O–C=O) due to nitrogen doping.

Table 4.6: Deconvoluted C1s data for Pt/HCSs and Pt/NHCSs

| Sample | C1s | | | | |
|---|---|---|---|---|---|
| | C = C | C - C | C - O | C = O | O – C = O |
| (BE/eV)Pt/HCSs | 284.1 | 284.5 | 285.8 | 287.1 | 288.5 |
| (BE/eV)Pt/NHCSs | 284.1 | 284.6 | 285.8 | 287.2 | 288.4 |
| Δ eV | 0 | 0.1 | 0 | 0.1 | 0.1 |
| (Atomic%)Pt/HCSs | 35.9 | 28.9 | 4.8 | 3.9 | 5.1 |
| (Atomic%)Pt/NHCSs | 31.5 | 35.4 | 4.1 | 3.3 | 4.2 |
| Δ Atomic % | 4.4 | 6.5 | 0.7 | 0.6 | 0.9 |

High-resolution N1s data for Pt/NHCSs was collected between the binding energy of 395–406 eV (Figure 4.9). [17,63]The resulting peaks were further deconvoluted into pyridinic nitrogen occurring at a binding energy of 398.1 eV, metal–nitrile nitrogen (399.1 eV), pyrrolic nitrogen (400.7 eV), quaternary nitrogen (401 eV) and a small contribution due to oxidized nitrogen (403.1 eV). (table 4.7) The contribution of all the N1s was calculated to be 4.8 at.%.

Table 4.7: Deconvoluted N1s data for Pt/NHCSs

| Sample | N1s | | | | |
|---|---|---|---|---|---|
| Pt/NHCS | Pyridinic N | Metal Nitrile | Pyrolic N | Graphitic N | Oxidized N |
| (BE/eV) | 398.1 | 399.1 | 400.7 | 401.9 | 403.1 |
| (Atomic%) | 1.2 | 0.3 | 1.8 | 0.9 | 0.6 |

The nitrogen groups contribute towards the enhancement of the oxygen reduction reaction. Studies have shown that nitrogen groups influence the carbon atoms close to them causing the carbon to be better oxygen reduction catalysts.[64,65] Apart from directly influencing ORR, nitrogen groups are rich in electron density. The electron density influences the nucleation and growth of platinum nanoparticles during deposition. Studies have confirmed that nitrogen doped support surfaces cause the formation of smaller metal nanoparticles compared to pristine surfaces.[21,66]

High-resolution Pt 4f spectra of the samples (Pt/HCSs and Pt/NHCSs) were used to investigate the bonding and the chemical environment in which the Pt existed for the two samples. (Figure 4.8 and 4.9) The Pt4f peaks were deconvoluted into the corresponding $Pt^{2+}$ (72.5 and 75.4 eV) and metallic Pt (71.2 and 74.5 eV) contributions.[32] Pt existed as PtO and metallic Pt in both samples with more than 95% of the Pt existing as unoxidized metal. Less than 5% was shown to exist as PtO ($Pt^{2+}$). Surface oxidation of the Pt surface decreased slightly as a result of the nitrogen doping [67]with the $Pt^{2+}$ decreasing from 1.2 at.% to 0.8 at.% after nitrogen doping. The contribution of the metallic Pt decreased correspondingly from 5.4 at.% to 4.8 at.% (Table 4.8).

Table 4.8: Deconvoluted Pt4f data for Pt/HCSs and Pt/NHCSs

| | Pt4f | | | |
|---|---|---|---|---|
| Sample | Pt4f7 metal | Pt4f7 PtO | Pt4f5 metal | Pt4f5 PtO |
| (BE/eV)Pt/HCSs | 71.2 | 72.5 | 74.5 | 75.4 |
| (BE/eV)Pt/NHCSs | 71.5 | 72.6 | 74.8 | 75.5 |
| Difference (Δ eV) | 0.3 | 0.1 | 0.3 | 0.1 |
| (Atomic%)Pt/HCSs | 2.8 | 0.8 | 2.6 | 0.4 |
| (Atomic%)Pt/NHCSs | 2.6 | 0.5 | 2.2 | 0.3 |
| Difference in Atomic % | 0.2 | 0.3 | 0.4 | 0.1 |

The change in surface oxidation of the Pt due to the nitrogen doping was accompanied by corresponding binding energy shifts of the Pt4f electronic states (0.1 – 03 eV) to higher binding energies. The literature data also shows that the Pt 4f spectra of the commercial Pt/Vulcan catalyst had Pt binding energy occurring at much lower values (0.1 – 0.2 eV) compared to Pt/HCSs.[43] The binding energy shifts in the samples were attributed to the different levels of surface oxidation of the platinum nanoparticles.[68,69,69] Also, the different nature of the supports caused different levels of charge transfer from the Pt to the support. The amount of charge transfer and equilibration influenced the metal to support interactions between the Pt and the different carbon supports on which the Pt is deposited. These varying metal–support interactions caused the shift in the binding energy of the Pt electronic states.[15,21,58,70]

The lower atomic percent contribution of the Pt was due to the XPS technique measuring only down to 10 nm into the sample structure. Most of the Pt was confined[71,72] deeper inside the shell of the HCSs and NHCSs.

## 4.11: Conclusions

In conclusion, HCSs with an external diameter of 318 ± 8 nm and with a thin shell thickness of 10 ± 4 nm were synthesized. Correspondingly, NHCSs with an external diameter of 320 ± 11 nm and with a shell thickness of 12 ± 6 nm were also synthesized. The materials had a high BET surface area and mesoporosity. Raman spectroscopy confirmed the presence of defects as well as a considerable extent of graphitization. The materials were thermally stable, completely decomposing at temperatures around 700 °C. Nitrogen doping was confirmed by XPS with an approximate incorporation of about 4.8 at. % N on the HCSs. The additional melamine layer caused more defects on the NHCSs and a small increase in the shell thickness. Nitrogen doping affected the thermal stability of the HCS. The successful deposition of Pt nanoparticles in the size range (3 – 5 nm) saw the reduction in thermal stability of the materials. Also, a decrease in the BET surface area, pore

widths and pore volumes of the materials was noted. The decrease in textual properties was suggested to be due to the Pt occupying the pores of the supports, a phenomenon known as pore confinement. Pt nanoparticles were well dispersed with a short average inter particle distance. The loading of the Pt on the supports was about 40 wt.% on both supports.

## 4.12: References


(1) Xie, F.; Shao, Z.; Hou, M.; Yu, H.; Song, W.; Sun, S.; Zhou, L.; Yi, B. Recent Progresses in $H_2$-PEMFC at DICP. *Journal of Energy Chemistry* **2019**, *36*, 129–140.

(2) Jo, Y. Y.; Cho, E. A.; Kim, J. H.; Lim, T.-H.; Oh, I.-H.; Jang, J. H.; Kim, H.-J. Effects of a Hydrogen and Air Supply Procedure on the Performance Degradation of PEMFCs. *International Journal of Hydrogen Energy* **2010**, *35* (23), 13118–13124.

(3) Yu, X.; Ye, S. Recent Advances in Activity and Durability Enhancement of Pt/C Catalytic Cathode in PEMFC: Part I. Physico-Chemical and Electronic Interaction between Pt and Carbon Support, and Activity Enhancement of Pt/C Catalyst. *Journal of Power Sources* **2007**, *172* (1), 133–144.

(4) Li, B.; Yan, Z.; Higgins, D. C.; Yang, D.; Chen, Z.; Ma, J. Carbon-Supported Pt Nanowire as Novel Cathode Catalysts for Proton Exchange Membrane Fuel Cells. *Journal of Power Sources* **2014**, *262*, 488–493.

(5) Zhou, Z. M.; Shao, Z. G.; Qin, X. P.; Chen, X. G.; Wei, Z. D.; Yi, B. L. Durability Study of Pt-Pd/C as PEMFC Cathode Catalyst. *International Journal of Hydrogen Energy* **2010**.

(6) Hasché, F.; Oezaslan, M.; Strasser, P. Activity, Stability and Degradation of Multi Walled Carbon Nanotube (MWCNT) Supported Pt Fuel Cell Electrocatalysts. In *Physical Chemistry Chemical Physics*; The Royal Society of Chemistry, 2010; Vol. 12, pp 15251–15258.

(7) Vijayaraghavan, G.; Stevenson, K. J. Synergistic Assembly of Dendrimer-Templated Platinum Catalysts on Nitrogen-Doped Carbon Nanotube Electrodes for Oxygen Reduction. *Langmuir* **2007**, *23* (10), 5279–5282.

(8) Zana, A.; Speder, J.; Reeler, N. E. A.; Vosch, T.; Arenz, M. Investigating the Corrosion of High Surface Area Carbons during Start/Stop Fuel Cell Conditions: A Raman Study. *Electrochimica Acta* **2013**.

(9) Liu, H.; Li, J.; Xu, X.; Wang, F.; Liu, J.; Li, Z.; Ji, J. Highly Graphitic Carbon Black-Supported Platinum Nanoparticle Catalyst and Its Enhanced Electrocatalytic Activity for the Oxygen Reduction Reaction in Acidic Medium. *Electrochimica Acta* **2013**, *93*, 25–31.

(10) Stariha, S.; Macauley, N.; Sneed, B. T.; Langlois, D.; More, K. L.; Mukundan, R.; Borup, R. L. Recent Advances in Catalyst Accelerated Stress Tests for Polymer Electrolyte Membrane Fuel Cells. *Journal of The Electrochemical Society* **2018**, *165* (7).

(11) He, T.; Kreidler, E.; Xiong, L.; Ding, E. Combinatorial Screening and Nano-Synthesis of Platinum Binary Alloys for Oxygen Electroreduction. *Journal of Power Sources* **2007**, *165* (1), 87–91.

(12) Van Der Vliet, D.; Wang, C.; Debe, M.; Atanasoski, R.; Markovic, N. M.; Stamenkovic, V. R. Platinum-Alloy Nanostructured Thin Film Catalysts for the Oxygen Reduction Reaction. *Electrochimica Acta* **2011**, *56* (24), 8695–8699.

(13) Chen, C.; Kang, Y.; Huo, Z.; Zhu, Z.; Huang, W.; Xin, H. L.; Snyder, J. D.; Li, D.; Herron, J. A.; Mavrikakis, M.; Chi, M.; More, K. L.; Li, Y.; Markovic, N. M.; Somorjai, G. A.; Yang, P.; Stamenkovic, V. R. Highly Crystalline Multimetallic Nanoframes with Three-Dimensional Electrocatalytic Surfaces. *Science* **2014**, *343* (6177), 1339–1343.

(14) Sahin, N. E.; Napporn, T. W.; Dubau, L.; Kadirgan, F.; Léger, J. M.; Kokoh, K. B. Temperature-Dependence of Oxygen Reduction Activity on Pt/C and PtCr/C

Electrocatalysts Synthesized from Microwave-Heated Diethylene Glycol Method. *Applied Catalysis B: Environmental* **2017**, *203*, 72–84.

(15) Yu, X.; Ye, S. Recent Advances in Activity and Durability Enhancement of Pt/C Catalytic Cathode in PEMFC. Part I. Physico-Chemical and Electronic Interaction between Pt and Carbon Support, and Activity Enhancement of Pt/C Catalyst. *Journal of Power Sources* **2007**, *172* (1), 133–144.

(16) Anwar, M. T.; Yan, X.; Shen, S.; Husnain, N.; Zhu, F.; Luo, L.; Zhang, J. Enhanced Durability of Pt Electrocatalyst with Tantalum Doped Titania as Catalyst Support. *International Journal of Hydrogen Energy* **2017**, *42* (52), 30750–30759.

(17) Wang, D. D.; Wu, G.; Zhang, C.; Yin, F.; Su, L.; Shrestha, S.; Zhang, Z.; Mustain, W.. Improved Durability of Pt Catalyst Supported on N-Doped Mesoporous Graphitized Carbon for Oxygen Reduction Reaction in Polymer Electrolyte Membrane Fuel Cells. *Applied Catalysis B: Environmental* **2017**, *42* (52), 265–274.

(18) Mohanta, P. K.; Glökler, C.; Arenas, A. O.; Jörissen, L. Sb Doped $SnO_2$ as a Stable Cathode Catalyst Support for Low Temperature Polymer Electrolyte Membrane Fuel Cell. *International Journal of Hydrogen Energy* **2017**, *42* (46), 27950–27961.

(19) Schonvogel, D.; Hülstede, J.; Wagner, P.; Kruusenberg, I.; Tammeveski, K.; Dyck, A.; Agert, C.; Wark, M. Stability of Pt Nanoparticles on Alternative Carbon Supports for Oxygen Reduction Reaction. *Journal of The Electrochemical Society* **2017**, *164* (9), F995–F1004.

(20) Kongkanand, A.; Kuwabata, S.; Girishkumar, G.; Kamat, P. Single-Wall Carbon Nanotubes Supported Platinum Nanoparticles with Improved Electrocatalytic Activity for Oxygen Reduction Reaction. *Langmuir* **2006**, *22* (5), 2392–2396.

(21) Ma, J.; Habrioux, A.; Luo, Y.; Ramos-Sanchez, G.; Calvillo, L.; Granozzi, G.; Balbuena, P. B.; Alonso-Vante, N. Electronic Interaction between Platinum Nanoparticles and

Nitrogen-Doped Reduced Graphene Oxide: Effect on the Oxygen Reduction Reaction. *Journal of Materials Chemistry A* **2015**, *3* (22), 11891–11904.

(22) Paulus, U. A.; Schmidt, T. J.; Gasteiger, H. A.; Behm, R. J. Oxygen Reduction on a High-Surface Area Pt/Vulcan Carbon Catalyst: A Thin-Film Rotating Ring-Disk Electrode Study. *Journal of Electroanalytical Chemistry* **2001**, *495* (2), 134–145.

(23) Zhou, Y.; Neyerlin, K.; S. Olson, T.; Pylypenko, S.; Bult, J.; N. Dinh, H.; Gennett, T.; Shao, Z.; O'Hayre, R. Enhancement of Pt and Pt-Alloy Fuel Cell Catalyst Activity and Durability via Nitrogen -Modified Carbon Supports. *Energy & Environmental Science* **2010**, *3* (10), 1437–1446.

(24) Zheng, F.; Mu, G.; Zhang, Z.; Shen, Y.; Zhao, M.; Pang, G. Nitrogen-Doped Hollow Macroporous Carbon Spheres with High Electrocatalytic Activity for Oxygen Reduction. *Materials Letters* **2012**, *68*, 453–456.

(25) Dai, X. Y.; Zhang, X.; Meng, Y. F.; Shen, P. K. Preparation of Hollow Carbon Spheres by Carbonization of Polystyrene/Polyaniline Core-Shell Polymer Particles. *Xinxing Tan Cailiao/New Carbon Materials* **2011**, *26* (5), 389–395.

(26) Hassan, M.; Qiu, W.; Song, X.; Mao, Q.; Ren, S.; Hao, C. Supercapacitive and ORR Performances of Nitrogen-Doped Hollow Carbon Spheres Pyrolyzed from Polystyrene@polypyrrole-Polyaniline. *Journal of Alloys and Compounds* **2020**, *818*, 152890–152890.

(27) Li, S.; Pasc, A.; Fierro, V.; Celzard, A. Hollow Carbon Spheres, Synthesis and Applications – a Review. *Journal of Materials Chemistry A* **2016**, *4* (33), 12686–12713.

(28) Phaahlamohlaka, T. N.; Kumi, D. O.; Dlamini, M. W.; Forbes, R.; Jewell, L. L.; Billing, D. G.; Coville, N. J. Effects of Co and Ru Intimacy in Fischer–Tropsch Catalysts Using Hollow Carbon Sphere Supports: Assessment of the Hydrogen Spillover Processes. *ACS Catalysis* **2017**, *7* (3), 1568–1578.

(29) Zhang, Z.; Qin, M.; Jia, B.; Zhang, H.; Wu, H.; Qu, X. Facile Synthesis of Novel Bowl-like Hollow Carbon Spheres by the Combination of Hydrothermal Carbonization and Soft Templating. *Chemical Communications* **2017**, *53* (20), 2922–2925.

(30) Melke, J.; Peter, B.; Habereder, A.; Ziegler, J.; Fasel, C.; Nefedov, A.; Sezen, H.; Wöll, C.; Ehrenberg, H.; Roth, C. Metal-Support Interactions of Platinum Nanoparticles Decorated N-Doped Carbon Nanofibers for the Oxygen Reduction Reaction. *ACS Applied Materials and Interfaces* **2016**, *8* (1), 82–90.

(31) Rabis, A.; Rodriguez, P.; Schmidt, T. J. Electrocatalysis for Polymer Electrolyte Fuel Cells: Recent Achievements and Future Challenges. *ACS Catalysis* **2012**, *2* (5), 864–890.

(32) Zhang, J.; Ma, L.; Gan, M.; Yang, F.; Fu, S.; Li, X. Well-Dispersed Platinum Nanoparticles Supported on Hierarchical Nitrogen-Doped Porous Hollow Carbon Spheres with Enhanced Activity and Stability for Methanol Electrooxidation. *Journal of Power Sources* **2015**, *288*, 42–52.

(33) Stöber, W.; Fink, A.; Bohn, E. Controlled Growth of Monodisperse Silica Spheres in the Micron Size Range. *Journal of Colloid and Interface Science* **1968**, *26* (1), 62–69.

(34) Yao, L.; Xu, G.; Dou, W.; Bai, Y. The Control of Size and Morphology of Nanosized Silica in Triton X-100 Based Reverse Micelle. *Colloids and Surfaces A: Physicochemical and Engineering Aspects* **2008**, *316* (1), 8–14.

(35) Yan, Z.; Hu, Z.; Chen, C.; Meng, H.; Shen, P. K.; Ji, H.; Meng, Y. Hollow Carbon Hemispheres Supported Palladium Electrocatalyst at Improved Performance for Alcohol Oxidation. *Journal of Power Sources* **2010**, *195* (21), 7146–7151.

(36) Cuesta, A.; Dhamelincourt, P.; Laureyns, J.; Martínez-Alonso, A.; Tascón, J. M. D. Raman Microprobe Studies on Carbon Materials. *Carbon* **1994**, *32* (8), 1523–1532.

(37) Parent, P.; Laffon, C.; Marhaba, I.; Ferry, D.; Regier, T. Z.; Ortega, I. K.; Chazallon, B.; Carpentier, Y.; Focsa, C. Nanoscale Characterization of Aircraft Soot: A High-Resolution

Transmission Electron Microscopy, Raman Spectroscopy, X-Ray Photoelectron and near-Edge X-Ray Absorption Spectroscopy Study. *Carbon* **2016**, *101*, 86–100.

(38) Okuda, H.; Young, R. J.; Wolverson, D.; Tanaka, F.; Yamamoto, G.; Okabe, T. Investigating Nanostructures in Carbon Fibres Using Raman Spectroscopy. *Carbon* **2018**, *130*, 178–184.

(39) Sadezky, A.; Muckenhuber, H.; Grothe, H.; Niessner, R.; Pöschl, U. Raman Microspectroscopy of Soot and Related Carbonaceous Materials: Spectral Analysis and Structural Information. *Carbon* **2005,** 43 (8), 1731-1742

(40) Kompan, M. E.; Krylov, D. S. Detecting Graphene-Graphane Reconstruction in Hydrogenated Nanoporous Carbon by Raman Spectroscopy. *Tech. Phys. Lett.* **2010**, *36* (12), 1140–1142.

(41) Chen, Z.; Higgins, D.; Tao, H.; Hsu, R. S.; Chen, Z. Highly Active Nitrogen-Doped Carbon Nanotubes for Oxygen Reduction Reaction in Fuel Cell Applications. *J. Phys. Chem. C* **2009**, *113* (49), 21008–21013.

(42) Ferrari, A. C.; Robertson, J. Raman Spectroscopy of Amorphous, Nanostructured, Diamond–like Carbon, and Nanodiamond. *Philosophical Transactions of the Royal Society of London. Series A: Mathematical, Physical and Engineering Sciences* **2004**, *362* (1824), 2477–2512.

(43) Jackson, C.; Smith, G. T.; Inwood, D. W.; Leach, A. S.; Whalley, P. S.; Callisti, M.; Polcar, T.; Russell, A. E.; Levecque, P.; Kramer, D. Electronic Metal-Support Interaction Enhanced Oxygen Reduction Activity and Stability of Boron Carbide Supported Platinum. *Nature Communications* **2017**, *8* (1), 15802–15802.

(44) Wu, G.; Li, D.; Dai, C.; Wang, D.; Li, N. Well-Dispersed High-Loading Pt Nanoparticles Supported by Shell−Core Nanostructured Carbon for Methanol Electrooxidation. *Langmuir* **2008**, *24* (7), 3566–3575.

(45) Fang, W.C. High Methanol Oxidation Activity of Well-Dispersed Pt Nanoparticles on Carbon Nanotubes Using Nitrogen Doping. *Nanoscale Res Lett* **2010**, *5* (1), 68–73.

(46) Fujimoto, Y.; Saito, S. Energetics and Electronic Structures of Pyridine-Type Defects in Nitrogen-Doped Carbon Nanotubes. *Physica E: Low-dimensional Systems and Nanostructures* **2011**, *43* (3), 677–680.

(47) Ma, Y.; Ricciuti, C.; Miller, T.; Kadlowec, J.; Pearlman, H. Enhanced Catalytic Combustion Using Sub-Micrometer and Nano-Size Platinum Particles. *Energy and Fuels* **2008**, *22* (6), 3695–3700.

(48) Låte, L.; Rundereim, J.-I.; Blekkan, E. A. Selective Combustion of Hydrogen in the Presence of Hydrocarbons: 1. Pt-Based Catalysts. *Applied Catalysis A: General* **2004**, *262* (1), 53–61.

(49) Pang, L. S. K.; Saxby, J. D.; Chatfield, S. P. Thermogravimetric Analysis of Carbon Nanotubes and Nanoparticles. *J. Phys. Chem.* **1993**, *97* (27), 6941–6942.

(50) Bom, D.; Andrews, R.; Jacques, D.; Anthony, J.; Chen, B.; Meier, M. S.; Selegue, J. P. Thermogravimetric Analysis of the Oxidation of Multiwalled Carbon Nanotubes: Evidence for the Role of Defect Sites in Carbon Nanotube Chemistry. *Nano Lett.* **2002**, *2* (6), 615–619.

(51) Bhambhani, M. R.; Cutting, P. A.; Sing, K. S. W.; Turk, D. H. Analysis of Nitrogen Adsorption Isotherms on Porous and Nonporous Silicas by the BET and As Methods. *Journal of Colloid and Interface Science* **1972**, *38* (1), 109–117.

(52) Schneider, P. Adsorption Isotherms of Microporous-Mesoporous Solids Revisited. *Applied Catalysis A: General* **1995**, *129* (2), 157–165.

(53) Niu, J.; Shao, R.; Liang, J.; Dou, M.; Li, Z.; Huang, Y.; Wang, F. Biomass-Derived Mesopore-Dominant Porous Carbons with Large Specific Surface Area and High Defect

Density as High Performance Electrode Materials for Li-Ion Batteries and Supercapacitors. *Nano Energy* **2017**, *36*, 322–330.

(54) Li, Z. Q.; Lu, C. J.; Xia, Z. P.; Zhou, Y.; Luo, Z. X-Ray Diffraction Patterns of Graphite and Turbostratic Carbon. *Carbon* **2007**. https://doi.org/10.1016/j.carbon.2007.03.038.

(55) Reinhard, D.; Hall, B. D.; Berthoud, P.; Valkealahti, S.; Monot, R. *Size-Dependent Icosahedral-to-Fcc Structure Change Confirmed in Unsupported Nanometer-Sized Copper Clusters*; **1997**, 7, 1462.

(56) Şen, F.; Gökağaç, G. Different Sized Platinum Nanoparticles Supported on Carbon: An XPS Study on These Methanol Oxidation Catalysts. *J. Phys. Chem. C* **2007**, 111(15), 5715–5720.

(57) Borchert, H.; Shevchenko, E. V.; Robert, A.; Mekis, I.; Kornowski, A.; Grübel, G.; Weller, H. Determination of Nanocrystal Sizes: A Comparison of TEM, SAXS, and XRD Studies of Highly Monodisperse $CoPt_3$ Particles. *Langmuir* **2005**, *21* (5), 1931–1936.

(58) Ometto, F. B.; Carbonio, E. A.; Teixeira-Neto, É.; Villullas, H. M. Changes Induced by Transition Metal Oxides in Pt Nanoparticles Unveil the Effects of Electronic Properties on Oxygen Reduction Activity. *Journal of Materials Chemistry A* **2019**, *7* (5), 2075–2086.

(59) Fiçicilar, B.; Bayrakçeken, A.; Eroğlu, I. Effect of Pd Loading in Pd-Pt Bimetallic Catalysts Doped into Hollow Core Mesoporous Shell Carbon on Performance of Proton Exchange Membrane Fuel Cells. *Journal of Power Sources* **2009**, *193* (1), 17–23.

(60) Shao, Y.; Zhang, S.; Engelhard, M. H.; Li, G.; Shao, G.; Wang, Y.; Liu, J.; Aksay, I. A.; Lin, Y. Nitrogen-Doped Graphene and Its Electrochemical Applications. *J. Mater. Chem* **2010**, 20, 7491-7496

(61) Chen, P.; Chew, L. M.; Xia, W. The Influence of the Residual Growth Catalyst in Functionalized Carbon Nanotubes on Supported Pt Nanoparticles Applied in Selective Olefin Hydrogenation. *Journal of Catalysis* **2013**, *307*, 84–93.

(62) Briggs, David.; Beamson, Graham. Primary and Secondary Oxygen-Induced C1s Binding Energy Shifts in x-Ray Photoelectron Spectroscopy of Polymers. *Anal. Chem.* **1992**, *64* (15), 1729–1736.

(63) Jung, W. S.; Popov, B. N. Improved Durability of Pt Catalyst Supported on N-Doped Mesoporous Graphitized Carbon for Oxygen Reduction Reaction in Polymer Electrolyte Membrane Fuel Cells. *Carbon* **2017**, 122, 746-755

(64) Shibuya, R.; Kondo, T.; Nakamura, J. Active Sites in Nitrogen-Doped Carbon Materials for Oxygen Reduction Reaction. *Carbon-Based Metal-Free Catalysts: Design and Applications* **2018**, *1–2* (6271), 227–249.

(65) Guo, D.; Shibuya, R.; Akiba, C.; Saji, S.; Kondo, T.; Nakamura, J. Active Sites of Nitrogen-Doped Carbon Materials for Oxygen Reduction Reaction Clarified Using Model Catalysts. *Science (New York, N.Y.)* **2016**, *351* (6271), 361–365.

(66) Bo, X.; Bai, J.; Ju, J.; Guo, L. Highly Dispersed Pt Nanoparticles Supported on Poly(Ionic Liquids) Derived Hollow Carbon Spheres for Methanol Oxidation. *Journal of Power Sources* **2011**, *196* (20), 8360–8365.

(67) Geng, D.; Yang, S.; Zhang, Y.; Yang, J.; Liu, J.; Li, R.; Sham, T.-K.; Sun, X.; Ye, S.; Knights, S. Nitrogen Doping Effects on the Structure of Graphene. *Applied Surface Science* **2011**, *257* (21), 9193–9198.

(68) Ning, X.; Yu, H.; Peng, F.; Wang, H. Pt Nanoparticles Interacting with Graphitic Nitrogen of N-Doped Carbon Nanotubes: Effect of Electronic Properties on Activity for Aerobic Oxidation of Glycerol and Electro-Oxidation of CO. *Journal of Catalysis* **2015**, *325*, 136–144.

(69) Jeon, Y.; Park, J.-I.; Ok, J.; Dorjgotov, A.; Kim, H.-J.; Kim, H.; Lee, C.; Park, S.; Shul, Y.-G. Enhancement of Catalytic Durability through Nitrogen-Doping Treatment on the

CNF-Derivatized ACF Support for High Temperature PEMFC. *International Journal of Hydrogen Energy* **2016**, *41* (16), 6864–6876.

(70) Ma, J.; Habrioux, A.; Morais, C.; Lewera, A.; Vogel, W.; Verde-Gómezgómez, Y.; Ramos-Sanchez, G.; Balbuena, P. B.; Alonso-Vante, N. Spectroelectrochemical Probing of the Strong Interaction between Platinum Nanoparticles and Graphitic Domains of Carbon, *ACS Catal*. **2013**, 3(9),1940–1950

(71) Galeano, C.; Meier, J. C.; Peinecke, V.; Bongard, H.; Katsounaros, I.; Topalov, A. A.; Lu, A.; Mayrhofer, K. J. J.; Schüth, F. Toward Highly Stable Electrocatalysts via Nanoparticle Pore Confinement. *J. Am. Chem. Soc.* **2012**, *134* (50), 20457–20465.

(72) Pizzutilo, E.; Knossalla, J.; Geiger, S.; Grote, J.-P.; Polymeros, G.; Baldizzone, C.; Mezzavilla, S.; Ledendecker, M.; Mingers, A.; Cherevko, S.; Schüth, F.; Mayrhofer, K. J. J. The Space Confinement Approach Using Hollow Graphitic Spheres to Unveil Activity and Stability of Pt-Co Nanocatalysts for PEMFC. *Advanced Energy Materials* **2017**, *7* (20), 1700835.

# Chapter 5

# Synthesis and characterization of small hemispherical BHCSs, BNHCSs and the Pt supported materials (Pt/BNHCSs and Pt/BNHCSs)

## 5.1: Introduction

The PEMFCSs has an ability to revolutionize the use of energy in transportation and home use due to the light weight, fuel efficiency and the low noise levels associated with their use. For decades, research into PEMFCSs has been growing and companies like Anglo American are adopting PEMFCS for home use and their mining operations.[1,2] PEMFCSs are fuel efficient, light weight and they use Pt as catalysts, which is abundant in South Africa. The challenge associated with PEMFCS is the low durability of the catalysts used in the electrodes especially the cathode where potentials reach above 1.5 V vs RHE during start-up and load sequences.[3–5] These high potentials lead to the electrochemical oxidation of the carbons that are normally used as supports in fuel cell catalysts. This results in the detachment of Pt nanoparticles from the carbon and subsequent agglomeration and loss of activity of the catalysts. Hence, most of the fuel cell catalysts made to date have been known to be highly active but have poor

durability. This has been an ongoing problem as it has hindered the adoption of fuel cells in automobiles and for use in other applications.

To mitigate for the low durability, structured carbon materials have been used as supports. The issue of the metal to support interaction is critical as it affects catalyst durability patterns.[6–8] Structured carbon has been adopted due to their numerous advantageous properties. In this chapter we describe the use of hemispherical bowl like materials derived from attempts to make small diameter hollow carbon spheres (HCSs) and which will be called BHCSs. The BHCSs were investigated as potential carbon supports for Pt as they are light weight, possess high surface area, have a network of pores, have defects and they also possess good thermal stability. Nitrogen doped BHCSs were also synthesized. The nitrogen doped bowl like hollow carbon spheres (BNHCSs) were also found to possess similar properties as found for the BHCSs. Furthermore, the nitrogen doping enhanced the surface properties of the materials introducing defects and generated an extended π conjugated system of overlapping orbitals. The defects enhanced metal to support interactions whereas the electron density of the nitrogen functionalities enhanced the electronic properties of the Pt nanoparticles. The advantage of these hemispherical carbons is the ability of the Pt nanoparticles to be deposited on either side of the curved support. This results in a thin carbon graphitic carbon shell surrounded by Pt nanoparticles on either side of the support resulting in better Pt utilization for catalysis, enhanced electronic conductivity between the Pt and the support, and more Pt per surface area compared to the Pt/HCSs and Pt/NHCSs where Pt is deposited only on the outside curvature of the support. Also, due to the hemispherical morphology of these materials, very thin shells can be synthesized. The advantages of the very thin shells with a sectional diameter less than 10 nm are that they can be heat treated and, graphitization and defects concentrations can be controlled. Graphitization promotes electronic conductivity and durability due to elimination of some amorphous parts of the materials (due to high temperature annealing at 900ºC) and the

defects provides nucleation sites[9] where Pt nanoparticles are deposited with favourable properties. The Pt deposited on the defects is less prone to degradation processes like agglomeration because of the restricted movement they possess due to the barrier effect of the defects. This is not the case with small Pt particles deposited on a flatter surface where restricted movement is not prevented. The other advantage of these small hemispherical carbons is the ease of packing compared to the bigger spheres. The smaller BHCSs and BNHCSs have a smaller diameter which results in numerous particles closely packing leaving less empty space between support particles. This enhances support – support conductivity resulting in better performing catalysts especially in electrocatalysis where the flow of electrons is critical. The smaller materials also possess a high surface area per unit volume of support due to the close packing and presence of numerous smaller support particles compared to the larger HCSs and NHCSs. The same applies to the concentration of defects where per unit volume of material, the smaller BHCSs and BNHCSs contains more defects compared to the larger HCSs and NHCSs.

While these types of materials have not been used in the ORR reactions, they have been used in other reactions as discussed in the review in Chapter 1 section 1.9.3

In this study BHCSs and BNHCSs were synthesized and Pt nanoparticles deposited on both sides of the carbon shell of these support materials.

## 5.2: Morphology of the BHCS and BNHCS

A modified Stober method[10] was used to synthesize the silica spheres with a diameter of 55 ± 0.9 nm. The SEM and TEM micrographs (Figure 5.1) confirmed the spherical morphology and uniform size of the silica spheres.

To form a carbon shell around the silica template, a resorcinol-formaldehyde resin[11] was synthesized in-situ. In the process, formaldehyde (0.5 ml) and resorcinol (0.5 g) were added to

$SiO_2$ (2 g) dispersed by sonication in absolute ethanol (15 ml), ammonia solution (3 ml) and deionised water (75 ml). The cetylammonium bromide (CTAB, 2 g) was added to the suspension with sonication as a pore forming surfactant. The brown resin, $SiO_2$@RF, was filtered from the solution after 24 h reaction. The product was then carbonized in a quartz tube reactor at 900 ºC for 2 h. The $SiO_2$@C black soot-like material that formed was subjected to a standard silica etching procedure to remove the silica template using a 10 % hydrofluoric acid (made from a 48% HF commercial sample) solution. The $SiO_2$@C was etched for 24 h without stirring to prevent excessive breakage of the carbon shells, followed by filtration and washing of the resulting carbon material. It was observed that the HCSs synthesized using this route were broken and produced bowl like carbon spheres (BHCSs) (Figure 5.2).

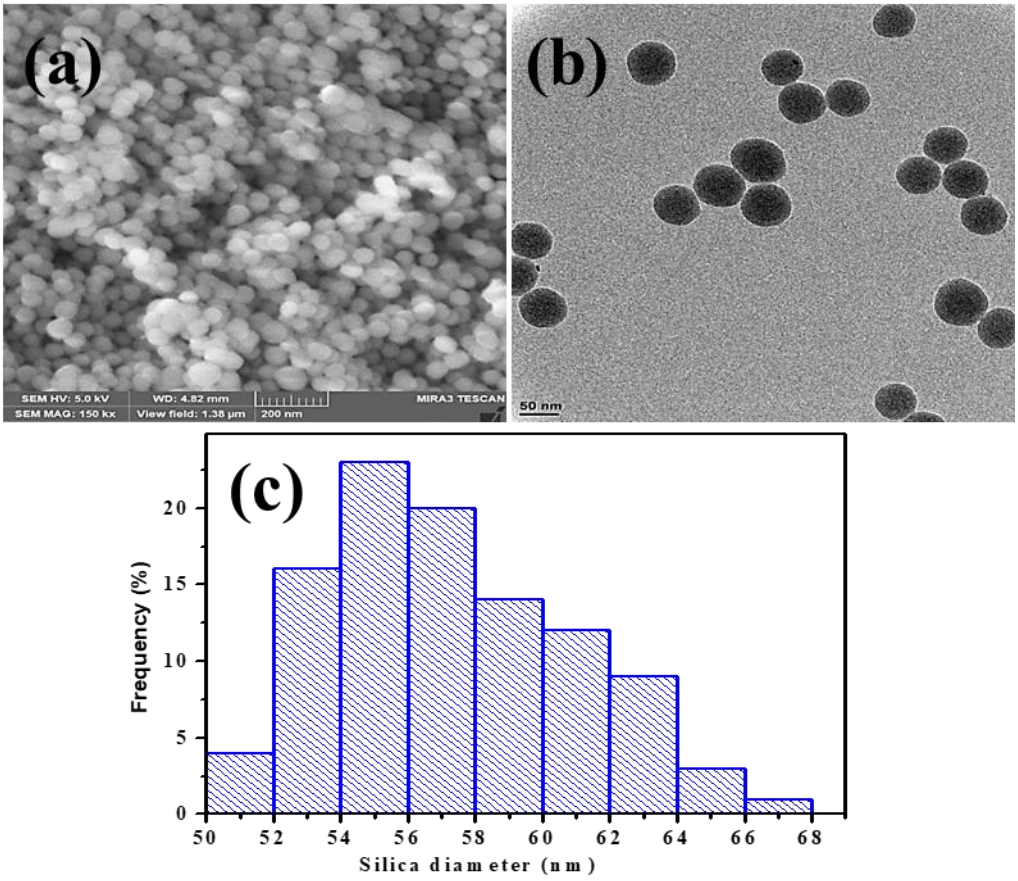



Figure 5.1: (a) SEM micrograph, (b) TEM micrograph of $SiO_2$ and (c) particle size distribution of the small silica particles.

The broken nature of the HCSs relates to the high surface energy of the small silica nano templates which stick together/aggregate after drying and annealing.[12,13] Addition of the resorcinol-formaldehyde coats the silica agglomerates rather than the individual silica particles. This provides stress due to the carbon coating at the juncture of two silica spheres resulting in breakage after silica etching.

To obtain nitrogen doped broken hollow carbon spheres (BNHCS), the $SiO_2$@RF (2g) was mixed with melamine (2g) and sonicated in methanol (20 ml) followed by drying in an oven at 50 ºC. The $SiO_2$@RF@melamine was then carbonized at 900 ºC for 2 h at a heating rate of 5 ºC/min. The melamine decomposed at the high temperatures forming a layer on top of the BHCS resulting in the formation of the BNHCSs.[14]

The SEM micrographs (Figure 5.2) confirms the spherical and broken bowl like morphology of the BHCSs and the BNHCSs. Each BHCS and BNHCS moiety appears to be attached to other neighbouring BHCSs and BNHCSs. There is no observable morphological change in the SEM images due to the nitrogen doping. This is an indication that the solid melamine used for the doping process covered the structure of the BHCSs altering the chemical composition but not the physical appearance of the material at the nanoscale.

The TEM micrographs (Figure 5.2) also confirmed the spherical morphology of the BHCSs and the BNHCSs. TEM images also showed the thin shells of the BHCSs and the BNHCSs. The open edges of the carbon material shown in the TEM images is an indication of the broken nature of the BHCSs and BNHCSs.

The particle size distribution of the formed BHCSs and BNHCSs (Figure 5.3) show diameters of 58 ± 0.9 nm and 60 ±1.1 nm and a carbon shell thickness of 4.5 ± 0.6 nm and 4.6 ± 0.9 nm respectively. The similarity in particle diameter and shell thickness for the materials indicates that the nitrogen doping process did not substantially impact on the size of the BHCSs.

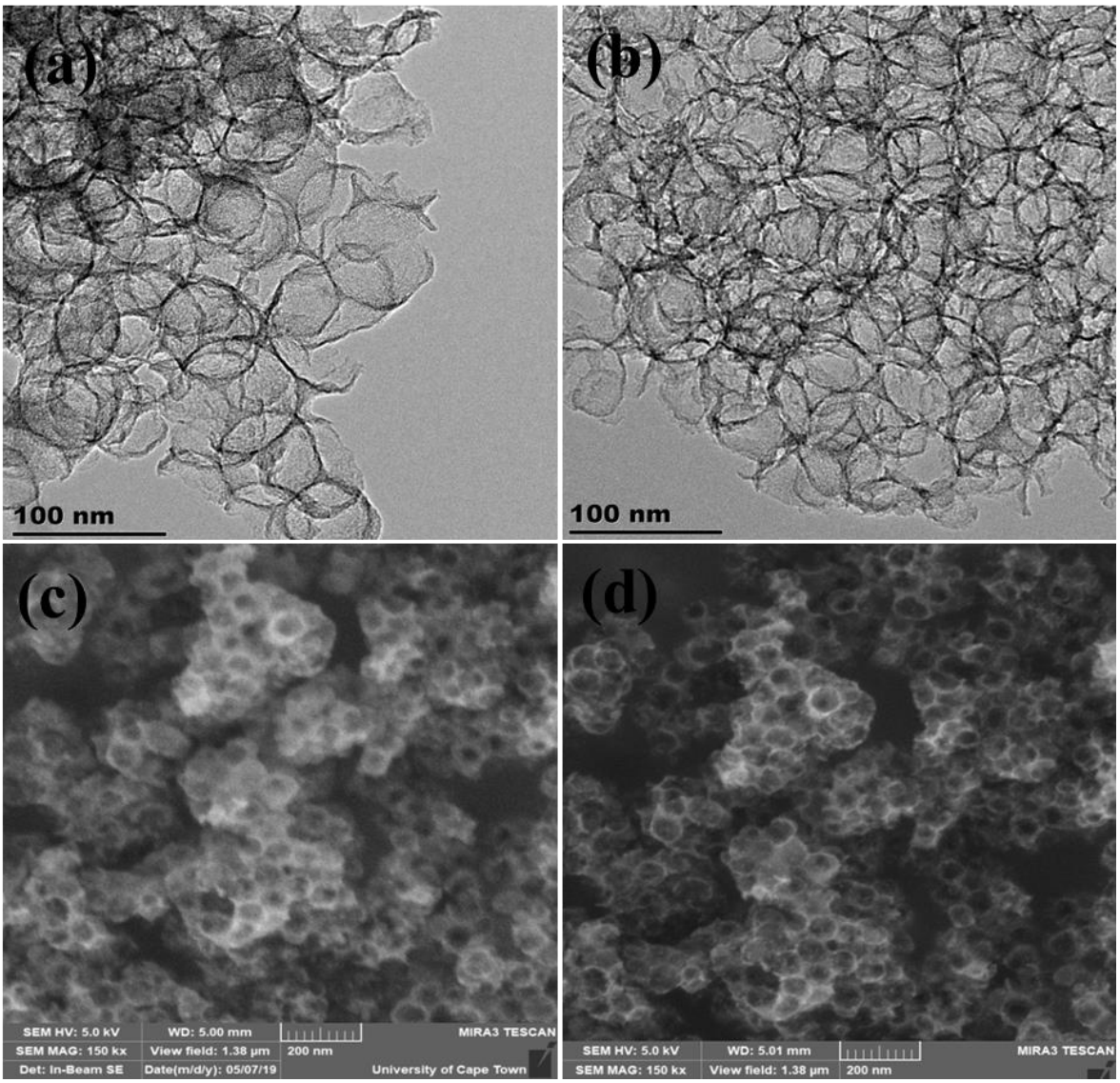



Figure 5.2: (a) TEM micrograph for BHCSs and (b) BNHCSs. (c) SEM micrograph of BHCSs and (d) BNHCSs.

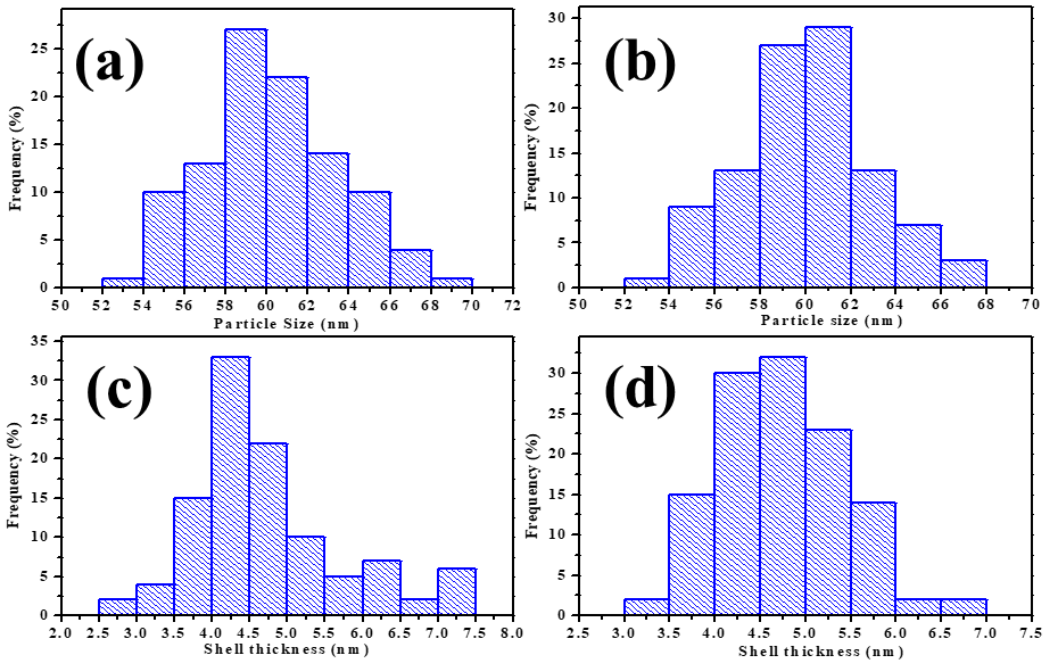



Figure 5.3: (a) Particle size distribution of BHCSs and (b) BNHCSs. Shell thickness of (c) BHCSs and (d) and BNHCSs.

## 5.3: Raman Spectroscopy

The materials were characterized with Raman spectroscopy to determine the structural order and defects in the new materials. Deconvolution of the Raman spectra (Figure 5.4) was used to separate the contributions of the respective D, D1, D2 and G bands. The G band of the materials is due to the contributions of the vibrational modes of the graphite like $sp^2$ hybridized carbon.[15] The D band contribution is due to the defective $sp^3$ hybridized carbon and the ratio of the contributions of the D and the G bands, the $\mathbf{I_D/I_G}$, ratio provides information on the extent of graphitization and defects in the materials.[16] BHCSs had an $\mathbf{I_D/I_G}$ of 0.97 whereas the BNHCSs had an $\mathbf{I_D/I_G}$ = 1.00 (table 5.1). The higher $\mathbf{I_D/I_G}$ ratio for BNHCSs shows that the amount of disordered carbon increased due to doping with nitrogen. However, the small difference in size of the $\mathbf{I_D/I_G}$ ratios indicates that the extent of disorder due to nitrogen doping is small.[17] Another measure of graphitization is the position of the G band which occurred at lower

frequency for the highly graphitic materials and at higher Raman frequency for the less graphitic or amorphous materials as suggested by Ferrari and co-workers. The BHCSs had a G peak position of 1586 $cm^{-1}$ whereas the BNHCSs had a G peak at 1595 $cm^{-1}$ (Table 5.1). The G peak position shift is also shown in the overlaid deconvoluted Raman spectra (Figure 5.4). The FWHM which shows the quality of the $sp^2$ hybridized carbon is smaller (68) with a higher intensity (773) for the BHCSs compared to the BNHCSs, (FWHM (72); and intensity (643))(Table 5.1). The higher intensity and the smaller FWHM for the BHCSs is an indication that BHCSs have more ordered and graphitized carbon with better quantity of the $sp^2$ hybridized carbon compared to the BNHCSs.[18,19]

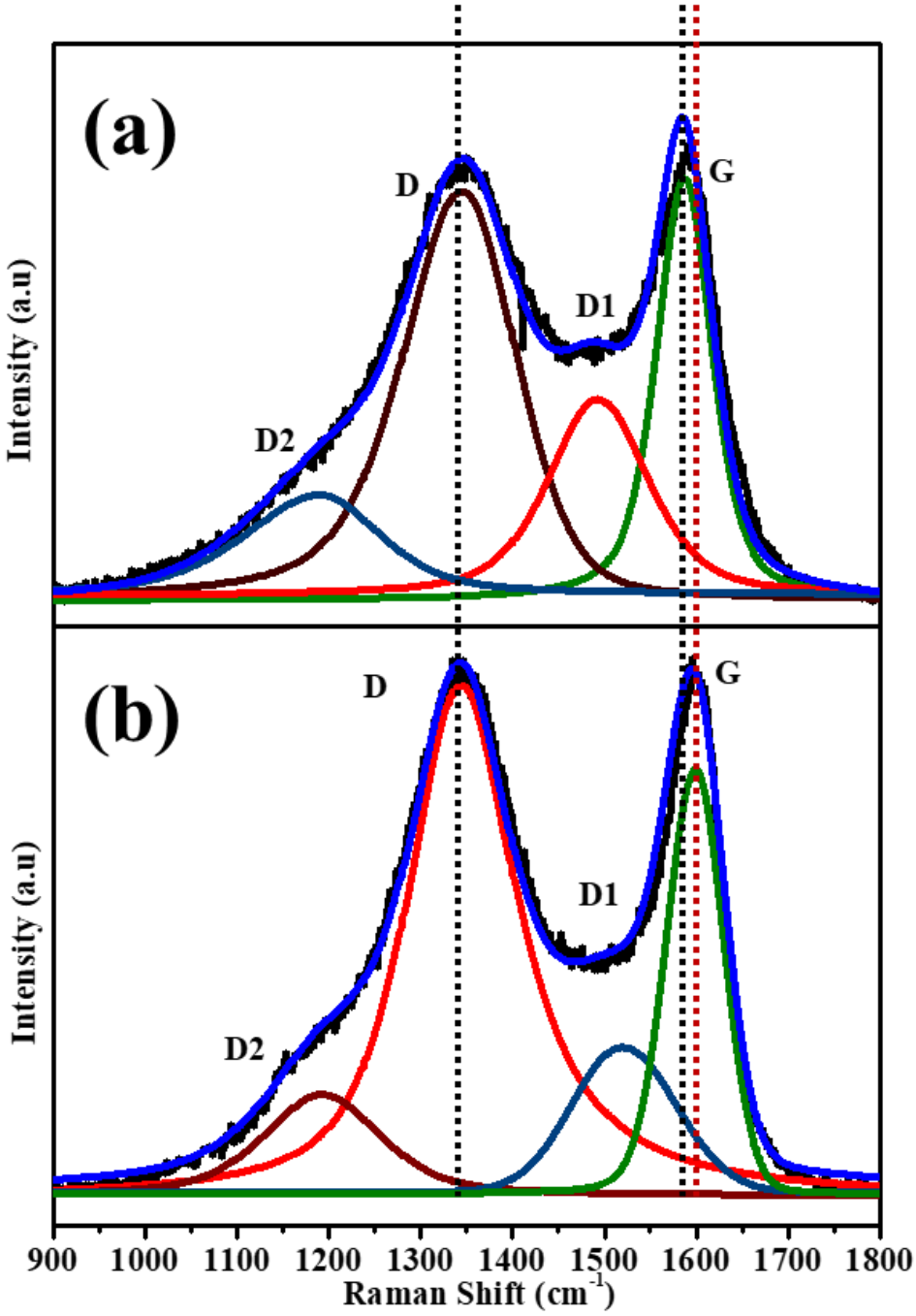



Figure 5.4: Deconvoluted Raman spectra for BHCSs(a) and BNHCSs(b) showing the shift in the G peak position (blue and red grid lines).

A similar profile was observed for the D band where the FWHM (150) for the BNHCSs was larger than that of the BHCSs (147) indicating that BNHCSs had more disordered diamond like

carbon. Both the pristine and doped BNHCSs had a characteristic Gaussian band centred at about 1175 $cm^{-1}$ which was attributed to the impurity ions and polyenes present in the samples.[20]

Table 5.1: Deconvoluted Raman spectra data for BHCSs and BNHCSs

| | D band | | | G band | | | |
|---|---|---|---|---|---|---|---|
| | FWHM | Intensity | Position | FWHM | Intensity | Position | $I_D/I_G$ |
| BNHCS | 150 | 643 | 1344 | 72 | 643 | 1595 | 1.00 |
| BHCS | 147 | 750 | 1345 | 68 | 773 | 1586 | 0.97 |

Though doping with nitrogen increased the defect density of the material, the $\mathbf{I_D/I_G}$ ratios did not significantly change and hence it was expected that these materials would exhibit similar properties due to their similar Raman spectra.

## 5.4: Synthesis of Pt/BHCSs and Pt/BNHCSs

Platinum nanoparticles were deposited on the BHCS and BNHCS supports using the metal-organic deposition technique. In this technique a requisite amount of $Pt(acac)_2$ (200 mg) and either the BHCSs or BNHCSs (150 mg) were mixed and dry sonicated for 30 min to enable homogenization. The mixture of the platinum precursor and the support were then transferred into a quartz reactor tube (Figure 5.5) and held at 100 ºC for 30 min for moisture removal. The furnace was then ramped to 350 ºC using a slow heating rate of 2.5 $ºC.min^{-1}$ to discourage agglomeration of the platinum nanoparticles. The reaction then proceeded at 350 ºC for 2 h. Argon gas was used at low flow rate of 20 $ml.min^{-1}$ to provide an inert environment. The slow flow rate was used to discourage the removal of the fluffy light weight material in the gas stream.

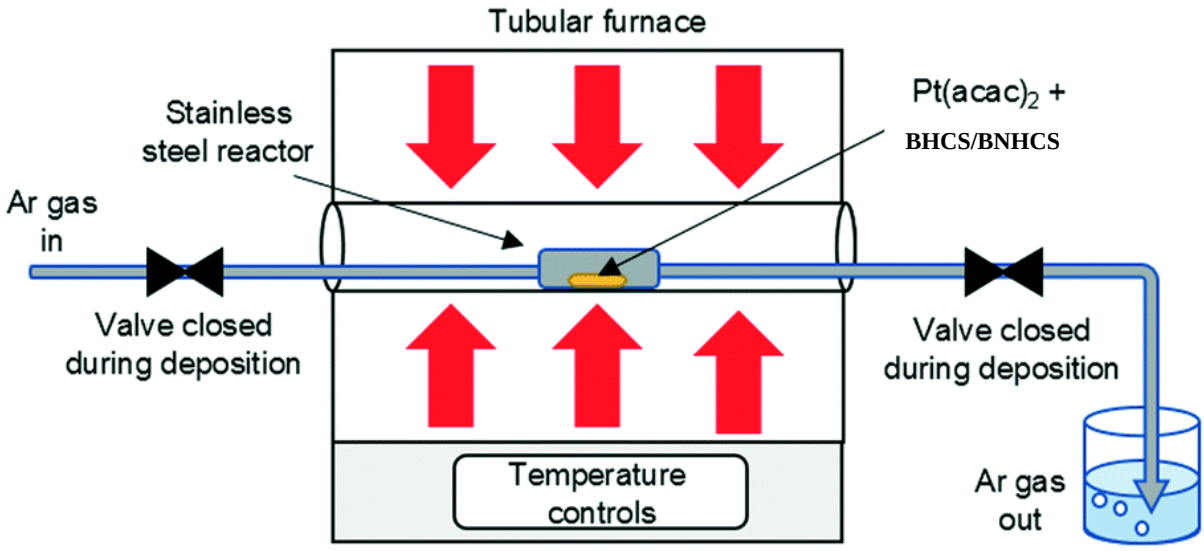



Figure 5.5: Schematic diagram of the metal-organic deposition equipment.[21]

## 5.5: Morphology of the Pt/BHCSs and Pt/BNHCSs

The platinum nanoparticles had a spherical morphology (Figure 5.6) with TEM particle sizes of 3.9 ± 0.5 nm and 3.8 ± 0.6 nm (Figure 5.7, Table 5.2) for the Pt/BHCSs and Pt/BNHCSs, respectively. The particle sizes as determined by TEM and other techniques are displayed in table 5.4. The Pt particles for both supports had a diameter like that of the shell thickness of the supports.

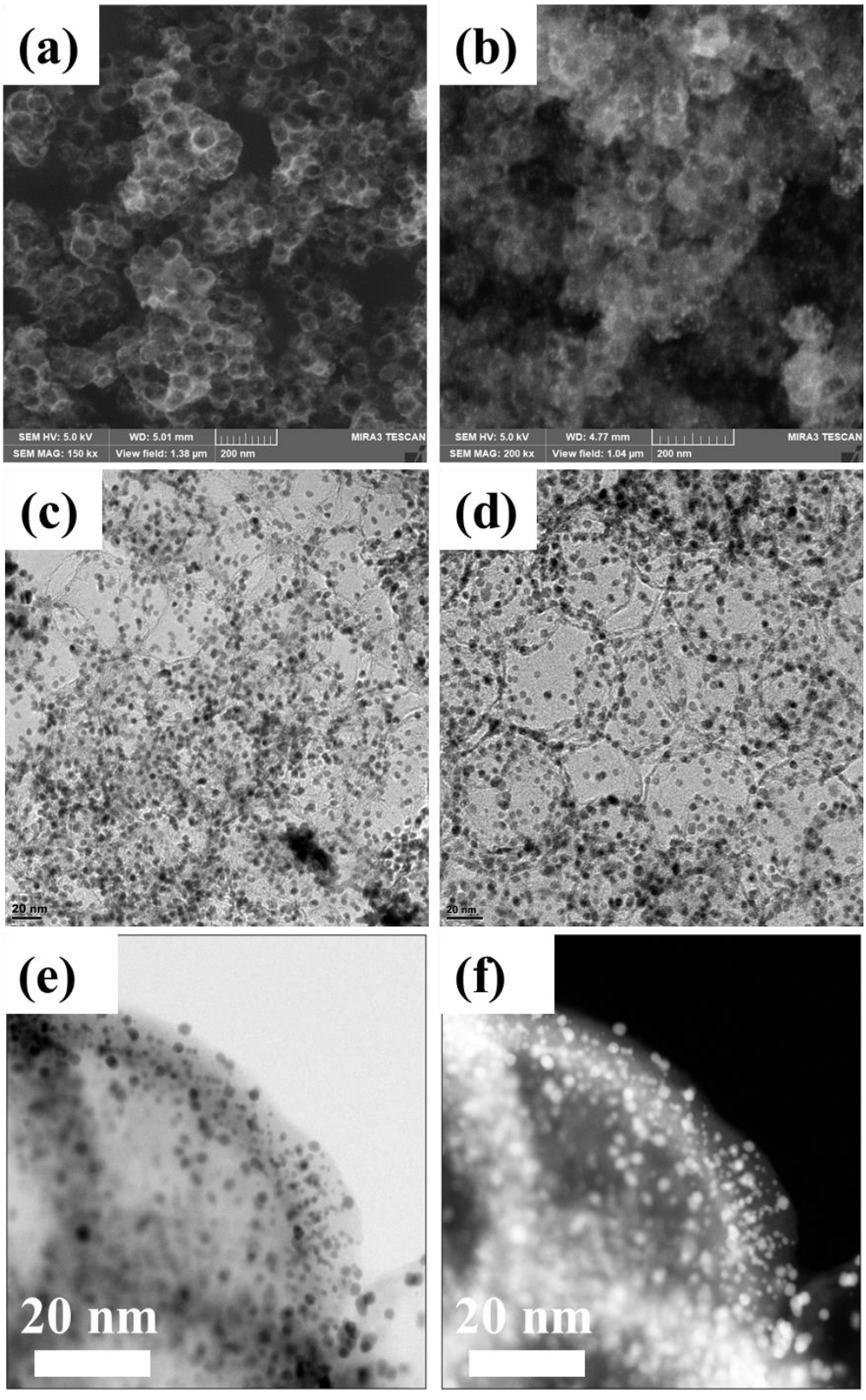



Figure 5.6: SEM micrographs of (a) Pt/BHCSs, (b) Pt/BNHCSs, TEM micrographs of (c) Pt/BHCSs, (d) Pt/BNHCSs, ADF-BF STEM images of (e-f) Pt/BNHCSs.

Using STEM ADF-BF, (Figure 5.6 (e-f)), it was shown that the Pt nanoparticles are mostly embedded within the shell of the support. This is reflected by the brighter ADF contrast in the shells compared to the hollow interior of the BHCSs and BNHCSs supports, and the lack of Pt nanoparticles protruding into the vacuum at the support surface. This embedding of Pt nanoparticles in the support pores and voids is known as pore confinement. Pt confined inside the pores and the voids of the support is strongly bound and more resistant to degradation due to detachment, dissolution, and agglomeration.

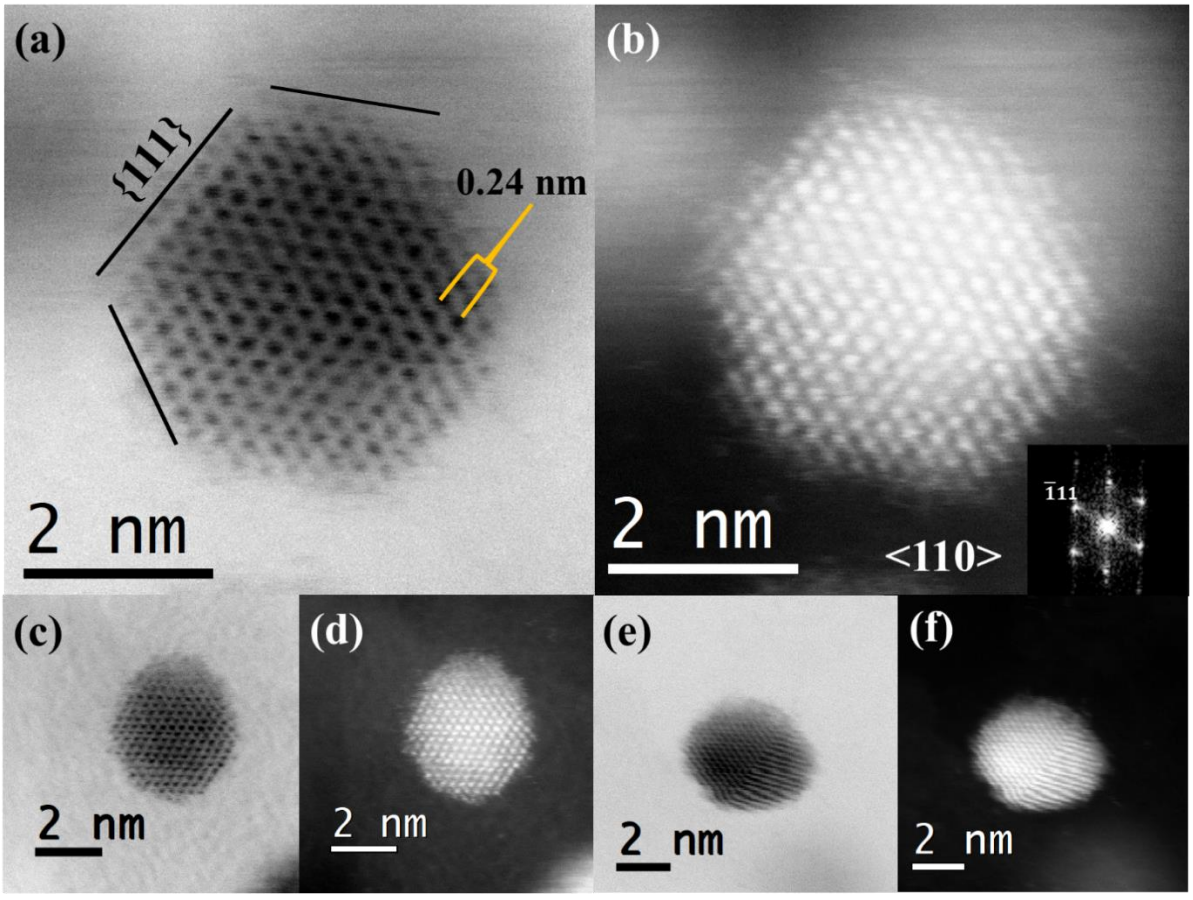



Figure 5.7: High resolution ADF-BF STEM images of (a-b) Pt/BHCSs and (c-f) Pt/BNHCSs. The insert in (b) is the power spectrum of a <110> projection of the fcc Pt.

The local atomic structure of the Pt/BHCSs and Pt/BNHCSs was investigated using aberration-corrected STEM ADF-BF imaging by defocusing the probe at the surface of the carbon support

to access the confined Pt within the support (Figure 5.7 (a – f)). Here, the two catalysts showed no differences in the crystallographic phase of the Pt nanoparticles at the local scale, consistent with the phase determined by bulk PXRD, discussed later. The high-resolution STEM ADF-BF images (Figure 3 (a-d)) showed hexagonal faceted Pt nanoparticles. Examination of the power spectrum (Figure 3 (b) insert) and the measured 0.24 nm interplanar spacing consistent with {111} planes is consistent with a typical <110> face-centred cubic (fcc) structure that is characteristic of Pt particles enclosed with {111} facets (Figure 3 (a)). Some of the Pt nanoparticles (Figure 3 (e-f)) exhibit twin boundary defect commonly observed in fcc transition metals due to symmetrically mirrored <111> fcc Pt grains.[22] According to DFT studies[23], {111} surfaces in fcc Pt are considered to be the active sites for ORR, however in contrast to flat facets, twin boundaries are essential defects in catalysis since they typically have higher adsorption energies in comparison to flat facets and are stable during chemical reactions.[24,25]

The Pt nanoparticles deposited on both supports had small inter platinum distances of 6.5 ± 0.5 nm for Pt/BHCSs and 6.4 ± 0.2 nm for Pt/BNHCSs respectively (Figure 5.8, Table 5.2). The smaller interparticle distances for these Pt catalysts are due to the deposition technique used and the numerous defects on the supports which provides for numerous nucleation sites during deposition.[26–28] Pt nanoparticles supported on the BNHCSs were expected to have a smaller inter-particle distance due to the presence of the electron rich nitrogen groups. The defects are accompanied by electronic effects associated with the nitrogen electron rich groups which facilitate and regulate the nucleation and growth process of the Pt.

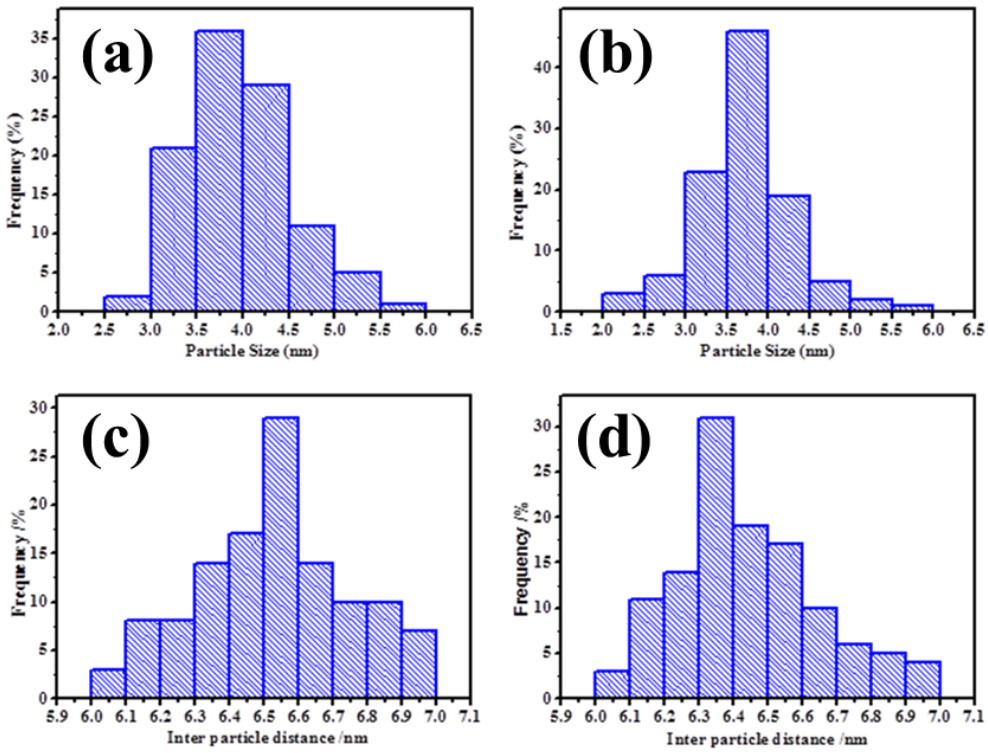



Figure 5.8: Pt particle size distribution of (a) Pt/BHCSs and (b) Pt/BNHCSs. Pt – Pt interparticle distance of (c) Pt/BHCSs and (d) Pt/BNHCSs.

Table 5.2: TEM Pt particle size and Pt – Pt distance for Pt/BHCSs and Pt/BNHCSs

| | TEM particles | |
|---|---|---|
| Sample | Pt size /nm | Pt – Pt distance /nm |
| Pt/BHCSs | 3.9 ± 0.5 | 6.5 ± 0.5 |
| Pt/BNHCSs | 3.8 ± 0.6 | 6.4 ± 0.2 |

## 5.6: Surface area and porosity of the supports and the catalysts

The textual properties and surface area of the materials were investigated using BET and BJH methods. The BHCSs and BNHCSs were both found to exhibit a type II BET isotherm (Figure

5.9) that is characterized by monolayer gas physisorption at low relative pressure and multilayer gas adsorption at high relative pressure.[29–31]

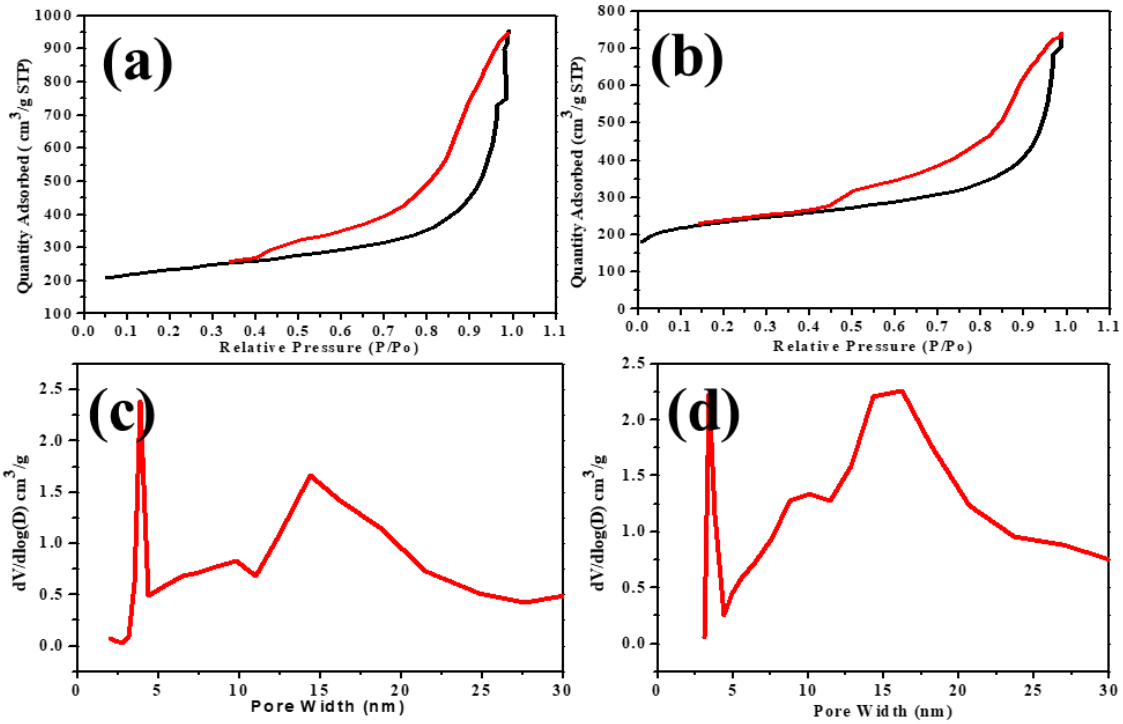



Figure 5.9: BET Isotherms for (a) BHCSs and (b) BNHCSs. Pore size distribution for (c) BHCSs and (d) BNHCSs.

The pristine BHCSs and the BNHCSs had a comparable high BET surface area of 755 $m^2/g$ and 782 $m^2/g$ (Table 5.3). After the deposition of the Pt nanoparticles the Pt/BHCS had a 39 % reduction in BET surface area leading to a BET surface area of 462 $m^2/g$ whereas for the Pt/BNHCS, had a 63 % reduction in BET surface area. The observed reduction in surface area is coupled with a 43 % reduction in pore volume and a 30 % reduction in pore width for the BHCS/ Pt/BHCS samples. For the BNHCSs/ Pt/BNHCSs there is an observed 80 % reduction in pore volume and a 47% reduction in pore width.[32]

Table 5.3: Textual properties of BHCSs, BNHCSs, Pt/BHCS and Pt/BNHCS

| Sample | BET Surface Area $m^2/g$ | BJH Pore Volume $cm^3/g$ | BJH Pore Width /nm |
|---|---|---|---|
| BHCSs | 755 | 1.12 | 8.6 |
| Pt/BHCSs | 462 | 0.64 | 6.8 |
| BNHCSs | 782 | 1.45 | 10.3 |
| Pt/BNHCSs | 347 | 0.31 | 5.5 |

There were no significant differences in terms of BET surface area, pore volume and pore width when the pristine support was compared to the doped broken hollow carbon spheres.

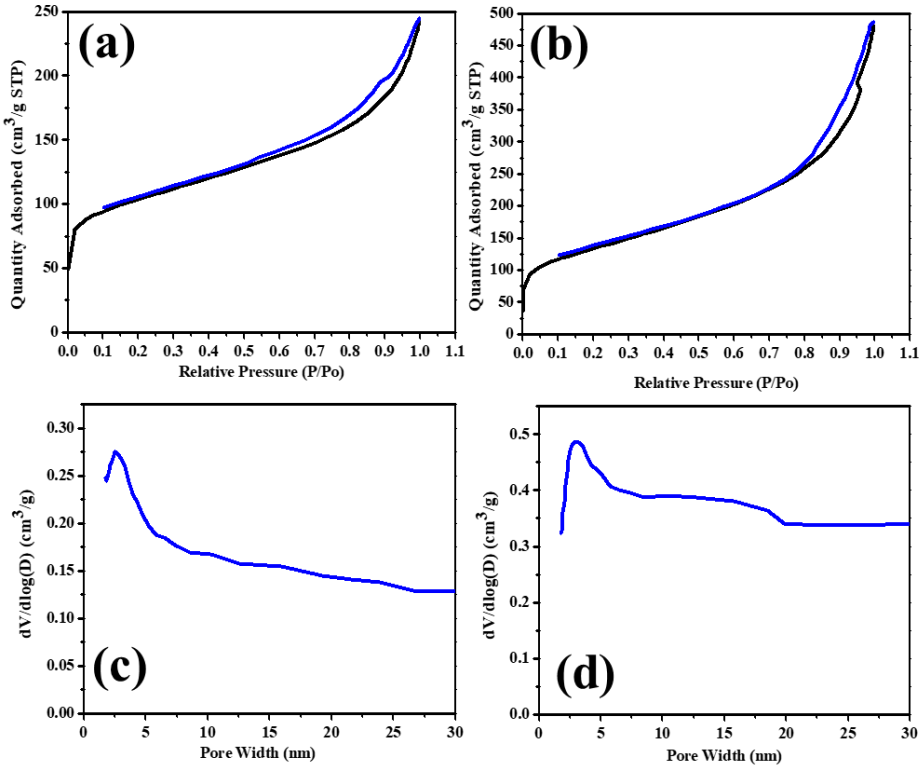



Figure 5.10: BET Isotherms for (a) Pt/BHCSs and (b) Pt/BNHCSs. Pore size distribution for (c) Pt/BHCSs and (d) Pt/BNHCS.

The reduction in textual properties due to the deposition of Pt was attributed to some of the Pt nanoparticles being confined inside the pores of the supports and hence changing the overall pore structure of the metal supported materials.[33–35] During inert gas physisorption the gas molecules are adsorbed on the surfaces of the material including inside the pores. Pore volume and pore size are reduced by the same phenomena.

Both the BHCSs and BNHCSs samples showed that they had a type II BET isotherm in terms of gas physisorption and desorption. This type of isotherm is characterized by monolayer inert gas adsorption at higher relative pressures multilayer physisorption occurs. At these higher relative pressures capillary condensation occurs of the inert gas molecules inside the mesopores leading to a hysteresis loop during desorption.[30] There is no difference in the isotherm type (type II) between the pristine and the doped supports, an indication that both materials are both mesoporous. This is also shown by the pores size distributions. (Figure 5.10 c and d). The isotherms show a significant change in the size of the hysteresis loop of the Pt/BHCSs and Pt/BNHCSs compared to the supports BHCSs and BNHCSs. The smaller hysteresis loop for the Pt supported catalysts indicate that there is less capillary condensation of the inert gas compared to the pristine supports.

There is an observable change also in the pore structure of the Pt supported materials versus the pristine and the nitrogen doped supports. The pores with significant volume are widely distributed between 5 and 30 nm for both supports (Figure 5.9). However, after the deposition of platinum the pores with significant volume were now mostly in the 1 to 10 nm range (Figure 5.10). The reduction can be attributed to the pore confinement and presence of Pt nanoparticles inside the pores hence causing a reduction in pore volume.

## 5.7: Thermogravimetric analysis (TGA)

The pristine and the nitrogen doped material were studied using TGA (from room temperature to 900ºC) to investigate the thermal stability of the materials.

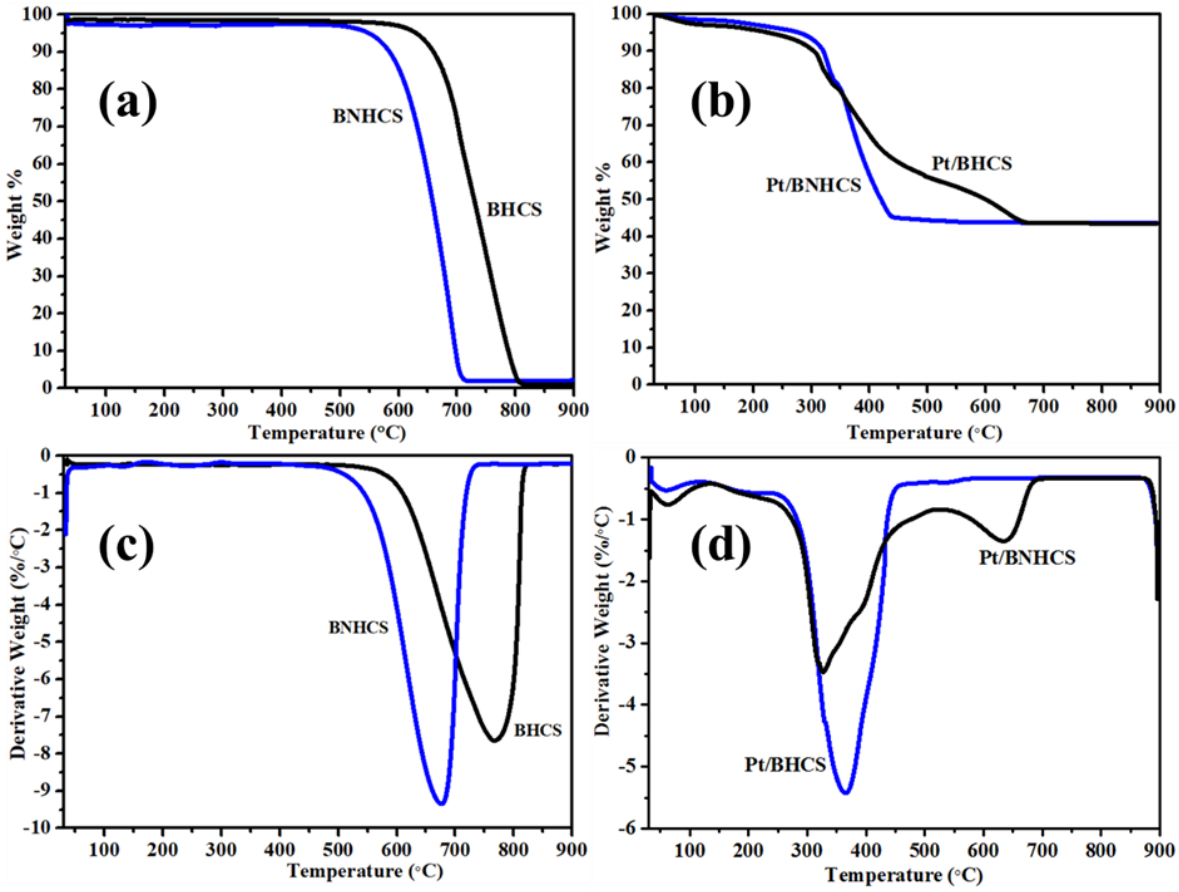



Figure 5.11: TGA profile for (a) BHCSs and BNHCSs, (b) Pt/BHCSs and Pt/BNHCSs. DTA profiles for (c) BHCSs and BNHCSs, (d) Pt/BHCSs and Pt/BNHCSs.

The pristine BHCSs were found to have a higher final decomposition temperature of 780ºC compared to 680ºC for the nitrogen doped carbon (Figure 5.11). The lower decomposition temperature for the doped BNHCSs was attributed to the defects in the structure of the carbon which makes it more prone to thermal degradation.[36,37] It has been concluded from previous studies that ordered and more graphitic carbon materials tend to me more thermally stable compared to defective carbon materials. For example, it is known that highly ordered carbon

nanotubes tend to be more thermally stable compared to soot which is mostly amorphous carbon.[38–40]

For both the materials, the final residual weight% is zero which is an indication that at 900ºC all the materials have decomposed completely. This is also an indication that the $SiO_2$ etching process was successful (error bar < 0.5%). $SiO_2$ does not decompose at temperatures below 900ºC hence its presence would show as a residual weight%.

After the deposition of platinum particles, the residual Pt was 40.5 wt% for Pt/BHCS and Pt/BNHCS respectively (Figure 5.11) as determined by TGA. The deposition of Pt enhanced the combustion of the catalysts and promoted the lowering of the thermal stability of the materials as shown by the lower decomposition temperature of Pt/BHCSs at 380ºC compared to 780ºC for BHCSs. The decomposition of Pt/BNHCSs also occurred at a much lower temperature (320ºC) compared to the BNHCSs (680ºC) as shown in the DTA profiles. The platinum is known for its combustion catalyst properties. Platinum has been shown to initiate the combustion of organics including hdrocarbons.[41–44] This catalytic effect of Pt enables the faster combustion of the carbon supports and hence enables the process to occur at lower temperatures than the unsupported materials. Addition of Pt on the surfaces and inside the pores of the support materials also tends to affect the structural integrity of the material. The presence of Pt has a similar effect as that due to the defects introduced by nitrogen doping.

The unsupported carbon materials show a single broad decomposition peak. However, for Pt/BNHCSs, the DTA profile shows multiple peaks. The numerous decomposition processes are attributed to the defects and changes in structure of the carbon due to doping and the presence of Pt.[39,40]

## 5.8: Powder X-ray diffraction (PXRD)

The crystallinity of the materials was investigated using PXRD. Both the BHCSs and BNHCSs showed a structure typical of turbostratic carbon made mostly of amorphous carbon (Figure 5.12).[45,46] The PXRD diffractograms showed the presence of the broad C (002) peak at around 25 degrees (2Θ) for both the pristine and the doped material. The C(002) peaks are sharper compared to peaks from amorphous soot, another indication of improved ordering in these carbons compared to highly amorphous soot.[45] There are no significant differences in the diffractograms between the BHCSs and the BNHCSs samples. After the deposition of platinum nanoparticles, the PXRD diffractograms showed the presence of the Pt through the different reflections which are characteristic of the face centred cubic (fcc) unit cell of Pt with the characteristic finger print peaks at various 2Θ values as shown in figure 3.10b[47,48]

Rietveld refinement of the Pt peaks yielded a Pt particle size of 4.8 ± 0.9 (Pt/BNHCSs) and 5.2 ± 1.2 (Pt/BHCSs), (Table 5.4). The Pt particle size as determined with the Scherrer equation[49] were 4.5 ± 0.7 nm and 4.3 ± 0.8 nm for Pt/BHCSs and Pt/BNHCSs respectively. As expected, the Pt nanoparticles are smaller in the nitrogen doped support as doping with heteroatoms increase defects on the supports whereupon the Pt grows during deposition [50,51] and also that the electron density on the nitrogen groups affects the growth and nucleation kinetics of Pt resulting in smaller Pt nanoparticles[27]

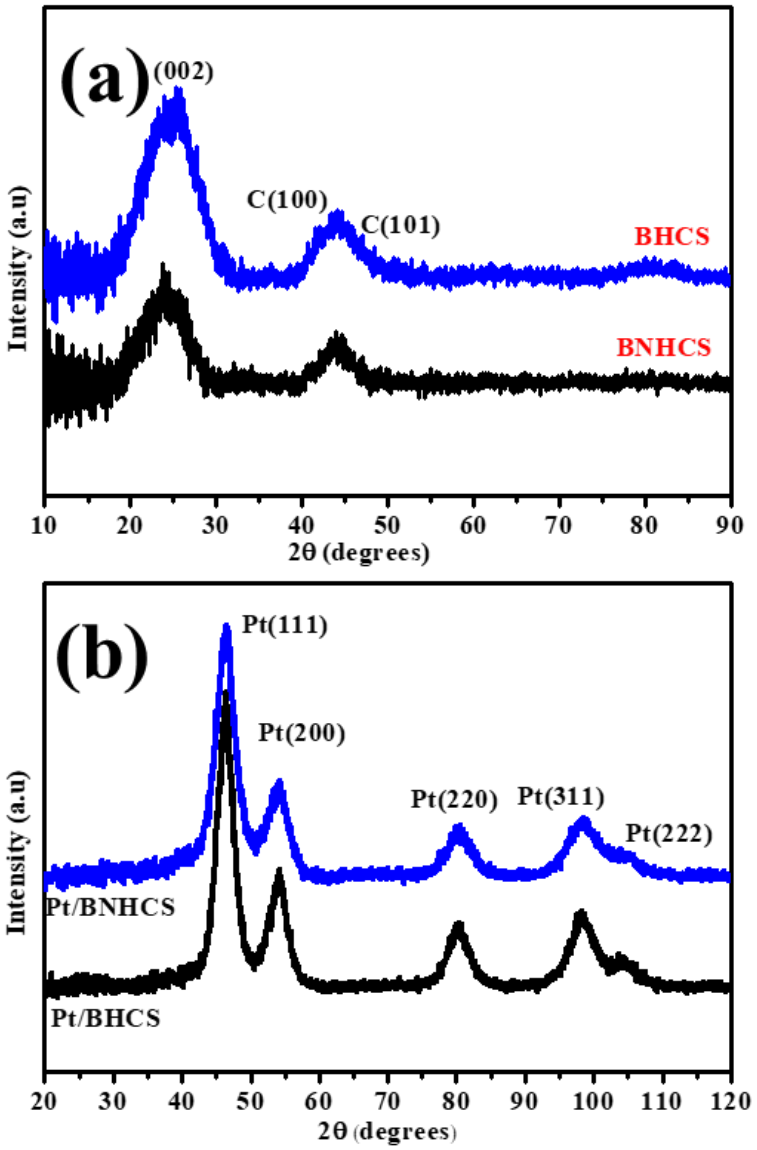



Figure 5.12: PXRD diffractograms of BHCSs and BNHCSs (a), Pt/BHCSs and Pt/BNHCSs (b).

The PXRD measured Pt nanoparticle sizes were slightly larger than the TEM measured nanoparticles due to the volume averaging of particle size determination in PXRD.[27,52] In PXRD particle size determination, particles smaller than 2 nm tend to not be detected and as a result the final average particle size is due to the effect on mostly bigger particles. In TEM, counting is mostly done manually. The counting includes the smaller Pt particles and the average tends to be give smaller particle sizes than measured by PXRD methods The Pt

particles for the novel Pt/BHCSs and Pt/BNHCSs were of comparable size to the Pt particles of the commercial Pt/Vulcan catalysts (Table 5.4).

Table 5.4: Pt particle sizes of Pt/BHCSs, Pt/Vulcan and Pt/BNHCSs as measured by TEM and PXRD techniques

| Size/nm | Pt/BHCS | Pt/BNHCS | Pt/Vulcan |
|---|---|---|---|
| TEM | 3.9 ± 0.5 | 3.8 ± 0.6 | 3.9 ± 0.9 |
| Scherrer | 4.5 ± 0.8 | 4.3 ± 0.7 | 4.1 ± 1.2 |
| Rietveld | 5.2 ± 1.2 | 4.8 ± 0.9 | 4.7 ± 0.6 |

## 5.9: X-ray photoelectron spectroscopy (XPS)

XPS was used for quantitative surface analysis of the support BHCSs, BNHCSs and for the supported Pt/BHCSs and Pt/BNHCSs.[53,54] The advantages of XPS are that it is a versatile technique which provides material surface information on elemental identification and the chemical state of the elements, relative composition of the constituents in the surface region and the valence band structure of the materials.[55] To compensate for sample charging effects, the binding energy of adventitious $sp^2$ carbon (284.4 eV) was used as a measurements calibration standard.[56]

The low-resolution surface survey scan were obtained in the 50–550 eV binding energy window (Figure 5.13) and the photoelectrons without energy loss were revealed by the distinct peaks associated with the Pt4f, C1s, O1s and N1s electronic states in both the Pt/BHCSs and Pt/BNHCSs samples.

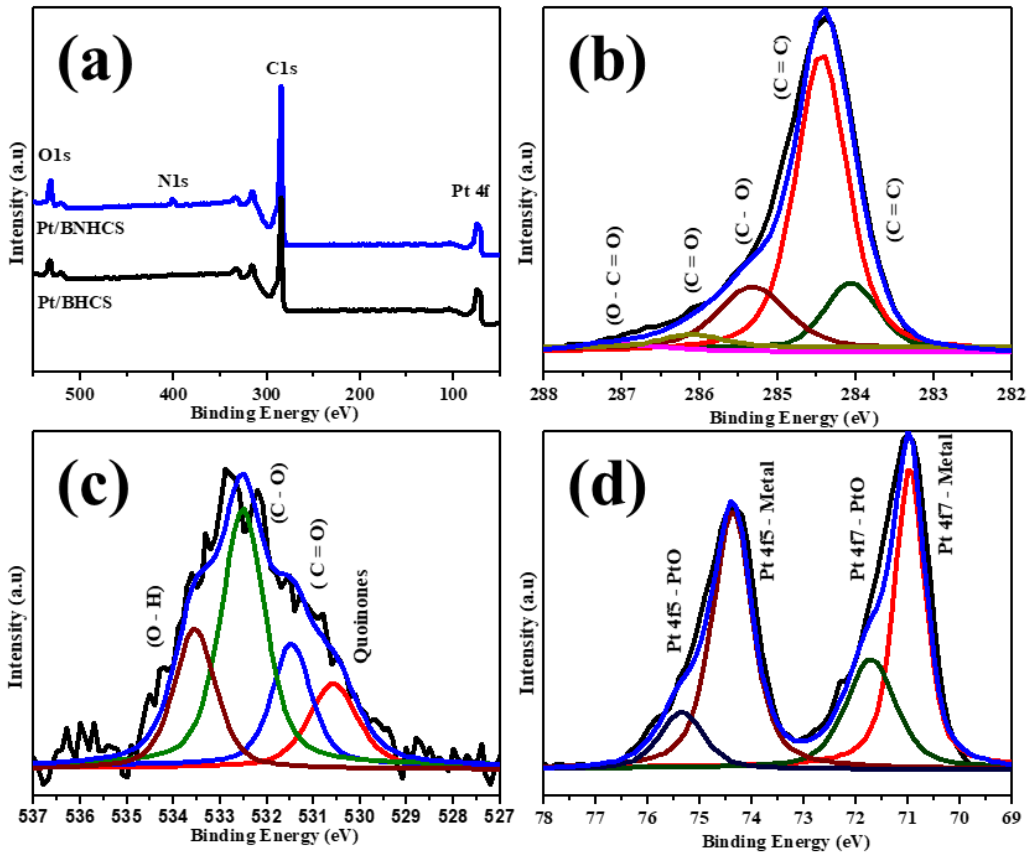



Figure 5.13: XPS surveys for (a) Pt/BHCSs and Pt/BNHCSs. High resolution (b) C1s, (c) O1s and (d) Pt4f spectra for Pt/BHCSs.

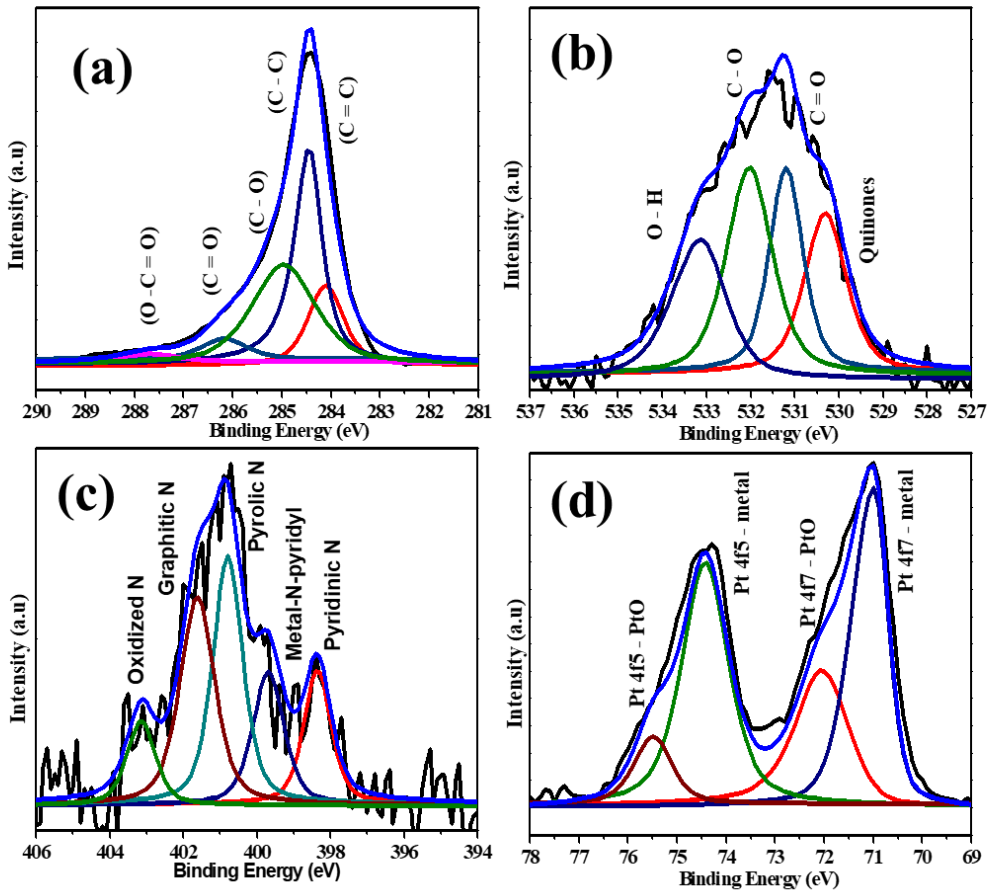



Figure 5.14: Deconvoluted high resolution (a) C1s, (b) O1s, (c) N1s and (d) Pt4f spectra for Pt/BNHCSs.

The C1s spectra were deconvoluted and no significant changes were found in the component peaks for both Pt/BHCSs and Pt/BNHCSs samples. These peaks were deconvoluted into the component C=C, C–C, C–C, O-C=O and C=O bonds (Figure 5.13 and Figure 5.14).[57] No significant changes were found in the position of the peaks for both the Pt/BHCS and Pt/BNHCS samples (Table 5.5). An upward binding energy shift of 0.5 eV for the O-C=O bond in the Pt/BNHCS sample was observed. The positive binding energy shifts in the deconvolution of the C1s peak was attributed to the different chemical environment of the carbon atoms enabled by nitrogen doping.[58,59]

Deconvolution of the carbon species present indicates the presence of about 31 at. % $sp^2$ (C=C) hybridized carbon for the Pt/BHCS compared to 26 at. % for Pt/BNHCS samples. More graphitic carbon in the Pt/BHCS sample is an indication that there are fewer defects in the sample compared to the nitrogen doped sample, which agrees with Raman analysis data (Table 5.1).[60]

Table 5.5: Data of deconvoluted high resolution C1s spectra for Pt/BHCSs and Pt/BNHCSs

| Sample | C1s | | | | ` |
|---|---|---|---|---|---|
| | C=C | C-C | C-O | C=O | O–C=O |
| (BE/eV)Pt/BNHCS | 284.3 | 284.7 | 285.6 | 286.2 | 287.7 |
| (BE/eV)Pt/BHCS | 284.3 | 284.6 | 285.3 | 286.1 | 287.1 |
| BE Difference (Δ eV) | 0 | 0.1 | 0.3 | 0.1 | 0.6 |
| (Atomic%)Pt/BNHCS | 26.3 | 36.2 | 12.8 | 3.2 | 1.7 |
| (Atomic%)Pt/BHCS | 30.4 | 39.0 | 13.9 | 3.3 | 1.7 |
| Atomic % difference | 3.9 | 2.8 | 1.1 | 0.1 | 0 |

Deconvolution of O1s spectra (Figure 5.13 and Figure 5.14) show the presence of quinones (530.3 eV), C=O bonds (531.2 eV), C–O bonds (532.0 eV) and terminal O–H bonds (533.1 eV).[61] There was an observed upward binding energy shift for the Pt/BNHCSs sample which was attributed to the varying chemical environment of the oxygen atoms.[58]

Table 5. 6: Data of deconvoluted high resolution O1s spectra for Pt/BHCSs and Pt/BNHCSs.

| O1s |
|---|

| Sample | C=O | C-O | O-H | Quinones |
|---|---|---|---|---|
| (BE/eV)Pt/BNHCS | 531.2 | 532.0 | 533.1 | 530.3 |
| (BE/eV)Pt/BHCS | 531.5 | 532.5 | 533.5 | 530.5 |
| Δ eV | 0.3 | 0.5 | 0.4 | 0.2 |
| (Atomic%)Pt/BNHCS | 2.9 | 3.2 | 0.5 | 0.6 |
| (Atomic%)Pt/BHCS | 2.1 | 3.5 | 0.8 | 0.5 |
| Δ Atomic % | 0.8 | 0.3 | 0.3 | 0.1 |

Deconvolution of the N1s high resolution spectra for Pt/BNHCSs show the presence of pyridinic nitrogen (398.3 eV), pyrrolic nitrogen (400.7 eV), graphitic nitrogen (401.6 eV), oxidized nitrogen (403.1 eV) and metal bonded nitrogen (metal-N-pyridyl) nitrogen (399.7 eV) (Table 5.7).[62]

The total atomic % contribution of the nitrogen groups was about 7.4% an indication that the doping process was completed. It is important to note that the electronic effects on the surface of the materials is mostly due to the interaction of the carbon material with the electronegative oxygen and nitrogen groups.[63]

Table 5. 7: Data of deconvoluted high resolution N1s spectra for Pt/BNHCSs.

| Sample | N1s | | | | |
|---|---|---|---|---|---|
| | Pyridinic N | Metal Nitrile | Pyrrolic N | Graphitic N | Oxidized N |
| (BE/eV)Pt/NHCS | 398.3 | 399.7 | 400.7 | 401.6 | 403.1 |

| | | | | | |
|---|---|---|---|---|---|
| (Atomic%)Pt/NHCS | 1.4 | 1.2 | 2.1 | 1.8 | 0.9 |

The Pt4f spectra for Pt/BHCSs and Pt/BNHCSs samples were deconvoluted (Figure 5.15) and the peaks were assigned (Table 5.8). An observed upward binding energy shifts for the Pt/BNHCSs samples compared to the Pt/BHCSs was observed.[58,64,65]

Table 5.8: Data of deconvoluted high resolution Pt4f spectra for Pt/BHCSs and Pt/BNHCSs

| | Pt4f | | | |
|---|---|---|---|---|
| Sample | Pt4f7 metal | Pt 4f7 – PtO | Pt4f5 - metal | Pt4f5 – PtO |
| (BE/eV)Pt/BHCS | 71.0 | 72.0 | 74.4 | 75.5 |
| (BE/eV)Pt/BNHCS | 70.9 | 71.7 | 74.2 | 75.2 |
| Δ eV | 0.1 | 0.3 | 0.2 | 0.3 |
| (Atomic%)Pt/BHCS | 2.0 | 0.6 | 2.0 | 0.6 |
| (Atomic%)Pt/BNHCS | 2.0 | 0.4 | 2.0 | 0.4 |
| Δ Atomic % | 0 | 0.2 | 0 | 0.2 |

The observed upward shift in the binding energies is attributed to the interaction between the Pt metal and the BHCSs and BNHCSs supports.[50,66,67] Due to the differences in the surface chemistry of these supports, the metal-support interaction is expected to vary. It is widely known through X-ray studies that charge transfer occurs between the platinum nanoparticles and the electronic groups on the surface of the supports.[63,68] The quantity of this charge transfer is different from support to support and the presence of these electronegative nitrogen groups causes the upward binding energy shift for the Pt4f spectra.

The Pt 4f spectra was deconvoluted into metallic Pt and oxidized Pt (PtO) with metallic Pt accounting for more than 90 at. % of Pt species present for both samples. This shows that most of the platinum on the surface and in the pores of both the catalysts exists as metallic Pt more than it exists as PtO. However, both Pt and PtO are useful in oxygen reduction reactions

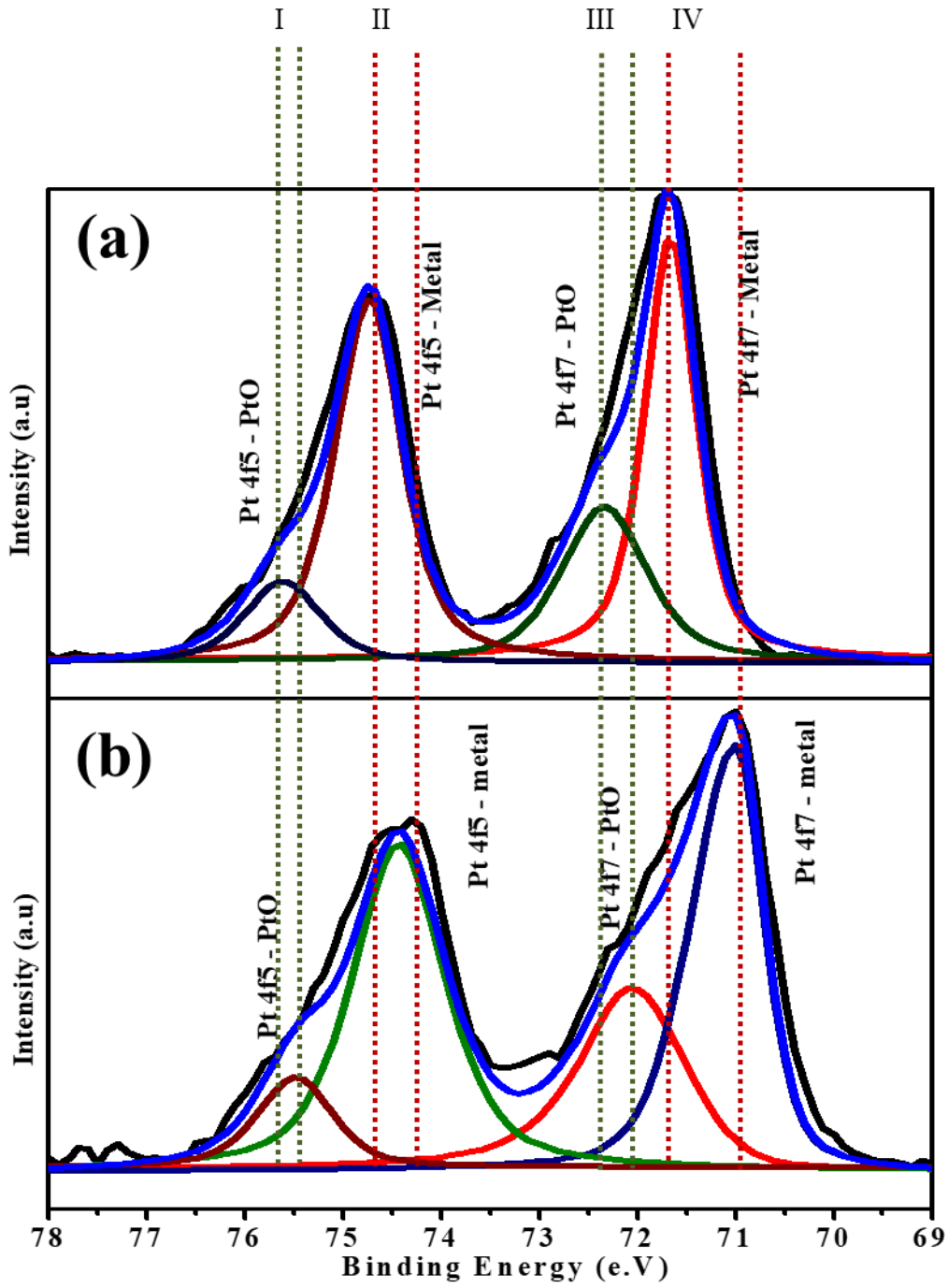



Figure 5.15: Stacked deconvoluted Pt4f XPS spectra for (a) Pt/BHCSs and (b) Pt/BNHCSs showing binding energy shifts.

## 5.10: Conclusions

In conclusion, the BHCSs and BNHCSs were synthesized with a diameter of 58 ± 0.9 nm and 60 ± 1.1 nm respectively. The materials possessed thin carbon shells of 4.5 ± 0.6 and 4.6 ± 0.9

nm respectively. Raman spectroscopy data indicated the presence of defects and a large extent of graphitization which would be beneficial for catalysis. The materials had high BET surface area and possessed a network of mesopores. XPS data confirmed the successful nitrogen doping and deposition of Pt. The BET surface area decreased after the deposition of Pt due to the blocking of the pores and possible Pt pore confinement. The Pt particles formed were small and suitable for electrocatalysis applications. The thermal stability significantly decreased after the deposition of Pt and the Pt loading was confirmed to be around 40 wt.%. The materials had distinct hemispherical morphology which could prove advantageous in electrocatalysis.

## 5.11: References


(1) Mwinga, M.; Groenewald, B.; McPherson, M. A DC – DC Converter for PEMFC Stack Power Conditioning Applications. *J. Phys.: Conf. Ser.* **2018**, *1074*, 012086.

(2) Ballard Partners with Anglo American to Push Fuel Cells in SA. *Fuel Cells Bulletin* **2012**, *2012* (5), 10.

(3) Cognard, G.; Ozouf, G.; Beauger, C.; Jiménez-Morales, I.; Cavaliere, S.; Jones, D.; Rozière, J.; Chatenet, M.; Maillard, F. Pt Nanoparticles Supported on Niobium-Doped Tin Dioxide: Impact of the Support Morphology on Pt Utilization and Electrocatalytic Activity. *Electrocatalysis* **2017**, *8* (1), 51–58.

(4) Dubau, L.; Castanheira, L.; Maillard, F.; Chatenet, M.; Lottin, O.; Maranzana, G.; Dillet, J.; Lamibrac, A.; Perrin, J.-C.; Moukheiber, E.; ElKaddouri, A.; Moor, G. D.; Bas, C.; Flandin, L.; Caqué, N. A Review of PEM Fuel Cell Durability: Materials Degradation, Local Heterogeneities of Aging and Possible Mitigation Strategies. *WIREs Energy and Environment* **2014**, *3* (6), 540–560.

(5) Dubau, L.; Durst, J.; Castanheira, L.; Maillard, F.; Lamibrac, A.; Dillet, J.; Maranzana, G.; Lottin, O.; Kaddouri, A. E.; Moor, G. D.; Bas, C.; Flandin, L.; Rossinot, E.; Caqué, N.; Chatenet, M. Various Scales of Aging Heterogeneities upon PEMFC Operation – A

Link between Local MEA Materials Degradation and the Cell Performance. *ECS Trans.* **2015**, *69* (17), 133.

(6) Anwar, M. T.; Yan, X.; Shen, S.; Husnain, N.; Zhu, F.; Luo, L.; Zhang, J. Enhanced Durability of Pt Electrocatalyst with Tantalum Doped Titania as Catalyst Support. *International Journal of Hydrogen Energy* **2017**, *42* (52), 30750–30759.

(7) Yu, X.; Ye, S. Recent Advances in Activity and Durability Enhancement of Pt/C Catalytic Cathode in PEMFC. Part I. Physico-Chemical and Electronic Interaction between Pt and Carbon Support, and Activity Enhancement of Pt/C Catalyst. *Journal of Power Sources* **2007**, *172* (1), 133–144.

(8) Ma, J.; Habrioux, A.; Luo, Y.; Ramos-Sanchez, G.; Calvillo, L.; Granozzi, G.; Balbuena, P. B.; Alonso-Vante, N. Electronic Interaction between Platinum Nanoparticles and Nitrogen-Doped Reduced Graphene Oxide: Effect on the Oxygen Reduction Reaction. *Journal of Materials Chemistry A* **2015**, *3* (22), 11891–11904.

(9) Zhang, J.; Ma, L.; Gan, M.; Yang, F.; Fu, S.; Li, X. Well-Dispersed Platinum Nanoparticles Supported on Hierarchical Nitrogen-Doped Porous Hollow Carbon Spheres with Enhanced Activity and Stability for Methanol Electrooxidation. *Journal of Power Sources* **2015**, *288*, 42–52.

(10) Stöber, W.; Fink, A.; Bohn, E. Controlled Growth of Monodisperse Silica Spheres in the Micron Size Range. *Journal of Colloid and Interface Science* **1968**, *26* (1), 62–69.

(11) Dlamini, M. W.; Phaahlamohlaka, T. N.; Kumi, D. O.; Forbes, R.; Jewell, L. L.; Coville, N. J. Post Doped Nitrogen-Decorated Hollow Carbon Spheres as a Support for Co Fischer-Tropsch Catalysts. *Catalysis Today* **2020**, *342*, 99–110.

(12) Kamiya, H.; Mitsui, M.; Takano, H.; Miyazawa, S. Influence of Particle Diameter on Surface Silanol Structure, Hydration Forces, and Aggregation Behavior of Alkoxide-Derived Silica Particles. *Journal of the American Ceramic Society* **2000**, *83* (2), 287–293.

(13) Kobayashi, M.; Juillerat, F.; Galletto, P.; Bowen, P.; Borkovec, M. Aggregation and Charging of Colloidal Silica Particles: Effect of Particle Size. *Langmuir* **2005**, *21* (13), 5761–5769.

(14) Liu, X.; Li, S.; Mei, J.; Lau, W.-M.; Mi, R.; Li, Y.; Liu, H.; Liu, L. From Melamine–Resorcinol–Formaldehyde to Nitrogen-Doped Carbon Xerogels with Micro- and Meso-Pores for Lithium Batteries. *Journal of Materials Chemistry A* **2014**, *2* (35), 14429–14438.

(15) Okuda, H.; Young, R. J.; Wolverson, D.; Tanaka, F.; Yamamoto, G.; Okabe, T. Investigating Nanostructures in Carbon Fibres Using Raman Spectroscopy. *Carbon* **2018**, *130*, 178–184.

(16) Bhalerao, G. M.; Sinha, A. K.; Sathe, V. Defect-Dependent Annealing Behavior of Multi-Walled Carbon Nanotubes. *Physica E: Low-dimensional Systems and Nanostructures* **2008**, *41* (1), 54–59.

(17) Li, Y.; Wang, J.; Li, X.; Liu, J.; Geng, D.; Yang, J.; Li, R.; Sun, X. Nitrogen-Doped Carbon Nanotubes as Cathode for Lithium–Air Batteries. *Electrochemistry Communications* **2011**, *13* (7), 668–672.

(18) Ferrari, A. C.; Robertson, J. Raman Spectroscopy of Amorphous, Nanostructured, Diamond–like Carbon, and Nanodiamond. *Philosophical Transactions of the Royal Society of London. Series A: Mathematical, Physical and Engineering Sciences* **2004**, *362* (1824), 2477–2512.

(19) Ferrari, A. C. Raman Spectroscopy of Graphene and Graphite: Disorder, Electron–Phonon Coupling, Doping and Nonadiabatic Effects. *Solid State Communications* **2007**, *143* (1–2), 47–57.

(20) Zana, A.; Speder, J.; Reeler, N. E. A.; Vosch, T.; Arenz, M. Investigating the Corrosion of High Surface Area Carbons during Start/Stop Fuel Cell Conditions: A Raman Study. *Electrochimica Acta* **2013**, 114(30), 455-461

(21) Mohamed, R.; Binninger, T.; J. Kooyman, P.; Hoell, A.; Fabbri, E.; Patru, A.; Heinritz, A.; J. Schmidt, T.; Levecque, P. Facile Deposition of Pt Nanoparticles on Sb-Doped SnO 2 Support with Outstanding Active Surface Area for the Oxygen Reduction Reaction. *Catalysis Science & Technology* **2018**, *8* (10), 2672–2685.

(22) Gontard, L. C.; Dunin-Borkowski, R. E.; Gass, M. H.; Bleloch, A. L.; Ozkaya, D. Three-Dimensional Shapes and Structures of Lamellar-Twinned Fcc Nanoparticles Using ADF STEM. *J Electron Microsc (Tokyo)* **2009**, *58* (3), 167–174.

(23) Duan, Z.; Wang, G. Comparison of Reaction Energetics for Oxygen Reduction Reactions on Pt(100), Pt(111), Pt/Ni(100), and Pt/Ni(111) Surfaces: A First-Principles Study. **2013**.

(24) Tang, C.; Shi, J.; Bai, X.; Hu, A.; Xuan, N.; Yue, Y.; Ye, T.; Liu, B.; Li, P.; Zhuang, P.; Shen, J.; Liu, Y.; Sun, Z. $CO_2$ Reduction on Copper's Twin Boundary. *ACS Catal.* **2020**, *10* (3), 2026–2032.

(25) Wilms, M.; Broekmann, P.; Kruft, M.; Stuhlmann, C.; Wandelt, K. STM Investigation of Step Orientation and Surface Dynamics of Cu(111) in Hydrochloric Acid Electrolyte. *Applied Physics A: Materials Science and Processing* **1998**, *66*(7), PS473

(26) Shrestha, S.; Asheghi, S.; Timbro, J.; Mustain, W. E. Temperature Controlled Surface Chemistry of Nitrogen-Doped Mesoporous Carbon and Its Influence on Pt ORR Activity. *Applied Catalysis A: General* **2013**, *464–465*, 233–242.

(27) Zhou, Y.; Neyerlin, K.; S. Olson, T.; Pylypenko, S.; Bult, J.; N. Dinh, H.; Gennett, T.; Shao, Z.; O'Hayre, R. Enhancement of Pt and Pt-Alloy Fuel Cell Catalyst Activity and Durability via Nitrogen -Modified Carbon Supports. *Energy & Environmental Science* **2010**, *3* (10), 1437–1446.

(28) Cheng, Q.; Hu, C.; Wang, G.; Zou, Z.; Yang, H.; Dai, L. Carbon-Defect-Driven Electroless Deposition of Pt Atomic Clusters for Highly Efficient Hydrogen Evolution. *J. Am. Chem. Soc.* **2020**, *142* (12), 5594–5601.

(29) Bhambhani, M. R.; Cutting, P. A.; Sing, K. S. W.; Turk, D. H. Analysis of Nitrogen Adsorption Isotherms on Porous and Nonporous Silicas by the BET and As Methods. *Journal of Colloid and Interface Science* **1972**, *38* (1), 109–117.

(30) Kierlik, E.; Monson, P. A.; Rosinberg, M. L.; Sarkisov, L.; Tarjus, G. Capillary Condensation in Disordered Porous Materials: Hysteresis versus Equilibrium Behavior. *Phys. Rev. Lett.* **2001**, *87* (5), 055701.

(31) Neimark, A. V.; Ravikovitch, P. I. Capillary Condensation in MMS and Pore Structure Characterization. *Microporous and Mesoporous Materials* **2001**, *44–45*, 697–707.

(32) Jauhar, A. M.; Ma, Z.; Xiao, M.; Jiang, G.; Sy, S.; Li, S.; Yu, A.; Chen, Z. Space-Confined Catalyst Design toward Ultrafine Pt Nanoparticles with Enhanced Oxygen Reduction Activity and Durability. *Journal of Power Sources* **2020**, *473*, 228607.

(33) Galeano, C.; Meier, J. C.; Peinecke, V.; Bongard, H.; Katsounaros, I.; Topalov, A. A.; Lu, A.; Mayrhofer, K. J. J.; Schüth, F. Toward Highly Stable Electrocatalysts via Nanoparticle Pore Confinement. *J. Am. Chem. Soc.* **2012**, *134* (50), 20457–20465.

(34) Pizzutilo, E.; Knossalla, J.; Geiger, S.; Grote, J.-P.; Polymeros, G.; Baldizzone, C.; Mezzavilla, S.; Ledendecker, M.; Mingers, A.; Cherevko, S.; Schüth, F.; Mayrhofer, K. J. J. The Space Confinement Approach Using Hollow Graphitic Spheres to Unveil Activity and Stability of Pt-Co Nanocatalysts for PEMFC. *Advanced Energy Materials* **2017**, *7* (20), 1700835.

(35) Jauhar, A. M.; Ma, Z.; Xiao, M.; Jiang, G.; Sy, S.; Li, S.; Yu, A.; Chen, Z. Space-Confined Catalyst Design toward Ultrafine Pt Nanoparticles with Enhanced Oxygen Reduction Activity and Durability. *Journal of Power Sources* **2020**, *473*, 228607.

(36) Bepete, G.; Tetana, Z. N.; Lindner, S.; Rümmeli, M. H.; Chiguvare, Z.; Coville, N. J. The Use of Aliphatic Alcohol Chain Length to Control the Nitrogen Type and Content in Nitrogen Doped Carbon Nanotubes. *Carbon* **2013**, *52*, 316–325.

(37) Pang, L. S. K.; Saxby, J. D.; Chatfield, S. P. Thermogravimetric Analysis of Carbon Nanotubes and Nanoparticles. *J. Phys. Chem.* **1993**, *97* (27), 6941–6942.

(38) Chizari, K.; Vena, A.; Laurentius, L.; Sundararaj, U. The Effect of Temperature on the Morphology and Chemical Surface Properties of Nitrogen-Doped Carbon Nanotubes. *Carbon* **2014**, *68*, 369–379.

(39) Rodríguez-Fernández, J.; Oliva, F.; Vázquez, R. A. Characterization of the Diesel Soot Oxidation Process through an Optimized Thermogravimetric Method. *Energy Fuels* **2011**, *25* (5), 2039–2048.

(40) Buzaglo, M.; Bar, I. P.; Varenik, M.; Shunak, L.; Pevzner, S.; Regev, O. Graphite-to-Graphene: Total Conversion. *Advanced Materials* **2017**, *29* (8), 1603528.

(41) Lyubovsky, M.; Smith, L.; Castaldi, M.; Today, H. K.-C.; Catalytic Combustion over Platinum Group Catalysts: Fuel-Lean versus Fuel-Rich Operation. *Catalysis Today* **2003**,83, 71-84.

(42) Deutschmann, O.; Maier, L.; Riedel, U.; today, A. S. Hydrogen Assisted Catalytic Combustion of Methane on Platinum. *Catalysis Today* **2000**,59 141-150

(43) Yazawa, Y.; Takagi, N.; Yoshida, H.; … S. K.-A. C. A. The Support Effect on Propane Combustion over Platinum Catalyst: Control of the Oxidation-Resistance of Platinum by the Acid Strength of Support Materials. *Applied Catalysis A: General* **2002,** 233,103-112

(44) Burch, R.; Loader, P. Some Aspects of Hydrocarbon Activation on Platinum Group Metal Combustion Catalysts. *Catalysis* Today **1996**, 27, 243-248.

(45) Lee, H. S.; Baek, G. Y.; Hwang, I. T.; Jung, C. H.; Choi, J. H. Preparation of Porous Carbon Films from Polyacrylonitrile by Proton Irradiation and Carbonization. *Radiation Physics and Chemistry* **2017**,141,369-374.

(46) Li, Z. Q.; Lu, C. J.; Xia, Z. P.; Zhou, Y.; Luo, Z. X-Ray Diffraction Patterns of Graphite and Turbostratic Carbon. *Carbon* **2007,** 45(8), 1686-1695.

(47) Şen, F.; Gökağaç, G. Different Sized Platinum Nanoparticles Supported on Carbon: An XPS Study on These Methanol Oxidation Catalysts. **2007**. *J. Phys. Chem. C* **2007**, 111(15), 5715–5720.

(48) Aricò, A. S.; Shukla, A. K.; Kim, H.; Park, S.; Min, M.; Antonucci, V. An XPS Study on Oxidation States of Pt and Its Alloys with Co and Cr and Its Relevance to Electroreduction of Oxygen. *Applied Surface Science* **2001**, *172* (1–2), 33–40.

(49) Solliard, C. *Structure and Strain of the Crystalline Lattice of Small Gold and Platinum Particles*; **1981**, 106, 63.

(50) Melke, J.; Peter, B.; Habereder, A.; Ziegler, J.; Fasel, C.; Nefedov, A.; Sezen, H.; Wöll, C.; Ehrenberg, H.; Roth, C. Metal-Support Interactions of Platinum Nanoparticles Decorated N-Doped Carbon Nanofibers for the Oxygen Reduction Reaction. *ACS Applied Materials and Interfaces* **2016**, *8* (1), 82–90.

(51) Jung, W. S.; Popov, B. N. Improved Durability of Pt Catalyst Supported on N-Doped Mesoporous Graphitized Carbon for Oxygen Reduction Reaction in Polymer Electrolyte Membrane Fuel Cells. *Carbon* **2017**, 122, 746-755.

(52) Takahashi, I.; Kocha, S. S. Examination of the Activity and Durability of PEMFC Catalysts in Liquid Electrolytes. *Journal of Power Sources* **2010**, *195* (19), 6312–6322.

(53) Bluhm, H.; Hävecker, M.; Knop-Gericke, A.; Kiskinova, M.; Schlögl, R.; Salmeron, M. In Situ X-Ray Photoelectron Spectroscopy Studies of Gas-Solid Interfaces at near-Ambient Conditions. *MRS Bulletin* **2007**, *32* (12), 1022–1030.

(54) Powell, C. J.; Conny, J. M. Evaluation of Uncertainties in X-Ray Photoelectron Spectroscopy Intensities Associated with Different Methods and Procedures for Background Subtraction. I. Spectra for Monochromatic al X-Ray. *Surface and Interface Analysis* **2009**, *41* (4), 269–294.

(55) Ling, X. Y.; Reinhoudt, D. N.; Huskens, J. Ferrocenyl-Functionalized Silica Nanoparticles: Preparation, Characterization, and Molecular Recognition at Interfaces. *Langmuir* **2006**, *22* (21), 8777–8783.

(56) Fiçicilar, B.; Bayrakçeken, A.; Eroğlu, I. Effect of Pd Loading in Pd-Pt Bimetallic Catalysts Doped into Hollow Core Mesoporous Shell Carbon on Performance of Proton Exchange Membrane Fuel Cells. *Journal of Power Sources* **2009**, *193* (1), 17–23.

(57) Baek, G. Y.; Lee, H. S.; Jung, J. M.; Hwang, I. T.; Shin, J.; Jung, C. H.; Choi, J. H. Preparation of Conductive Carbon Films from Polyacrylonitrile/Graphene Oxide Composite Films by Thermal Treatment. *Journal of Industrial and Engineering Chemistry* **2018**, 58(25), 87-91.

(58) Tao, J. G.; Pan, J. S.; Huan, C. H. A.; Zhang, Z.; Chai, J. W.; Wang, S. J. Origin of XPS Binding Energy Shifts in Ni Clusters and Atoms on Rutile TiO2 Surfaces. *Surface Science* **2008**, *602* (16), 2769–2773.

(59) Jackson, C.; Smith, G. T.; Inwood, D. W.; Leach, A. S.; Whalley, P. S.; Callisti, M.; Polcar, T.; Russell, A. E.; Levecque, P.; Kramer, D. Electronic Metal-Support Interaction Enhanced Oxygen Reduction Activity and Stability of Boron Carbide Supported Platinum. *Nature Communications* **2017**, *8* (1), 15802–15802.

(60) Hou, J.; Cao, C.; Idrees, F.; Ma, X. Hierarchical Porous Nitrogen-Doped Carbon Nanosheets Derived from Silk for Ultrahigh-Capacity Battery Anodes and Supercapacitors. *ACS Nano* **2015**, *9* (3), 2556–2564.

(61) Parent, P.; Laffon, C.; Marhaba, I.; Ferry, D.; Regier, T. Z.; Ortega, I. K.; Chazallon, B.; Carpentier, Y.; Focsa, C. Nanoscale Characterization of Aircraft Soot: A High-Resolution Transmission Electron Microscopy, Raman Spectroscopy, X-Ray Photoelectron and near-Edge X-Ray Absorption Spectroscopy Study. *Carbon* **2016**, *101*, 86–100.

(62) Galeano, C.; Meier, J. C.; Soorholtz, M.; Bongard, H.; Baldizzone, C.; Mayrhofer, K. J. J.; Schüth, F. Nitrogen-Doped Hollow Carbon Spheres as a Support for Platinum-Based Electrocatalysts. *ACS Catal.* **2014**, *4* (11), 3856–3868.

(63) Rigsby, M. A.; Zhou, W. P.; Lewera, A.; Duong, H. T.; Bagus, P. S.; Jaegermann, W.; Hunger, R.; Wieckowski, A. Experiment and Theory of Fuel Cell Catalysis: Methanol and Formic Acid Decomposition on Nanoparticle Pt/Ru. *Journal of Physical Chemistry C* **2008**, *112* (39), 15595–15601.

(64) Bagus, P. S.; Illas, F.; Pacchioni, G.; Parmigiani, F. Mechanisms Responsible for Chemical Shifts of Core-Level Binding Energies and Their Relationship to Chemical Bonding. *Journal of Electron Spectroscopy and Related Phenomena* **1999**, *100* (1–3), 215–236.

(65) Stec, W. J.; Morgan, W. E.; Albridge, R. G.; Van Wazer, J. R. Measured Binding Energy Shifts of the "3p" and "3d" Electrons1 in Arsenic Compounds. *Inorganic Chemistry* **1972**, *11* (2), 219–225.

(66) Tauster, S. J.; Fung, S. C.; Garten, R. L. *Strong Metal-Support Interactions. Group 8 Noble Metals Supported on $Ti0_2$ J. Am. Chem. Soc* **1978**, 100(1).

(67) Fung, S.C. XPS Studies of Strong Metal-Support Interactions (SMSI)-Pt/TiO/$Sub_2$. *osti.gov*. *J. Catal* **1982**,76

(68) Imai, H.; Izumi, K.; Matsumoto, M.; Kubo, Y.; Kato, K.; Imai, Y. In Situ and Real-Time Monitoring of Oxide Growth in a Few Monolayers at Surfaces of Platinum Nanoparticles in Aqueous Media. *J. Am. Chem. Soc* **2009**, *131* (17), 6293–6300.

# Chapter 6

# ORR activity and durability studies of the Pt/HCSs, Pt/NHCSs, Pt/BHCSs and Pt/BNHCSs prepared using a metal-organic deposition method.

## 6.1: Introduction

Proton exchange membrane fuel cells (PEMFCs) are advantageous when compared to other fuel cells because they have excellent properties. They are known to have a neutral carbon footprint if the hydrogen fuel is sourced from water electrolysis using solar energy. Also they can be used in many applications including automobiles and portable devices.[1,2]

To operate PEMFCs, hydrogen gas fed at the anode is electrolysed into protons and electrons. The produced electrons flow across an external circuit generating a current that can power equipment while the protons migrate across a proton selective membrane into the cathode[1]

**Sections of this chapter were submitted for publication to the Journal of power sources under the title: *Platinum supported on pristine and nitrogen doped bowl-like broken hollow carbon spheres as oxygen reduction reaction catalysts.* The manuscript is under review.**

compartment. At the cathode the fed oxygen gas reacts with the electrons and protons from the anode forming water and completing the PEMFCs reactions.[3]

These PEMFCs reactions are known to occur faster and more efficiently on platinum catalyst electrodes for both the anode hydrogen splitting (HOR) and cathode oxygen reduction reaction (ORR).[4,5] Other metals like palladium, iron and nickel are also known to exhibit ORR properties; however, their mass specific activity (MA) and surface area specific activity (SA) are not as high as found for Pt. Interestingly, for improved ORR activity, Fe and Ni have been alloyed with Pt to result in catalyst systems with MA and SA two to three fold better than found for the Pt catalysts.[6–9]

Bulk Pt is not convenient to use as  a PEMFC catalyst as it is expensive and has a low surface area compared to Pt nanoparticles supported on high surface area, porous carbons or conductive metal oxides like antimony doped tin oxide (ATO) or cerium oxide (ACO).[10–12] The challenge with these oxides is their low conductivity and porosity which in some cases also leads to low SA and MA values compared to conductive carbon supports.

During operations like start-up of the fuel cell, cathode potentials can reach above 1.5 V vs RHE, causing degradation of Pt catalysts supported on carbon.[13] The degradation process due to the carbon corrosion, Pt dissolution, detachment and agglomeration, results in the loss of the electrochemically active surface area (ECSA) of the Pt catalysts and thereby negatively affects the MA and SA of the catalysts.[14,15]

The mass specific activity and area specific activities are important parameters when determining the usefulness and surface cost effectiveness of a catalyst system. The MA gives information on how much of the precious metal Pt is needed to achieve a specific current in a PEMFC. The SA gives information on how much catalyst surface area and active phases are available in the catalysts system to achieve a given current.

Researchers on PEMFCs have studied and investigated Pt or Pt alloy catalysts systems in an attempt to obtain higher MA, SA and durability in order to accelerate the commercialization and acceptance of PEMFCs as energy conversion technology. These new catalysts must have MA (> 0.44 $A.mg^{-1}_{Pt}$ @ 0.90 V vs. RHE) , SA (> 0.72 $\mu A.cm^{-2}$ @ 0.90 V vs. RHE) and durability values higher than the DoE (USA Department of Energy) requirements and also electrocatalyst support stability in order for the catalysts to be adopted for commercialization.[16–18]

Herein we report on a study of Pt nanoparticles (3.8 – 4.2 nm) supported on broken bowl like hollow carbon spheres, Pt/BHCSs and Pt supported on nitrogen doped broken bowl like hollow carbon spheres, Pt/BNHCSs. The in-depth physical characterization and elucidation of the properties of the supports and catalysts were discussed in chapter 4 and chapter 5 of this thesis. The synthesized catalysts were investigated by ECSA, MA and SA while Pt catalyst durability studies were performed in a 3-electrode electrochemical setup that mimics a PEMFC electrode. The catalysts were compared to catalysts that had Pt nanoparticles (3.8 – 4.2 nm) supported on complete hollow carbon spheres (HCSs), Pt/HCSs and Pt supported on complete nitrogen doped hollow carbon spheres, Pt/NHCSs. The new catalysts have shown improved MA, SA and catalyst durability as benchmarked against a commercial Pt/C (Hispec) referred to as Pt/Vulcan with a nominal 40 wt.% catalyst from Johnson and Matthey as well as DoE values.

## 6.2: Experimental

The synthesized catalysts were physically characterized using various techniques including PXRD, XPS, BET, TGA, TEM, TGA, Raman spectroscopy and SEM. Detailed discussions of these techniques are given in Chapter 3 in this thesis.

## 6.3: Electrochemical Characterization

All experiments were performed in a three-electrode setup at room temperature (approx. 25 ºC) in a solution of 0.1 M $HClO_4$ (Merck, Suprapur). The 0.1 M concentration of the $HClO_4$ was chosen to minimise the chloride contamination of the Pt catalyst and Suprapur brands are known for their high purity. The perchloric acid electrolyte was in all cases either saturated with argon or oxygen (Afrox, 99.99%) for the cyclic voltammetry (CV) or ORR experiments.

A high surface area Pt wire was used as the counter electrode, mercury/mercurous sulphate ($Hg/HgSO_4$) as a reference electrode and a catalyst coated glassy carbon (GC) electrode with a working area of 0.196 $cm^2$ was used as the working electrode. The reference electrode was calibrated against the reversible hydrogen electrode by measuring the potential difference between the Pt wire in a hydrogen saturated electrolyte. All potentials in these studies were reported against the reversible hydrogen electrode potential (vs. RHE).

Catalyst inks were prepared by mixing about 5 mg of the catalyst with 1.5 ml of Ultrapure water (18.2 MΩ·cm – resistivity), 3.5 ml isopropyl alcohol (Merck, HPLC grade) and 20 µl Nafion perfluorinated resin solution (Merck) (5 wt. % in a mixture of lower aliphatic alcohols and water). The nafion resin was used to enhance the binding of the catalyst particles to the glassy carbon electrode surface. The ink mixture was ultra-sonicated in a cold-water bath for 30 minutes to obtain a homogeneous ink solution before analysis.[19]

Loading of the platinum on the working electrode (WE) was calculated as follows: 5 mg of a 40 wt% Pt catalyst was made into an ink consisting of 5 mL solvent (isopropyl alcohol and ultrapure water) and 20 µL Nafion resin, then a 10 µL aliquot of the ink that contained 3.984 µg of Pt spread over the 0.196 $cm^2$ of the WE. Thus, the loading $L_{Pt\ was}$ 20.32 $\mu g.cm^{-2}$.

viz: (0.4 x 5mg) x (10µL/5020µL) x (1000µg/1mg) x ($1cm^2$/0.196 $cm^2$)

$$= 20.32\ \mu g_{Pt}.cm^{-2}$$

The resulting black ink (10 µL) was pipetted onto the GC electrode (Pine Research Instrumentation) coupled to an RDE710 Gamry rotator box and dried under rotation for 20 minutes under ambient conditions. This formed a thin film of uniformly distributed catalyst on the GC. The Ultrapure water and isopropyl alcohol were evaporated during the drying process.

The electrochemical cell, electrolyte volumetric flasks, purge tubes and reference electrode bridge tubes were all soaked overnight in a solution of Nochromix (Gordax laboratories) and concentrated sulfuric acid (Merck). This was followed by a 7 times rinse in Ultra-pure water (18.2 mΩ.cm). After rinsing, the glassware was boiled at 100 ºC for 5 h and before use, the glassware was filled with new clean ultra-pure water (18.2 mΩ.cm - resistivity) and sealed in a 5 L beaker to maintain an ultra-clean interior.

The GC electrodes were prepared before ink deposition and drying. Even though the catalyst film thickness was not measured, It was maintained to a few micrometres thickness to promote good mass transport of reactive gases and the removal of the water product. The electrode was cleaned by first using a 1 µm alumina (Buehler) and a wet micro-smooth polishing cloth pad (Buehler). A figure eight cleaning protocol was adopted followed by rinsing in ultra-pure water and ultra-sonication in isopropyl alcohol and ultra-pure water. The routine was repeated with a smoother 0.05 µm alumina (Buehler) followed by thorough rinsing to remove the dirt and the sticking alumina. The GC electrode was polished to a mirror finish and allowed to dry under an inverted beaker before ink deposition.

Perchloric acid electrolyte was made using a low chloride impurity 70% stock solution (Merck, Suprapur). Chlorides bind irreversibly to the Pt surface reducing the surface area of the catalysts. The 0.1 M perchloric acid was chosen as the standard electrolyte because it simulates

a perfluoro-sulfonic acid ionomer in RDE measurements. A Biologic SP300 potentiostat coupled to a Gamry RDE710 Rotator was used for CV and RDE measurements.

## 6.4: Cyclic Voltammetry (CV)

For CV measurements the thoroughly cleaned electrochemical cell was filled with fresh 0.1 M $HClO_4$ and de-aerated or purged with a steady stream of pure argon for about 30 minutes. The working electrode (WE) made of a catalyst coated GC was screwed to the rotator shaft and immersed into the de-aerated acid electrolyte. The WE was placed close to the tip of the reference electrode by use of a luggin capillary bridge tube to minimise solution resistance between the WE and the RE and guided into the electrolyte. Any gas bubbles present on the WE were removed by rotation at about 500 rpm prior to testing. After the immersion of the WE the argon (Ar) gas stream was restored but this time at a slower steady rate to avoid the formation of gas bubbles that could stick to the surface of the WE. All electrodes were connected to the Biologic SP300 potentiostat using shielded cables for potential control. In an argon saturated electrolyte, the potential of the WE was swept between 0.075 – 1.225 V vs. RHE for 100 cycles at 100 $mV.s^{-1}$ for the electrochemical oxidation of all the impurities on the surface of the catalyst coated WE. The scan rate was then reduced to 50 $mV.s^{-1}$ and the 3$^{rd}$ cycle was used for the calculation of the ECSA (electrochemical active surface area) assuming a monolayer charge associated with hydrogen adsorption of 210 $\mu C.cm^{-2}$. The area under the CV curve associated with the under potential deposition of hydrogen was integrated and used for the calculation of ECSA using the formulae in Equation 6.1.

$$ECSA_{Pt} = (Q_{des}) / (210\ \mu C.cm^{-2} \times L_{Pt}) \qquad (6.1)^{20}$$

where $Q_{des}$ is the integrated charge on the CV associated with the under potential deposition of hydrogen, $L_{Pt}$ is the loading of platinum on the surface of the working electrode normalised to

the 0.196 $cm^2$ area of the GC electrode. The charge associated with the adsorption of a monolayer of protons on the clean surface of Pt is 210 $\mu C.cm^{-2}$.[21]

## 6.5: Linear Sweep Voltammetry (LSV)

Oxygen reduction reaction (ORR) I-V polarization curves were obtained at 1600 rpm from the electro-catalyst coated working electrode. The WE was swept at 10 $mV.s^{-1}$ between 0.075 – 1.225 V vs. RHE. To correct for a non–ORR background current, the LSV obtained in an argon saturated electrolyte without rotation was subtracted from that obtained from the $O_2$ saturated electrolyte. The ORR polarization I-V curves were used to calculate the kinetic current (Equation 6.2), a parameter required in the determination of the electrocatalyst area specific (SA) and mass specific (MA) activities of the catalysts.

$$I_K = (I_{lim} \times I) / (I_{lim} - I) \qquad (6.2)^{22}$$

where $I_k$ is the kinetic current (A) and $I_{lim}$ is the measured limiting current (A). Then, I is the current value of the ORR polarization curve at E° = 0.90 V and $I_{lim}$ is the current value that is at E° = 0.40 V versus RHE (Figure 2.5, Chapter 2) (Equation 6.3)

$$SA = I_k / ( Q_{des} / 210\ \mu C.cm^{-2}) \quad (6.3)^{19}$$

The Pt specific activities were estimated via calculation of $I_k$ and normalization to the Pt-loading of the disk electrode.

Normalization of the $I_k$ with the under potential deposition of hydrogen charge as shown in the equation above was used to estimate the area specific activity (SA). The mass specific activity (MA) of the catalysts were estimated when the kinetic current ($I_k$) was normalized with the loading and the catalysts on the working electrode. The simplified equation for MA (Equation 6.4), is

$$MA = SA \times ECSA \quad (6.4)$$

## 6.6: Durability measurements

Durability load cycling was carried out after the measurement of the beginning of life (BOL) CV and activity. Initially the WE was swept between 0.075 – 1.225 V vs. RHE at 100 $mV.s^{-1}$ to clean the catalysts of any impurities and contaminants. This was followed by 5 CVs at a lower scan rate of 20 $mV.s^{-1}$ for ECSA measurements (Figure 6.1).

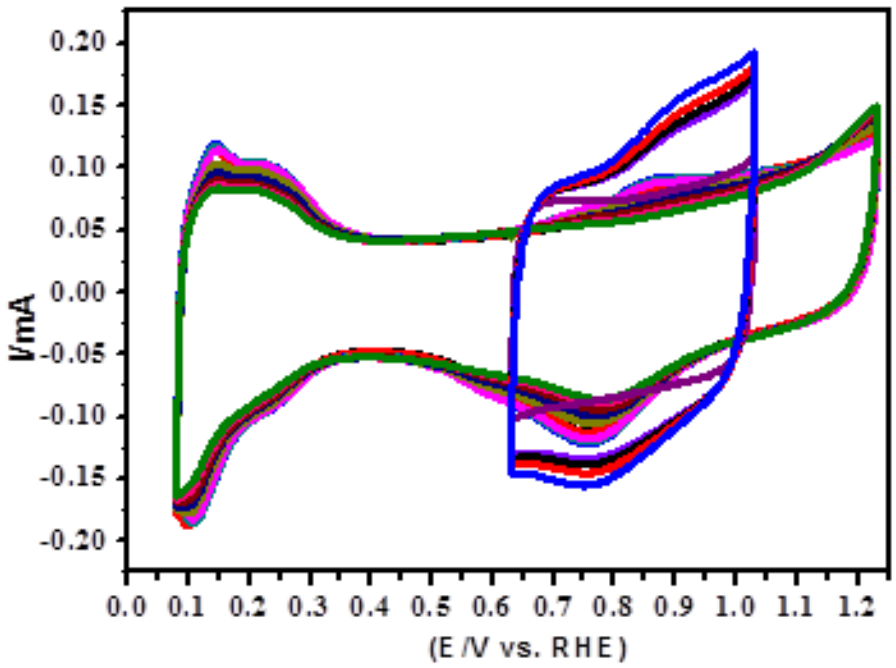



Figure 6. 1: Cyclic voltammograms for ECSA and load cycling (catalyst durability cycle) recorded in 0.1 M $HClO_4$ (room temperature and in argon saturated electrolyte) for Pt/BHCSs.

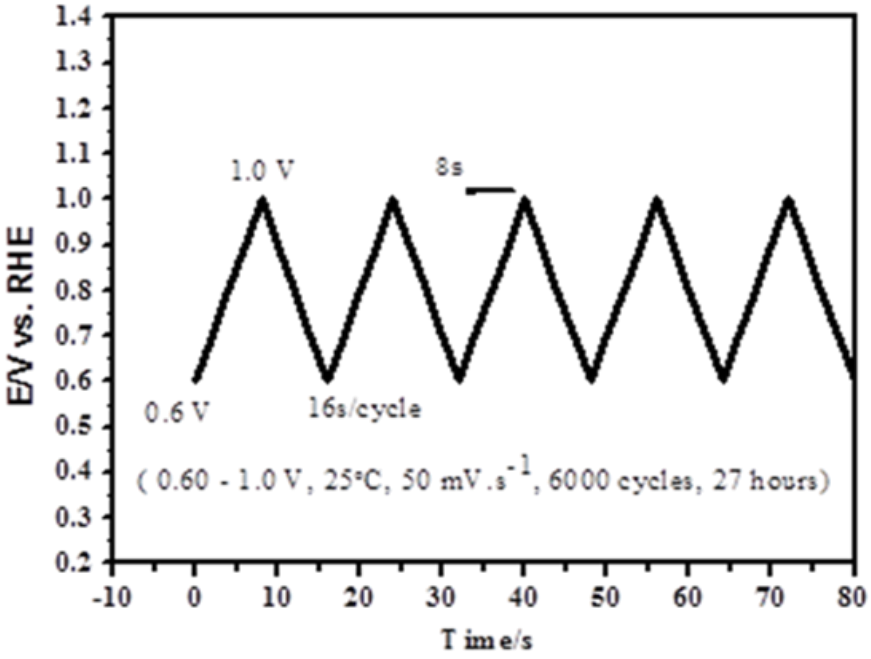



Figure 6.2: Load cycle durability test protocol for the Pt corrosion test.

At the end of each load cycling CV set, five ECSA CVs were obtained and the 3rd was used for the calculation of the new ECSA.

Load cycling for catalyst durability measurements was carried out in a 0.1 M $HClO_4$ solution at 25 ºC, in an argon saturated solution. The WE was cycled at 50 $mV.s^{-1}$ between 0.6 – 1.0 V vs. RHE using a triangular wave profile with a zero seconds hold at each potential and a complete cycle duration of 16 seconds (Figure 6.1 and Figure 6.2).[23]

Load cycling was carried out in units of 10, 100, and 1000 cycles until when the 6000th cycle was reached after 27 h of continuous cycling and argon saturation.

## 6.7: Results and Discussion

### 6.7.1: Electrochemical Characterization

The ECSA of all the catalysts were determined using CV in argon saturated 0.1 M $HClO_4$ at room temperature. The WE was cycled in the 0.075 – 1.225 V (Figure 6.5a) voltage range at a

50 $mV.s^{-1}$ scan rate. All samples exhibited typical features of a Pt/C catalyst. These features included the peaks for the under potential deposition of hydrogen, $H_{UPD,}$ in the region from 0.0 – 0.4 V vs. RHE. Also present are the peaks for the desorption of hydrogen in the same potential window. For all the catalysts there was no observable peak in the 0.4-0.5 V vs RHE window as this is the double layer region of the CV due to the capacitive effects of the materials. Pt oxidation occurred as shown from the peaks between 0.75-1.2 V vs RHE. In this region pure metallic Pt was oxidised to PtO and at the reversal of the cycle, in the same region of 1.2-0.75 V, the PtO was reduced again to metallic Pt in its zero oxidation state.[19]

All the materials had a different size of the capacitive double layer due to the variety in the chemical nature of the support materials used in the making of these catalysts. It is known that doping with nitrogen, or even altering the size of carbon materials affects the capacitive effects of these materials (Figure 6.5a).[24–26] The respective ECSA values were between 57–69 $m^2.g^{-1}$ and consistent with the TEM observed particle sizes (Table 6.1). Also, the $H_{des}$ obtained ECSA values are consistent with the theoretical metal surface area (MSA) calculated based on the particle sizes (Figure 6.3, Table 6.1). The theoretical metal surface area, according to the parameters used, will always be above the $H_{UPD}$ obtained ECSA value. Assuming uniformly spherical Pt nanoparticles deposited on the supports, the MSA of an ideal monodisperse Pt catalyst per unit mass is related to its diameter d[27,28] as

$$MSA = 6/\rho d \quad (6.5)$$

where $\rho$ is the density of Pt (21.45 $g.cm^{-3}$). For a Pt nanoparticle of diameter of 5 nm, the corresponding MSA would be 56 $m^2.g^{-1}$ and for a 2.2 nm Pt nanoparticle, it would be 127 $m^2.g^{-1}$ (Figure 6.3). The largest attainable MSA for the studied catalysts would be for Pt/BNHCSs with a particle diameter of 3.8 ± 0.6 nm at a value of 74 $m^2.g^{-1}$. It must be noted however that these Pt nanoparticles do not all have a uniform size such that some are smaller than the average

whilst some agglomeration of the Pt particles might also exist. The lower values of ECSA compared to the MSA could be due to some of the Pt nanoparticles being partly embedded in the shell of the supports such that they are not available for electrochemical processes. In this study we have also confirmed the pore confinement of Pt (Figure 6.14 and Figure 6.15) which is also consistent with the Pt durability during cycling. It is however safe to apply the MSA formulae (Equation 6.5) as a guide to avoid overestimation of ECSA in these calculations.

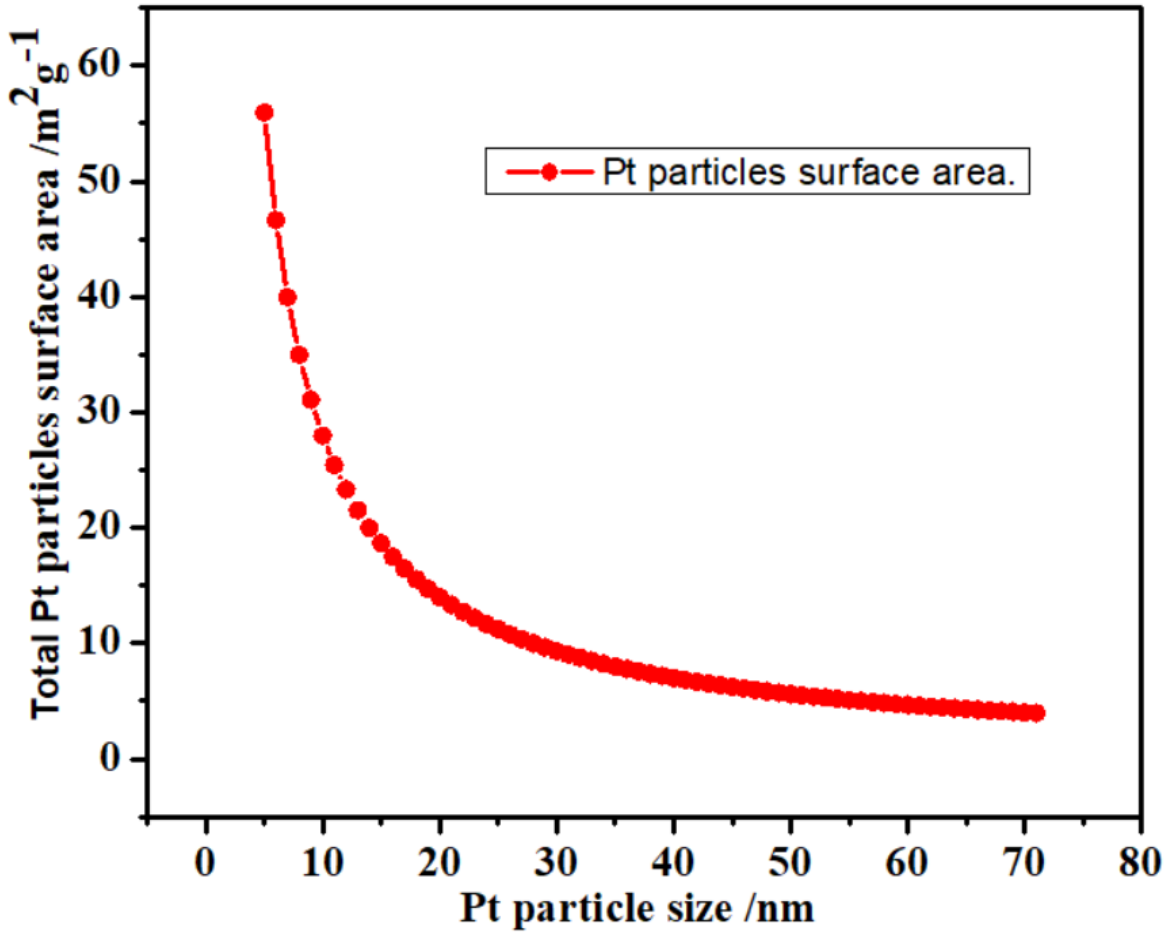



Figure 6.3: Theoretical total Pt surface area (MSA) as calculated using the density of Pt, assuming uniform spherical morphology and a given particle diameter.

The ECSA of the synthesized catalysts was found to be between 57 and 69 $m^2.g^{-1}$ which is consistent with the theoretical metal surface area (MSA) values calculated. The MSA values calculated for the given Pt average diameters are between 67 and 74 $m^2.g^{-1}$. To validate the

MSA method, the ECSA for the commercial Pt/Vulcan catalyst was calculated using the $H_{UPD}$ method and the value was found to be 61 ± 4 $m^2.g^{-1}$ and when calculated using the MSA method, the MSA was found to be 72 $m^2.g^{-1}$. Assuming the MSA method holds, Pt metal utilization for $H_{UPD}$ was calculated, to determine the utilization of the Pt nanoparticles in the determination of ECSA. The data are shown in table 4.5. The data shows that the Pt utilization was between 85 – 96%.

Table 6. 1: Calculated ECSA and theoretical metal nanoparticles surface area based on average particle size. Platinum utilization was calculated based on the theoretical surface area (MSA)

| Catalyst | ECSA /$m^2.g^{-1}$ | Pt - d /nm | MSA /$m^2.g^{-1}$ | Pt Utilization ECSA/MSA(%) |
|---|---|---|---|---|
| Pt/Vulcan | 61 ± 4 | 3.9 ± 0.9 | 72 | 85 |
| Pt/HCS | 57 ± 6 | 4.2 ± 0.5 | 67 | 85 |
| Pt/NHCS | 67 ± 3 | 4.0 ± 0.6 | 70 | 96 |
| Pt/BHCS | 62 ± 9 | 3.9 ± 0.5 | 72 | 86 |
| Pt/BNHCS | 69 ± 4 | 3.8 ± 2.9 | 74 | 93 |

Figure 6.10 shows the I-V polarization curves of all the studied catalysts for ORR. Oxygen reduction reaction activity is one of the best ways to compare catalysts activities using a rotating disk electrode. Catalysts studied here were of moderate Pt loading ranging between 18 – 22 $\mu g.cm^{-2}_{Pt}$ on the working electrode. The observed higher diffusion limiting current in the Pt/BNHCSs could be due to the structure of the catalyst, as the catalysts displayed an unusually higher ECSA at 69 $m^2.g^{-1}$ for a 3.9 nm average diameter even though other similar particle sizes for the Pt/BHCSs and Pt/Vulcan had lower ECSA values (Figure 6.5). The higher diffusion limiting current was not due to an increased rotation rate as all the catalysts were

studied at a pre-set 1600 rpm. The higher limiting current can be attributed to the roughness of the catalyst film with more exposed active sites. Unlike the Pt catalysts where the Pt was deposited only on the outside surface of the supports, in this catalyst system, Pt is deposited both the inside and outside of the broken shell.

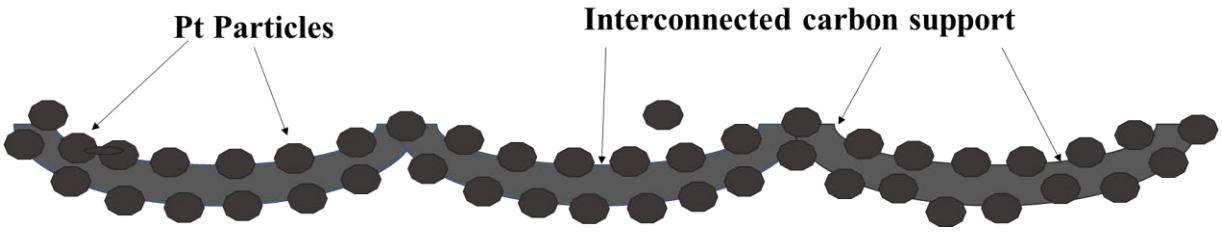



Figure 6.4: Schematic illustration of the Pt nanoparticles supported on top and inside pores of interconnected broken bowl like and broken bowl like nitrogen doped hollow carbon spheres.

Therefore, more Pt active sites are exposed to the oxygen saturated electrolyte for the Pt/BHCSs and Pt/BNHCSs compared to the Pt/HCSs and Pt/NHCSs. This is supported by the observed SA trend viz. Pt/BNHCSs > Pt/BHCSs > Pt/NHCSs > Pt/HCSs with the commercial Pt/Vulcan having the lowest SA, an indication of lower activity.

Kinetic currents were normalized with the loading of the catalysts on the WE yielding the mass specific activities (MA). The observed trend is similar with the one observed for SA with Pt/BNHCS being the highest at 188 $A.g^{-1}$ compared to Pt/Vulcan at 65 $A.g^{-1}$. ORR activity data seems to be lower than literature because cathodic sweeps were used for ORR.[29]

The catalysts had similar ECSA values and similar Pt particle sizes however different SA and MA values. The differences in activity could be due to the nature of the supports introduced by parameters like nitrogen doping which affects the electronic properties of the catalysts.[30,31] XPS data (Chapter 5) confirmed the presence of N1s electronic states for Pt/NHCSs and Pt/BNHCSs. These were not present in the Pt/Vulcan, Pt/BHCSs and Pt/HCSs catalysts. The deconvoluted N1s spectra showed the presence of pyridinic, pyrrolic and metal-n-pyridyl

groups. The metal-N-pyridyl groups indicated that metal–nitrogen bonding is evident. An electronic interaction between these species would promote better activity for the doped materials when compared to the pristine catalysts.[32,33]

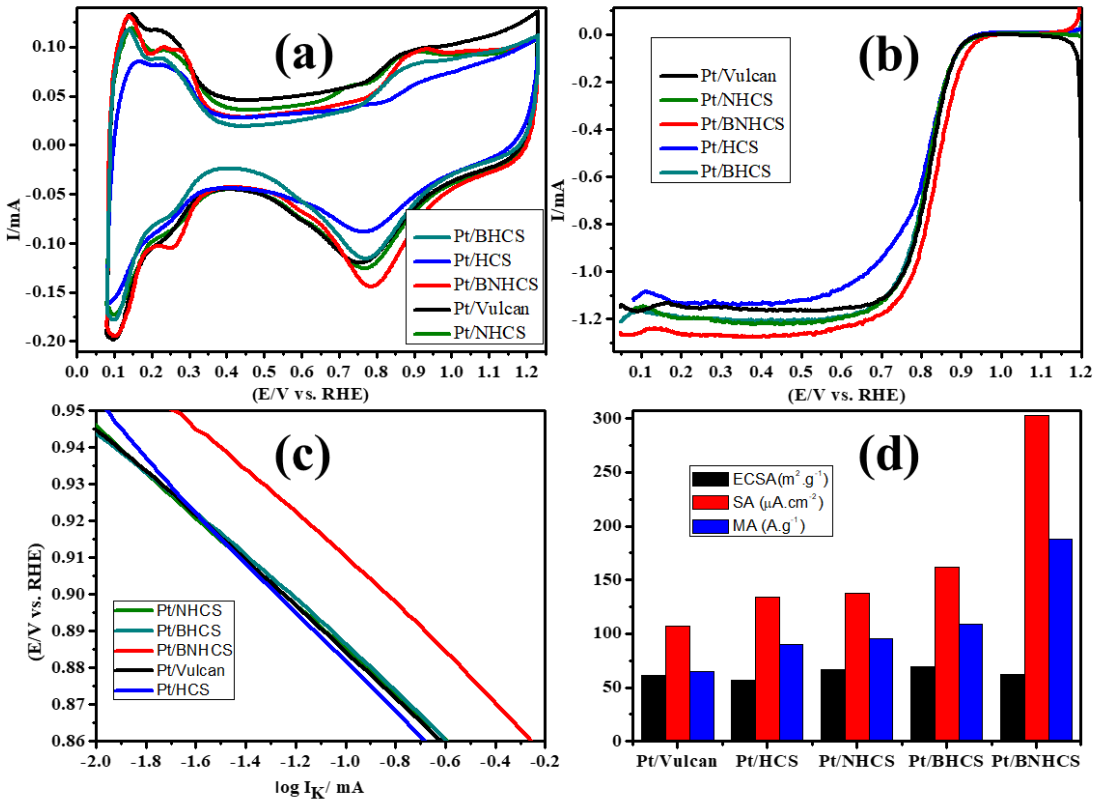



Figure 6.5: Electrocatalysis characterization data for the 40 wt% catalysts showing (a) Cyclic voltammograms, (b) ORR polarization I-V curves, (c) Tafel plots and (d) Mass specific (MA), area specific (SA) activities and electrochemical surface area (ECSA).

At 0.90 V vs RHE, the Tafel plots shows the order of catalysts activity to follow the trend Pt /BNHCS > Pt/BHCS > Pt/NHCS > Pt/Vulcan with the least active catalysts being the Pt supported on hollow carbon spheres. Table 6.4 data summarises the activities of the catalysts. The kinetic currents at 0.90 V vs. RHE confirms the activities as discussed above. Pt/BHCS has the highest kinetic current at 2956 μA.cm$^{-2}$ compared to the lowest, for Pt/HCS at a very low 290 μA.cm$^{-2}$. The kinetic currents were normalised with the ECSA to yield area specific activities (SA) of the catalysts. All the synthesized catalysts had higher SA activities compared

to the commercial catalysts with the Pt/BNHCSs having a SA value that were 65% larger than the commercial benchmark Pt/Vulcan catalyst (table 6.4).

Table 6.2: Calculated ECSA and ORR activity for the 40 wt% catalysts at 0.90 V vs RHE

| Catalyst | ECSA /$m^2.g^{-1}$ | MA (0.90 V) /$A.g^{-1}$ | SA (0.90 V) /$\mu A.cm^{-2}$ | $I_k$ (0.90 V) /($\mu A.cm^{-2}$) |
|---|---|---|---|---|
| Pt/Vulcan | 61 ± 4 | 65 ± 13 | 107 ± 19 | 1099 ± 10 |
| Pt/HCS | 57 ± 6 | 90 ± 22 | 134 ± 16 | 290 ± 20 |
| Pt/NHCS | 67 ± 3 | 95 ± 16 | 138 ± 12 | 1431 ± 10 |
| Pt/BHCS | 62 ± 9 | 109 ± 14 | 162 ± 22 | 1346 ± 18 |
| Pt/BNHCS | 69 ± 4 | 188 ± 25 | 303 ± 10 | 2956 ± 30 |

The catalysts are also known to have varying BET surface areas (Chapter 5). The higher activity Pt/BNHCS and Pt/BHCS have twice as large a BET surface area when compared to the Pt/Vulcan catalyst with a BET surface are of 220 $m^2.g^{-1}$. Also, of note are the higher pore widths for the Pt/BHCS and Pt/BNHCS at 6.8 nm and 5.5 nm respectively compared to a value of 4.8 nm for the Pt/Vulcan catalyst. The bigger pore size allows for the confinement of Pt nanoparticles inside the pores of the supports forming a matrix of Pt/C that in turn promotes metal to support electronic conductivity. This kind of metal–support interaction and resulting enhanced activity is normally higher when compared to metal nanoparticles that are deposited mostly on the surface of the catalyst.

## 6.7.2: Catalyst durability

Catalyst durability is of fundamental importance if the PEMFCs are to be utilized as a reliable renewable energy conversion technology. In this study the WE was cycled at 50 $mV.s^{-1}$ for

6000 cycles between 0.6 – 1.0 V vs RHE (Figure 6.1) using a triangular wave profile (Figure 6.2) in order to determine the Pt catalyst durability. It is in this potential window where Pt–oxide formation and Pt-oxide reduction occurs to produce a clean Pt surface at the reversal of the potential cycling. The choice of the potential window to be used was based on the changes of Pt surface from an oxide-free surface at about 0.6 V vs RHE to an oxide-covered surface at about 1.0 V vs RHE.[27] It is in this potential window that the chemical nature of the Pt catalysts changes due to potential cycling leading to ECSA degradation. This is a typical load cycle window which specifically induces Pt dissolution and agglomeration and hence was chosen so as to be able to investigate the effect of the different support structure and pore network. Also, in consideration is the fact that when the chemical nature of the Pt catalyst changes during a PEMFC life cycle, this can prove to be detrimental in its application, for example, as a source of energy in automobiles. Cycles were limited to 6000 to mitigate the effects of electrolyte and subsequently catalyst contamination and occasional flaking from the electrode tip that occurs during cycling experiments that run beyond many days. Figure 6.11 show the changes in the CVs of the catalysts due to potential cycling. It can be seen for all catalysts that there was a change in the size of the regions associated with hydrogen adsorption and desorption, the size becomes smaller with potential cycling. The change in size of this region is denoted by the arrows which show the direction of the changes. Figure 6.11 (a) depicts the CVs for the change in the peak position of the Pt/HCSs for the reduction of the Pt-oxide. The CV curves show that for all the catalysts, the intensities of the signals relating to hydrogen adsorption and desorption in the 0.0–0.4 V vs. RHE region as well as in the Pt - oxide formation and reduction region above 0.5 V vs. RHE decrease as a result of the potential cycling (Figure 6.6). Two parameters were used when investigating the support durability. These were the changes in the double layer capacitance and the formation of hydroquinone/quinone (HQ/Q) functionalities as carbon is partially oxidised.[34,35]

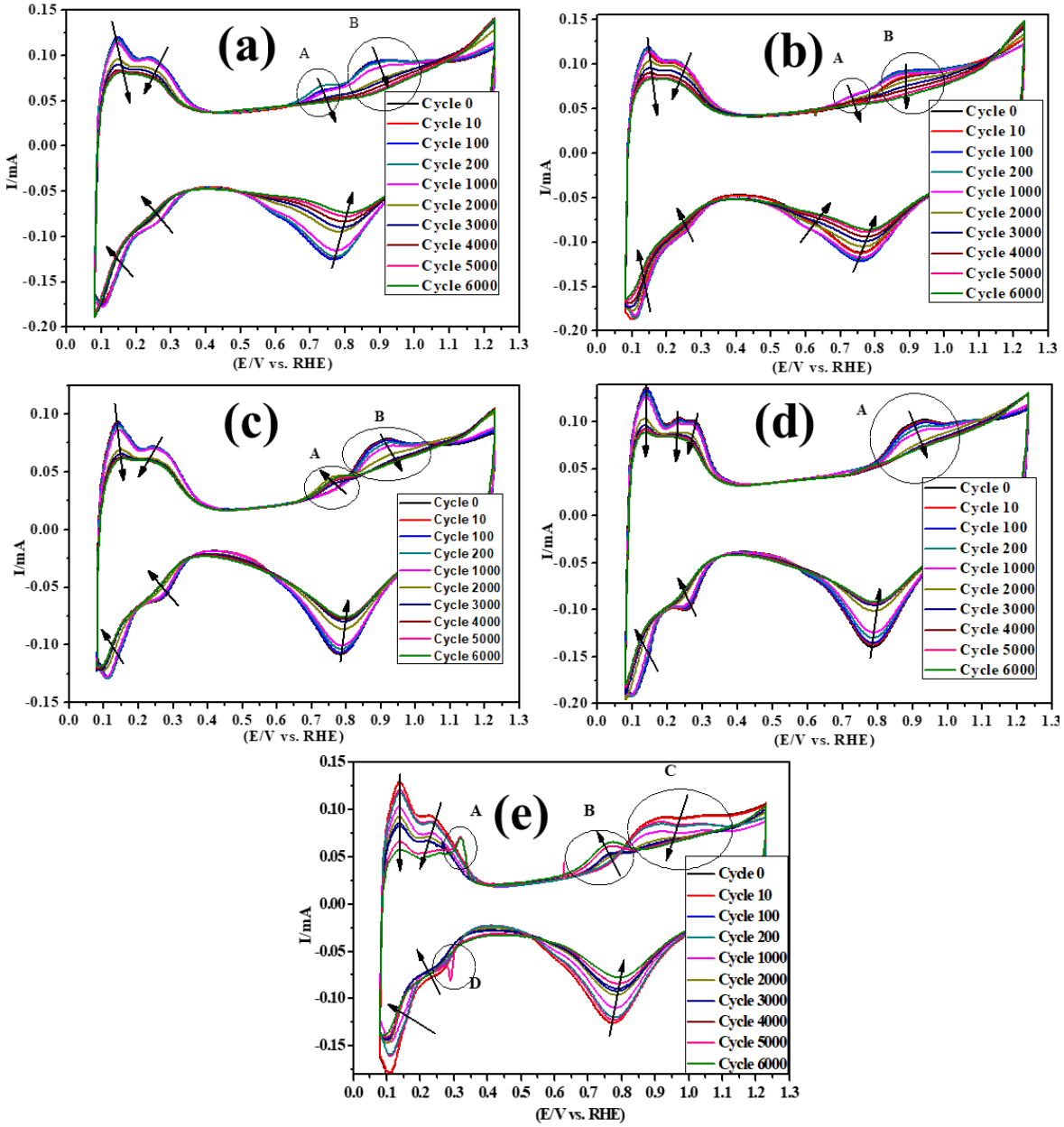



Figure 6.6: Durability cyclic voltammograms from beginning of life (BOL) to 6000 cycles showing the change in the structure due to the accelerated degradation for (a) Pt/HCS, (b) Pt/NHCS and (c) Pt/BHCSs, (d) Pt/BNHCSs and (e) the commercial benchmark Pt/Vulcan catalyst. Cycling was done between 0.6 – 1.0 V vs RHE at 20 $mV.s^{-1}$ and at room temperature (25ºC).

Carbon corrosion is observed from the CV curves during the oxidation of hydroquinone to quinone and this normally occurs as a redox peak at about 0.6 V vs. RHE. The released charge coupled to partial oxidation in the HQ/Q reaction is proportional to the amount of hydroquinone

species that forms on the surface of the carbon supports due to the degradation. For all the catalysts studied, the HQ/Q peak did not form. This shows that the protocol used in the intentional degradation of the catalysts results in minimal carbon corrosion and that the predominant cause of ECSA reduction is due to the degradation of only the Pt. This is expected, when using the 0.6–1.0 V vs. RHE potential cycle for Pt. This is the potential window in which the Pt surface is chemically oxidised followed by the reduction of the Pt-oxide back to Pt. Degradation in fuel cells is known to occur via processes that include Pt dissolution, Ostwald ripening, agglomeration, particle detachment as well as support corrosion.[20,36–39] In this study support corrosion is ruled out as there is no observable increase in the double layer 0.35–0.50 V vs. RHE region. This therefore leaves Pt dissolution, Ostwald ripening, particle detachment and agglomeration as the possible mechanisms of degradation of the Pt. The degradation of the Pt was observed as a decline in ECSA as load cycling was carried out.

Figure 6.7 shows the changes in normalized ECSA during the different stages of the cycling protocol. During the initial 100 cycles, there is an observed increase in ECSA for the Pt/BNHCSs while most of the other catalysts have the ECSA declining in size. The ECSA increase could be attributed to the cleaning effect of the cycling protocol which results in some organics, presumably from the Pt precursor salt being electrochemically oxidized leaving a cleaner Pt surface available for electrochemical reactions.[40] At this stage the number of Pt active sites increases and as a result ECSA initially improves. Another possible explanation is the roughening of the surface of the Pt due to initial Ostwald ripening leading to a rougher Pt surface with a higher surface area compared to the initial surface area.[41] During the initial 1000 potential cycles, the Pt/BNHCSs catalyst loses a mere 0.2% of the initial ECSA. The biggest loss occurred for the Pt/Vulcan catalyst which loses about 24% of the initial value in a steep decline of its ECSA. The catalysts Pt/HCS and Pt/NHCS lose about 13% of the initial ECSA. The near identical loss for the catalysts supported on unbroken HCSs suggests that in this cycle

duration, the chemical nature of the supports is not significantly different and hence the interaction of the Pt with the supports could be identical. The Pt/BHCSs catalyst had the second least reduction in ECSA, which was comparable to the Pt/BNHCSs. The observed durability was attributed to the structure of the supports used for these two catalysts.

A correlation is indicated between the degradation and the structure of the supports used. Particle size effects for the catalysts could be ruled out as all the catalysts studied had particle sizes in the same size range. Also, the catalysts studied were of similar Pt loading between 38 – 41 wt.% Pt. Another explanation for the sudden reduction in ECSA for the Pt/Vulcan catalyst can be found in its textual properties. The Vulcan carbon support used in the commercial benchmark catalyst material had a BET surface area of about 250 $m^2.g^{-1}$ whereas when loaded with Pt the BET surface area is reduced to about 220 $m^2.g^{-1}$. This was a relatively small change in surface area of about 12% compared to other catalysts. For example, the Pt/BNHCS showed a reduction from 780 $m^2.g^{-1}$ to 347 $m^2.g^{-1}$, which is a 45% reduction in surface area. BNHCS to Pt/BNHCS experienced a 39% reduction in BET surface area during the same process of metal deposition. This suggests that these surface area reductions are due to a process known as Pt pore confinement.

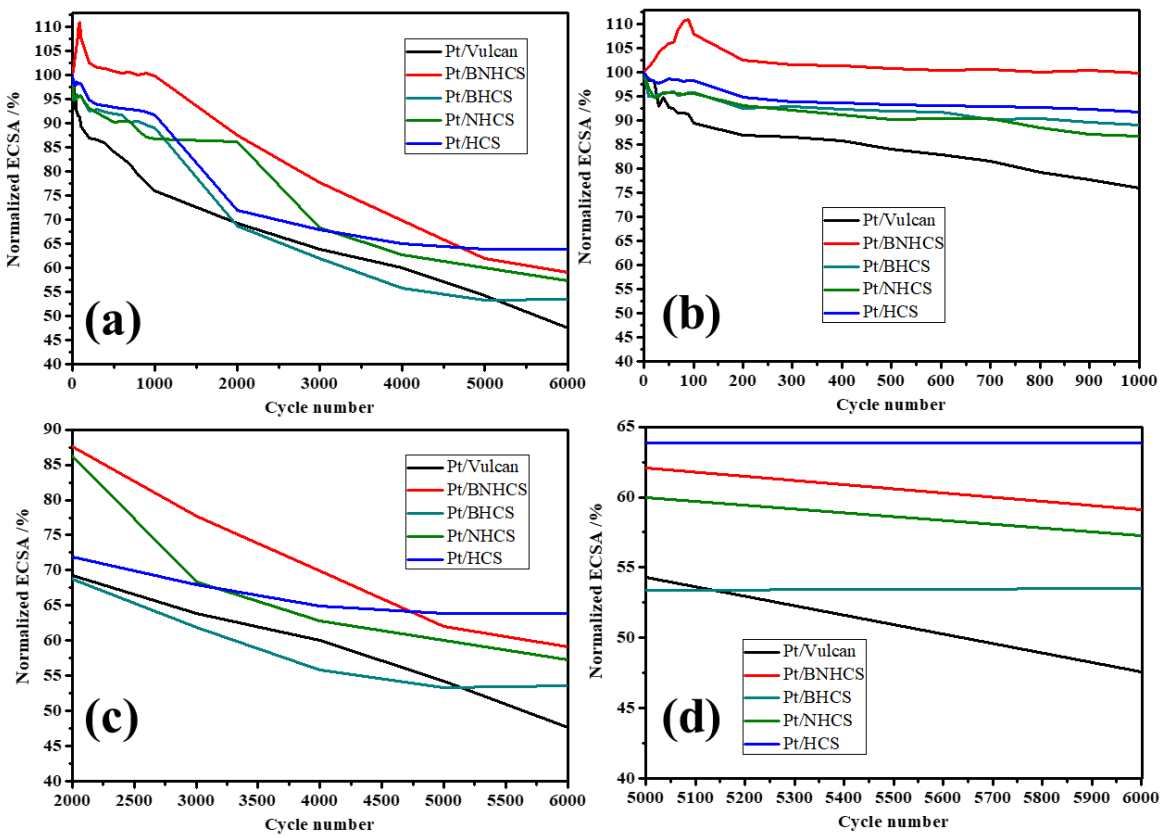



Figure 6.7: Catalyst durability study showing the change in normalized ECSA (a) from BOL to 6000 cycles, (b) From BOL to 1000 cycles, (c) from 2000 to EOL (end of life – 6000 cycles) and (d) from the 5000$^{th}$ to the end of life (EOL) 6000$^{th}$ cycle.

Table 6.3: Comparison of normalized ECSA between BOL and after 1000 cycles. Also shown is the percentage loss in ECSA due to accelerated cycling

| Sample | Normalized BOL ECSA /% | Normalized 1000 cycles ECSA /% | ECSA Change /% |
|---|---|---|---|
| Pt/Vulcan | 100 | 76.1 | 23.9 |
| Pt/HCS | 100 | 86.4 | 13.6 |
| Pt/NHCS | 100 | 86.8 | 13.2 |
| Pt/BHCS | 100 | 94.5 | 5.5 |
| Pt/BNHCS | 100 | 99.8 | 0.2 |

This improved tethering reduces agglomeration and dissolution of the Pt due to the strong bonds that occur with the supports.[30] Another point to note is the comparable pore sizes for the supports and the size of the resulting Pt nanoparticles. The Pt nanoparticles (3.9 nm) on average and the average pore widths for Pt/BHCS (6.8 nm) and Pt/BNHCS (5.5 nm) (Table 6.4) respectively could conveniently have resulted in Pt nanoparticles that can fit into the pores. These Pt nanoparticles have improved contact with the supports and hence higher durability compared to less strongly bound Pt on the carbon surface as suggested for the less porous Pt/Vulcan catalyst.

Table 6.4: Comparison of the textual properties of the supports and the complete catalysts showing reductions in BET surface area, BJH pore volume and BJH pore widths due to Pt deposition

| Material | BET SA /$m^2.g^{-1}$ | | | BJH PV /$cm^3.g^{-1}$ | | | BJH PW /nm | | |
|---|---|---|---|---|---|---|---|---|---|
| | Support | Catalyst | % change | Support | Catalyst | % change | Support | Catalyst | % change |
| Pt/Vulcan | 250 | 220 | 12.0 | 0.28 | 0.24 | 14.3 | 5.2 | 4.8 | 7.3 |
| Pt/HCS | 520 | 313 | 39.8 | 0.31 | 0.19 | 38.8 | 6.8 | 4.5 | 33.8 |
| Pt/NHCS | 570 | 368 | 35.4 | 0.32 | 0.20 | 37.5 | 6.5 | 5.0 | 23.1 |
| Pt/BHCS | 735 | 462 | 38.8 | 1.12 | 0.64 | 42.9 | 8.6 | 6.8 | 20.9 |
| Pt/BNHCS | 782 | 347 | 55.6 | 1.45 | 0.31 | 78.6 | 10.3 | 5.5 | 46.6 |

Similar trends were observed for the Pt/HCS and Pt/NHCS where reductions in surface area of about 40% and 35% are observed. We propose pore confinement in these supports as the predominant mechanism in which durability is enhanced.

In respect of the above argument where Pt/Vulcan, Pt/HCS and Pt/NHCS all have similar particle sizes in the 3.9 – 4.2 nm,[42,43] pore widths in the 4.8 – 5.8 nm and a small pore width to Pt particle size ratio, the improved durability in the Pt/HCS and Pt/NHCS relates to the BET surface area reduction which is higher for the Pt/HCS and Pt/NHCS catalysts suggesting improved pore confinement.[44–46] During the initial 1000 durability cycles, the catalyst/support system with the smallest change in textual properties had the highest ECSA loss whereas those with high changes in textual properties (Table 6.4), had small losses in ECSA. The explanation for this is Pt pore confinement.

Table 6.5: Comparison of normalized ECSA between 1000$^{th}$ and EOL (6000$^{th}$ cycles) The total loss in ECSA due to accelerated cycling is shown.

| Sample | Normalized 1000 cycles ECSA /% | Normalized 6000 cycles ECSA /% | ECSA lost /% |
|---|---|---|---|
| Pt/Vulcan | 76.1 | 47.6 | 28.5 |
| Pt/HCS | 86.4 | 64.4 | 22.0 |
| Pt/NHCS | 86.8 | 57.3 | 29.5 |
| Pt/BHCS | 94.5 | 65.4 | 29.1 |
| Pt/BNHCS | 99.8 | 59.1 | 40.7 |

During the 5000 cycles that followed the initial 1000 cycles, the highest durability loss as shown by ECSA reduction occurred in Pt/BNHCS catalyst. This catalyst system loses about

40.5 % ECSA in this region compared to Pt/HCS with a coupled 22% loss (table 6.5). As discussed above, it had been proposed that pore confinement of Pt is highest in this catalyst system (Pt/BNHCS), meaning that the durability loses could be due to other properties of the catalyst. The durability loss is attributed to the small initial particle size for the Pt/BNHCS (3.8 nm).[47,48] The small Pt nanoparticles have higher surface energy compared to bigger Pt nanoparticles. Therefore agglomeration, Ostwald ripening and Pt dissolution could be the driving force behind this durability loss.

Pt nanoparticles agglomeration could occur as a result of higher surface energy which would lead to migration and coalescence. In this case, the process is independent of support corrosion as shown in the durability CVs (Figure 6.6) where there is no double layer change or formation of the HQ/Q redox couple. The ECSA losses for this catalyst system could also suggest that a substantial amount of Pt is not pore confined and due to particle size effects on durability, these Pt nanoparticles could have agglomerated resulting in a dramatic ECSA loss. Particle size dependent degradation could also be observed in the Pt/Vulcan, Pt/NHCS and Pt/BHCS where mild losses of between 28.5 – 29.5% were observed for the smaller Pt particles in the 3.9 – 4.0 nm size range (Table 6.1). The ECSA decreases for these catalysts systems which have similar particle sizes were also comparable. This was further supported by the minimal ECSA loss of 22% which is the lowest, for the Pt/HCS system which has the largest Pt particle size of 4.2 nm.

The bigger durability loss in the Pt/BNHCS and the Pt/NHCS systems could have been exacerbated by the nitrogen doping of the support.[49,50] N-doping affects the long range crystallinity of the supports and this normally leads to a more amorphous support. Amorphous supports could be degraded more easily through the electrochemical degradation of carbon or they could experience negative electronic effects, negative metal – support interaction and reduced tethering of the Pt and hence possible reduced durability.[51,52]

Table 6.6: Comparison of normalized ECSA between 5000$^{th}$ and EOL (6000$^{th}$ cycles). The loss in ECSA in the final 1000 cycles due to accelerated cycling

| Sample | Normalized 5000 cycles ECSA /% | Normalized 6000 cycles ECSA /% | ECSA lost /% |
|---|---|---|---|
| Pt/Vulcan | 54.3 | 47.6 | 6.7 |
| Pt/HCS | 64.5 | 64.4 | 0.1 |
| Pt/NHCS | 59.9 | 57.2 | 2.7 |
| Pt/BHCS | 66.2 | 65.4 | 0.8 |
| Pt/BNHCS | 62.1 | 59.1 | 3.0 |

After 5000 cycles of durability testing, the ECSA losses decreased for most catalysts. During the last 1000 cycles, the highest ECSA loss was experienced by the Pt/Vulcan catalyst with a loss in ECSA of 6.7%. This was followed by the Pt/BNHCSs and the Pt/NHCSs with loses of 3.0 and 2.7 respectively. Minimal loses of 0.8 and 0.1 % were experienced by the Pt/HCS and Pt/BHCS respectively. As all these catalysts are in a similar size range, we propose the ECSA loses to be due to changes in the textual properties of the supports used. We propose that the smaller value of BET surface area of the Vulcan enhances the degradation of Pt, as it is less porous and less defective and hence minimal confinement of Pt. For all the supports studied, the Pt/Vulcan had a lower $I_D/I_G$ ratio (Table 6.7) indicating that it was more crystalline and hence less defective and has less anchor sites for Pt than other catalyst supports. Pt/Vulcan also had the smallest Pt–Pt distance (Table 6.7) making agglomeration to occur easier when the surface energy of the Pt nanoparticles is increased during potential cycling.

Table 6.7: Correlation between $I_D/I_G$ ratio, TEM particle sizes and Pt-Pt interparticle distances for the catalysts

| Sample | $I_D/I_G$ ratio | TEM particle size/nm | Pt inter particle distance /nm |
|---|---|---|---|
| Pt/Vulcan | 0.69 | 3.9 ± 0.9 | 5.3 ± 2 |
| Pt/HCS | 1.12 | 4.2 ± 0.5 | 5.8 ± 3 |
| Pt/NHCS | 1.06 | 4.0 ± 0.6 | 5.1 ± 3 |
| Pt/BHCS | 0.97 | 3.9 ± 0.5 | 6.2 ± 4 |
| Pt/BNHCS | 1.00 | 3.8 ± 0.6 | 6.0 ± 4 |

The Pt/Vulcan had a lower $I_D/I_G$ ratio compared to Pt/HCS. This relationship could be used to explain the final ECSA after 6000 cycles where Pt/Vulcan had the highest degradation whereas Pt/HCS had the least degradation.

After 6000 cycles, it was the Pt/BHCS catalyst that retained the highest ECSA (table 6.5). The catalyst maintained 65.4% of the initial surface area. Pt/NHCS maintains 64.4% of the initial ECSA indicating that particles size dependant degradation, pore confinement and favourable metal-supports interactions between the Pt and the support led to a more stable catalyst. Pt/HCS had a slightly higher value of initial ECSA however the value at 57.3% was still high. When comparing the Pt/HCS and Pt/NHCS catalyst systems, the higher durability of the nitrogen doped system is ascribed to the smaller inter Pt distance and better anchoring of Pt due to the induced favourable electronic effects due to nitrogen doping. We would expect the nitrogen doped catalyst to have a lower durability because of the smaller Pt size of 4.0 nm (). However, the Pt size difference of 0.2 nm is not significant enough to claim a particle size dependant

degradation. Therefore, we conclude that Pt-support interactions and pore confinement are the major influences to explain the enhanced durability of these catalysts.

Table 6.8: Comparison of normalized ECSA between BOL and EOL (6000 cycles), also shown is the total loss in ECSA due to accelerated cycling

| Sample | Normalized BOL ECSA /% | Normalized 6000s cycle ECSA /% | ECSA LOST /% | ECSA kept /% |
|---|---|---|---|---|
| Pt/Vulcan | 100 | 47.6 | 52.4 | 47.6 |
| Pt/HCS | 100 | 57.3 | 42.7 | 57.3 |
| Pt/NHCS | 100 | 64.4 | 35.6 | 64.4 |
| Pt/BHCS | 100 | 65.4 | 34.6 | 65.4 |
| Pt/BNHCS | 100 | 59.1 | 40.9 | 59.1 |

Under in-situ PXRD conditions, heating the catalysts from 25–725 ℃ in an inert gas (nitrogen) resulted in a Pt crystallite size increase from 5.20 nm at 25 ℃ to 5.34 nm at 725 ℃. The Pt crystallites for Pt/BHCSs managed an increase of 3% over the temperature range compared to a change of 70.6% for the Pt/HCS and 75.5% for the benchmark Pt/C catalysts (Figure 6.8, Table 6.9 and Figure 6.10 and Table 6.10, Table 6.11 and Figure 6.12). The small change in Pt crystallite size shows that even though the Pt particles were provided with enough energy to degrade and agglomerate, the extent of the agglomeration process was minimal for the Pt/C sample.

Table 6.9: Growth of Pt crystallite size (Rietveld refinement) for Pt/BHCSs as a function of reaction temperature

| Parameters | Pt/BHCSs | | | | | | | | |
|---|---|---|---|---|---|---|---|---|---|
| Temperature/°C | 25 | 75 | 125 | 175 | 225 | 275 | 325 | 375 | 425 |
| Pt crystallite size /nm | 5.20 | 5.20 | 5.21 | 5.22 | 5.25 | 5.28 | 5.30 | 5.31 | 5.31 |

| Temperature/°C | 475 | 525 | 575 | 625 | 675 | 725 |
|---|---|---|---|---|---|---|
| Pt crystallite size /nm | 5.32 | 5.33 | 5.34 | 5.34 | 5.34 | 5.34 |

Also, the Pt/HCS sample did not experience the same agglomeration due to in-situ PXRD conditions. The minimal increase in particle size for the in-house Pt/BHCSs and Pt/HCSs is attributed to the structure of the supports used in the preparation of these samples. As confirmed by Raman spectroscopy, XPS and BET studies, the BHCSs support had many defects and the Pt nanoparticles were lodged and supported in the pores resulting in strong Pt-support interactions.[53,54] The strong Pt-support interactions were revealed by XPS data (figure 6.8) which were manifested as Pt4f binding energy shifts for the various supports employed.[55,56] The high initial BET surface area and the array of micropores allowed for the deposition of Pt inside the pores resulting in the confinement of the Pt inside the pores (Figure 6.14 and Figure 6.15). The pore confinement is thought to have existed in all the synthesized catalysts. This is because all the catalysts had similar support properties as elucidated by XPS, Raman, BET and many other characterization techniques.

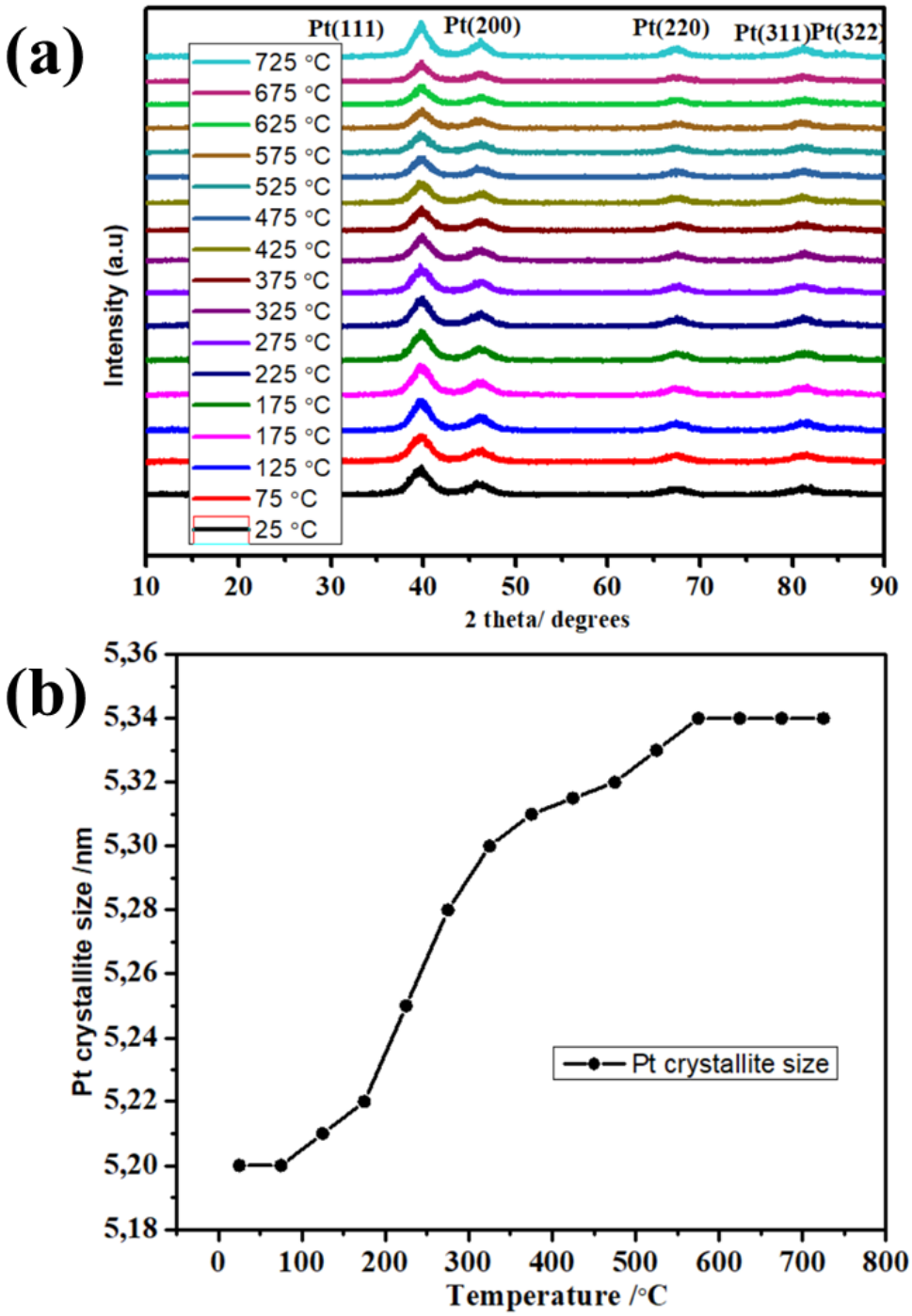



Figure 6.8: Variable temperature PXRD diffractograms for Pt/BHCSs (a) and the corresponding variable temperature dependent Pt crystallite growth (b). See Table 6.7: In-situ PXRD Pt crystallite size changes due to the variable temperature for Pt/BHCSs.

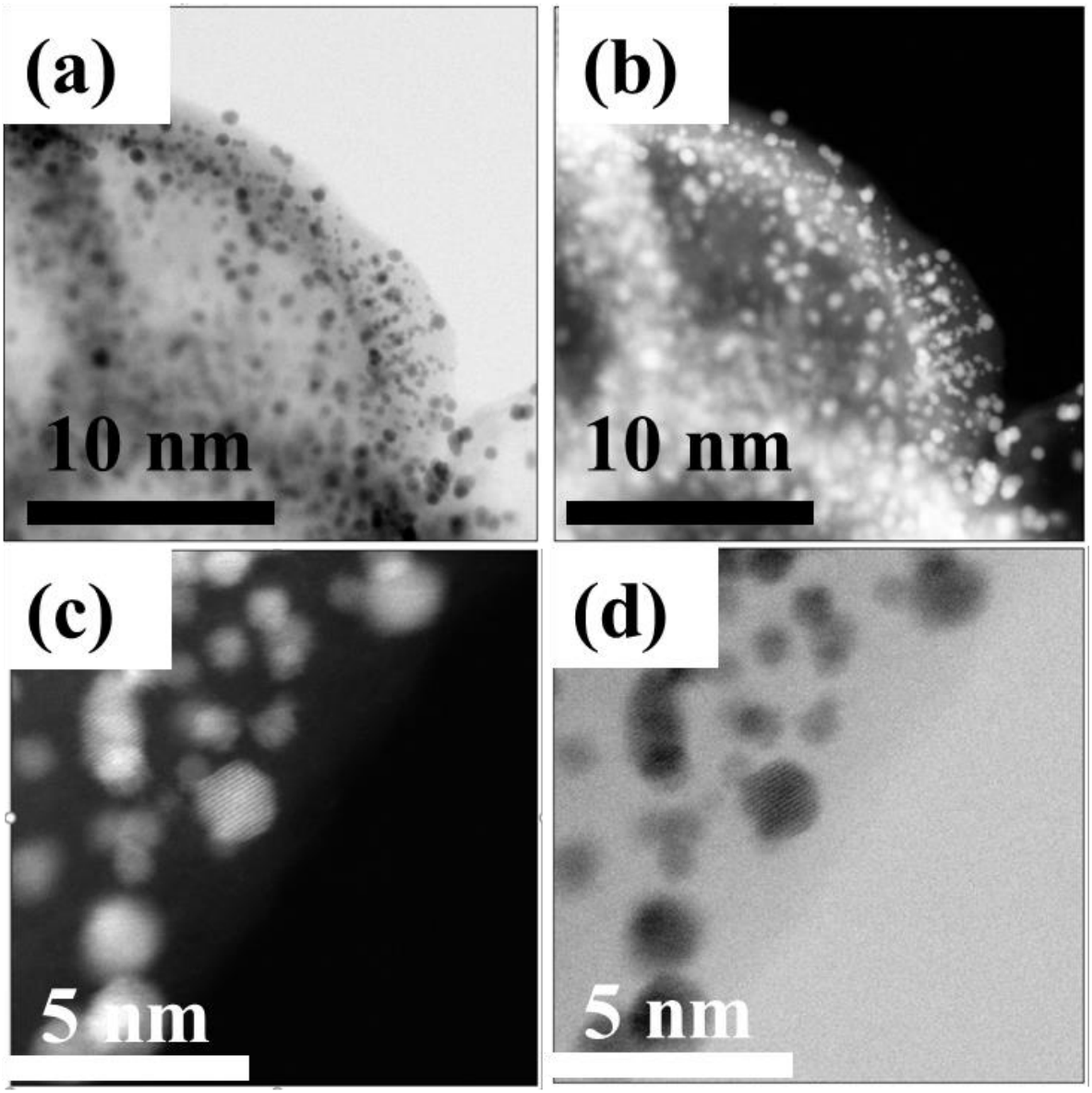



Figure 6.9: DF-STEM images (a – d) of platinum particles confined inside the carbon shell of the supports for the Pt/BHCSs sample.

These pore confined Pt particles were typically found below the surface of the support (Figure 6.9 and Figure 6.11) and as a result they their interaction with other Pt nanoparticles would be reduced and thus limit processes like agglomeration. Also, pore confined Pt nanoparticles have improved anchoring to the supports due to the enhanced contact as a result of pore enclosure and restricted ease of migration.[57]

Table 6.10: Growth of Pt crystallite size (Rietveld refinement) for commercial Pt/HCSs as a function of reaction temperature

| Parameters | Pt/HCSs | | | | | | | | |
|---|---|---|---|---|---|---|---|---|---|
| Temperature/°C | 30 | 100 | 150 | 200 | 250 | 300 | 350 | 400 | 450 |
| Pt crystallite size /nm | 2.88 | 2.92 | 3.40 | 4.96 | 5.30 | 6.32 | 7.69 | 8.85 | 9.17 |

| Temperature/°C | 500 | 550 | 600 | 650 | 700 | 750 |
|---|---|---|---|---|---|---|
| Pt crystallite size /nm | 9.33 | 9.64 | 9.95 | 9.64 | 9.73 | 9.81 |

In Pt pore confinement, when the nanoparticles are reduced at the end of the reduction and deposition process, most of these Pt occupy the pores, voids and defects of the support and thereby lead to a BET surface reduction due to pore blockage and subsequent pore volume reduction. The reduction has also been shown to occur in the pore volumes and pore width data.

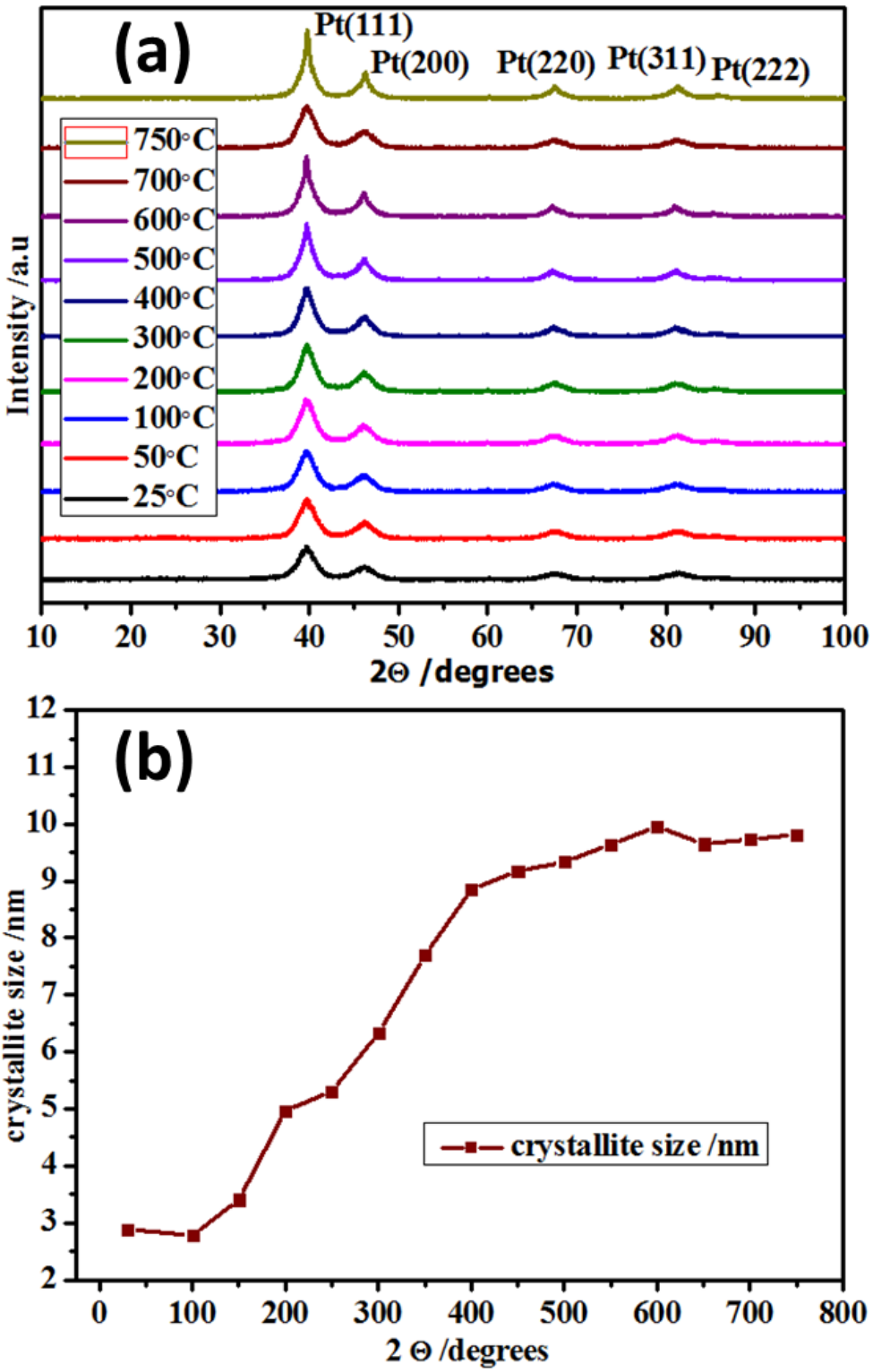



Figure 6.10: Variable temperature PXRD diffractograms for commercial Pt/HCS (a) and the corresponding variable temperature dependent Pt crystallite growth (b). See Table 6.8: In-situ PXRD Pt crystallite size change due to the variable temperature for Pt/BHCSs.

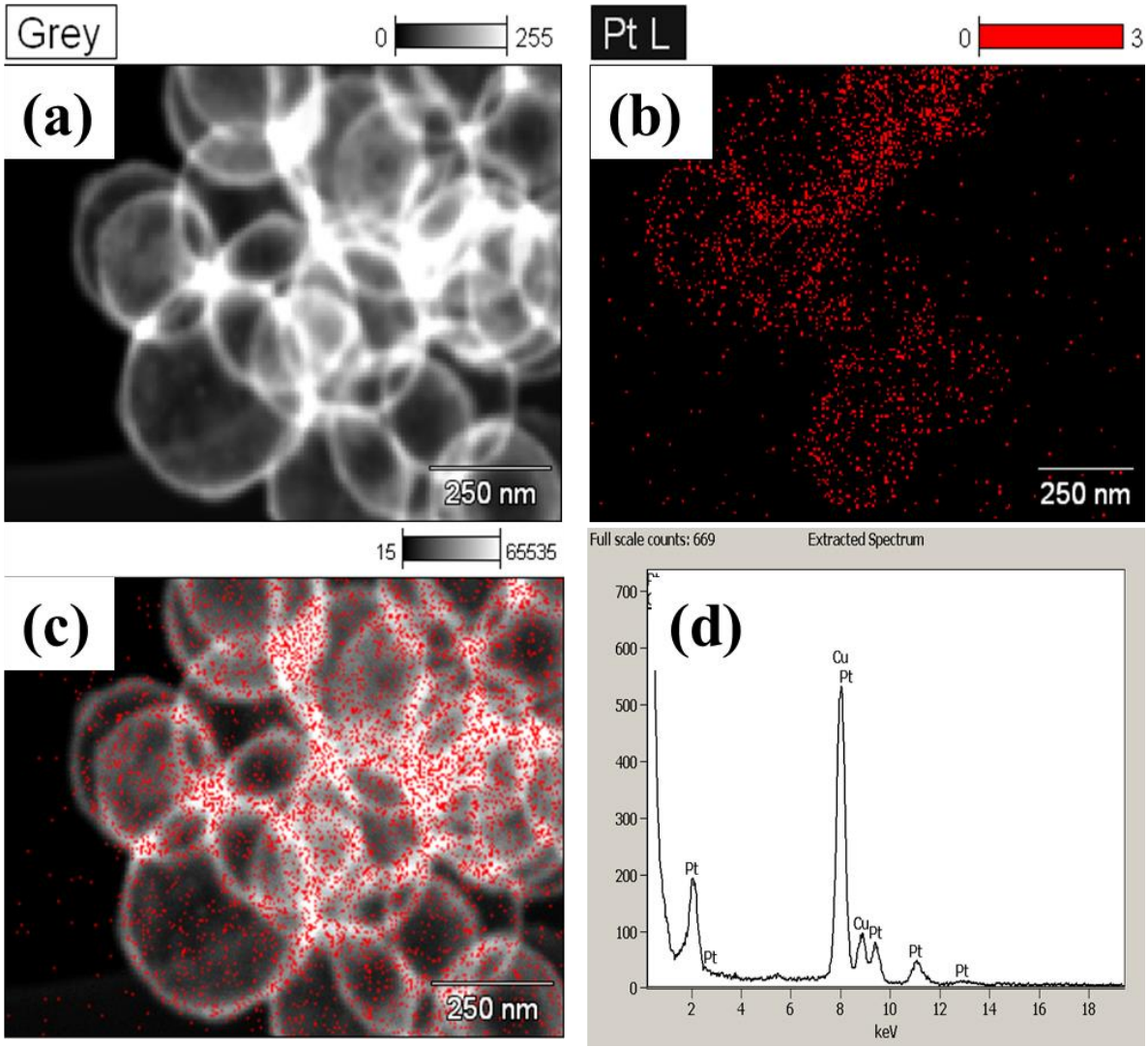



Figure 6.11: (a) DF-STEM images of Pt/HCSs showing the bright edges of the HCSs support due to Pt. (b) and (c) Pt map showing location of Pt in the shell region of the support. (d) EDX showing the presence of Pt on the supports, the copper is due to the copper grid used for analysis.

Table 6.11: Growth of Pt crystallite size (Rietveld refinement) for commercial Pt/C as a function of reaction temperature

| Parameters | Benchmark Pt/C | | | | | | | | |
|---|---|---|---|---|---|---|---|---|---|
| Temperature/°C | 30 | 100 | 150 | 200 | 250 | 300 | 350 | 400 | 450 |
| Pt crystallite size /nm | 2.89 | 2.78 | 3.40 | 4.96 | 6.30 | 7.32 | 7.69 | 7.85 | 8.18 |

| Temperature/°C | 500 | 550 | 600 | 650 | 700 | 750 |
|---|---|---|---|---|---|---|
| Pt crystallite size /nm | 8.33 | 8.64 | 8.95 | 9.64 | 10.73 | 11.81 |

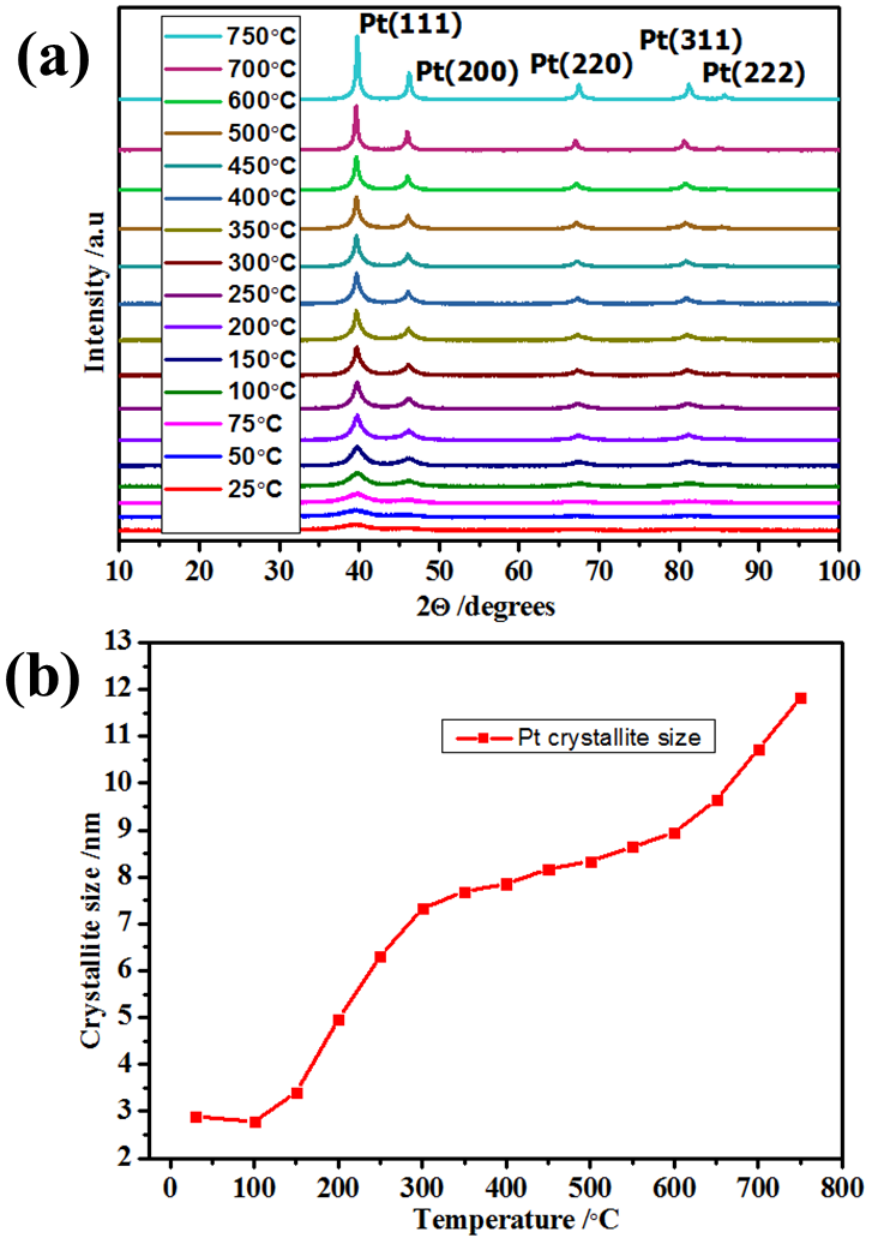



Figure 6.12: Variable temperature PXRD diffractograms for commercial Pt/C (a) and the corresponding variable temperature dependent Pt crystallite growth (b). See Table 6.8: In-situ PXRD Pt crystallite size change due to the variable temperature for Pt/BHCSs.

## 6.8: Conclusion

Pt catalysts were deposited on hollow and broken carbon and nitrogen doped carbon supports (Pt/HCSs, Pt/NHCSs, Pt/BHCSs and Pt/BNHCSs). The textual properties showed that the new

Pt-carbon catalysts had higher surface areas than the commercial Pt/Vulcan benchmark catalyst. The higher surface area and better pore widths and volumes of the new materials enabled Pt pore confinement and enhanced catalyst durability.

Pt nanoparticles were smaller on the nitrogen doped and high surface area supports as compared to the Pt particles deposited on the pristine supports. As discussed, the nitrogen groups, confirmed by XPS, had positive electronic effects that restricted Pt particle growth during deposition. The smaller Pt particles from nitrogen doped supports had a higher ECSA compared to the bigger Pt particles supported on pristine supports. Pt utilization in ECSA data showed no particle size dependent correlation.

All the synthesized catalysts had higher mass specific activity (MA) compared to the commercial catalyst. The Pt/Vulcan had the lowest MA value (65 $A.g^{-1}$) compared to the highest value for the Pt/BNHCS at 188 $A.g^{-1}$; this is a 172% increase. For the other catalysts MA increases were between 19 - 32%. Similar trends were observed for the specific activity (SA) where the commercial Pt/Vulcan had a value of 107 $\mu A.cm^{-2}$ (anodic) compared to the 303 $\mu A.cm^{-2}$ for the Pt/BNHCS; a 128% increase, for a similar particle size and comparable ECSA.

Particle size effects were not related to SA, ECSA and MA trends, as all the materials had similar Pt sizes. The possible explanations for the observed dramatic increase in MA and SA were attributed to the textual properties of the new supports as well as the nitrogen doping. The higher BET surface area for the Pt/BNHCSs could have permitted better diffusion of the oxygen allowing better ORR. Nitrogen doping could have influenced the electronic properties of the supports allowing for favourable charge transfer and equilibration between the Pt and the support, and better Pt ORR activity as a result.

The Raman data confirmed the presence of defects on the supports allowing for small particles of Pt to be deposited effectively. The higher defect density of the synthesized materials, as confirmed by the $I_D/I_G$ ratios, allowed for numerous sites for Pt deposition with a high degree of dispersion and support utilization. These uniformly dispersed Pt particles with small Pt-Pt distances were near each other and hence allowed for better conductivity for the ORR electrons, resulting in the higher SA and MA values obtained.

Higher durability was observed for the Pt/BNHCSs compared to the Pt/Vulcan benchmark catalyst. At the end of load cycling, this catalyst retained about 59% of the initial ECSA compared to about 48% for the Pt/Vulcan. The other catalyst durability values were in between these extreme values. There was a correlation between BET surface area, $I_D/I_G$ ratio and small contributions due to particle size effects of the Pt catalysts and their activities.

Nitrogen doping was shown to enhance the MA and SA of the catalysts; however, the durability of Pt was negatively affected. Nitrogen doped supported catalysts had lower durability compared to the pristine materials. The lower durability was attributed to the higher defect density on these supports which could have contributed to Pt degradation possibly by detachment or dissolution.

The new synthesized catalysts had higher MA, SA and ECSA compared to the commercial catalyst. Further studies on support durability would allow these materials to be used in membrane electrode assembles (MEA). The MEA could then be tested in real fuel cell test stations, followed by commercialization if the further testing gave positive outcomes.

Therefore, through the careful tailoring of the support structure of the carbon fuel cell supports, we proved that tailored carbons can still be used as cathode supports. The HCSs, NHCS, BHCSs and BNHCSs supports can be applied in fuel cells as they offer better mass and specific activity as well as conferring better durability to Pt than the commercial Vulcan.

## 6.9: References


(1) Zohuri, B. Hydrogen-Powered Fuel Cell and Hybrid Automobiles of the Near Future. In *Hydrogen Energy*; Springer International Publishing: Cham, **2019**, 37–59.

(2) Seo, D. J.; Yoon, W.-L.; Yoon, Y.-G.; Park, S.-H.; Park, G.-G.; Kim, C.-S. Development of a Micro Fuel Processor for PEMFCs. *Electrochimica Acta* **2004**, *50* (2), 719–723.

(3) Behling, N. H. Chapter 2 - Fuel Cells and the Challenges Ahead. In *Fuel Cells*; Behling, N. H., Ed.; Elsevier, **2013**, 7–36.

(4) Chen, W.; Huang, J.; Wei, J.; Zhou, D.; Cai, J.; He, Z. D.; Chen, Y. X. Origins of High Onset Overpotential of Oxygen Reduction Reaction at Pt-Based Electrocatalysts: A Mini Review. *Electrochemistry Communications* **2018**, *96*. 71-76.

(5) Rau, M. S.; Gennero de Chialvo, M. R.; Chialvo, A. C. Kinetic Study of the Hydrogen Oxidation Reaction on Pt over the Complete Overpotential Range. *Journal of Power Sources* **2013**, *229*, 210–215.

(6) Chattot, R.; Asset, T.; Bordet, P.; Drnec, J.; Dubau, L.; Maillard, F. Beyond Strain and Ligand Effects: Microstrain-Induced Enhancement of the Oxygen Reduction Reaction Kinetics on Various PtNi/C Nanostructures. *ACS Catalysis* **2017**, *7* (1), 398–408.

(7) Dubau, L.; Nelayah, J.; Moldovan, S.; Ersen, O.; Bordet, P.; Drnec, J.; Asset, T.; Chattot, R.; Maillard, F. Defects Do Catalysis: CO Monolayer Oxidation and Oxygen Reduction Reaction on Hollow PtNi/C Nanoparticles. *ACS Catalysis* **2016**, *6* (7), 4673–4684.

(8) Li, X.; An, L.; Chen, X.; Zhang, N.; Xia, D.; Huang, W.; Chu, W.; Wu, Z. Durability Enhancement of Intermetallics Electrocatalysts via N-Anchor Effect for Fuel Cells. *Sci Rep.* **2013**, 3, 3234.

(9) Chung, Y. H.; Chung, D. Y.; Jung, N.; Park, H. Y.; Sung, Y. E.; Yoo, S. J. Effect of Surface Composition of Pt-Fe Nanoparticles for Oxygen Reduction Reactions. *International Journal of Hydrogen Energy* **2014**, *39* (27), 14751–14759.

(10) Mohanta, P. K.; Glökler, C.; Arenas, A. O.; Jörissen, L. Sb Doped SnO2 as a Stable Cathode Catalyst Support for Low Temperature Polymer Electrolyte Membrane Fuel Cell. *International Journal of Hydrogen Energy* **2017**, *42* (46), 27950–27961.

(11) Serrano-Ruiz, J. C.; Huber, G. W.; Sánchez-Castillo, M. A.; Dumesic, J. A.; Rodríguez-Reinoso, F.; Sepúlveda-Escribano, A. Effect of Sn Addition to Pt/CeO2–Al2O3 and Pt/Al2O3 Catalysts: An XPS, 119Sn Mössbauer and Microcalorimetry Study. *Journal of Catalysis* **2006**, *241* (2), 378–388.

(12) Schierbaum K.D, Ordered Ultra-Thin Cerium Oxide Overlayers on Pt (111) Single Crystal Surfaces Studied by LEED and XPS. *Surface Science* **1998**,399, 29-38.

(13) Cognard, G.; Ozouf, G.; Beauger, C.; Jiménez-Morales, I.; Cavaliere, S.; Jones, D.; Rozière, J.; Chatenet, M.; Maillard, F. Pt Nanoparticles Supported on Niobium-Doped Tin Dioxide: Impact of the Support Morphology on Pt Utilization and Electrocatalytic Activity. *Electrocatalysis* **2017**, *8* (1), 51–58.

(14) Kreitmeier, S.; Wokaun, A.; Büchi, F. N. Local Catalyst Support Degradation during Polymer Electrolyte Fuel Cell Start-up and Shutdown. *Journal of the Electrochemical Society* **2012**, *159* (11), F787-F793

(15) Takei, C.; Kakinuma, K.; Kawashima, K.; Tashiro, K.; Watanabe, M.; Uchida, M. Load Cycle Durability of a Graphitized Carbon Black-Supported Platinum Catalyst in Polymer Electrolyte Fuel Cell Cathodes. *Journal of Power Sources* **2016**, *324*, 729–737.

(16) Garland, N. L.; Benjamin, T. G.; Kopasz, J. P. ECS Transactions DOE Fuel Cell Program: Durability Technical Targets and Testing Protocols DOE Fuel Cell Program: Durability Technical Targets and Testing Protocols. https://doi.org/10.1149/1.2781004.

(17) Marcinkoski, J.; Kopasz, J. Progress in the US DOE Fuel Cell Subprogram Efforts in Polymer Electrolyte Fuel Cells. *International Journal of Hydrogen Energy* **2008**,33,3894 - 3902

(18) Garland, N.; Benjamin, T.; Kopasz, J. DOE Fuel Cell Program: Durability Technical Targets and Testing Protocols. *ECS Trans.* **2007**, *11* (1), 923.

(19) Garsany, Y.; Baturina, O. A.; Swider-Lyons, K. E.; Kocha, S. S. Experimental Methods for Quantifying the Activity of Platinum Electrocatalysts for the Oxygen Reduction Reaction. *Analytical Chemistry* **2010**, *82* (15), 6321–6328.

(20) Zhang, J.; Ma, L.; Gan, M.; Yang, F.; Fu, S.; Li, X. Well-Dispersed Platinum Nanoparticles Supported on Hierarchical Nitrogen-Doped Porous Hollow Carbon Spheres with Enhanced Activity and Stability for Methanol Electrooxidation. *Journal of Power Sources* **2015**, *288*, 42–52.

(21) Chaiburi, C.; Hacker, V. Catalytic Activity of Various Platinum Loading in Acid Electrolyte at 303 K. *Energy Procedia* **2017**, *138*, 229–234.

(22) Masa, J.; Batchelor-McAuley, C.; Schuhmann, W.; Compton, R. G. Koutecky-Levich Analysis Applied to Nanoparticle Modified Rotating Disk Electrodes: Electrocatalysis or Misinterpretation. *Nano Research* **2014**, *7* (1), 71–78.

(23) Jackson, C.; Smith, G. T.; Inwood, D. W.; Leach, A. S.; Whalley, P. S.; Callisti, M.; Polcar, T.; Russell, A. E.; Levecque, P.; Kramer, D. Electronic Metal-Support Interaction Enhanced Oxygen Reduction Activity and Stability of Boron Carbide Supported Platinum. *Nature Communications* **2017**, *8* (1), 15802–15802.

(24) Yoda, T.; Uchida, H.; Watanabe, M. Effects of Operating Potential and Temperature on Degradation of Electrocatalyst Layer for PEFCs. *Electrochimica Acta* **2007**, *52* (19), 5997–6005.

(25) Yasuda, K.; Taniguchi, A.; Akita, T.; Ioroi, T.; Siroma, Z. Characteristics of a Platinum Black Catalyst Layer with Regard to Platinum Dissolution Phenomena in a Membrane Electrode Assembly. *Journal of the Electrochemical Society* **2006**, *153* (8), A1599-A1603.

(26) Iden, H.; Ohma, A. An in Situ Technique for Analyzing Ionomer Coverage in Catalyst Layers. *Journal of Electroanalytical Chemistry* **2013**, *693*, 34–41.

(27) Takahashi, I.; Kocha, S. S. Examination of the Activity and Durability of PEMFC Catalysts in Liquid Electrolytes. *Journal of Power Sources* **2010**, *195* (19), 6312–6322.

(28) Garsany, Y.; Singer, I. L.; Swider-Lyons, K. E. Impact of Film Drying Procedures on RDE Characterization of Pt/VC Electrocatalysts. *Journal of Electroanalytical Chemistry* **2011**, *662* (2), 396–406.

(29) Subramanian, N. P.; Greszler, T. A.; Zhang, J.; Gu, W.; Makharia, R. Pt-Oxide Coverage-Dependent Oxygen Reduction Reaction (ORR) Kinetics. *J. Electrochem. Soc.* **2012**, *159* (5), B531.

(30) Zhou, Y.; Neyerlin, K.; S. Olson, T.; Pylypenko, S.; Bult, J.; N. Dinh, H.; Gennett, T.; Shao, Z.; O'Hayre, R. Enhancement of Pt and Pt-Alloy Fuel Cell Catalyst Activity and Durability via Nitrogen -Modified Carbon Supports. *Energy & Environmental Science* **2010**, *3* (10), 1437–1446.

(31) Hou, J.; Cao, C.; Idrees, F.; Ma, X. Hierarchical Porous Nitrogen-Doped Carbon Nanosheets Derived from Silk for Ultrahigh-Capacity Battery Anodes and Supercapacitors. *ACS Nano* **2015**, *9* (3), 2556–2564.

(32) Ma, J.; Habrioux, A.; Luo, Y.; Ramos-Sanchez, G.; Calvillo, L.; Granozzi, G.; Balbuena, P. B.; Alonso-Vante, N. Electronic Interaction between Platinum Nanoparticles and Nitrogen-Doped Reduced Graphene Oxide: Effect on the Oxygen Reduction Reaction. *Journal of Materials Chemistry A* **2015**, *3* (22), 11891–11904.

(33) Ning, X.; Li, Y.; Ming, J.; Wang, Q.; Wang, H.; Cao, Y.; Peng, F.; Yang, Y.; Yu, H. Electronic Synergism of Pyridinic- and Graphitic-Nitrogen on N-Doped Carbons for the Oxygen Reduction Reaction. *Chem. Sci.* **2019**, *10* (6), 1589–1596.

(34) Schonvogel, D.; Hülstede, J.; Wagner, P.; Kruusenberg, I.; Tammeveski, K.; Dyck, A.; Agert, C.; Wark, M. Stability of Pt Nanoparticles on Alternative Carbon Supports for Oxygen Reduction Reaction. *Journal of The Electrochemical Society* **2017**, *164* (9), F995–F1004.

(35) Speder, J.; Zana, A.; Spanos, I.; Kirkensgaard, J. J. K.; Mortensen, K.; Arenz, M. On the Influence of the Pt to Carbon Ratio on the Degradation of High Surface Area Carbon Supported PEM Fuel Cell Electrocatalysts. *Electrochemistry Communications* **2013**, *34*, 153–156.

(36) Tada, M.; Murata, S.; Asakoka, T.; Hiroshima, K.; Okumura, K.; Tanida, H.; Uruga, T.; Nakanishi, H.; Matsumoto, S. I.; Inada, Y.; Nomura, M.; Iwasawa, Y. In Situ Time-Resolved Dynamic Surface Events on the Pt/C Cathode in a Fuel Cell under Operando Conditions. *Angewandte Chemie - International Edition* **2007**, *46* (23), 4310–4315.

(37) Simonsen, S. B.; Chorkendorff, I.; Dahl, S.; Skoglundh, M.; Sehested, J.; Helveg, S. Ostwald Ripening in a Pt/SiO2 Model Catalyst Studied by in Situ TEM. *Journal of Catalysis* **2011**, *281* (1), 147–155.

(38) Schmies, H.; Bergmann, A.; Drnec, J.; Wang, G.; Teschner, D.; Kühl, S.; Sandbeck, D. J. S.; Cherevko, S.; Gocyla, M.; Shviro, M.; Heggen, M.; Ramani, V.; Dunin-Borkowski, R. E.; Mayrhofer, K. J. J.; Strasser, P. Unravelling Degradation Pathways of Oxide-Supported Pt Fuel Cell Nanocatalysts under In Situ Operating Conditions. *Advanced Energy Materials* **2018**, *8* (4),1701663

(39) Zana, A.; Speder, J.; Reeler, N. E. A.; Vosch, T.; Arenz, M. Investigating the Corrosion of High Surface Area Carbons during Start/Stop Fuel Cell Conditions: A Raman Study. *Electrochimica Acta* **2013**, 114(30), 455-461

(40) Mohamed, R.; Binninger, T.; J. Kooyman, P.; Hoell, A.; Fabbri, E.; Patru, A.; Heinritz, A.; J. Schmidt, T.; Levecque, P. Facile Deposition of Pt Nanoparticles on Sb-Doped SnO

2 Support with Outstanding Active Surface Area for the Oxygen Reduction Reaction. *Catalysis Science & Technology* **2018**, *8* (10), 2672–2685.

(41) Becknell, N.; Kang, Y.; Chen, C.; Resasco, J.; Kornienko, N.; Guo, J.; Markovic, N. M.; Somorjai, G. A.; Stamenkovic, V. R.; Yang, P. Atomic Structure of Pt3Ni Nanoframe Electrocatalysts by in Situ X-Ray Absorption Spectroscopy. *Journal of the American Chemical Society* **2015**, *137* (50), 15817–15824.

(42) Antolini, E. Structural Parameters of Supported Fuel Cell Catalysts: The Effect of Particle Size, Inter-Particle Distance and Metal Loading on Catalytic Activity and Fuel Cell Performance. *Applied Catalysis B: Environmental* **2016**, *181*, 298–313.

(43) Yano, H.; Watanabe, M.; Iiyama, A.; Uchida, H. Particle-Size Effect of Pt Cathode Catalysts on Durability in Fuel Cells. *Nano Energy* **2016**, *29*, 323–333.

(44) Pizzutilo, E.; Knossalla, J.; Geiger, S.; Grote, J.-P.; Polymeros, G.; Baldizzone, C.; Mezzavilla, S.; Ledendecker, M.; Mingers, A.; Cherevko, S.; Schüth, F.; Mayrhofer, K. J. J. The Space Confinement Approach Using Hollow Graphitic Spheres to Unveil Activity and Stability of Pt-Co Nanocatalysts for PEMFC. *Advanced Energy Materials* **2017**, *7* (20), 1700835.

(45) Yin, Y.; Liu, T.; Liu, D.; Wang, Z.; Deng, Q.; Qu, D.; Xie, Z.; Tang, H.; Li, J. Confining Nano-Sized Platinum in Nitrogen Doped Ordered Mesoporous Carbon: An Effective Approach toward Efficient and Robust Hydrogen Evolution Electrocatalyst. *Journal of Colloid and Interface Science* **2018**, *530*, 595–602.

(46) Jauhar, A. M.; Ma, Z.; Xiao, M.; Jiang, G.; Sy, S.; Li, S.; Yu, A.; Chen, Z. Space-Confined Catalyst Design toward Ultrafine Pt Nanoparticles with Enhanced Oxygen Reduction Activity and Durability. *Journal of Power Sources* **2020**, *473*, 228607.

(47) Kinoshita, K. Particle Size Effects for Oxygen Reduction on Highly Dispersed Platinum in Acid Electrolytes. *Journal of the Electrochemical Society* **1990**, *137* (3), 845–848.

(48) Campbell, C. T.; Parker, S. C.; Starr, D. E. The Effect of Size-Dependent Nanoparticle Energetics on Catalyst Sintering. *Science* **2002**, *298* (5594), 811–814.

(49) Sui, S.; Wang, X.; Zhou, X.; Su, Y.; Riffat, S.; Liu, C. A Comprehensive Review of Pt Electrocatalysts for the Oxygen Reduction Reaction: Nanostructure, Activity, Mechanism and Carbon Support in PEM Fuel Cells. *Journal of Materials Chemistry A* **2017**, *5* (5), 1808–1825.

(50) Castanheira, L.; Silva, W. O.; Lima, F. H. B.; Crisci, A.; Dubau, L.; Maillard, F. Carbon Corrosion in Proton-Exchange Membrane Fuel Cells: Effect of the Carbon Structure, the Degradation Protocol, and the Gas Atmosphere. *ACS Catalysis* **2015**, *5* (4), 2184–2194.

(51) Park, Y. C.; Kakinuma, K.; Uchida, M.; Tryk, D. A.; Kamino, T.; Uchida, H.; Watanabe, M. Investigation of the Corrosion of Carbon Supports in Polymer Electrolyte Fuel Cells Using Simulated Start-up/Shutdown Cycling. *Electrochimica Acta* **2013**, *91*, 195–207.

(52) Brandão, L.; Passeira, C.; Gattia, D. M.; Mendes, A. Use of Single Wall Carbon Nanohorns in Polymeric Electrolyte Fuel Cells. *Journal of Materials Science* **2011**, *46* (22), 7198–7205.

(53) Calvillo, L.; Gangeri, M.; Perathoner, S.; Centi, G.; Moliner, R.; Lázaro, M. J. Effect of the Support Properties on the Preparation and Performance of Platinum Catalysts Supported on Carbon Nanofibers. *Journal of Power Sources* **2009**, *192* (1), 144–150.

(54) Wang, D. D.; Wu, G.; Zhang, C.; Yin, F.; Su, L.; Shrestha, S.; Zhang, Z.; Mustain, W. Improved Durability of Pt Catalyst Supported on N-Doped Mesoporous Graphitized Carbon for Oxygen Reduction Reaction in Polymer Electrolyte Membrane Fuel Cells. *Applied Catalysis B: Environmental* **2017**, *42* (52), 265–274.

(55) Peters, S.; Peredkov, S.; Al-Hada, M.; Neeb, M.; Eberhardt, W. Positive XPS Binding Energy Shift of Supported CuN-Clusters Governed by Initial State Effects. *Journal of Electron Spectroscopy and Related Phenomena* **2014**, 192, 52-54

(56) Tao, J. G.; Pan, J. S.; Huan, C. H. A.; Zhang, Z.; Chai, J. W.; Wang, S. J. Origin of XPS Binding Energy Shifts in Ni Clusters and Atoms on Rutile $TiO_2$ Surfaces. *Surface Science* **2008**, *602* (16), 2769–2773.

(57) Galeano, C.; Meier, J. C.; Peinecke, V.; Bongard, H.; Katsounaros, I.; Topalov, A. A.; Lu, A.; Mayrhofer, K. J. J.; Schüth, F. Toward Highly Stable Electrocatalysts via Nanoparticle Pore Confinement. *J. Am. Chem. Soc.* **2012**, *134* (50), 20457–20465.

# Chapter 7

# Study of the activity and durability of Pt/HCS and Pt/NHCS prepared by the ethanol reflux method using $Pt(acac)_2$

## 7.1: Introduction

The proton exchange membrane fuel cell (PEMFC) has demonstrated that it has promising characteristics for application in automobiles due to its light weight and high-power density.[1,2] The primary reaction in these fuel cells, the oxygen reduction reaction (ORR) is one of the important chemical reactions for the conversion of chemical to electrical energy.[3] This reaction, $O_2 + 4H^+ + 4e^- \rightarrow 2H_2O$, proceeds mostly via a four-electron pathway that is catalyzed by Platinum (Pt).[2]

Even though Pt is an excellent ORR catalyst, the sluggish kinetics at the cathode requires that huge loadings of Pt be used for the reaction to be useful for purposes of its application in

---

**This chapter will be submitted for publication with the title: *Pristine and nitrogen doped hollow carbon spheres promotes the activity and durability of platinum oxygen reduction reaction catalysts.* There is some duplication of the experimental section form earlier chapters in this chapter, this arises since this chapter has been written in paper format for the publication**

automobiles. The use of high loading of Pt in fuel cell electrodes has driven up the cost of fuel cell systems, hence hindering their fast commercialization, which is disadvantageous as these energy conversion systems have an efficiency better than internal combustion engines and also possesses good characteristics of sustainability. These PEMFCs have a neutral carbon footprint if the hydrogen fuel is sourced from the solar electrolysis of water.[4] This therefore suggests that the current regimen of Pt based catalysts must be improved in such a way that the activity and durability increase while the amount of Pt in the electrode must be reduced dramatically.

The USA Department of Energy set fuel cell commercialization targets for the year 2020 prioritizing catalysts with a mass activity > 0.44 $A.mg^{-1}$, and more than 5000 h of cycling durability.[5] To that effect, a number of research efforts have been made to sustain and enhance Pt catalysts in the fuel cell reactions.

One of the approaches used to enhance the activity of Pt is to use an appropriate support. To date, conventional ORR catalysts have been Pt nanoparticles supported on high surface area and conductive carbons or conductive metal oxides including Sb doped $SnO_2$.[6] However, the metal oxide support can be expensive, possess low conductivity, low porosity and low surface area resulting in poor dispersion of the active Pt or Pt alloy catalysts. This can, in some cases, also lead to low SA and MA values compared to Pt deposited on the standard conductive and porous carbon supports. For these reasons, carbon is currently the support of choice. However, during the start-up of the fuel cell cathode potentials can reach above 1.5 V vs. RHE, causing degradation of both the Pt catalysts and the C supports.[7]

Another approach to produce highly active and durable ORR catalysts has been to alloy Pt with other transition metals like cobalt or manganese. Fundamental studies of the well-defined extended surfaces of these alloy catalysts demonstrated that the improved activity stems from

the modified electronic structure of the Pt which causes a reduction in the adsorption of oxygenated species on the Pt surface. This causes an increase in the number of Pt active sites accessible to the oxygen. Challenges with these alloy catalysts is the dissolution of the transition metals causing a reduction in the number of active sites of the Pt as the electronic effects are diminished. Also, it is difficult to use the conventional synthetic procedures to obtain catalysts that demonstrates the same level of activity enhancement.

Even though high surface area graphitic carbons are characterized by low durability in fuel cells, structured carbon supports are known to exhibit characteristics that can be exploited to generate suitable Pt or Pt-alloy catalyst supports for fuel cell applications.[8] The low cost, high BET surface area, arrays of mesopores and micropores, electronic conductivity, high thermal stability, ability to be moulded into various shapes and allotropes, light weight for mobile applications and mechanical durability makes structured carbons suitable candidates for ORR catalysis. In-situ or post-synthesis functionalization of these structured carbons modifies the surface chemistry of these supports, sometimes resulting in better tethering of the Pt to the support and subsequently promoting durability.[9]

Despite the promising properties of the various carbon supports, it is the metal nanoparticle preparation that needs to be mastered in order to produce catalysts that have small particles and a small particle size distribution. To date several synthetic approaches have been adopted and these include the pylol method[10], the microwave assisted deposition[11], the chemical reduction route[12] and the metal-organic deposition.[13] Even though these methods have produced Pt particles with promising properties, there are still some challenges associated with these approaches, especially the wet chemistry-based methods. The challenges associated with these methods are the complexities of the synthetic methodology which makes unpredictable the particle size and dispersion of the nanoparticles. In some cases, agglomerated nanoparticles are

formed and in other cases, dispersion is hindered, or poly dispersity of the nanoparticles has been experienced. Agglomeration, poor dispersion, bigger particles and poly dispersed nanoparticles results in a lowered electrochemical surface area (ECSA) and subsequently poor activity.

Therefore, synthetic procedures that produces Pt particles of good dispersion, high surface coverage, small particle size distribution, good support -Pt anchorage are a requirement if these Pt catalysts are to reach their full potential. In this study Pt nanoparticles prepared by the reflux in ethanol of a platinum precursor salt were deposited on the hollow carbon spheres (HCSs) and the nitrogen doped hollow carbon spheres (NHCSs). As the HCSs and NHCSs were completely spherical and unbroken, unlike the BHCSs and BNHCSs (discussed in Chapter 6), the Pt nanoparticles were only deposited on the outside shell of these supports and possibly inside the pores when forming the Pt/HCSs and Pt/NHCSs. As discussed in previous Chapters, these support materials possess defects that enable good dispersion of metal catalysts. Further, N doping provides anchoring sites for the adsorption of platinum ions and this controls the nucleation and growth of Pt particles which results in the formation of smaller particles with better dispersion. [15] The metal-support interactions of the Pt with the N doped supports thus promote better activity and durability.[16] The Pt nanoparticles prepared by the ethanol reflux method should possess similar properties to the Pt particles prepared by the other methods like metal-organic deposition method (discussed in Chapter 4 and Chapter 5). In this case we wished to investigate if properties like dispersion of the catalysts would be affected by this method of synthesis. Also, the presence of these organic moieties (ethanol from the refluxing), was also investigated for its possible in the hindrance of the oxygen reduction reaction. The thin carbon shell of the support can also promote the better metal-support interaction resulting in better electronic conductivity in ORR catalysis.

The new Pt containing materials described in this study were characterized and tested for ORR activity and durability. These catalysts have shown improved MA, SA and catalyst durability as benchmarked against a commercial Pt/C catalyst with a nominal 40 wt.% Pt/C loading.

## 7.2: Experimental

### 7.2.1: Chemicals

Hydrofluoric acid (48%), cetyltrimethylammonium bromide (CTAB), melamine (99%), methanol (99%), sulfuric acid (98%), platinum acetylacetonate ($Pt(acac)_2$, 97%), tetraethyl orthosilicate (TEOS, 98%), resorcinol, formaldehyde (37%), and nafion perflourinated resin solution (5 wt% in water) were all purchased from Sigma-Aldrich and used without further purification. Nochromix crystals (Gordax laboratories), ammonia solution (25%, Associated Chemical Enterprises), absolute ethanol (99.6%, MK chemicals), perchloric acid (70%, Suprapur, Merck), ultrapure water (18.2 MΩ.cm, Merk-Millipore), alumina polish (0.05µm and 0.1 µm and polishing cloths, Buehler), argon gas (99.99%), oxygen gas (99.99%), nitrogen gas (99.99%), were sourced from Afrox and also used as received without further purification.

### 7.2.2: Synthesis of silica templates

The details of the preparation of the spherical silica templates is provided in Chapter 2.2 and Chapter 3. Silica particles were prepared according to the method described by Stober and colleagues.[17]Typically, absolute ethanol (500 mL) was mixed with tetraethyl orthosilicate (100 mL) and deionized water (50 mL) and allowed to stir at room temperature on a magnetic stirrer for 30 minutes. To this mixture was added 50 mL ammonia solution (25%) and the reaction was allowed to stir for a further 6 h. Meanwhile, the reaction vessel was sealed to prevent the room temperature evaporation of the ammonia solution. The silica particles were separated from solution by centrifugation for 30 minutes followed by washing with 200 mL of a 50:50

vol% absolute ethanol: deionized water solution. The silica particles were separated by centrifugation and allowed to dry in an oven at 100°C overnight. The silica was placed in a ceramic crucible and calcined at 500°C in air in a muffle furnace for 5 h. The weighed silica powders (18.5 g) amounted to a yield of 88% based on the TEOS used.

## 7.2.3: Synthesis of hollow carbon spheres (HCSs) and nitrogen doped hollow carbon spheres (NHCSs)

The detailed description of the preparation of the HCSs is provided in Chapter 4.2. In a typical synthesis, a solution of EtOH (280 mL) and DI water (60 mL) was mixed with the $SiO_2$ spheres (4 g) by sonication. To the solution, a previously sonicated mixture of CTAB (2 g), 37% formaldehyde solution (1.5 mL) and resorcinol (1.5 g) were added. A 25% $NH_4OH$ solution (10 mL) was added and the system was magnetically stirred at room temperature. The solution turned from an off-white color to brown with stirring. After 24 h the $SiO_2$@RF (resorcinol formaldehyde resin covering the silica) was filtered and washed with copious amounts of DI water, followed by drying in an oven overnight at 100°C.

The dried brown product was carbonized in a tubular horizontal furnace under an argon flow at 900°C. Typically, the $SiO_2$@RF (200 mg) was loaded into a quartz boat and placed in the furnace connected to an argon gas line flowing at 50 mL $min^{-1}$. The furnace was ramped up to 900 °C at a heating rate of 10 °C $min^{-1}$ and kept isothermal for 2 h followed by a natural cooling process overnight. The black soot ($SiO_2$@C) was etched using a 10% HF solution in water (200 mL) for 24 h to remove the $SiO_2$ template. The solution was vacuum filtered, washed with 500 mL of DI water and dried in an oven at 80 °C overnight. The formed HCSs were annealed in a tubular horizontal furnace at 900 °C for 2 h at a heating rate of 10°C.$min^{-1}$ under argon flowing at a rate of 50 ml.$min^{-1}$. The weighed HCSs (250 mg) amounted to a yield of 94% based on the amount of resorcinol used.[18]

For the preparation of NHCSs, typically, 3 g of $SiO_2$@RF was mixed with 3 g of melamine in a borosilicate vial containing methanol (20 mL). The composite was sonicated for 30 minutes followed by drying in an oven at 80 ℃ for 2 h. The $SiO_2$@RF@melamine composite was carbonized at 900 ℃ for 2 h using a heating rate of 10 ℃ $min^{-1}$ under argon, followed by etching to remove the silica with a 10% HF solution (200 mL) for 24 h. The product was filtered and washed with DI water (500 ml) followed by drying at 80℃ in an oven overnight. The BNHCSs were annealed at 900 ℃ for 2 h at a heating rate of 10 ℃ $min^{-1}$ under argon flowing at a rate of 50 mL $min^{-1}$. The weighed BNHCSs (265 mg) amounted to a yield of 92 % based on the amount of resorcinol used. [18]

## 7.2.4: Synthesis of Pt/HCSs and Pt/NHCSs.

To achieve a nominal 40wt.% Pt/HCSs or Pt/NHCSs catalysts, HCSs or NHCSs (100 mg) were mixed with $Pt(acac)_2$ (135 mg) in a solution of absolute ethanol (200 mL) and sonicated for 30 min to allow for thorough mixing. The composite was then transferred into a round bottom flask which was placed in a oil bath heater. The oil bath heater was ramped to 100 ℃ and kept isothermal for 30 min to drive moisture off the sample. The reactor was further ramped up to 250 ℃ at a heating rate of 2.5 ℃ $min^{-1}$ and kept isothermal for 2 h while the reaction continued under reflux. The reactor was allowed to cool naturally to room temperature, and the products were washed twice with 300 mL deionized water followed by drying at 80 weighed.[19]

## 7.2.5: Catalyst characterization

TEM analysis was performed using a Tecnai F20 transmission electron microscope with a field emission gun (FEG) operating at 200 kV. Spatula tips of samples were dispersed in ethanol by ultrasonication and a few droplets were transferred to lacy carbon coated copper grids for TEM analysis. Particle size analysis was carried out by measuring the diameter of at least 100 particles from different TEM images and using the software ImageJ. The particle size

distribution was plotted using Origin lab version 8.5. SEM analysis was performed on a Tescan MIRA3 RISE scanning electron microscope operating at 30kV. Spatula tips of samples were spread on a carbon tape mounted on an aluminium stub and coated with a gold-palladium layer before the analysis to enhance sample conductivity and to reduce charging effects. PXRD measurements were carried out on a Bruker D8 Advance diffractometer with a Cu Kα radiation source operating at 40 kV to determine the crystalline phases present in the catalyst with 2Θ between 0° and 120°. Rietveld refinement of the PXRD patterns was completed using Bruker AXS TOPAS software, Version 4.1. The Scherrer equation was also used to deduce the sizes of the Pt particles. In-situ PXRD experiments were performed under nitrogen on a Bruker D8 Advance diffractometer fitted with an Anton Paar XRK 900 in situ cell. The diffractometer used a sealed copper tube as the X-ray source operating at 40 kV and 40 mA that provided X-rays with a wavelength of 0.15418 nm in a parallel beam geometry. The Rietveld refinement method was used to analyse the PXRD profiles. Indexing the compounds detected by the PXRD technique was achieved using the EVA software. TGA was performed with a Perkin-Elmer STA6000 analyser using $N_2$ as the purge and coolant gas (20 ml.min$^{-1}$) and air for combustion (10 ml.min$^{-1}$) and a heating rate of 10 °C min$^{-1}$. Small amounts of sample (10 mg) were used for TGA analyses. Nitrogen physisorption experiments were conducted using a Micromeritics Tristar 3000 surface area and porosity analyser set at -195ºC, with sample degassing conducted at 150 °C overnight. The BET surface area was obtained from adsorption data in a relative pressure range from 0.05 to 0.30. The total pore volumes were calculated from the amount of nitrogen gas adsorbed at a relative pressure of 0.99. The pore size distributions were evaluated from the desorption branches of the isotherms using the Barrett-Joyner-Halenda (BJH) method. The micropore surface area and volume were calculated using t-plot data. Raman spectroscopy measurements were performed on a Horiba Jobin-Yvon Raman spectrometer with a laser wavelength of ($\lambda$ = 514 nm). The XPS measurements were carried out at the National Institute

of Meteorology South Africa (NMISA) at the Council for Scientific and Industrial Research (CSIR) in Pretoria, using a Thermo Scientific ESCALAB 250Xi spectrometer with a Monochromatic Al kα (1486.7eV) source operating with an X-ray power of 300 W, X-ray spot size of 900 µm, low resolution pass energy of 100eV, high resolution pass energy of 20 eV and a pressure of $10^{-8}$ mBar. The catalysts were also studied using scanning transmission electron microscopy (STEM) in a probe corrected JEOL ARM200F at the David Cockayne Centre for Electron Microscopy, University of Oxford, operated at 200 kV. A probe current of 13 pA, convergence semi-angle of 14 mrad, annular dark field (ADF) inner and outer detector angles of 77.43–241.21 mrad, and a bright-field (BF) outer detector angle of 13.2 mrad were used for simultaneous acquisition of both ADF and BF signals.

## 7.2.6: Electrochemical characterization

Details of the electrochemical procedures and methods are provided in Chapter 6.2 – 6.6. In summary, all experiments were performed in a three-electrode cell at room temperature (approx. 25 ºC) in a solution of 0.1 M $HClO_4$. As discussed, the perchloric acid electrolyte was in all cases saturated with either argon or oxygen for the cyclic voltammetry (CV) or oxygen reduction reaction (ORR) experiments, respectively. A high surface area Pt wire was used as the counter electrode, a $Hg/HgSO_4$ electrode with a bridge tube as a reference electrode and a catalyst coated glassy carbon (GCE) electrode with a working area of 0.196 $cm^2$ as the working electrode (WE). The reference electrode was calibrated against the reversible hydrogen electrode by measuring the potential difference between the Pt wire in a hydrogen saturated electrolyte. All potentials in these studies were reported against the reversible hydrogen electrode potential (vs. RHE). Catalyst inks were prepared by mixing about 5 mg of the catalyst with 1.5 ml of ultrapure water (18.2 MΩ·cm), 3.5 ml isopropyl alcohol (HPLC grade) and 20 µl Nafion per fluorinated resin solution (5 wt. % in a mixture of lower aliphatic alcohols and water). The ink mixture was ultra-sonicated in a cold-water bath for 30 minutes to obtain a

homogeneous ink solution before analysis. The resulting black ink (10 µl) was pipetted onto the GC electrode (Pine Research Instrumentation or Metrohm) coupled to an RDE710 (Gamry) or RDE-2 (Metrohm-Autolab) rotator box and dried under rotation (250 rpm) for 20 minutes in ambient conditions. This formed a thin film of uniformly distributed catalyst on the GC electrode. The ultrapure water and isopropyl alcohol were evaporated during the rotational drying process. The electrochemical cell, electrolyte volumetric flasks, purge tubes and reference electrode bridge tubes were all soaked overnight in a solution of Nochromix and concentrated sulfuric acid. This was followed by a 7 times rinse in ultra-pure water. The GC electrodes were prepared before ink deposition and drying, first using 1 µm alumina and a wet micro-smooth polishing cloth pad. A figure eight cleaning protocol was adopted followed by rinsing in ultra-pure water and ultra-sonication in isopropyl alcohol and ultra-pure water. The routine was repeated with a smoother 0.05 µm alumina polish followed by thorough rinsing to remove the dirt and the sticking alumina. A Biologic SP300 potentiostat or Metrohm Autolab PGSTAT302N coupled to a Gamry RDE (rotating disk electrode) 710 Rotator or a Autolab RDE-2 rotator was used for CV and RDE measurements.

In an Ar saturated electrolyte, the potential of the WE was cycled between 0.0 and 1.2 V vs. RHE for 100 cycles at 100 $mV.s^{-1}$ for the electrochemical oxidation of all the impurities on the surface of the catalyst coated WE. The scan rate was then reduced to 50 $mV.\ s^{-1}$ and the 3$^{rd}$ cycle was used for the calculation of the electrochemical active surface area (ECSA) assuming a monolayer charge associated with hydrogen adsorption of 210 $\mu C.cm^{-2}$.[20] The area under the CV curve, associated with the under potential deposition of hydrogen, was integrated and used for the calculation of ECSA. Oxygen reduction reaction (ORR) I-V polarization curves were obtained at 1600 rpm of the electro-catalyst coated working electrode. The WE was cycled at $10mV.s^{-1}$ between 0.075 – 1.225 V vs. RHE in the cathodic direction. To correct for non-ORR background current, the LSV obtained in an argon saturated electrolyte without rotation was

subtracted from that obtained from the oxygen saturated electrolyte. The kinetic ORR currents ($I_k$) were extracted from the measured ORR currents (I) and the limiting currents ($I_{lim}$) determined at 0.4 V vs. RHE using the Koutecky-Levich equation. Finally, kinetic currents were normalised with the ECSA and the initial Pt mass loading to obtain the surface area specific activity (SA) and the mass-specific activity (MA), respectively. All the activity data reported was obtained with cathodic scans and not corrected for mass transport and solution resistance.

Durability load cycling was carried out after the measurement of the beginning of life (BOL) CV and ORR activity.[21] Initially the WE was cycled between 0.075 – 1.225 V vs. RHE at 100 $mV.s^{-1}$ to clean the catalysts of any impurities and contaminants and to produce a reproducible CV. This was followed by 3 CVs at a lower scan rate of 20 $mV.s^{-1}$ for ECSA measurements. At the end of each load cycling CV set, three CVs were obtained, and the 3$^{rd}$ was used for the calculation of the new ECSA. Load cycling for catalyst durability measurements was carried out in a 0.1 M $HClO_4$ solution at 25 ºC, in an argon saturated solution. The WE was cycled at 50 $mV.s^{-1}$ between 0.6 – 1.0 V vs. RHE using a triangular wave profile with zero seconds hold at each potential and a complete cycle duration of 16 seconds (Figure 6.1 and Figure 6.2).[22] Load cycling was carried out in units of 10, 100, and 1000 cycles until when the 6000$^{th}$ cycle was reached after 27 h of continuous cycling and argon saturation. As Pt durability was under investigation, in all durability experiments, the Pt counter electrode was replaced with a gold counter electrode of high surface area.

## 7.3: Results and Discussion

### 7.3.1: Synthesis and characterization of HCSs and NHCSs

The $SiO_2$ spheres were reacted with formaldehyde and resorcinol mixture, together with CTAB to produce $SiO_2$@RF as a porous structure, under hydrothermal conditions. Removal of the silica produced the hollow carbon spheres (HCSs). Reaction of $SiO_2$@RF with melamine, a nitrogen source, produced $SiO_2$@RF@Melamine and after thermal reaction and removal of the silica, the nitrogen covered HCSs (NHCSs) were produced. A schematic showing the synthesis procedure is shown in Figure 7.1.

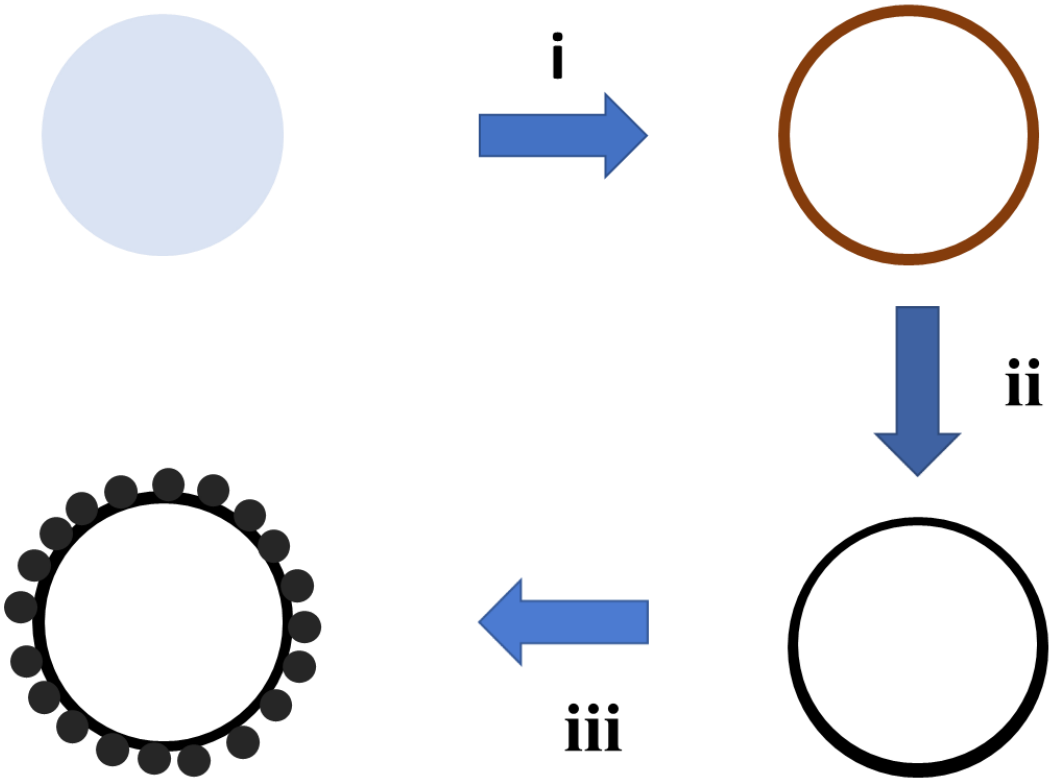



Figure 7.1: Schematic of the formation of Pt/HCSs and Pt/NHCSs. (i) $SiO_2$ to $SiO_2$@RF (ii) $SiO_2$@RF to HCSs or NHCSs, (iii) HCSs or NHCSs to Pt/HCSs or Pt/NHCSs.

The spherical morphology of the HCSs and the NHCSs was confirmed by SEM, (discussed in Chapter 4.2).

The HCSs and NHCSs were characterized using Raman spectroscopy to determine the structural order and defects in the material. The area under the Raman spectra (Figure 7.2) was deconvoluted to separate the contributions of the respective D, D1, D2 and G bands. The G band of the occurs as a result of the contribution of the vibrational modes of the graphitic carbon [23] while the D band occurs as a result of the contribution of the diamond like carbon with an $sp^3$ hybridization. The extent of graphitization and defects in the materials is measured by the ratio of the area under the D and G band using a formula known as the $I_D/I_G$ ratio. For a comparison of two materials, the one with a lower ratio is considered more graphitic as the contribution of its G band is more pronounced than that of the D band which is due to defective amorphous carbon. The HCSs had an $I_D/I_G$ of 0.98 while the NHCSs had an $I_D/I_G$ of 1.22 (Table 7.1). Comparatively, the carbon of the commercial benchmark catalyst had a much lower ratio of 0.68 indicating a higher extent of graphitization. It was expected that the NHCSs would exhibit a much higher $I_D/I_G$ ratio compared to the pristine HCS. This is due to the nitrogen disturbing the long-range order of the carbon in the pristine material resulting in the in cooperation of defects in the structure of the carbon of the HCS. The presence of these defects increases the disorder of the carbon[24]. For more graphitic materials, the G peak occurs at lower Raman frequency as seen in the HCS (1586 $cm^{-1}$), (Table 1) while the less graphitic materials exhibit G peaks at higher Raman frequency. In the case of NHCS, the G peak occurs at 1601 $cm^{-1}$. [25]

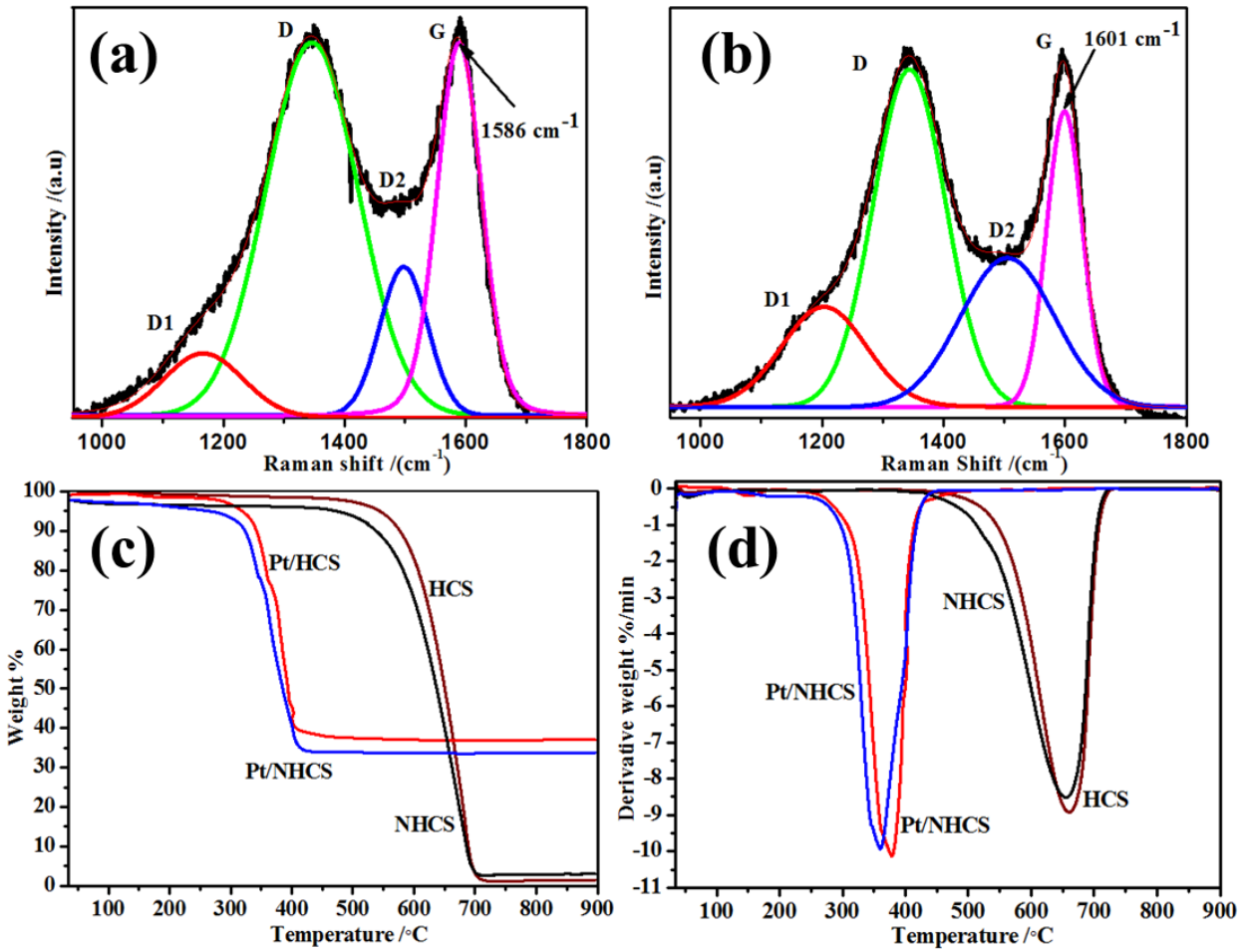



Figure 7.2: Raman spectra of HCSs (a) Raman spectra of NHCSs (b) TGA profiles of HCSs, NHCSs, Pt/HCSs and Pt/NHCSs (c) TGA derivative profiles of HCSs, NHCSs, Pt/HCSs and Pt/NHCSs.

Table 7.1: Deconvoluted Raman spectra data for HCSs and NHCSs

| | D band | | | G band | | | |
|---|---|---|---|---|---|---|---|
| | FWHM | Intensity | Position | FWHM | Intensity | Position | $I_D/I_G$ |
| Vulcan | 44 | 449 | 1345 | 38 | 649 | 1576 | 0.69 |
| NHCSs | 152 | 79 | 1353 | 73 | 79 | 1601 | 1.22 |
| HCSs | 138 | 105 | 1334 | 61 | 98 | 1586 | 0.98 |

The HCSs and NHCSs were analysed using TGA (up to 900ºC) in air to investigate the thermal stability of the materials under oxidizing conditions. The TGA (Figure 7.2 (c)) and DTGA (differential TGA) (Figure 7.2 (d)) profiles of the HCSs and NHCSs are reported are shown above. The pristine HCSs completely decomposed at a slightly higher temperature of 660ºC compared to 658ºC for the N doped carbon. Also shown is the earlier onset of the thermal degradation of the NHCSs (400ºC) compared to the HCS (450ºC). The slightly lower decomposition temperature for the doped NHCSs is attributed to the defects in the carbon structure introduced by doping with Nitrogen atoms. These defects make the carbon more prone to chemical processes like combustion, compared to the more ordered, pristine HCS[18]. For both support materials, the final residual weight (%) is less than 2% indicating that at 900ºC all the carbon has decomposed and that the $SiO_2$ etching process was successful. The TGA and DTGA profiles of Pt/HCSs and Pt/NHCSs are shown in Figure 7.2 (c) and 7.2 (d). The residual Pt was found to be approximately 38 wt.% for both the Pt/HCSs and Pt/NHCSs catalysts. The deposition of Pt nanoparticles enhanced the combustion of the carbon and consequently lowered the thermal stability of the materials as shown by the lower decomposition temperatures of the Pt/HCSs. The decomposition of Pt/NHCSs also occurred at a lower temperature compared to the NHCSs. This catalytic effect of Pt enables the faster combustion of the carbon supports and hence enables the process to occur at lower temperatures than for the support materials.[26] The Pt/HCSs and Pt/NHCSs showed multiple decomposition temperatures corresponding to disordered and ordered carbon for the low and high decomposition temperatures, respectively.[27]

The HCSs or NHCSs supports were reacted with $Pt(acac)_2$ in ethanol under reflux to give Pt/HCSs and Pt/NHCSs catalysts with a weight loading of approximately 40wt.%.[19]

The synthesized Pt nanoparticles appear to have spherical morphology under TEM (Figure 7.3) with measured particle sizes of 3.9 ± 0.5 nm and 3.8 ± 0.6 nm for the Pt/HCSs and Pt/NHCSs respectively (Table 7.3).

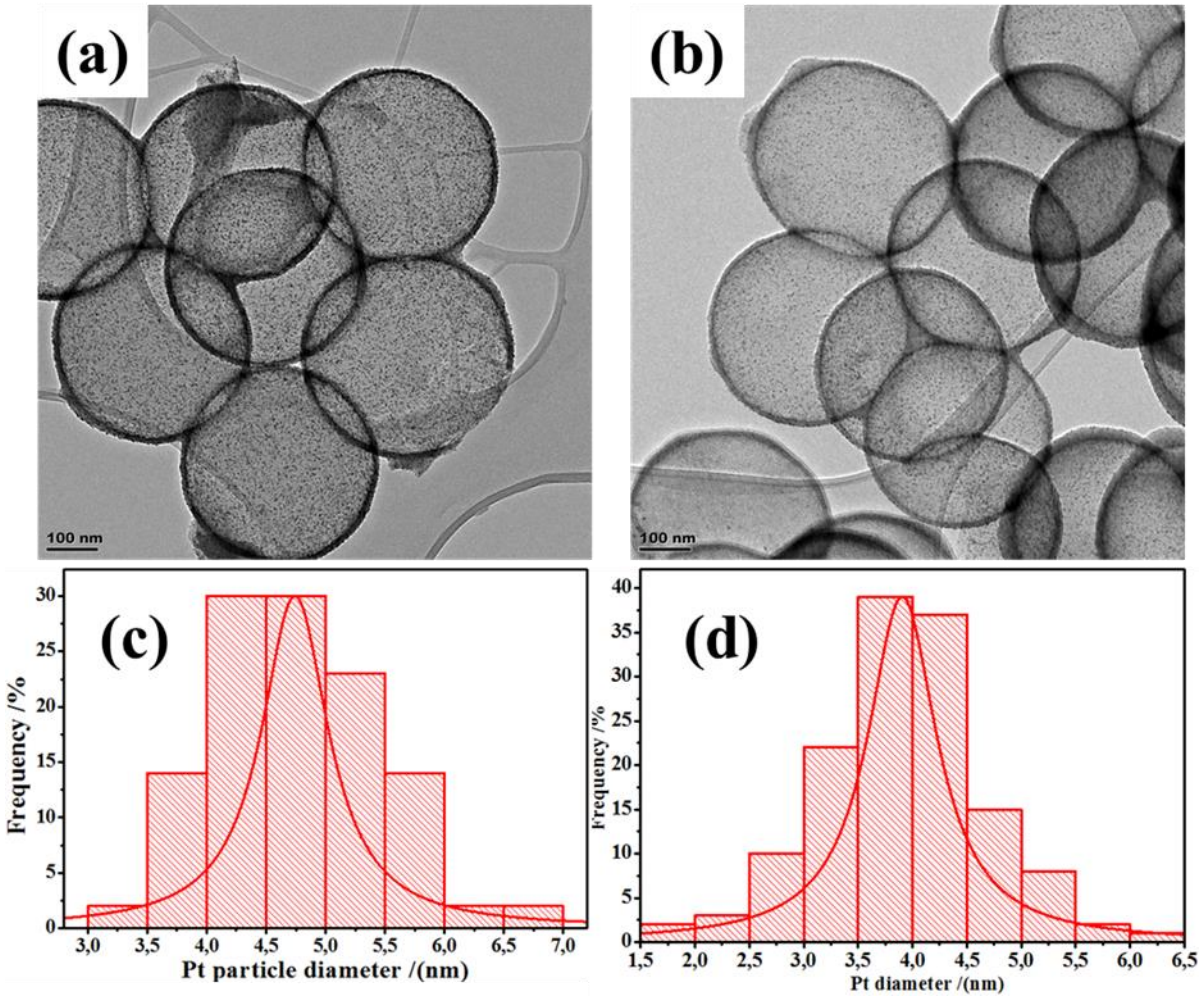



Figure 7.3: TEM image of (a) Pt/HCSs, (b) Pt/NHCSs, (c) particle size distribution of Pt on Pt/HCSs and (d) particle size distribution of Pt on Pt/NHCSs.

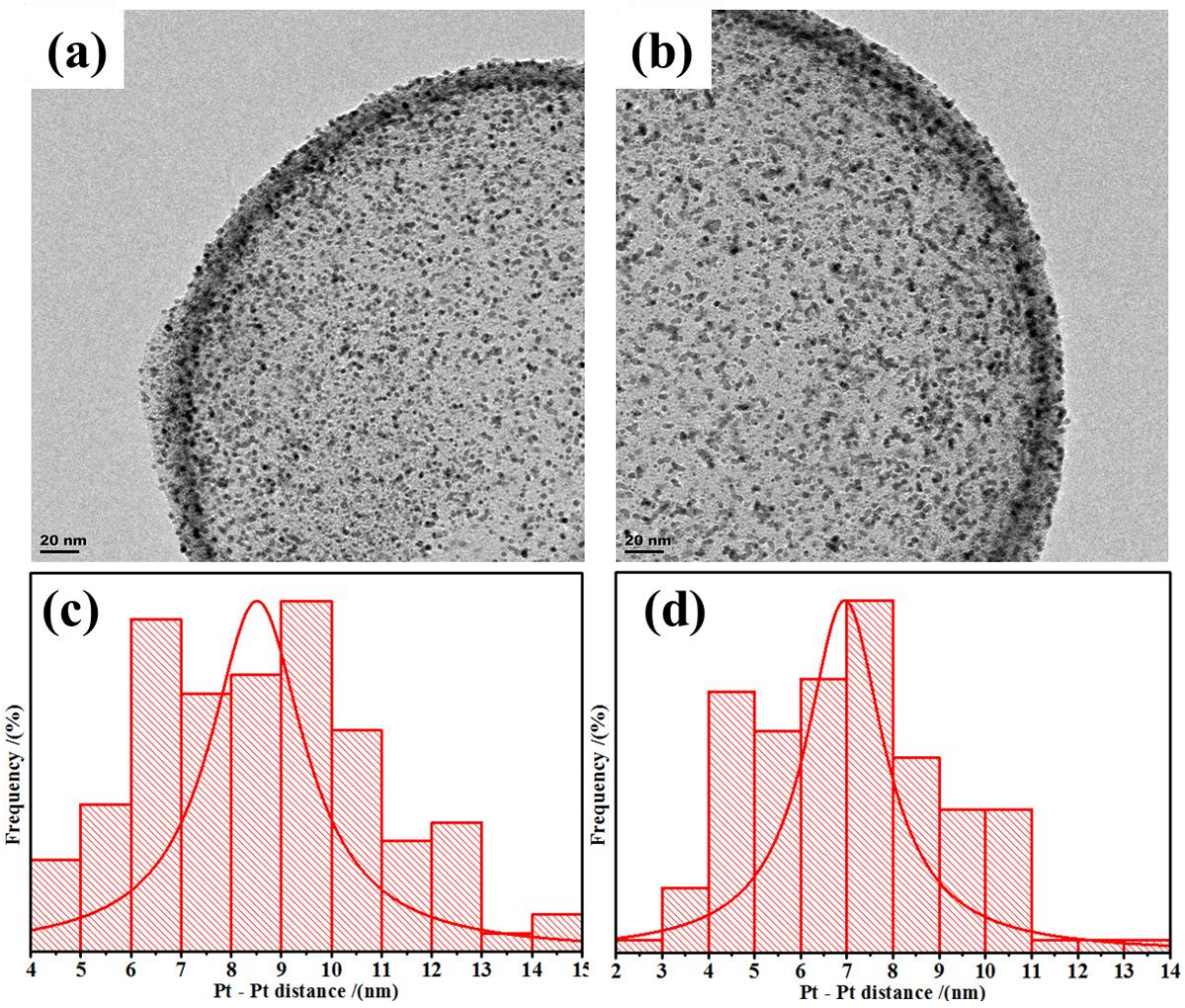



Figure 7.4: TEM image of (a) Pt/HCSs (b) Pt/NHCSs (c) Pt – Pt interparticle distance of Pt/HCSs (d) Pt – Pt interparticle distance of Pt/NHCSs.

A strong support interaction is suggested by the small inter-particle distances of the Pt nanoparticles deposited on both supports (6.5 ± 1.9 nm for Pt/HCSs and 6.1 ± 1.1 nm for Pt/NHCSs (Figure 7.4, table 7.3)). The smaller Pt interparticle distances are due to the numerous defects on the supports that provides numerous nucleation sites for Pt during deposition.[28] The Pt nanoparticles supported on NHCSs were expected to have smaller inter-particle distance due to the combination of electron rich nitrogen groups and defects that improved the nucleation and growth dynamics of the Pt particles.[29] The average Pt size increased after catalyst durability studies (figure 7.5) whereby Pt/HCS (4.8 ± 1.2 nm) and Pt/NHCSs ( 4.9 ± 1.7 nm).

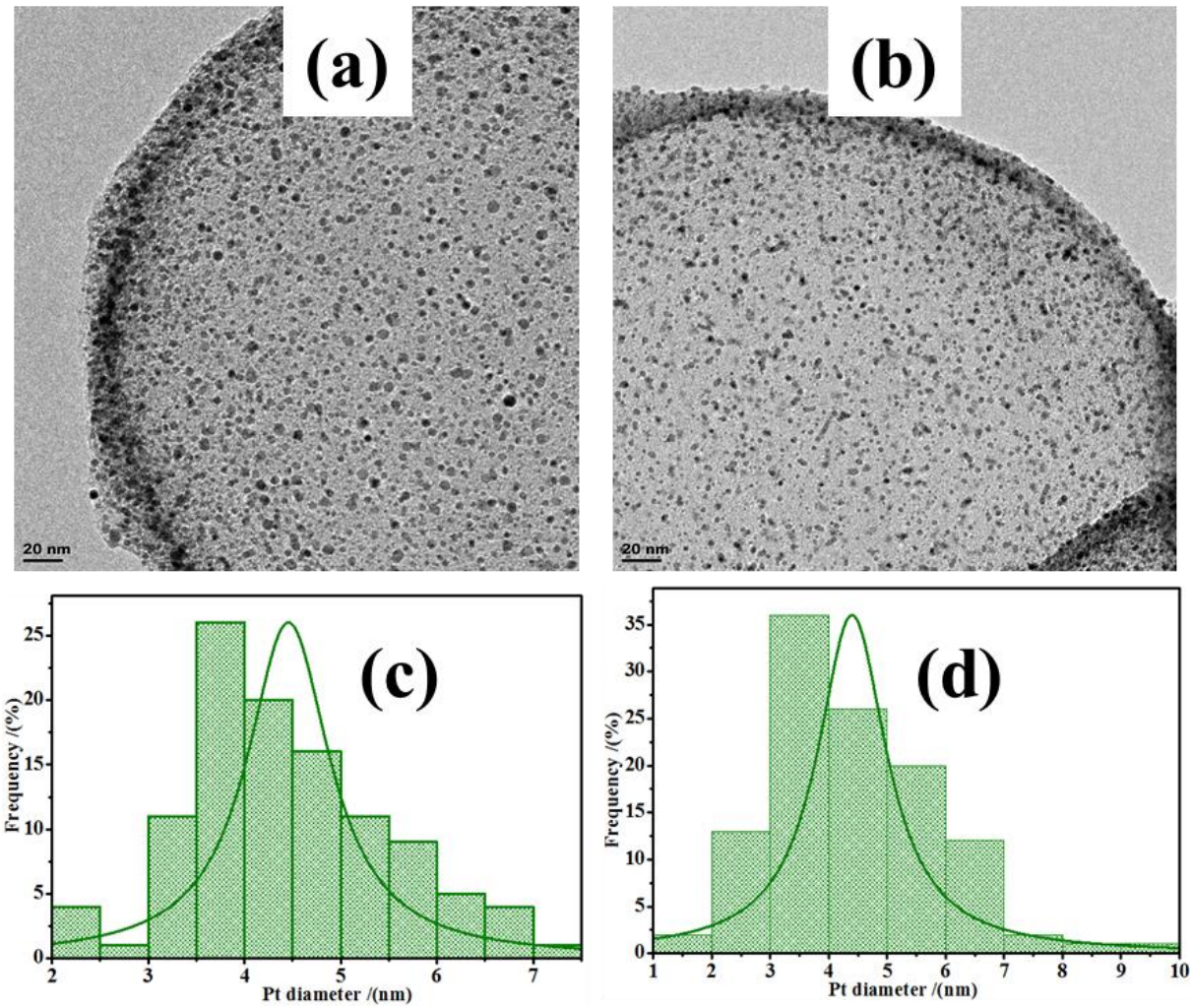



Figure 7.5: After durability study TEM image of (a) Pt/HCSs (b) Pt/NHCSs (c) particle size distribution of Pt on Pt/HCSs (d) particle size distribution of Pt on Pt/NHCSs.

The textual properties and surface area of the materials were investigated using BET. The materials were both found to exhibit type II BET isotherms (Figure 7.6) that is characterized by monolayer gas physisorption at low relative pressure and multilayer gas adsorption at high relative pressure.[30]

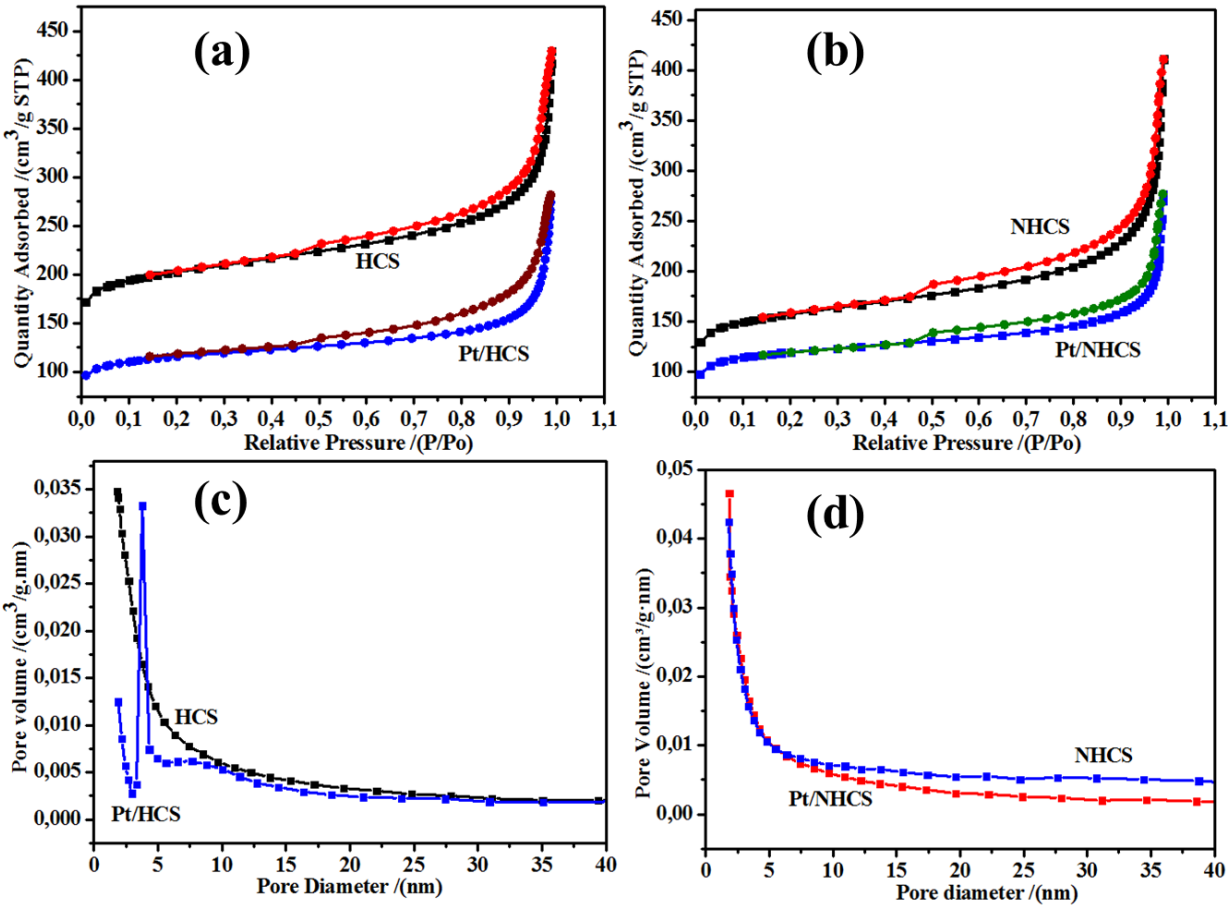



Figure 7.6: BET isotherms for (a) HCSs and Pt/HCSs and (b) NHCSs and Pt/NHCSs. Pore size distribution plots for (c) HCSs and Pt/HCSs and (d) NHCSs and Pt/NHCSs.

The pristine HCSs and the NHCSs had comparably high BET surface areas of 832 $m^2/g$ and 604 $m^2/g$ (Table 7.2), respectively. This was coupled with micropore surface areas of 595 $m^2/g$ and 322 $m^2/g$ respectively. The micropore surface area for the supports contributed 72 % of total BET surface area for HCS and 53 % for the NHCS. After deposition of the Pt nanoparticles the Pt/BHCSs had a BET surface area of 555 $m^2/g$ while the Pt/NHCSs, had a surface area of 309 $m^2/g$. After deposition of Pt, the contribution of micropores for the Pt/HCS decreased to 62% whereas for the Pt/NHCSs, the contribution of micropores increased to 65%.

Table 7. 1: Textual properties of HCSs, NHCSs, Pt/HCSs and Pt/NHCSs

| Sample | BET SA $m^2/g$ | Micropore SA $m^2/g$ | % micropore SA | Pore Volume $cm^3/g$ | Micropore volume $cm^3/g$ | % micropore volume | Pore Width /nm |
|---|---|---|---|---|---|---|---|
| HCS | 832 | 595 | 72 | 0.53 | 0.29 | 55 | 12.1 |
| Pt/HCS | 555 | 343 | 62 | 0.70 | 0.18 | 26 | 5.1 |
| Δ | 277 | 252 | 91 | 0.22 | 0.10 | 45 | 7 |
| NHCS | 604 | 322 | 53 | 0.62 | 0.16 | 26 | 8.3 |
| Pt/NHCS | 309 | 199 | 64 | 0.35 | 0.10 | 29 | 4.1 |
| Δ | 295 | 123 | 42 | 0.27 | 0.06 | 22 | 4.2 |

This reduction in surface area is coupled with a 29% reduction in micropore volume for the HCSs sample. For the NHCSs and Pt/NHCSs, there is an observed 7% reduction in pore volume (Table 7.2).

From the data, the deposition of the platinum resulted in some of the Pt nanoparticles occupying the pores of the supports, hence changing the overall pore structure of the support materials.[31] As discussed in Chapter 6, this phenomenon is known as pore confinement.

The crystallinity of the materials was investigated using PXRD and the corresponding diffractograms were also used to estimate the Pt particle size using Rietveld refinement and the Scherrer equation. Both the HCSs and NHCSs showed a structure typical of a mix of both graphitic and amorphous carbons, which is characterized by the PXRD peak broadness (Figure 7.7). The Pt on the HCSs and NHCSs showed reflections characteristic of the fcc unit cell of Pt [32] (Figure 5b). Rietveld refinement of the Pt peaks yielded a Pt crystallite size of 5.2 ± 1.2 (Pt/HCSs) and 4.8 ± 0.9 (Pt/NHCSs) (Table 7.3). The Pt crystallite sizes as determined using

the Scherrer equation were 4.5 ± 0.8 nm and 4.3 ± 0.8 nm for Pt/HCSs and Pt/NHCSs respectively. As expected, the Pt nanoparticles are smaller on the nitrogen doped support [33] and the particle diameters measured using PXRD are comparable to the TEM particle diameters.

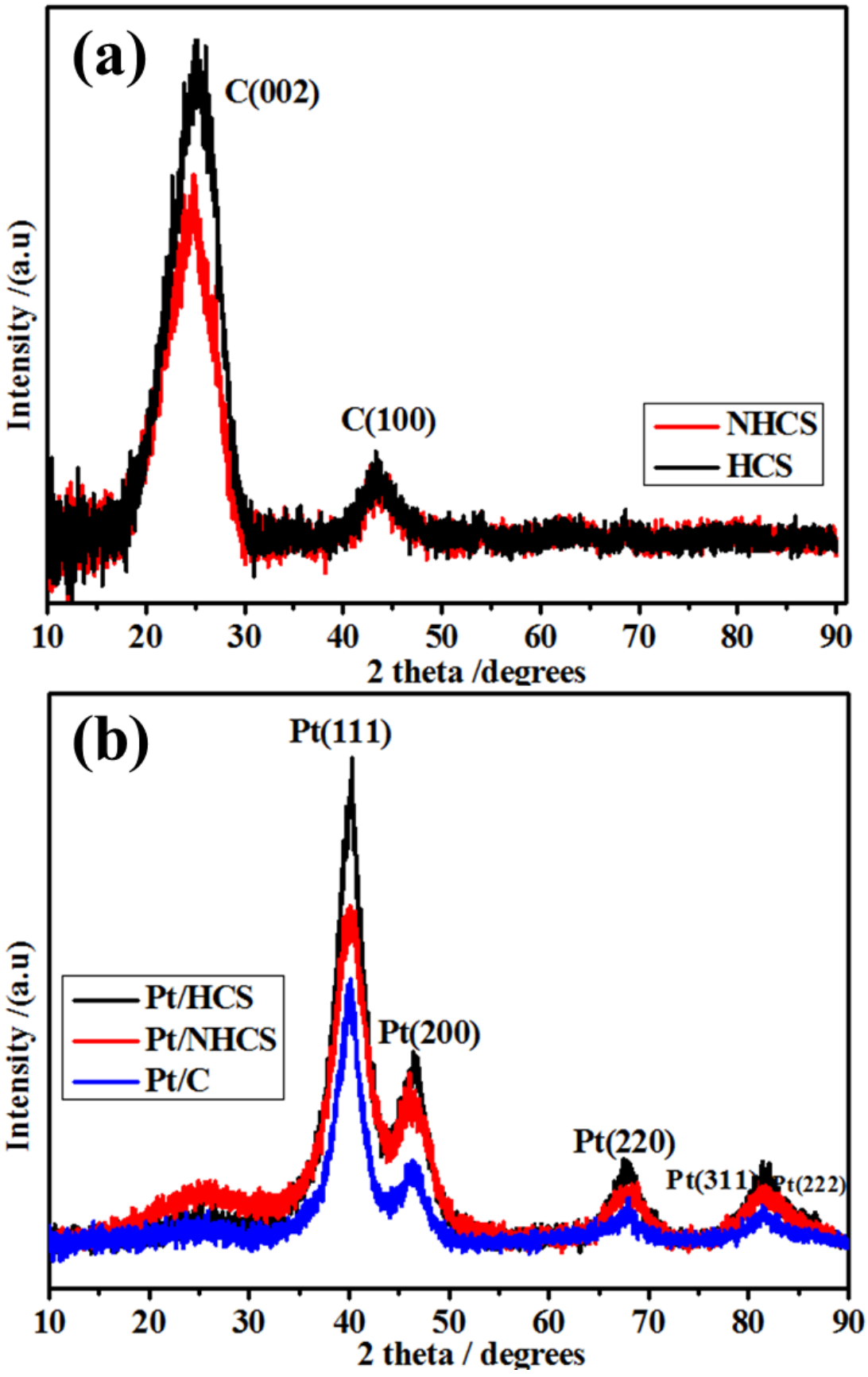



Figure 7.7: PXRD diffractograms of (a) HCSs and NHCSs, (b) Pt/HCSs and Pt/NHCSs.

The Pt nanoparticle sizes were slightly bigger than the TEM measured nanoparticles as expected from the volume averaging of particle sizes, as done in PXRD measurement of crystallite size, which tend to overlook the smaller crystallites over the larger ones.[34] Further, the reported particle sizes follow a similar trend as found for the NHCSs with smaller nanoparticles than the HCSs.

Table 7.3: Pt crystallite sizes of Pt/HCSs, Pt/NHCSs and the commercial benchmark Pt/C as measured by TEM, the Scherrer equation and Rietveld refinement

| Size/nm | Pt/HCSs | Pt/NHCSs | Pt/C |
|---|---|---|---|
| TEM | 3.9 ± 0.5 | 3.8 ± 0.6 | 3.9 ± 0.9 |
| Scherrer | 4.5 ± 0.8 | 4.3 ± 0.8 | 4.1 ± 1.2 |
| Rietveld | 5.2 ± 1.2 | 4.8 ± 0.9 | 4.7 ± 0.6 |
| Pt-Pt distance/nm | 6.5 ± 1.9 | 6.1 ± 1.1 | 6.7 ± 0.8 |

The analysis of the chemical bonding of the constituents in the surface regions of the materials was studied using XPS. For both Pt/HCSs and Pt/NHCSs, the surface surveys were measured from 50 – 550 eV binding energy. (Figure 7.8(b)). Deconvolution of the O1s spectra (Figures 7.8 and Figure 7.9) showed the presence of quinones (530.1 eV), C = O and C – O bonds (531.8 eV) and terminal O –H bonds (533.9 eV). The N1s spectra of the Pt/NHCS was deconvoluted into pyridinic nitrogen (398.1 eV), pyrrolic nitrogen (400.7 eV), graphitic N (401.9 eV), oxidized N (403.1 eV) and metal bonded N (metal-N-pyridyl) nitrogen (399.1 eV) (table 7.4).[35] The total atomic % contribution of the N groups were about 4.8 at. %, an indication that the

doping process was successful. The C1s spectra were deconvoluted into their component peaks (C = C, C – C, C – C, O - C = O and C = O bonds) for both Pt/HCSs and Pt/NHCSs (Figures 7.8 and Figure 7.9). Deconvolution of the C species present indicates the presence of ca. 29 at. % $sp^2$ (C = C) hybridized carbon for the Pt/HCSs compared to 23 at. % for the Pt/NHCSs. The increased graphitic carbon in the Pt/HCSs indicates the presence of fewer defects in the C of this sample compared to the N doped Pt/NHCSs. The functional groups shown by the deconvolution of the XPS spectra indicated the presence of a chemically active support surface able to influence the behaviour of the Pt catalyst through processes such as charge transfer, better Pt-support contact, and better Pt-support interactions.[36]

Table 7.4: Data for the deconvoluted high resolution N1s spectra for Pt/NHCSs

| Sample | N1s | | | | |
|---|---|---|---|---|---|
| Pt/NHCS | Pyridinic N (i) | Metal N (ii) | Pyrrolic N (iii) | Graphitic N (iv) | Oxidized N (v) |
| (BE/eV) | 398.1 | 399.1 | 400.7 | 401.9 | 403.1 |
| (Atomic%) | 1.2 | 0.3 | 1.8 | 0.9 | 0.6 |

The Pt4f spectra for Pt/HCSs and Pt/NHCSs samples were also deconvolved (Figures 7.8 and Figure 7.9) with peak assignments are shown in Table 7.5. Upward Pt binding energy shifts were observed for the Pt/NHCSs when compared to the Pt/HCSs.

Table 7.5: Data for the deconvoluted high resolution Pt 4f spectra for Pt/HCSs and Pt/NHCSs

| | Pt4f | | | |
|---|---|---|---|---|
| Sample | Pt4f7 metal | Pt4f7 PtO | Pt4f5 - metal | Pt4f5 – PtO |
| (BE/eV) Pt/HCSs | 71.2 | 72.0 | 74.5 | 75.9 |
| (BE/eV) Pt/NHCSs | 71.1 | 72.1 | 74.5 | 75.9 |
| Δ eV | 0.1 | 0.1 | 0 | 0 |
| (Atomic%) Pt/HCSs | 2.7 | 0.9 | 2.6 | 0.3 |
| (Atomic%)Pt/NHCSs | 2.6 | 0.5 | 2.2 | 0.3 |
| Δ Atomic % | 0.1 | 0.4 | 0.4 | 0.1 |

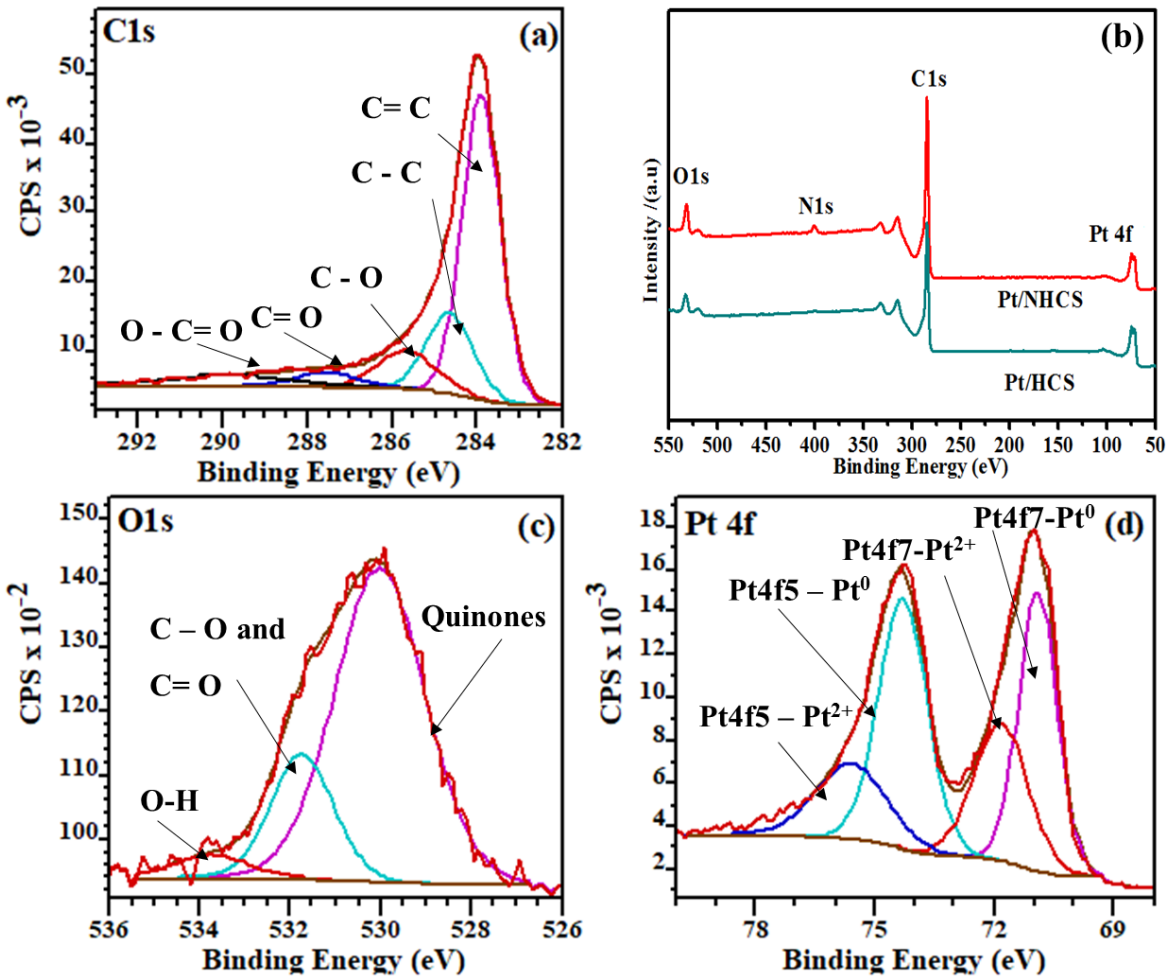



Figure 7.8: Deconvoluted high resolution XPS spectra for Pt/HCSs (a) C1s, (b) low resolution surveys of Pt/HCS and Pt/NHCS (c) O1s and (d) Pt 4f.

The shifts in the binding energies are attributed to different interactions between the Pt and the HCSs and NHCSs supports. The Pt 4f spectra were deconvolved into metallic Pt and oxidized Pt (PtO) with metallic Pt accounting for more than 90 at. % of Pt species present in both samples. This shows that most of the Pt on the surface and in the pores of both the catalysts is metallic Pt.

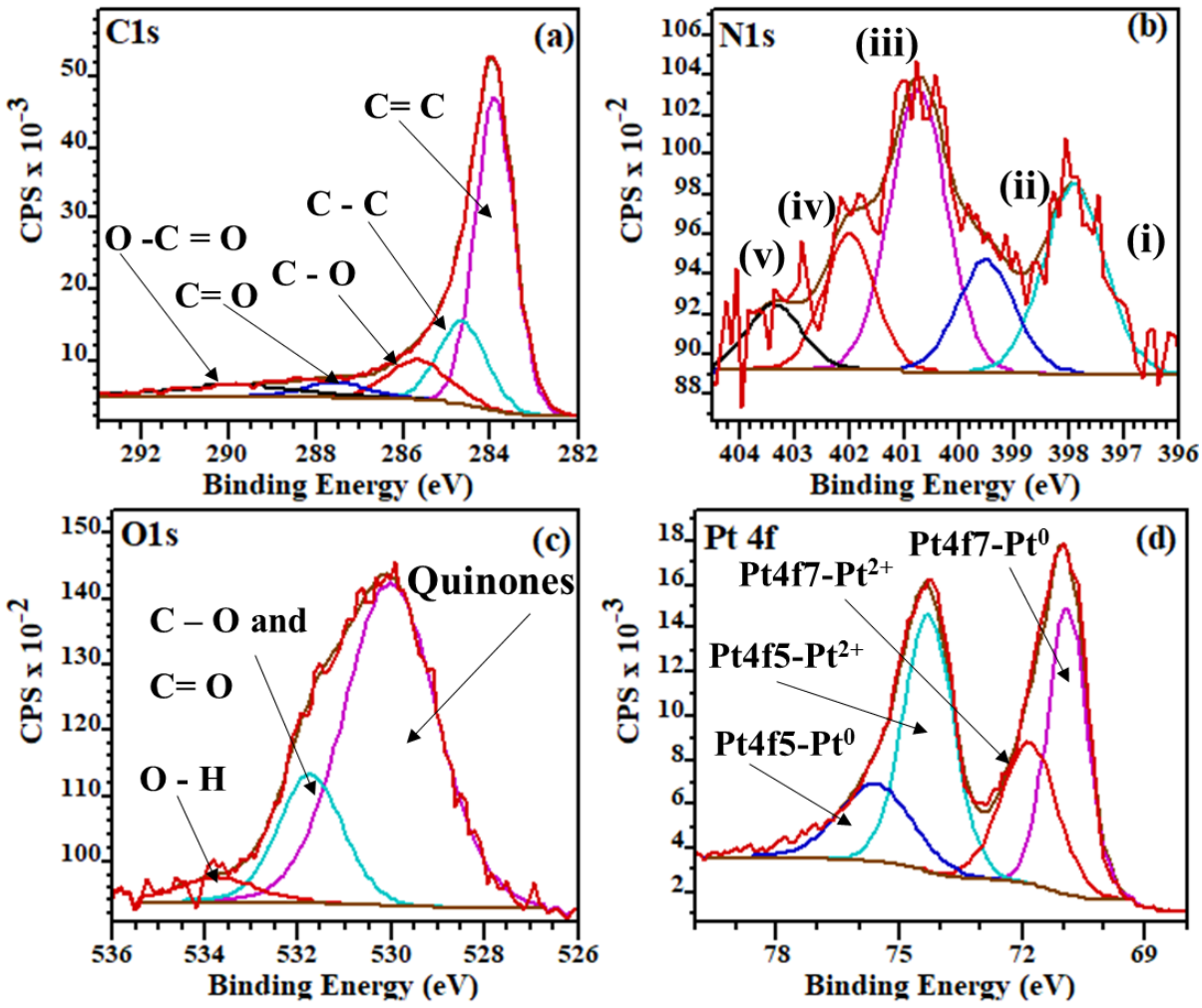



Figure 7. 9: Deconvoluted high resolution XPS spectra for Pt/NHCSs (a) C1s, (b) N1s (c) O1s and (d) Pt 4f.

## 7.4: Electrochemical characterization

### 7.4.1: Catalyst activity

Electrocatalysis characterisation of the catalysts are presented in Figure 7.10. The materials were studied using cyclic voltammetry and linear sweep voltammetry for ORR activity. All samples exhibited typical features of a Pt/C catalyst (Figure 7.10a) specifically the peaks for under potential deposition of $H_2$, $H_{UPD,}$ region, 0.0 – 0.4 V vs. RHE and peaks for the desorption of $H_2$ in the same potential window in the positive scan direction. The oxidation of a clean Pt surface occurs between 0.75 - 1.2 V vs RHE and in the same window, in the reverse scan, the PtO – Pt reaction occurs. The materials exhibited ECSA values between 58 – 68 $m^2/g$ consistent with the metal surface area calculated from the measured TEM particle sizes (Table 7.3).[37] At an electrode potential of 0.90 V vs. RHE, the kinetic current as provided by the Tafel plots (Figure 7.10c) shows that the Pt/NHCS sample is the most active followed by the Pt/HCSs and lastly the commercial Pt/C. ORR kinetics as supported by the Tafel plots (Figure 7.10e) supports the kinetic current data. The Pt/NHCS sample has the lowest Tafel slope of 92 ± 2.9 $mVdec^{-1}$ compared to 96 ± 6.5 $mVdec^{-1}$ (Pt/HCS) and 102 ± $mVdec^{-1}$ (commercial Pt/C). The Tafel slops confirms that ORR kinetics are more favourable on the nitrogen doped catalyst followed by the Pt/HCS.[38]

The area specific activities (SA) of the catalysts were obtained from the normalization of the kinetic current with the ECSAs of the catalysts. The Pt/NHCSs had a SA (391±16 $\mu A.cm^{-2}$) that is 10.5% larger than the commercial Pt/C (350 ± 10 $\mu A.cm^{-2}$) catalyst sown in table 7.6 whereas the Pt/HCSs had a SA value (387 ± 8 $\mu A.cm^{-2}$) that is 9.5 % larger than that of the benchmark Pt/C catalyst. The kinetic current of the catalysts were then normalized with the loading of platinum on the catalysts on the WE to yield the mass specific activities (MA) shown in figure 7.9(d). The observed trend shows that the Pt/NHCSs has a MA (263 ± 13 $A.g^{-1}$) that.

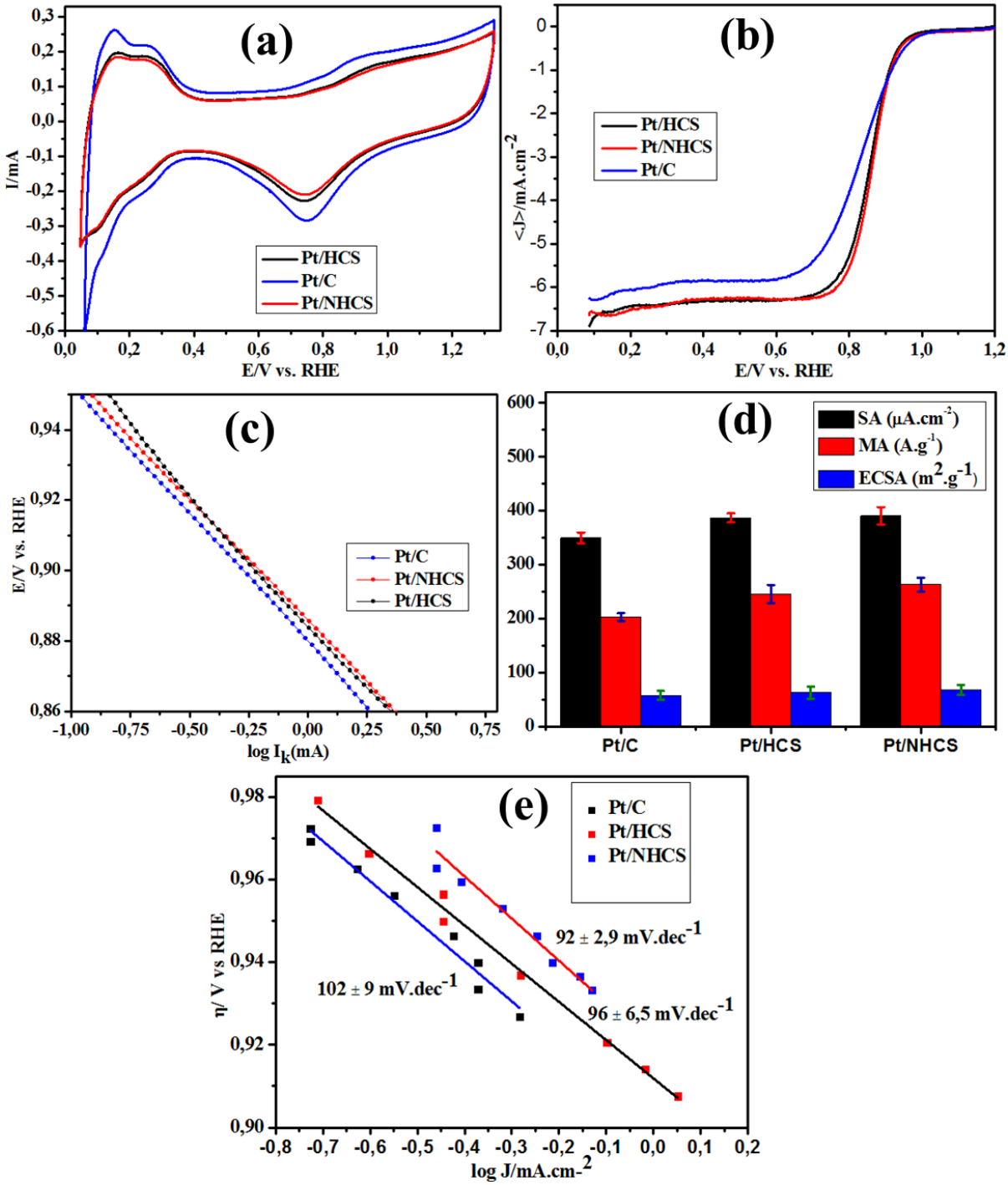



Figure 7.10: The (a) cyclic voltammograms, (b) ORR polarization I-V curves, (c) log ($I_k$)Tafel plots and (d) ORR activity and ECSA data for the Pt/HCSs, Pt/NHCSs and the commercial benchmark Pt/C (e) Tafel plots for the three catalysts.

is 22.8% compared to Pt/C (203 ± 7 $A.g^{-1}$). The MA value for Pt/HCS (246 ± 17 $A.g^{-1}$) is 17.5% larger than that of the benchmark Pt/C. The $E_{1/2}$ and $E_{onset}$ data (from Figure 7.9(b)) supports

the trends observed in the MA and SA data. The Pt/NHCS has an ORR onset potential of 1.028 V vs. RHE and an $E_{1/2}$ value of 0.862 V vs. RHE compare to 1.027 and 0.854 V vs. RHE (Pt/HCS) and 1.022 and 0.831 V vs. RHE (Pt/C). The catalysts activity data is summarized in Table 7.6

Table 7.6: Calculated ECSA and ORR activity for the Pt/HCSs, Pt/NHCSs and the commercial benchmark Pt/C catalysts. MA, SA, $I_k$ measurements obtained at 0.90 V vs. RHE

| Catalyst | ECSA / ($m^2.g^{-1}$) | MA (0.90V) / ($A.g^{-1}$) | SA (0.90V) /($\mu A.cm^{-2}$) | $I_k$(0.90V) /($mA.cm^{-2}$) | $E_{1/2}$ V. vs RHE | $E_{onset}$ V. vs RHE |
|---|---|---|---|---|---|---|
| Pt/C | 58 ± 8 | 203 ± 7 | 350 ± 10 | 2.7 ± 6 | 0.831 | 1.022 |
| Pt/HCSs | 63 ± 11 | 246 ± 17 | 387 ± 8 | 2.9 ± 11 | 0.854 | 1.027 |
| Pt/NHCSs | 68 ± 9 | 263 ± 13 | 391 ± 16 | 3.1 ± 6 | 0.862 | 1.028 |

The variation of the catalysts in terms of activity were ascribed to the nature of the supports and N doping which affected the electronic properties of the catalysts. The interaction of the Pt and the N groups alters the electronic properties of the Pt resulting in better activity and better Pt-support interaction. This interaction and enhanced electronic properties of Pt is absent in the pristine supports.[39]

The higher BET surface area of the Pt/HCS (555 $m^2/g$) and Pt/NHCS (309 $m^2/g$) and an array of micro and mesopores promotes better mass transport of oxygen reaching the Pt active faster compared to the less porous Pt/C benchmark with a surface area less than 200 $m^2/g$. The larger pores in the Pt/HCSs (5.1 nm, 0.70 $cm^3/g$) and Pt/NHCSs (4.1 nm, 0.35 $cm^3/g$) facilitates better confinement of the Pt inside the pores and thereby promoting Pt-support contact. This is advantageous as it can result in better support – Pt electronic conductivity.

A comparison with other similar Pt loaded (Pt/C) catalysts has been made (Table 7.7), and from the results provided, the materials described here exhibit ECSA, mass specific activity and area specific activity comparable to other carbon based supports as well as to other catalysts where confinement of Pt has been reported.

Table 7.7: Comparison of Pt/NHCSs and Pt/HCSs to other Pt/C catalysts reported. MA, and SA data are calculated from data at 0.90V vs. RHE

| Sample | Pt loading (wt.%) | ECSA ($m^2.g^{-1}$) | MA ($A.g^{-1}$) | SA ($\mu A.cm^{-2}$) | Comments | Ref |
|---|---|---|---|---|---|---|
| Pt/HCSs | 40 | 63 ± 11 | 246 | 387 | Pt pore confinement | This work |
| Pt/NHCSs | 40 | 68 ± 9 | 263 | 391 | Pt pore confinement | This work |
| Pt/C (HiSpec4000) | 38 | 58 ± 8 | 203 | 350 | No Pt pore confinement | This work |
| $Pt_{inside}$/KJ600 | 40 | 113 | 550 | 492 | Pt Pore confinement | 41 |
| Pt@GB-1 | 28 | - | 175 | - | Pt pore confinement | 42 |
| Pt@GB-2 | 52 | - | 134 | - | Pt pore confinement | 42 |
| Pt@HGS | 20 | 75±11 | 350 | 470 | Pt pore confinement | 40 |

## 7.4.2: Catalyst Durability

The durability LSVs of the catalysts are shown in Figure 7.11b. The bold lines are cycles before durability testing and the dashed lines are LSVs after durability testing (6000 cycles).

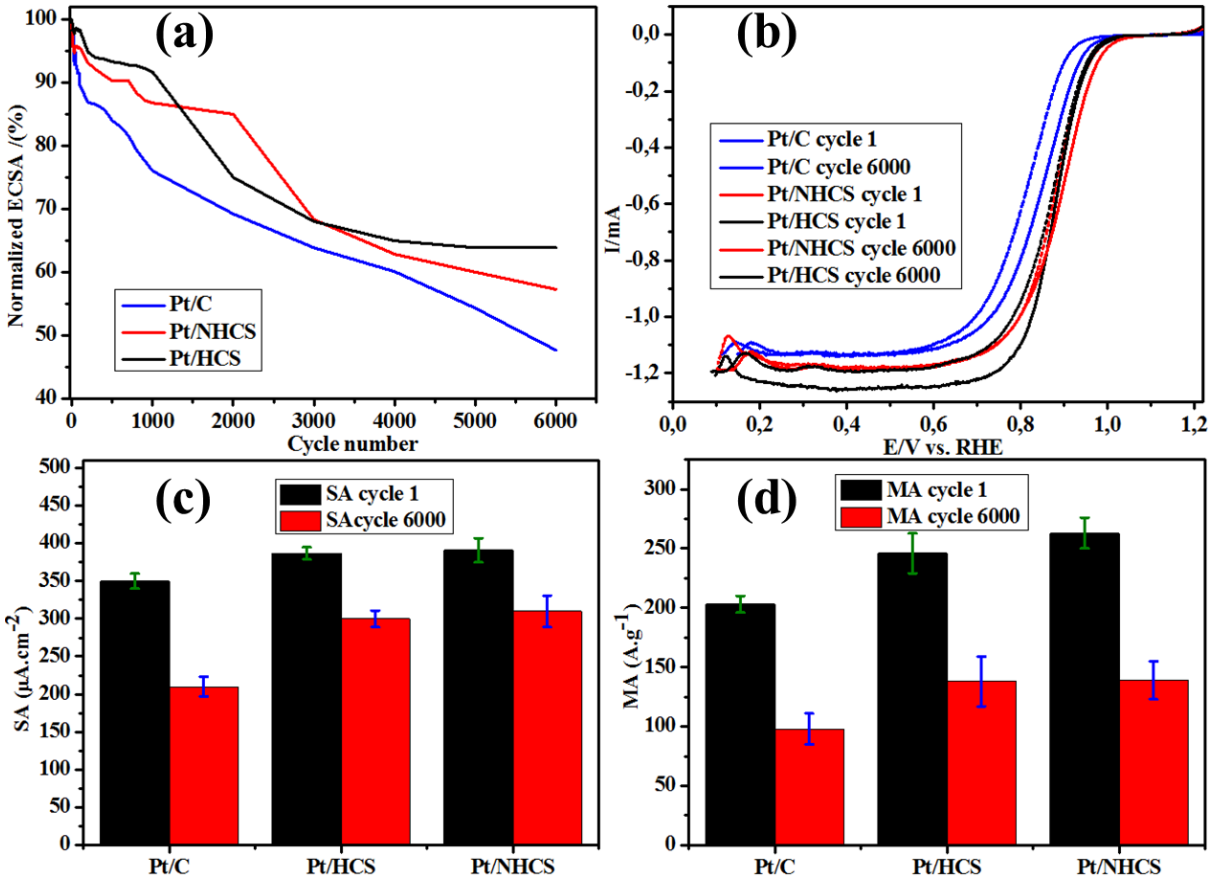



Figure 7. 11: (a) Normalized ECSA% degradation of the catalysts, (b) catalyst LSVs before and after durability studies for the Pt/HCSs, Pt/NHCSs and the commercial benchmark Pt/C catalysts (c) SA data before and after durability studies (d) MA data before and after durability studies.

For the Pt/C catalyst, there is an observed 30 mV shift in the LSV whereas for the Pt/HCS (18 mV) and Pt/NHCS (22mV) the shifts are smaller. This shift in LSVs is attributed to the loss of activity due to degradation of the Pt catalysts. The shift in the LSVs is also observed in the changes in the MA and SA of the catalysts after durability tests (Figure 7.11 c and d). There is an observed 51.7% change in MA for the benchmark Pt/C catalyst compared to 43.9% (Pt/HCS) and 20.7% (Pt/NHCS). The decline in MA was also coupled a decline in SA. For the benchmark Pt/C, a 40% decline was observed compared to a 22.4% (Pt/HCS) and 20.7% (Pt/NHCS) decline for the two new catalysts. Degradation in fuel cells is known to occur via processes that include Pt dissolution, Ostwald ripening, agglomeration, particle detachment as

well as support corrosion.[43] The degradation of Pt was observed as a decline in normalized ECSA % as load cycling was carried out. During the initial 1000 cycles (Table 7.9), the benchmark Pt/C maintained 76.1% of the initial ECSA compared to 94.5 % (Pt/HCS) and 99.8 % (Pt/NHCS). After 5000 cycles, the benchmark catalysts maintain 54.3 % of initial ECSA compared to Pt/HCS (66.2%) and Pt/NHCS (62.1%). After 6000 cycles, the largest ECSA loss was observed for Pt/C (52.4%) compared to Pt/HCS (34.6%) and Pt/NHCS (37.9%).

Table 7. 9: Comparison of the activity of the Pt/HCSs, Pt/NHCSs and commercial Pt/C before and after 6000 durability cycles

| Catalyst | MA/(0.90 V) ($m^2.g^{-1}$) Cycle 1 | MA (0.90V) / ($A.g^{-1}$) Cycle 6000 | SA (0.90V) /($\mu A.cm^{-2}$) Cycle 1 | SA (0.90V) /($\mu A.cm^{-2}$) Cycle 6000 | Δ MA/% | Δ SA/% |
|---|---|---|---|---|---|---|
| Pt/C | 203 ± 7 | 98 ± 13 | 350 ± 10 | 210 ± 13 | 51.7 | 40.1 |
| Pt/HCSs | 246 ± 17 | 138 ± 21 | 387 ± 8 | 300 ± 11 | 43.9 | 22.5 |
| Pt/NHCSs | 263 ± 13 | 139 ± 16 | 391 ± 16 | 310 ± 21 | 47.1 | 20.7 |

The loss in ECSA, MA and SA was attributed to the agglomeration of Pt particles forming bigger ones with less surface area. The growth in Pt particles can be seen from the comparison of Figures 7.3 and 7.4 above. As shown in these figures, the Pt particle size increased from 3.9 ± 0.5 nm to 4.8 ± 1.2 nm (Pt/HCS). A similar increase is observed for the Pt/NHCS sample where Pt particle size increased from 3.8 ± 0.6 nm to 4.9 ± 1.7 nm. The slightly higher particle size increase in the N doped sample is due to the initial smaller size of Pt which is more prone to agglomeration due to its higher surface energy compared to bigger particles.[44] The higher durability of the hollow carbon sphere-based supports is attributed to the structure of these materials. The HCS (832 $m^2/g$) and NHCS (604 $m^2/g$) supports have higher BET surface area and an array of mesopores and micropores which promotes the confinement of Pt particles resulting in better support to metal contact. Also confined Pt particles are more resistant to

migration and agglomeration. The higher loss in activity of the benchmark Pt/C is ascribed to low pore confinement compared to the new materials hence the Pt is easily migrated forming larger aggregates with lower surface area. Pore confinement of the Pt in the structure of the HCSs based supports was confirmed in in-situ pxrd studies discussed in Chapter 6.

Table 7.2: Loss of ECSA due to durability cycling for the Pt/HCSs, Pt/NHCSs and the commercial benchmark Pt/C catalysts

| Sample | ECSA% 0 cycles | ECSA% 1000 cycles | ECSA% 5000 cycles | ECSA% 6000 cycles | ECSA % lost |
|---|---|---|---|---|---|
| Pt/C | 100 | 76.1 | 54.3 | 47.6 | 52.4 |
| Pt/HCSs | 100 | 94.5 | 66.2 | 65.4 | 34.6 |
| Pt/NHCSs | 100 | 99.8 | 62.1 | 59.1 | 37.9 |

## 7.5: Conclusions

The Pt/HCSs and Pt/NHCSs catalysts were prepared by the ethanol reflux reduction method. Small Pt particle sizes were obtained, and the porosity of the supports and high surface area promoted good dispersion of the nanoparticles. Pore confinement of the Pt inside the pore cavities was confirmed by the enhanced durability as well as in-situ PXRD studies. The Pt nanoparticles were smaller on the nitrogen doped supports due to the modification of deposition dynamics on nitrogen rich surface. Nitrogen functional groups forms numerous defects on the surface of the support where nucleation and growth of small Pt particles can be initiated. The high BET surface area of the supports also promoted the deposition of smaller Pt particles. The Pt catalysts prepared by the ethanol reflux method demonstrated high activity and durability (Tables 7.7 – 7.9) comparable to other pore confined Pt catalysts indicating that regardless of the synthetic route, if the Pt particles are of an optimum size and supported on a chemically active support, ORR catalysis can proceed favourably.

## 7.6: References


(1) Gasteiger, H.A.; Kocha, S.S.; Sompalli, B.; Wagner, T.F. Activity Benchmarks and Requirements for Pt, Pt-Alloy, and Non-Pt Oxygen Reduction Catalysts for PEMFCs. *Applied Catalysis B: Environmental* (**2005)**, 56, 9-35.

(2) Guerrero-Moreno, N.; Cisneros-Molina, M.; Gervasio, D.; Pérez-Robles, J. F. Approaches to Polymer Electrolyte Membrane Fuel Cells (PEMFCs) and Their Cost, *Renewable and Sustainable Energy Reviews* (**2015)**, 52, 897-906

(3) Wang, J.X.; Zhang, J.; Adzic, R.R. Double-Trap Kinetic Equation for the Oxygen Reduction Reaction on Pt (111) in Acidic Media. *J. Phys. Chem. A* (**2007**), 111, 49, 12702–12710.

(4) Chen, X.; Qian, L.; Xu,J.; Chen, Y.; Li, W.; Yuan, Z.; Wan, Z.; Wang, X. Thermodynamic study of a hybrid PEMFC-solar energy multi-generation system combined with SOEC and dual Rankine cycle. *Energy Conversion and Management* (**2020**), 226(15), 113512.

(5) Garland, B. DOE Fuel Cell Program Durability Technical Targets and Testing Protocols DOE Fuel, *ECS Transactions* (**2007**), 11, 923.

(6) Yin, M.; Xu, J.; Li, Q.; Jensen, J.O.; Huang, Y.; Cleemann, L.N.; Bjerrum, N.; Xing. W. Highly active and stable Pt electrocatalysts promoted by antimony doped $SnO_2$ supports for oxygen reduction reactions. *Applied Catalysis B: Environmental* (**2014**), 144, 112–120.

(7) Wang, J.; Yin, G.; Shao, Y.; Zhang, S.; Wang, Z.; Gao, Y. Effect of Carbon Black Support Corrosion on the Durability of Pt/C Catalyst. *Journal of Power Sources,* (**2007)** 171, 331-339.

(8) Liu, G.; Liu, X.; Ganesan, P.; Popov, B.N. Development of non-precious metal oxygen-reduction catalysts for PEM fuel cells based on N-doped ordered porous carbon. *Applied Catalysis B: Environmental* (**2009**), 93, 156‑165.

(9) Hernandez-Fernandez, P.; Montiel, M.; Ocon, P.; Gomez de la Fuente, J. L.; Garcia-Rodriguez, S.; Rojas, S.; Fierro, J.L.G. Functionalization of multi-walled carbon nanotubes and application as supports for electrocatalysts in proton-exchange membrane fuel cell. *Applied Catalysis B: Environmental* (**2010**), 99, 343–352.

(10) Ha, H.; Kim, I.Y.; Hwang, S.J.; Ruoff, R.S. One-Pot Synthesis of Platinum Nanoparticles Embedded on Reduced Graphene Oxide for Oxygen Reduction in Methanol Fuel Cells. *Electrochemical and Solid-State Letters*, (**2011**), 14 (7), B70-B73.

(11) Liang, J.; Li, C.; Li, W.; Qi, J.; Liang, C. Microwave-assisted polyol preparation of reduced graphene oxide nanoribbons supported platinum as a highly active electrocatalyst for oxygen reduction reaction. J*ournal of Applied Electrochemistry* (**2018**), 48, 1069–1080.

(12) Rao, C.V, Viswanathan, B. Monodispersed Platinum Nanoparticle Supported Carbon Electrodes for Hydrogen Oxidation and Oxygen Reduction in Proton Exchange Membrane Fuel Cells. *J. Phys. Chem. C* (**2010**), 114, 18, 8661–8667.

(13) Rajan, Z.H.S.; Kooyman, P.J.; Susac, D.; Mohamed, R. Organometallic chemical deposition of crystalline iridium oxide nanoparticles on antimony-doped tin oxide support with high-performance for the oxygen evolution reaction. *Catal. Sci. Technol.*, (**2020**), 10, 3938-3948.

(14) Kim, J.H.; Cheon, J.Y.; Shin, T.J.; Park, Y.J.; Joo, S.H. Effect of surface oxygen functionalization of carbon support on the activity and durability of Pt/C catalysts for the oxygen reduction reaction. Carbon (**2016**), 101, 449-457.

(15) Zhou, Y.; Neyerlin, K.; Olson, T. S.; Pylypenko, S.; Bult, J.; Dinh, H. N.; Gennett, T.; Shao, Z.; O'hayre, R. Enhancement of Pt and Pt-Alloy Fuel Cell Catalyst Activity and Durability via Nitrogen-Modified Carbon Supports. *Energy & Environmental Science* **(2010)**, 3, 1437.

(16) Liu, J.; Li, W.; Cheng, W, R.; Wu, Q.; Zhao, J.; He, D.; Mu, S. Stabilizing Pt Nanocrystals Encapsulated in N-Doped Carbon as Double-Active Sites for Catalyzing Oxygen Reduction Reaction. *Langmuir* (**2019)** , 35, 2580–2586.

(17) Stöber, W.; Fink, A.; Bohn, E. Controlled Growth of Monodisperse Silica Spheres in the Micron Size Range. *Journal of Colloid and Interface Science* (**1968)** ,26, 62–69.

(18) Dlamini, M. W.; Phaahlamohlaka, T. N.; Kumi, D. O.; Forbes, R. Jewell, L. L.; Coville, N.J. Post Doped Nitrogen-Decorated Hollow Carbon Spheres as a Support for Co Fischer-Tropsch Catalysts. *Catalysis Today* (**2020)**, 342, 99–110.

(19) Mohamed, R.; Binninger, T.; Kooyman, P.J.; Hoell, A.; Fabbri, E.; Patru, A.; Heinritz, A.; Schmidt. T.J.; Levecque, P. Facile Deposition of Pt Nanoparticles on Sb-Doped $SnO_2$ Support with Outstanding Active Surface Area for the oxygen reduction reaction. *Catal. Sci. Technol* (**2018)**, 8, 2672-2685.

(20) Garsany, Y.; Baturina, O.A.; Swider-Lyons, K.E.; Kocha, S.S. Experimental Methods for Quantifying the Activity of Platinum Electrocatalysts for the Oxygen Reduction Reaction. *Anal. Chem.* (**2010)**, 82, 6321–6328.

(21) Inaba, M. Durability of Electrocatalysts in Polymer Electrolyte Fuel Cells. *ECS Trans.* (**2009)** ,25, 573.

(22) Takahashi, I.; Kocha, S.S. Examination of the Activity and Durability of PEMFC Catalysts in Liquid Electrolytes. *Journal of Power Sources* (**2010)**, 195, 6312–6322.

(23) Sadezky, A.; Muckenhuber, H.; Grothe, H.; Niessner, R.; Pöschl, U. Raman Microspectroscopy of Soot and Related Carbonaceous Materials Spectral Analysis and Structural Information. *Carbon* (**2005),** 43,1731-1742.

(24) Parent, P.; Laffon, C.; Marhaba, I.; Ferry, D.; Regier, T.Z.; Ortega, I.K.; Chazallon, B.; Carpentier, Y.; Focsa, C. Nanoscale Characterization of Aircraft Soot: A High-Resolution Transmission Electron Microscopy, Raman Spectroscopy, X-Ray

Photoelectron and near-Edge X-Ray Absorption Spectroscopy Study. *Carbon* (**2016)**, 101, 86–100.

(25) Ferrari, A.C. Raman Spectroscopy of Graphene and Graphite Disorder, Electron–Phonon Coupling, Doping and Nonadiabatic Effects. *Solid State Communications* (**2007)**, 143, 47-57.

(26) Ma, Y.; Ricciuti, C.; Miller, T.; Kadlowec, J.; Pearlman, H. Enhanced Catalytic Combustion Using Sub-Micrometer and Nano-Size Platinum Particles. *Energy and Fuels* (**2008)**, 22, 3695–3700.

(27) Li, Z.Q.; Lu, C.J.; Xia, Z.P.; Zhou, Y.; Luo, Z. X-Ray Diffraction Patterns of Graphite and Turbostratic Carbon. *Carbon* **(2007)**, 45, 1686-1695.

(28) Geng, D.; Yang, S.; Zhang, Y.; Yang, J.; Liu, J.; Li, R.; Sham, T.K.; Sun, X.; Ye, S.; Knights, S. Nitrogen Doping Effects on the Structure of Graphene. *Applied Surface Science* (**2011)**, 257, 9193–9198.

(29) Mardle, P.; Ji, X.; Wu, J.; Guan, S.; Dong, H.; Du, S. Thin film electrodes from Pt nanorods supported on aligned N-CNTs for proton exchange membrane fuel cells. *Applied Catalysis B: Environmental* (**2020**), 260, 118031.

(30) Fagerlund, G. Determination of Specific Surface by the BET Method. *Matériaux et Construction volume (1973), 6 ,239–245.*

(31) Prieto, G.; Shakeri, M.; de Jong, K.P.; de Jongh, P.E. Quantitative Relationship between Support Porosity and the Stability of Pore-Confined Metal Nanoparticles Studied on CuZnO/$SiO_2$ Methanol Synthesis Catalysts. *ACS Nano* (**2014)** ,8, 2522–2531.

(32) Jung, S.W.; Popov, B.N. Improved Durability of Pt Catalyst Supported on N-Doped Mesoporous Graphitized Carbon for Oxygen Reduction Reaction in Polymer Electrolyte Membrane Fuel Cells. *Carbon* (**2017)**, 42, 265–274.

(33) Chen, Y.; Wang, J.; Liu, H.; Li, R.; Sun, X.; Ye, S. Knights, S. Enhanced Stability of Pt Electrocatalysts by Nitrogen Doping in CNTs for PEM Fuel Cells. *Electrochemistry Communications* (**2009)**, 11, 2071–2076.

(34) Borchert, H.; Shevchenko, E.V.; Robert, A.; Mekis, I.; Kornowski, A.; Grübel, G.; Weller, H. Determination of Nanocrystal Sizes: A Comparison of TEM, SAXS, and XRD Studies of Highly Monodisperse CoPt3 Particles. *Langmuir* (**2005)** ,21, 1931–1936.

(35) Wang, Y.; Shao, Y.; Matson, W.D.; Li, J.; Lin, Y. Nitrogen-Doped Graphene and Its Application in Electrochemical Biosensing. *ACS Nano* (**2010)**, 4, 1790–1798.

(36) Jackson, C.; Smith, G.; Inwood, D.; Leach, A.S.; Whalley, P.S.; Callisti, M.; Polcar, T.; Russell, A.E.; Levecque, P.; Kramer, D. Electronic metal-support interaction enhanced oxygen reduction activity and stability of boron carbide supported platinum. *Nat Commun.* (**2017),**8,15802.

(37) Jiang, S.; Zhu, L.; Ma, Y.; Wang, X.; Liu, J.; Zhu, J.; Fan, Y.; Zou, Z.; Hu, Z. Direct Immobilization of Pt–Ru Alloy Nanoparticles on Nitrogen-Doped Carbon Nanotubes with Superior Electrocatalytic Performance. *Journal of Power Sources* (**2010)** ,195, 7578–7582.

(38) Ipadeola, A.K.; Barik, R.; Ray, S.C.; Ozoemena, K.I. Bimetallic Pd/$SnO_2$ Nanoparticles on Metal Organic Framework (MOF)-Derived Carbon as Electrocatalysts for Ethanol Oxidation *Electrocatalysis* (**2019**), 10, 366–380.

(39) Dubau, L.; Lopez-Haro, M.; Castanheira, L.; Durst, J.; Chatenet, M.; Bayle-Guillemaud, P.; Guetaz, L.; Caque, N.; Rossinot, E.; Maillard. F. Probing the structure, the composition and the ORR activity of $Pt_3Co$/C nano crystallites during a 3422 h PEMFC ageing test *Applied Catalysis B: Environmental* (**2013**), 142, 801– 808.

(40) Galeano, C.; Meier, J.C.; Peinecke, V.; Bongard, H.; Katsounaros, I.; Topalov, A.A.; Lu, A.; Mayrhofer, K.J.J.; Schüth, F. Toward Highly Stable Electrocatalysts via Nanoparticle Pore Confinement. *J. Am. Chem. Soc*. (**2012)**, 134, 20457–20465.

(41) Jauhar, A.M.; Ma, Z.; Xiao, M.; Jiang, G.; Sy, S.; Li, S.; Yu, A.; Chen, Z. Space-Confined Catalyst Design toward Ultrafine Pt Nanoparticles with Enhanced Oxygen Reduction Activity and Durability. *Journal of Power Sources* (**2020)**, 473, 228607.

(42) Lv, Y.; Fang, Y.; Wu, Z.; Qian, X.; Song, Y.; Che, R.; Asiri, A.M.; Xia, Y.; Tu, B.; Zhao, D. In-Situ Confined Growth of Monodisperse Pt Nanoparticle@Graphene Nanobox Composites as Electrocatalytic Nanoreactors. *Small* (**2015)**, 11, 1003–1010.

(43) Zhang, L.; Zhao, Y.; Banis, M.N.; Adair, K.; Son, Z.; Yang, L.; Markiewicz, M.; Li, J.; Way, S.; Li, R.; Ye, S.; Sun, X.; Rational design of porous structures via molecular layer deposition as an effective stabilizer for enhancing Pt ORR performance. *Nano Energy* (**2019**), 60, 111-118.

(44) Liu, J.; Li, W.; Cheng, R.; Wu, Q.; Zhao, J.; He, D.; Mu, S. Stabilizing Pt Nanocrystals Encapsulated in N-Doped Carbon as Double-Active Sites for Catalysing Oxygen Reduction Reaction. *Langmuir* (**2019**), 35, 7, 2580–2586.

# Chapter 8

## 8.1 General Conclusions

In this study we demonstrated that silica particles of various sizes can be prepared as moulds for supports of Pt catalysts. Even though we did not go in depth in elucidating the various growth mechanisms to make silica particles from the precursor TEOS, DIW, EtOH and ammonia solution, we manged to show that ammonia is required for the hydrolysis, condensation and to produce the spherical morphology of the silica. Dilute concentrations of reagents are suitable for a slow silica formation process. Use of large volumes of solvent requires the requisite conditions for the formation of small aggregated silica particles with a diameter approximately 60 nm. The use of concentrated reagents was needed for the formation of silica particles with a wider diameter. Holding the concentration of the other reagents constant, a comparison between the use of 1.2 L and 0.4 L of ethanol solvent resulted in silica particles varying between 60 nm and 318 nm respectively. We also manged to show that very dilute concentrations of ammonia solution can actually slow down the formation and generation of the spherical morphology. In reactions where less than optimum amount of ammonia was used, the silica did not form spheres.

The formed silica particles were used to prepare thin shell HCSs with confirmed spherical morphology and using an additional step involving melamine, NHCS were prepared. Raman spectroscopy and thermogravimetric analysis studies showed that the extent of graphitization and thermal stability of the HCSs decreases upon nitrogen doping. This lower thermal stability and low graphitization was attributed to the defects incorporated into the structure of the carbon by the nitrogen functional groups. The presence of the nitrogen groups was confirmed by XPS with an average nitrogen incorporation of approximately 7 at.%.

The textual properties of the materials revealed that they had high BET surface area with an array of meso and micropores for the supports. This was observed for the HCS, NHCS, BHCS supports. Nitrogen doping using the melamine route showed the BET surface area was reduced, however, the reduction in the BET surface area, micropore surface area, pore widths and pore volumes was not as significant as compared to when the Pt particles were deposited on the supports. Upon Pt deposition, it was observed that for all the new materials that the textual properties exhibited approximately about 50 % surface area reduction. The reduction in textual properties was attributed to the confinement of the Pt inside the pores of the HCS and NHCSs. Further, due to the similarity between the shell thickness of the BHCS and the BNHCSs with the Pt diameter, some of the Pt was actually confined with exposure on both ends of these supports. The pore confinement was confirmed by ABF-DF STEM studies as well as in situ PXRD measurements. In in situ PXRD measurements, Pt crystallite size was measured as function of the reaction temperature. It was observed that even though the Pt particles were provided with enough heat energy to agglomerate, the extent of agglomeration was low for the new Pt/HCS, Pt/NHCSs, Pt/BHCSs and Pt/BNHCSs catalysts. When compared to the commercial benchmark catalyst, the crystallite growth was minimal for these new materials. High degradation of the commercial benchmark Pt/C catalyst was attributed to its low BET surface area and low porosity which resulted in low confinement of the Pt.

TGA studies of the Pt loaded samples showed that all the new materials were loaded with approximately 40 wt.% Pt comparable with the benchmark Pt/C catalyst. The thermal stability loss of these materials compared to the unsupported supports was attributed to the catalytic properties of Pt in combustion reactions. The numerous degradation steps of the Pt supported catalysts was attributed to the various carbon arrangements in the supports. These various carbons were the more ordered graphitic carbon decomposing at higher temperature and the less ordered defective amorphous carbon decomposing at lower temperatures.

Deposition of Pt on the supports using the metal-organic deposition and ethanol reflux method resulted in Pt particles of comparable dispersion and particle size.

In oxygen reduction reaction activity and durability studies the novel materials Pt/HCSs, Pt/NHCSs, Pt/BHCSs and Pt/BNHCSs demonstrated superior activity and durability compared to the commercial benchmark Pt/C of similar Pt loading and dispersion. For the new materials durability was attributed to the pore confinement of the Pt as well as the favourable interaction between the Pt and the supports as confirmed by the XPS core levels binding energy shifts. Higher activity for the Pt/BHCSs, Pt/HCSs was attributed to a higher number of active sites exposed due to the hemispherical morphology of the support, the thin carbon support shells, high porosity, and the deposition of Pt on either side of the hemispherical support resulting in better Pt utilization and exposure of numerous active sites. Also, the pore confined Pt was exposed on both sides of the carbon shell enhancing its electronic conductivity.

The Pt/NHCSs and Pt/BNHCS samples exhibited much higher activity than the pristine samples due to the initial Pt size caused by nitrogen doping resulting in much higher Pt active sites. The slightly lower durability of the nitrogen doped supports was attributed to the defects in the structure of the carbons supports which was more prone to degradation.

## 8.2: Outlook

Pt/C materials need to be produced with a balance between high graphitization for conductivity, thermal stability and electrochemical stability and materials with enough defects to enable Pt deposition to generate a higher number of exposed Pt active sites. Using the promising BHCS and BNHCSs supports, it may be possible to alloy Pt with other ORR active metals like Ni or Co to enhance activity. The use of thinner graphitic carbon layers must also be probed as these promotes electronic conductivity of the supports and possible better anchoring of the metal nanoparticles.